MINISTRY OF EDUCATION
AND TRAINING

VIETNAM ACADEMY
OF SCIENCE AND TECHNOLOGY

GRADUATE UNIVERSITY OF SCIENCE AND TECHNOLOGY

BÙI MINH HUỆ

STUDY OF ISOMERIC RATIO AND RELATED EFFECTS IN PHOTONUCLEAR AND NEUTRON CAPTURE REACTIONS

ATOMIC AND NUCLEAR PHYSICS DOCTORAL THESIS

Ha Noi – 2022

BỘ GIÁO DỤC VÀ ĐÀO TẠO

VIỆN HÀN LÂM KHOA HỌC
VÀ CÔNG NGHỆ VIỆT NAM

HỌC VIỆN KHOA HỌC VÀ CÔNG NGHỆ

BÙI MINH HUỆ

NGHIÊN CỨU TỶ SỐ ĐỒNG PHÂN VÀ CÁC HIỆU ỨNG LIÊN QUAN TRONG PHẢN ỨNG QUANG HẠT NHÂN VÀ PHẢN ỨNG BẮT NEUTRON

LUẬN ÁN TIẾN SỸ VẬT LÝ NGUYÊN TỬ VÀ HẠT NHÂN

Hà Nội – 2022

MINISTRY OF EDUCATION
AND TRAINING

VIETNAM ACADEMY
OF SCIENCE AND TECHNOLOGY

GRADUATE UNIVERSITY OF SCIENCE AND TECHNOLOGY

BÙI MINH HUỆ

Major: Atomic and Nuclear Physics

Code: 9440106

STUDY OF ISOMERIC RATIO AND RELATED EFFECTS IN PHOTONUCLEAR AND NEUTRON CAPTURE REACTIONS

ATOMIC AND NUCLEAR PHYSICS DOCTORAL THESIS

SUPERVISORS:

1. Prof. Dr Trần Đức Thiệp
2. Dr. Sergey Mikhailovich Lukyanov

Ha Noi – 2022

Declaration of Authorship

I, Bui Minh Hue, declare that this thesis titled, "STUDY OF ISOMERIC RATIO AND RELATED EFFECTS IN PHOTONUCLEAR AND NEUTRON CAPTURE REACTIONS" and the work presented in it are my own. I confirm that:

- This work was done wholly or mainly while in candidature for a research degree at the Graduate University of Science and Technology.
- Where any part of this thesis has previously been submitted for a degree or any other qualification at this Graduate University or any other institution, this has been clearly stated.
- The data in this thesis have not been used in other publications by anyone else.
- Where I have consulted the published work of others, this is always clearly attributed.
- Where I have quoted from the work of others, the source is always given. With the exception of such quotations, this thesis is entirely my own work.
- I have acknowledged all main sources of help.

Signed:

_____

Date:

_____

Abstract

The isomeric ratios (IRs) of ^{152m1,m2}Eu, $^{195m,g;197m,g}$Hg, ^{115m,g}Cd, ^{109m,g}Pd, ^{137m,g}Ce and ^{81m,g}Se produced from photonuclear reactions (γ, n) with bremsstrahlung endpoint energies in Giant Dipole Resonance region and that of $^{115m,g;117m,g}$Cd, $^{109m,g;111m,g}$Pd, ^{137m,g}Ce and ^{81m,g}Se in thermal-epithermal neutron capture reactions (n, γ) have been determined experimentally by using the activation technique and off-line γ-ray spectroscopy measurement. The bremsstrahlung photons and neutrons were generated using the MT-25 Microtron of the Flerov Laboratory of Nuclear Reaction (FLNR), JINR, Dubna, Russia. The activity of radioisotopes was determined with a HPGe detector together with essential corrections. This work reports, obtained from (γ, n) reactions, the IRs of $^{195m,g}Hg$ withing 14 - 24 MeV, $^{197m,g}Hg$ within 18 - 24 Mev, and $^{152m1,m2}Eu$ at 19, 21 and 23 Mev for the first time. Moreover, the obtained results of $^{109m,g;111m,g}Pd$ and $^{115m,g;117m,g}Cd$ in mixed thermal-resonant neutron capture reactions (n, γ) as well as that of $^{111m,g}Pd$ in resonance neutron capture reaction (n, γ) have been the first measurements. The impact of four effects including the nucleon configuration, spin difference, excitation energy, and reaction channel effect on the experimental IRs was investigated. The measured IRs were compared not only with the literature but also with the theoretically calculated IRs for the cases in the photonuclear reaction. The calculated IRs were yielded from TALYS 1.95 code-based calculated cross section in conjunction with GEANT4 toolkit-based simulated bremsstrahlung. The six level density models and eight radiative strength functions were taken into consideration for the theoretical calculations.

Acknowledgements

Honestly, I could not complete this thesis without the support and help of many people. First and foremost, I owe special and great thanks to my supervisors, Prof.Dr.Tran Duc Thiep and Dr.Sergey Mikhailovich Lukyanov, for allowing me to start my Ph.D. and for their guidance, support, and inspiration. I am always thankful and consider them not only as my supervisor but also as my father. Prof.Dr. Tran Duc Thiep inspired and encouraged me on the abrupt road to science since 2012, when I started as a junior researcher at the Center for Nuclear Physics, Institute of Physics. He was always available to illuminate my questions. I have gained much knowledge and experience in research, work, and life from him.

I would also like to thank Dr. Truong Thi An, Dr. Phan Viet Cuong and Dr. Le Tuan Anh for cooperating on the research projects. I am grateful to the Director, Mrs. Nguyen Thi Dieu Hong and staffs of Institute of Physics as well as my colleagues at the Center for Nuclear Physics for always helping, encouraging, and giving me convenience.

I had precious time and beautiful memories in Dubna. I always remember the warm hugs and the advice of Prof.Dr. Y.E. Penionzhkevich. I am thankful for the opportunity to exchange ideas and discuss work with my colleagues at the FLNR, JINR, made me feel like part of their group. I express my deepest gratitude to the MT-25 Microtron crew for providing the irradiation beam as well as the Chemistry of transactinides department of the Flerov Laboratory of Nuclear Reaction, JINR for furnishing the experimental apparatus. I am also grateful to Mrs. Trinh Thi Thu My and my Vietnamese friends in Dubna for making my stay there very pleasant. I always had you by my side when taking a lunch break or gathering for BBQs on the Volga riverside.

I am also thankful to Dr. S.Nishimura for lending me the equipment when I was at RIKEN.

I am grateful to the Board of Directors, and employees of Graduate University of Science and Technology for helping and supporting me throughout the process of doing this thesis. I would like to acknowledge the scientific research support for excellent Ph.D. students at the Graduate University of Science and Technology in 2021. And I offer my gratitude and special thanks to Vingroup JSC and Ph.D. Scholarship Programme of Vingroup Innovation Foundation (VINIF), Institute of Big Data funded and supported my Ph.D. studies within two years under VINIF.2020.TS.18 and VINIF.2021.TS.081 codes.

Last but not least, at the bottom of my heart, I would like to express my deepest gratitude to my family and parent-in-law for supporting and loving me during this long journey. I am very thankful for my aunt, N.T.Mai, for helping and taking care of me in the stressful period of finalizing this thesis. Specially, I would like to spend a great thank my honey husband, who helped me a lot with coding. He has always encouraged and given me a happy life. He is the principal motivation for me to accomplish the present thesis.

Contents

List of Abbreviations

ADC	Analogue to Digital Converter
BCS	Bardeen-Cooper-Schrieffer
BSFG	Back-Shifted Fermi Gas
CTM	Constant Temperature Model
EXFOR	Experimental Nuclear Reaction Data Library
ENSDF	Evaluated Nuclear Structure Data File
FLNR	Flerov Laboratory of Nuclear Reaction
GDR	Giant Dipole Resonance
GEANT	GEometry ANd Tracking
GEDR	Giant Electric Dipole Resonance
GMR	Giant Monopole Resonance
GLO	Generalized Lorentzian Model
GQR	Giant Quadrupole Resonance
GSM	Generalized Superfluid Model
HF	Hauser-Feshbach
HFB	Hartree-Fock-Bogolyubov
HPGe	High Purity Germanium
HVM	Huizenga-Vandebosch Model
IAEA	International Atomic Energy Agency
IC	Internal Conversion
IR	Isomeric Ratio
JINR	Joint Institute for Nuclear Research
LD	Level Density
PDR	Pygmy Dipole Resonance
RIB	Radioactive Ion Beam
RIPL	Reference Input Parameter Library
QD	Quasi-Deuteron
QRPA	Quasiparticle Random Phase Approximation
SLO	Standard Lorentzian
γSF	γ-ray Strength Function

List of Physical Quantities

A	mass number
a	level density parameter
$\tilde{a}$	asymptotic level density parameter
$a(S_n)$	LD parameter at the neutron separation energy
D_0	experimental and theoretical average resonance spacing
J	angular momentum
L	multipolarity
π_i, π_f	parities of the initial and final states
$t_{1/2}$	half-life
λ	decay constant
N	neutron number
Z	atomic number
R	nuclear radius
ϵ_0	electric constant (= 8.8542 x 10^{-12} F/m)
$\hbar$	reduced Planck's constant (= 1.0546 x 10^{-34} J.s)
c	velocity of light (= 3.10^8 m/s)
E_γ	gamma-ray energy
σ_i	cross-section
Y	yield
ϕ	flux
ρ	level density
f_{XL}	gamma strength function
T_{XL}	transmission coefficient
σ	spin cut-off parameter
Γ	decay width
γ	shell damping parameter
Δ	pairing energy
δW	shell correction energy
N_{low}, N_{top}	levels for the matching problem
T	nuclear temperature

$\sigma(S_n)$	spin cut-off parameter at the neutron separation energy
σ_0(M1)	strengths of magnetic dipole resonance peak
σ_0(E1)	strengths of electric dipole resonance peak
E(M1)	centroid energy of magnetic dipole resonance peak
E(E1)	centroid energy of electric dipole resonance peak
Γ(M1)	width of magnetic dipole resonance peak
Γ(E1)	width of electric dipole resonance peak

List of Tables

List of Figures

Introduction

Understanding the structure and properties of an atomic nucleus via forces between nucleons has always been a major challenge in Nuclear Physics. It can be studied by using natural radioactivity and nuclear reactions. Both processes result in the emission of radiations carrying important information about the characteristics of nucleus. Detecting, measuring and analyzing those radiations reveal the nuclear structure and properties. While the number of natural radionuclides is limited to only a few dozen nuclei, nuclear reactions offer a more convenient method for studying all nuclei. The nuclear reaction may occur in various processes such as compound, pre-equilibrium, or direct ones depending on the type of projectile and target as well as the incident energy. As a result of nuclear reaction, the residual nucleus can exist in the isomeric or ground states. The isomeric state (isomer) is a meta-stable excited state of the nucleus, which experienced a hindrance in its decay. The half-lives of isomers range from *nanoseconds* to *years*. Since the last couple of decades, there has been a rapid growth in the radioactive isotope and rare isotope beam (RIB) facilities, and cutting-edge nuclear experimental techniques relative to the development of nuclear detectors, digital electronics, analyzers, and computational power resulting in the remarkably theoretical and experimental studies on isomers. Nowadays, increasing numbers of isomers are discovered in diverse regions of the nuclear landscape. Isomers play crucial role in fundamental research in nuclear physics and astrophysics but also can be utilized in many applications such as therapy, medical imaging, γ-ray lasers, nuclear battery and nuclear clock.

Along with the isomeric investigation, the isomeric ratio (IR), being the probability ratio of the formation of isomeric and ground states, is also a very fascinating issue since it can disclose considerable details about the nuclear structure and features, and the involved reaction mechanism. Besides, the IR correlates strongly to the energy and angular momentum of projectile, nuclear level density and spin distribution of the excited nucleus, and many other characteristics. Therefore, IRs can be also precious data not only for studying the nuclear structure, reaction mechanism

and nuclear applications but for examining different nuclear reaction models. The experimental IR can be measured with the high accuracy since the isomeric pair is generated simultaneously throughout the nuclear reaction process under the identical experimental setup. To compare the measured IRs with theoretical predictions, several nuclear model codes can be used to calculate IRs. The TALYS code is currently most often employed to simulate nuclear reactions and predict the cross-section and IR. The TALYS is a flexible and easy-to-use code containing the latest nuclear reaction models. The TALYS code can implement reactions between the projectiles γ, n, p, d, t, ^{3}He, and ^{4}He with energies of 1 keV up to 200 MeV and target nuclei with the mass of 12 to 339 a.m.u. It is worth noting that the photon-induced reactions mainly irradiate by the bremsstrahlung photons due to the lack of a mono-energetic photon source with high intensity. The TALYS code, however, only computes the reaction cross-section bombarded by mono-energetic projectiles. Hence, the TALYS code is often combined with the bremsstrahlung simulation code to obtain the integrated cross-section, flux-weighted average cross-section, and IR in photonuclear reaction irradiated by bremsstrahlung. The GEANT4, a transportation/Monte-Carlo simulation toolkit with a free, open-source software package, can simulate the bremsstrahlung spectra.

This thesis aims to study the experimental IRs in photonuclear reactions (γ, n) with bremsstrahlung endpoint energies in the GDR region on heavy nuclei $^{196,198}Hg$ and ^{153}Eu as well as IRs in thermal, resonant and mixed thermal-resonant neutron-induced reactions (n, γ) on $^{108,110}Pd$ and $^{114,116}Cd$ nuclides. The experiments were conducted using the MT-25 Microtron of FLNR laboratory, JINR, Dubna, Russia. The research method was the activation method in conjunction with the offline γ-spectrum measurement. The principal reasons for selecting the targets and two kinds of nuclear reactions are insufficient IRs and/or the large discrepancy between the data, and well-known reaction mechanisms. For the photon-induced reaction in the GDR region, the process taking place is mainly the absorption of an electric dipole γ quantum (E1) by a target nucleus with spin J_0, constituting the compound nucleus at excitation states with spins $J_C = J_0, J_0 \pm 1$. Thus, in this case, the theoretical consideration becomes unambiguous. The even-even nuclei $^{196,198}Hg$ with spin of 0^+ belong to nuclear range with Z = 73–81 and A = 182–206. They lie between strongly deformed nuclear region and the spherical nuclear region in the neighborhood of A = 208. Because of the high angular momentum of the last protons ($1h_{\frac{11}{2}^-}$) and neutrons ($1i_{\frac{11}{2}^-}$), isomers are expected to

populate at the high-spin states through the nuclear reactions. Odd-even target nucleus ^{153}Eu is strongly deformed and its ground state spin is $\frac{5}{2}^+$ defined by spin of the last proton single-particle state ($\frac{5}{2}^+[413]$) in the Nilsson diagram. By means of (γ, n) reaction, the residual nucleus ^{152}Eu can be formed and existed either in the ground state ^{152g}Eu with spin of 3^- or in isomeric states $^{152m1}Eu$ and $^{152m2}Eu$ with spins of 8^- and 0^-, respectively. Up till now, there have been the missing IR data of isomeric pairs of Hg and Eu isotopes in the photon-irradiated reactions in the GDR region. The number of literature data are, moreover, much scattered. For the thermal and resonant neutron capture reaction, it presumed that only s-wave neutrons were captured. Thus, this type of reaction presents definite interest on account of the following striking features: (a) the compound nucleus is excited to the energy level equivalent to its neutron binding energy since the kinetic energies of thermal and resonant neutrons are negligible compared with the binding energy; (b) the total angular momentum of compound nucleus may occupy three values J_0, $J_0 \pm 1/2$; and (c) the incident neutron transferred the angular momentum $1/2\hbar$ to the target nucleus. These features hinder the spin values of excitation levels leading to the reaction elucidation in a simple and easily understandable way. Accordingly, the study of IR in this type of reaction can provide valuable information on the nuclear level structure, the dependence of level density on the spin. Up to date, there have been a few works on the measurement of IRs in thermal and resonant neutron capture reactions of $^{108,110}Pd$ and $^{114,116}Cd$ nuclei, especially no data for mixed thermal-epithermal neutron capture reactions on all these nuclei and resonant neutron capture on ^{110}Pd nucleus.

In this thesis, we have carried out the following works:

- Determination of the experimental IRs of isomeric pairs $^{195m,g;197m,g}Hg$ and $^{152m1,m2}Eu$ in $^{196,198}Hg(\gamma, n)$ and $^{153}Eu(\gamma, n)$ reactions, respectively, irradiated by bremsstrahlung with endpoint energy within the whole GDR region.

- Measurement of IRs of $^{109m,g;111m,g}Pd$ and $^{115m,g;117m,g}Cd$ in $^{108,110}Pd(n, \gamma)$ and $^{114,116}Cd(n, \gamma)$ reactions, respectively, induced by thermal, resonant and mixed thermal-resonant neutrons.

- Consideration of several effects affecting IRs as spin difference, excitation energy, nucleon configuration, angular momentum transfer and reaction channel effects

in the above-mentioned isomeric pairs, formed by various nuclear reactions. Noting that the consideration included the investigated photonuclear and neutron-captured reactions caused by thermal, resonant and mixed thermal-resonant neutrons, which have not been exposed in the existing literature before.

- Application of the TALYS 1.95 with six nuclear density models and eight γ-ray strength functions in combination with the GEANT4 toolkit to predict the IRs in the photonuclear reactions and compare with our experimental data as well as the literature data.

As is well known, nuclear data have a vital role in atomic energy application and the investigation of nuclear structure and reaction mechanism. Therefore, nuclear data from each type of reaction should measure by numerous laboratories with various approaches and data analysis methods. In that sense, the IR data with high accuracy presented in this thesis may devote new ones exclusively or contribute additional data to the nuclear data reservoir. Additionally, evaluating the impact of several quantities as the energy and angular momentum of projectiles transferred to the target nucleus, spin of target nucleus, spin of the ground and excited states of the residual nucleus on IR values elucidate the role of these quantities and lead to the systematic and reliable IRs. Furthermore, studying the IR in photonuclear reactions by TALYS code allows drawing conclusions about the nuclear structure, model parameters, and nuclear reaction mechanism embodying the factors of equilibrium, direct, and pre-equilibrium processes.

This thesis is organised as follows:

Chapter 1 outlines nuclear isomers, the IR and related effects. This chapter also reviews briefly photonuclear and neutron capture reactions. Besides, the calculated programs for nuclear reactions, namely, the TALYS code and the GEANT4 toolkit are also introduced.

Chapter 2 presents and explains the experimental and theoretical methods in detail. The necessary corrections to obtain accurate experimental results are also presented in this chapter.

Chapter 3 demonstrates and discusses the experimental results and theoretically calculated outcomes of this work in comparison with the literature.

Finally, the conclusion and outlook are drawn.

The thesis includes 22 tables and 58 figures and presents on 119 pages.

Chapter 1

Overview

Nuclear isomers are metastable states of nuclei undergoing a hindrance in their decay. The half-live of isomers ranges from *nanoseconds* to millions of *years*. Currently, nuclear isomers lodge in the center position in the study of nuclear physics since they can be employed to elucidate the nuclear structure and properties in abnormal conditions and to apply in numerous applications such as therapy, medical imaging, nuclear clock, γ-ray lasers and nuclear batteries. Recent advances in RIB facilities, nuclear detectors, digital electronics and analyzers lead to observing new isomers with very short lifetimes and measuring their detailed properties. One of the research directions relating to isomers is the determination of IR being of great interest. The study of IR can provide invaluable information on the level structure and density, as well as the involved reaction mechanisms. Besides, the IRs can use as precious data for examining nuclear reaction models.

This chapter reviews the historical aspects of nuclear isomers and the inhibition mechanisms resulting in their formation and classification. As a central part, the definition and calculation of IR and its related effects in photonuclear and neutron capture reactions by experimental and theoretical methods are expressed in section 1.2.

1.1 Formation and classification of isomers

Nuclear isomers attracted attention since 1917 when Soddy stated *"We can have isotopes with the identity of atomic weight, as well as of chemical character, which is different in their stability and mode of breaking up"* [1]. In 1921, Hahn reported the first experimental measurement about isomers in Uranium salts [2], UZ and UX2, later known as ^{234}Pa and ^{234m}Pa. By 15 years later, the first explanation of isomers concerning the hindered γ-decay was provided by Weizsäcker [3]. It is related to considerable

angular momentum variation, specially when combined with low electromagnetic transition energies leading to the slow transition rate, i.e., the population of isomers with the half-life longer than normal excited states. In the early 1950s, the non-spherical shape of several nuclei were unveiled, which expanded the study of isomeric states in deformed nuclei. Bohr and Mottelson evolved the existence and decay characteristics of isomers of the axially-symmetric deformed nucleus ^{180}Hf [4] as a result of electromagnetic transitions in the rotational band. While the role of the magnitude of angular momentum in the formation of isomers had been discussed by Weizsäckers [3], the change in nuclear spin orientation could also be important as the case of ^{180}Hf, leading to the population of different type of isomers.

The interpretation of the existence of isomers in terms of hindered gamma transition is based on various physical reasons directly relevant to the selection rules in γ-decay and electromagnetic transition probability. The widely known selection rules in γ-decay arise from the preservation law of parity and angular momentum. The transition from an initial state i to a final state f, having angular momentum $\vec{J}_i$ and $\vec{J}_f$, respectively, can take place as the electromagnetic deexcitation by the γ-ray emission carrying away an angular momentum $\vec{L}$. This transition process obeys the angular momentum preservation law: $\vec{J}_f = \vec{J}_i + \vec{L}$ corresponding to the condition:

$$\left|J_i - J_f\right| \leq L \leq J_i + J_f. \tag{1.1}$$

The multipolarity L of the emitted γ-rays is the non-zero positive values since the intrinsic spin of photon is 1 $\hbar$, the photon transition $0 \to 0$ with $L = 0$ is absolutely prohibited. Besides, the conservation law of parity of nuclear states helps to determine the electric or magnetic transition. A L-multipole transition is the electric one when $\pi_i\pi_f = (-1)^L$, and is the magnetic one if $\pi_i\pi_f = (-1)^{L+1}$, here $\pi_{i(f)}$ is the parity of the initial (final) state. In a classical picture, electric γ-ray transition occurs when radiation field is generate by the displacement of charge distribution, while magnetic one is due to the change in current distribution.

Originating from the Fermi's golden rule, the electromagnetic transition probability per unit of time denoted as T_{fi} is reduced to the following formula [5]:

$$T_{fi}^{\alpha L} = \frac{2}{\epsilon_0 \hbar} \frac{L+1}{L[(2L+1)!!]^2} \left(\frac{E_\gamma}{\hbar c}\right)^{2L+1} B(\alpha L; J_i \to J_f), \tag{1.2}$$

where $B(\alpha L; J_i \to J_f)$ is the reduced transition probability, given as:

$$B(\alpha L; J_i \to J_f) = \frac{1}{2J_i+1} \left| < J_f || \widehat{O}_{\alpha L} || J_i > \right|^2, \tag{1.3}$$

with $\alpha = E$ or M indicates the electric or magnetic field, $\widehat{O}_{\alpha L}$ is the operator with regard to the multipole radiation field αL.

The average lifetime and half-life are given by $t = 1/T_{fi}$, and $t_{1/2} = ln(2)/T_{fi}$, respectively.

Competing with γ-decay is the internal conversion process (IC) being the deexcitation of the excited nucleus through the energy transfer to kick the electrons off the atomic orbital. This process becomes crucial when low decay energy and therefore may change the half-life significantly for low-energy isomeric transition. The IC process is the unique probable decay mode in the $0^+ \to 0^+$ ($E0$) transitions where γ-decay is impossible, as mentioned earlier. The IC process vie with γ-decay is quantified by the total internal conversion factor a:

$$a = N_e/N_\gamma, \tag{1.4}$$

where $N_{e(\gamma)}$ is the number of conversion electrons (γ-rays) released from the identical time of an excited nuclide. When factor a is taken into account, total transition probability becomes:

$$T_{fi}^{\alpha L} = \frac{2}{\epsilon_0 \hbar} \frac{L+1}{L[(2L+1)!!]^2} \left(\frac{E_\gamma}{\hbar c}\right)^{2L+1} B(\alpha L; J_i \to J_f)(1+a). \tag{1.5}$$

Following the (1.2) and (1.3) expressions, the electromagnetic decay probability is affected not only by the multipolarity and the γ-decay energy but also by the transition matrix element with respect of the interaction operator and wave function of the initial and final states carrying the nuclear structure information. It is tricky to calculate the matrix element due to involving the characteristics of actual wave function.

For the case of the spherical nuclei with radius $R = R_0 A^{1/3} = 1.2A^{1/3}$ fm and the electromagnetic transition of a single nucleon ($J_i = 1/2$ and $J_f = L+1/2$), Weisskopf [6] estimated and represented the reduced transition probability in the approximate expressions:

$$B_W(EL) = \frac{1.2^{2L}}{4\pi} \left(\frac{3}{L+3}\right)^2 A^{\frac{2L}{3}} e^2 f m^{2L}, \tag{1.6}$$

$$B_W(ML) = \frac{10 \times 1.2^{2L-2}}{4\pi} \left(\frac{3}{L+3}\right)^2 A^{\frac{2L-2}{3}} (\mu_N/c)^2 fm^{2L-2}. \tag{1.7}$$

Substituting the expressions (1.6) and (1.7) into (1.2) results in the transition probability (T_W) in Weisskopf unit ($W.U$). Then, the Weisskopf estimate-based lifetime (t_W) of certain nuclear state can be given by:

$$t_W = \frac{1}{T_W} = \frac{\epsilon_0 \hbar}{2} \frac{L[(2L+1)!!]^2}{L+1} \left(\frac{E_\gamma}{\hbar c}\right)^{-(2L+1)} \frac{1}{B_W(\alpha L)}. \tag{1.8}$$

Since this estimation originated from the assumption of changing the single-particle state of only one nucleon in the nucleus during the decay, it is the so-called Weisskopf single-particle estimate. The Weisskopf single-particle estimate is particularly beneficial to compare with the experimental half-life. Although these estimates are not exact theoretical calculations, they can provide reasonable comparative transition rates. If one observes the experimental transition rate of a γ-decay with the order of magnitude much lower than Weisskopf prediction, one can assume a worse fitting of initial and final wave functions while if the measured decay rate is much higher than Weisskopf prediction, there must be the multinucleon transition. Stemming from Weisskopf estimate (1.8), one can deduce two features: (1) Dominant transition modes are with low multipolarities because the increase of one unit in the multipole order leads to the reduction of the transition probability about 10^{-5} times. (2) In medium and heavy nuclides, the electric radiation is more possible than magnetic one by about two magnitude orders for a given multipole order, .

From Eq. (1.2), it is clear that the electromagnetic decay probability depends on three main elements consist of the multipolarity L, the transition matrix element and γ-decay energy E_γ. The larger the electromagnetic decay probability the longer the lifetime results in the existence of isomeric states when the electromagnetic transition with high multipolarity, the small matrix element, and/or small decay energy of the transition. Most of this type of isomer is figured out in spherical nuclei near the magic numbers, so-called spin isomers. The knowledge of the level scheme of shell model and the magic numbers, together with the selection rules of γ-decay is adequate to recognize the existence of high-spin isomers close to magic nuclides. For odd-odd or even-even nuclides, the additional rules were revealed by Nordheim [7] and Brennan and Bernstien [8] for allowed and favored spins. In these cases, isomers can be identified due to the excitation of 2-quasiparticle (qp) or $4-qp$. For odd-A nuclides, isomers can

be populated from the excitation of $3-qp$ or $5-qp$.

For heavy, deformed rugby-ball-shaped nuclides, there are the selection rules for quantum number K (the projection of the intrinsic angular momentum on the symmetry axis of the nucleus). The existence of this type of isomer relies on the magnitude of the nuclear spin vector and its orientation. In other words, this type of isomer arises from the K conservation and a large alteration in K entailing the significant alteration in the orientation of the total angular momentum. An absolute selection rule demands the multipolarity of the decay radiation to be at least equal to the change of the K ($L \geq \Delta K$). Nevertheless, in several cases, K-forbidden transitions are inhibited or the K-selection rule is prohibited resulting in $\Delta K > L$ because of possible transitions from symmetry-breaking processes. The forbidden degree ν is determined by $\nu = \Delta K$ - L correlating with the Weisskopf hindrance factor $F_W = t_\gamma/t_W$ and reduced inhibition $f_v = F^{1/\nu} = (t_\gamma/t_W)^{1/\nu}$, here $t_{\gamma(W)}$ is the experimental partial mean lifetime of γ-ray (Weisskopf estimate) as in Eq. 1.8. The f_ν value depends on the nuclear structure. The expected reduced hindrance is within the range $f_\nu \sim 30-300$ [9].

In another case, the long lifetime of isomers might arise from the difference in nuclear shape between the isomeric state and the ground state. For instance, it is demonstrated in spontaneously fissile isomers and fission isomers in the actinide region. This type of isomer is characterized by the large quadrupole deformation parameter and great hindrance of γ transitions to the ground state.

In general, based on the inhibition mechanism, the isomers are classified into five main types [10]: (1) spin isomer in the spherical nuclides, (2) seniority isomer in the semi-magic nuclides, (3) K-isomer in the axially-symmetric deformed nuclides, (4) fission isomer in the heavy-fissionable nuclides, and (5) shape isomer in the shape coexistence nuclides. Furthermore, one mentioned to another type of isomer, which is extremely low energy isomer (ELE isomer) as 8 eV isomer in ^{229}Th [5]. The ELE isomers is expected for be observed in the future, especially for the heavy-mass nuclear region where ELE isomers are more possible to appear. These isomers can have prospective applications in atomic-nuclear physics, as well as in nuclear astrophysics. To interpret the existence of the spin isomers and the seniority ones, the single-particle shell model for spherical nuclei plays a key role, while the Nilsson deformed model can be employed to elucidate the K-isomers. To explain the population of fission isomers and shape isomers, the collective models can be employed.

With the rapid growth of accelerators, RIB facilities, and nuclear experimental

techniques, more and more new isomers in various nuclear regions have been discovered to date. The half-life illustration of isomers has also changed to lower limits due to the advanced detector and electronic techniques. The first version of Nubase 1997 defined the isomer to be the excited state with the half-life larger than 1 ms; the ENSDF database [11] also defined the same isomeric half-life. Afterwards, the Nubase 2003 [12] defined the lower limit of 100 ns. In the Nubase 2020 [13], one still insisted on that limit. However, in the "Atlas of Nuclear Isomers" [14], the limit of isomers is down to 10 ns. These half-life definitions are not based on certain fundamental reasons, only as the expedience and measurableness. In the Nubase 2020 version, 1938 excited isomeric states ($T_{1/2} \geq 100ns$) were listed as shown in Fig. 1.1, while the recent "Atlas of Nuclear Isomers" second edition listed 2623 isomers with the lower half-life limit of 10 ns [5]. There are about 866 odd-odd isomers, 445 even-even isomers, 679 even-N odd-Z isomers and 633 odd-N even-Z isomers. There are almost equal numbers of isomers in odd-A nuclei (1312) and even-A nuclei (1311).

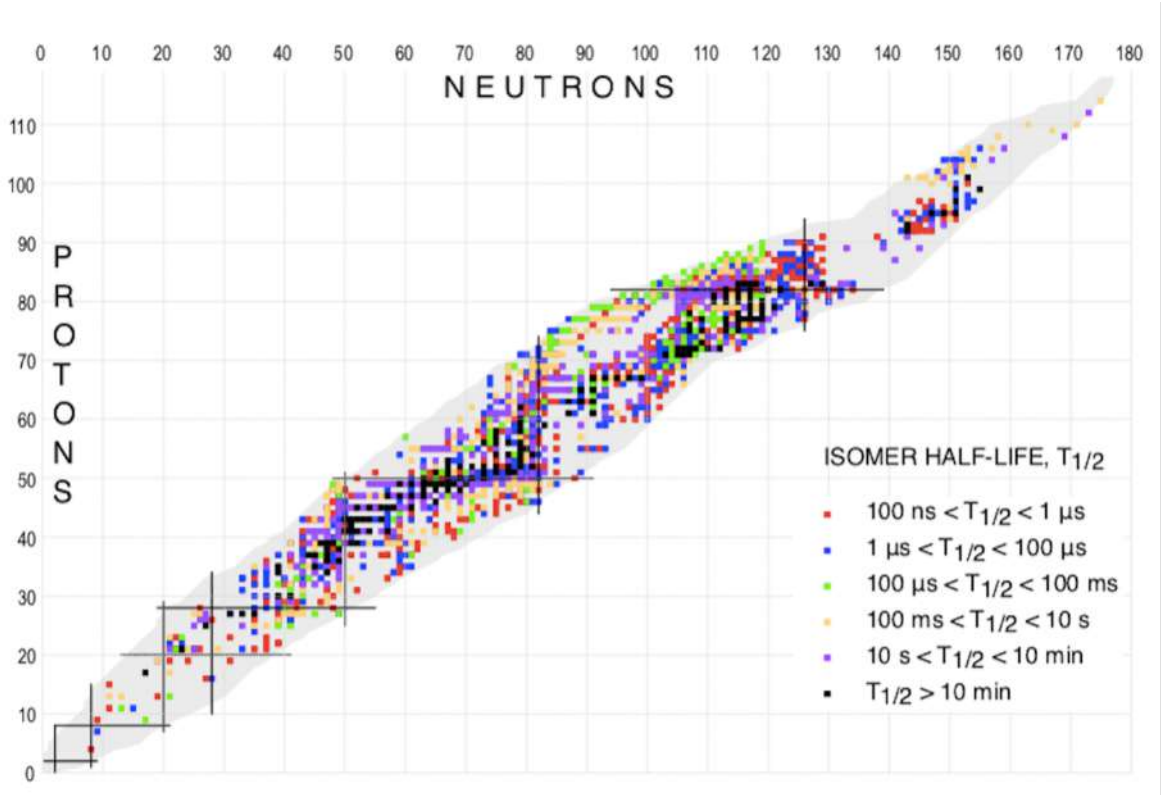

FIGURE 1.1: Nuclear chart displaying isomeric states with $T_{1/2} \geq 100$ ns (NUBASE 2020) [13].

Until now, the whole nuclear landscape has been vastly covered by the nuclear isomers with their characteristics changing from region to region. Apart from isomeric transitions (IT), namely, γ-decay and/or internal conversion, which is the most common

decay mode of isomers, isomers can decay following by different modes such as β-decay [15], α-decay [16], spontaneous fission, p-decay [17], $2p$-decay [18], εp-decay [19], β^+p-decay [20], and β^-n-decay [21], etc., depending on the location of isomers in the nuclear chart. These peculiar decay modes of isomers have shed light on the structure of the complicated nuclides and provide a benchmark for probing the wave function, locations of single-nucleon orbitals, and features of the nuclear interaction.

In addition to the study on the population and characteristics of isomers, the investigation of the isomeric ratio (IR) is particularly interested. The IR can provide important insights about the nuclear level density and structure, and involved reaction processes. The IR values are relevant to various target and projectiles, excitation energy, spin of target nuclei, and many other nuclear effects. Some of them are demonstrated in the following section.

1.2 Isomeric ratio and related effects

1.2.1 Definition of isomeric ratio

The IR is defined as the measured relative population of an isomeric state and an unstable ground state of a nucleus in a nuclear reaction. In the calculation, IR is expressed as the ratio of the cross-sections ($IR = \sigma_m/\sigma_g$) wherein sample irradiation with a monoenergetic beam or the ratio of reaction yields ($IR = Y_m/Y_g$) with a continuous energy beam. As the isomeric and ground states differ in spin, IR is also commonly defined by the ratio of cross-sections or that of yields for forming the high- and low-spin states ($IR = \sigma_h/\sigma_l$ or Y_h/Y_l) [22, 23].

So far, a large number of IRs have been investigated in nuclear reactions bombarded by diverse projectiles as photon [24, 25, 26]; neutron [27, 28] tritium [29], alpha [30], deuteron and light ion [28], heavy ion [31] as well as in fission product [32, 33]. The investigation of nuclear reactions irradiated by the different projectiles and targets with a broad energy range is crucial for understanding the nuclear structure and processes.

In the case of photonuclear reactions induced by bremsstrahlung, IR is analytically calculated by the expression below:

$$IR = \frac{Y_m}{Y_g} = \frac{N_0 \int_{E_{th}^m}^{E_\gamma^m} \sigma_m(E)\phi(E)dE}{N_0 \int_{E_{th}^m}^{E_\gamma^g} \sigma_g(E)\phi(E)dE}, \tag{1.9}$$

where E_{γ}^{m}, $\phi(E)$, N_0 are the bremsstrahlung endpoint energy, the bremsstrahlung photon flux, the number of the target nuclei, respectively, $\sigma_{m(g)}(E)$ is the cross-sections of the isomeric (ground) state ans $E_{th}^{m(g)}$ is the threshold reaction energies for the isomeric (ground) state.

In the case of thermal and resonance neutron capture reactions, the IR is also calculated by the yield ratio since the energy spectrum of thermal neutrons obeys Maxwellian distribution extending to about 0.2 eV, of which the most probable energy at 20°C is 0.025 eV. And the energy spectrum of resonance neutrons ranges from 10 eV to 300 eV.

The IR is connected to various nuclear effects, some of them are demonstrated in the following subsection.

1.2.2 Nuclear effects on isomeric ratio

Excitation energy

The excitation energy affected the IRs in photonuclear reaction (γ, n) induced by bremsstrahlung in the GDR as proved in refs. [34, 35, 36, 37, 38, 39]. The obtained experimental results showed that the trend of IR increases or decreases with the increase of end-point energy and reaches the maximum (or minimum) value at the end of the GDR and slightly changes (or almost unchanged) for higher energies. These depend on the fact that the yield of the isomeric state increases faster or slower than that of the ground state when the bremsstrahlung end-point energy increases in the GDR region. The pre-equilibrium and direct processes are taken into account for the steady value of IRs at the end and beyond the GDR. The contributions of direct and pre-equilibrium processes can be found in ref. [40]. Moreover, the contribution of other competitive channels to the IR of an isomeric pair produced in (γ, n) reaction at the end of the GDR and up to 65 MeV is insignificant as in the ref. [41] for the case of ^{85m,g}Sr. In which, the obtained results at the former and the latter are almost equal or in other words, the authors estimated the contribution of the $(\gamma, 2n)$ and $(\gamma, 3n)$ reactions to be negligible. In neutron-induced reactions, the IR is also a function of the incident neutron energy. This fact is presented by Nesaraja [42] for ^{69m,g}Zn and ^{71m,g}Zn with identical metastable and ground-state spin produced via (n, α), (n, p), and $(n, 2n)$ reactions in the neutron energy range of 6 to 12 MeV. The low-spin isomer is favored at low energies, but with the increasing neutron energy, the population of high-spin isomer increases leading to the increasing trend of the IR. Furthermore, the

IR of ^{69m,g}Zn is larger than that of ^{71m,g}Zn revealing the other effect relating to the mass number.

Nucleon configuration

The IRs in the isotone nuclei depend on the mass numbers presented by N. Tsoneva et al [39] measuring the IRs in (γ, n) reactions on the beam of bremsstrahlung in $N = 81$ isotone nuclei (^{137}Ba, ^{139}Ce, ^{141}Nd and ^{143}Sm) having approximately the same excitation energy of residual nuclei and identical spins and parities in their isomeric and ground states. The large difference of the IR for those nuclei were observed despite similar properties of isomeric states.

In more details, the IR of two lighter nuclei equals about twice that of two heavier nuclei and the IR decreases with the increase of proton number or the IRs depend on the mass numbers. Likewise, T.D. Thiep by studying the IRs in (γ, n) reaction of $N = 81$ isotones (^{141}Nd and ^{143}Sm) and $Z = 51$ isotopes of Sb [43], $Z = 56$ isotopes of Ba [36] and $Z = 34$ isotopes of Se [35] concluded that the IR decreases with the increase of neutron/proton number. The dependence of IR on masses of isotones and isotopes is called the effect on nucleon configuration.

Reaction channel

The different IR values of an isomeric pair produced via different nuclear reactions have been investigated as the influence of the reaction channel by Cserpak [44] for ^{60m,g}Co in three neutron induced reactions, by Sudar for ^{58m,g}Co in the neutron, proton, deuterium, and α-induced reactions [27], by Qaim for ^{73m,g}Se and ^{52m,g}Mn in nuclear reactions induced by projectiles of α, ^{3}He, p, d and n [45, 46], by Strohmaier for ^{94m,g}Tc in three nuclear processes [47], by Nesaraja for ^{69m,g}Zn and ^{71m,g}Zn in neutron induced reactions [47], by Tonchev for ^{152m1,m2}Eu in inverse reaction (γ, n) and (n, γ) [34] and by T. D. Thiep and references cited therein studying on Ba, Se, In, Ho, Lu, Ag, Mo and Ce targets in reactions induced by bremsstrahlung and neutrons [34, 43, 48, 36]. It is concluded from the observed trends that the reaction channel affects the IR considerably, particularly when the channels differ widely. This effect can be explained by the intake impulse of the projectiles. The higher the intake impulse of the projectile the higher the IR. T.D.Thiep presented in detail the case of $(n, 2n)$ and (γ, n) reactions which populate the same isomeric pair on Ba, Se, Ce, In, Ag and Lu target with the same energy of projectiles. The intake impulse in the former reaction is higher than that in the latter since the rest mass of the photon is zero according to electromagnetic theory. As the result, the IR in $(n, 2n)$ reaction is notable higher than that in (γ, n)

reaction.

Intermediate state structure

The IR is, moreover, governed by the structure of intermediate states. Huber [49] and Carroll [50] evaluated the crucial role of intermediate state structure on the populating mechanism of the isomeric and ground states in the photonuclear reaction using bremsstrahlung with the end-point energies in the range of 2 – 7 MeV.

Spin and spin difference

The other effect is the spin dependence of the isomeric state. In ref. [36], T.D. Thiep has studied the IRs of the isomeric pairs such as ^{129m,g}Ba, ^{131m,g}Ba and ^{133m,g}Ba formed in (γ, n) reactions with the same ground-state spin of $1/2^+$ but various isomeric state spins of $7/2^+$, $9/2^-$ and $11/2^-$, respectively. The results showed that the IR decreases with the increase of the isomeric state spin. The difference between spins of isomeric and ground states also has an impact on the IR value. In general, the higher the spin difference is, the lower the IR is [51].

1.2.3 Theoretical IR calculation

The experimental IRs can be used as precious data for examining different nuclear reaction models. There are three well-known models for describing nuclear reactions, based on the interaction time between the bombarding particles and the target nucleus or based on incident energy. They are the compound nuclear model, the pre-equilibrium model, and the direct reaction model. At low energy, the compound reaction is the major one occurring when the projectile is absorbed by the target nucleus leading to the formation of a compound nucleus with the lifetime (typically from 10^{-19} to 10^{-15}s) much longer than the time necessary for an incident particle to travel across the nucleus (about 10^{-21} s). Due to the statistical fluctuation, the excitation energy will distribute to one or more nucleons near the nuclear surface and release these nucleons as an evaporation process from the compound nucleus to form the residual nucleus. Subsequently, this residual one will deexcite by the direct γ-decay or cascade transition. The decay probability of the compound nucleus is independent of its formation. The compound process is described in detail by the statistical model in the Hauser-Feshbach theory [52] based on Bohr's independence hypothesis [53]. At the higher projectile energy, the pre-equilibrium (pre-compound) process occurs owing to interactions between the projectile and the target nucleus resulting in the particle emission before reaching statistical equilibrium of the compound nucleus. The exciton model characterized by

particles above and holes below the Fermi surface is often used for explaining the pre-equilibrium process [54]. In the high-energy region, the direct reaction dominates, in which the projectile directly transfers kinetic energy to the nucleons without forming an intermediate nucleus. The ejected particles show a distinctive forward orientation. This process is described by the Distorted Wave Born Approximation (DWBA) for (near-) spherical nuclei and by coupled-channels equations for deformed nuclei [54].

On the basis of the statistical model for compound nuclear reaction, the first theoretical IR calculations were studied and proposed by Huizenga and Vandebosch in the 1960s [55, 56]. Afterwards, this IR calculation model is called Huizenga-Vandebosch model (HVM).

Huizenga-Vandebosh model

The HVM was able to apply for calculating the IR in (n, γ) and (γ, n) reactions based on the spin distribution. In the initial interaction between the incident particle and the target nucleus, the compound nucleus formed with the determined spin distribution. After the emission of particle and γ-ray, the spin distribution was modified and calculated. By fitting the IRs calculated by the HVM with the experimental values, one can obtain the information about the dependence of the level density on the spin cut-off and level density parameters. The IR was determined from the final spin distribution, depending on the spins of the isomeric pair. In refs. [48, 51, 57], for the photonuclear reaction, the calculated IRs according to the HVM with certain spin cut-off were in good agreement with the experimental data at relatively low energies, where the compound process was the main one. Kolev [58] has improved the HVM by including a more detailed deexcitation calculation of the charged particle emission process.

In the case of photoneutron reaction (γ, n), HVM is represented by the following stages [48, 51]:

1. *Formation of a compound nucleus by absorbing an E1 γ-ray*

   The relative population probability of compound nucleus with spin J_c (positive value) through the absorption of an E1 γ-ray by target nucleus with initial spin J_0 is:

$$P(J_c) \approx 2J_c + 1 \quad , where \quad J_c = J_0, J_0 \pm 1. \tag{1.10}$$

2. *Emission of a neutron from the excited compound nucleus and formation of a residual nucleus*

   The relative probability for the compound nucleus to emit a neutron with orbital angular momentum l leading to a residual nucleus with spin J is given by

$$P(J) \approx \rho(J, E^*) \sum_{S=\left|J-\frac{1}{2}\right|}^{\left|J+\frac{1}{2}\right|} \sum_{l=|J_c+S|}^{J_c+S} T_l(E_n), \tag{1.11}$$

   where $T_l(E_n)$ - the penetrability (transmission coefficient) for the neutron with angular momentum l and kinetic energy E_n; $\rho(J, E^*)$- the level density of the residual nucleus.

   The emitted neutrons are supposed to obey Maxwell distribution. The evaporation energy E_n is replaced by an average energy $\overline{E_n}$,

$$\overline{E_n} = \frac{1 + \sqrt{1 + 4aU}}{2a}, \tag{1.12}$$

   where U – the excitation energy of compound nucleus, $U = at^2 - t$ with t is thermodynamic temperature, a – the level density parameter.

   The excitation energy of residual nucleus E^* is given by:

$$E^* = U - S_n - E_n, \tag{1.13}$$

   here S_n and E_n – the separation and kinetic energies of the emitted neutron.

   The level density of the residual nucleus is represented by the following formula:

$$\rho(J, E^*) = \rho(E^*)\rho(J) \sim exp\left[2(aE^*)^{1/2}\right](2J+1)exp\left[-\frac{(J+1/2)^2}{2\sigma^2}\right], \tag{1.14}$$

   where σ - the spin cut-off parameter, $\sigma^2 = \frac{\theta t}{\hbar^2}$ with θ – the moment of inertia of nucleus.

3. *Emission of γ-ray cascade from the residual nucleus leads to the population of the isomeric and ground states*

   The residual nucleus is assumed to deexcite predominantly by E1 gamma-ray emission with average energy for $(i+1)^{th}$ γ-ray:

$$E_{\gamma(i+1)} = 4\left[\frac{E^* - \sum E_{\gamma i}}{a} - \frac{5}{a^2}\right]^{1/2}. \tag{1.15}$$

Here it is supposed that $E_{\gamma 0} = 0$.

The γ-ray transition probability from states with spin J_i to those with spin J_f is assumed to be

$$P(J_f) \sim \sum_{J_i} P(J_i)\rho(J_f). \tag{1.16}$$

The γ-ray cascades continue to occur until the residual energy, i.e. $E = E^* - \sum E_{\gamma i}$ is smaller than "γ-ray cut-off region" (E_u, E_d). Then, "deciding γ-ray" emits and feeds the state to which the transition has the lowest multipolarity. When the residual γ-ray energy lies within the cut-off region, a subsequent E1 γ-ray and "deciding γ-ray" are partly emitted. In this situation, one must consider the competing channel with the transition probability $P = (E - E_d)/(E_u - E_d)$, which lead to the calculation of IR by following formula:

$$IR = P\frac{\sum_{J_f=COS}^{J_f=\infty+} P(J_f, E - E_d)}{\sum_{J_f=0}^{J_f=COS} P(J_f, E - E_d)} + (1 - P)\frac{\sum_{J_f=COS}^{J_f=\infty+} P(J_f, E)}{\sum_{J_f=0}^{J_f=COS} P(J_f, E)}, \tag{1.17}$$

where $COS = (S_h + S_l)/2$ is the center of spin with S_h and S_l - spins of high and low spin states. States with spins $> COS$ would feed the isomeric state, while states with spin $< COS$ would feed the ground state, and states with spins $= COS$ feed both states equally.

However, there are several drawbacks of HVM-based IR calculation. It assumed that the spin cut-off parameter σ was constant, independent of excitation energy. The HVM-based IR is sensitive to the supposed the spin cut-off parameter σ, which is assumed to be constant and independent of excitation energy. The IR is also dependent on the assumed multiplicity and multipolarity of the γ-ray cascade following neutron evaporation or the neglect of the actual nuclear level structure in the calculation of final γ-cascades. The HVM has taken into account only the E1 transition in the γ-ray cascade and the application of this model has been limited to nuclear reactions at relatively low energies and spins.

In the case of the (n, γ) reaction induced by thermal and resonant neutrons, it is supposed that only s-wave neutrons with a spin of $1/2\hbar$ are captured and governed

by the compound mechanism. Therefore, the spin of excited state in the compound nucleus can be $J_c = J_0, J_0 \pm 1/2$. To calculate IR in this type of reaction, HVM is also applied as the case of (γ, n) reaction except for the second stage being absent, and the transitions of primary and intermediate levels of the excited compound nucleus should follows by the formation of the isomeric and ground states.

Until now, to calculate the cross-section and IR, several codes have been developed and employed based on the computational scheme for sophisticated nuclear models. Kolev calculated the IR of ^{117m,g}In and ^{120m,g}Sb produced in photonuclear reaction with bremsstrahlung end-point energies of 43 and 18 MeV by means of the code STAPRE and the code COMPLET to interpret the role of angular momentum removal [40]. Currently, similar to EMPIRE, TALYS is a nuclear reaction modeling code employed often for calculating cross-sections and the IR.

TALYS code

TALYS is a nuclear reaction program for the analysis and the prediction of nuclear reactions created and developed at NRG Petten, the Netherlands, CEA Bruyeres-le-Chatel France, University Libre, Brussels, and at the IAEA, Vienna in recent years. TALYS code can be used to simulate nuclear reactions that involve neutron, gamma, proton, deuteron, triton, helium-3, and α particle in the energy range of 1 keV - 200 MeV on target nuclei of mass 12 and heavier. Unfortunately, the TALYS code has not been resolved completely for the case of thermal and epithermal neutron capture reactions. The code considers different nuclear reaction models, i.e., the optical, compound nucleus, pre-equilibrium, direct reaction, fission models, and the problems connected to level density and γ-ray strength as illustrated in Fig. 1.2.

The TALYS database of nuclear structure parameters based on the IAEA Reference Input Parameter Library (RIPL) provides validated nuclear-model input parameters. The outputs of this code comprise complete sets of reaction data such as the cross-section, energy spectra, and angular distribution of the emitted particles.

There are two main purposes of TALYS, which are strongly connected. First, it is a nuclear physics tool that can be used for the analysis of nuclear reaction experiments. Second, it is a nuclear data tool. Using available experimental data, TALYS can generate nuclear data for all open reaction channels after fine-tuning the adjustable parameters of the various reaction models. It can interpolate between and extrapolate beyond experimental data, on user-defined energy and angle grid beyond the resonance region. TALYS offers a complete set of quantitative outputs for a nuclear reaction for all open

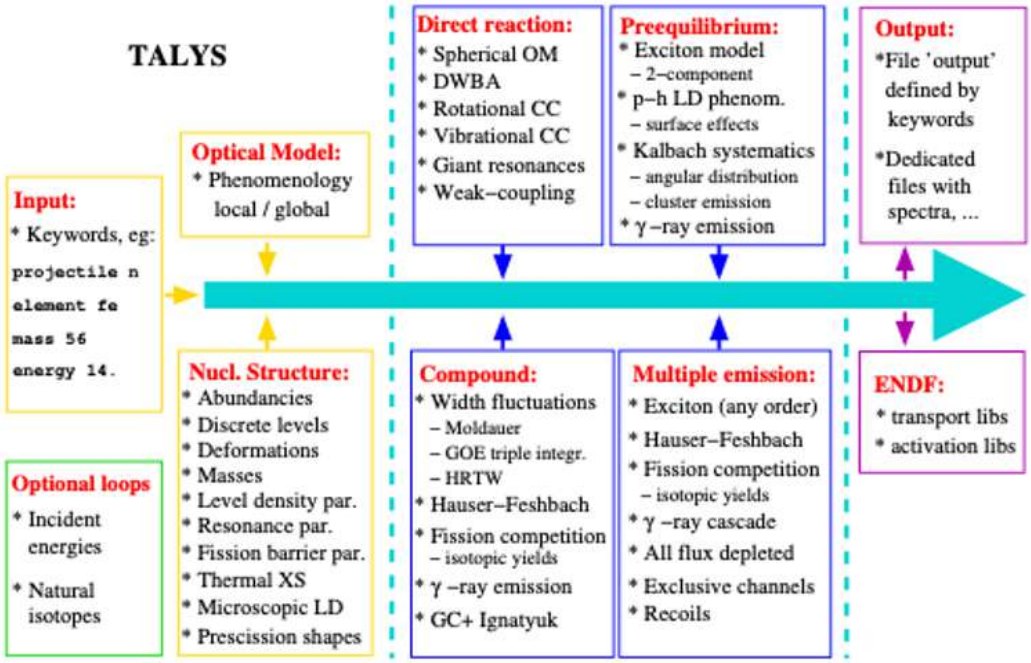

FIGURE 1.2: Organization of input-ouput flows and nuclear model components in TALYS program. Image taken from [59].

channels together with associated cross-sections, spectra, and/or angular distributions. TALYS update itself depending on the current status of nuclear reaction theory, providing that the current capability to model that theory. The TALYS outputs can be generated by more or less sophisticated physical methods or by simpler phenomenological approaches. The latest version of the TALYS code is TALYS 1.96 (release date: December 30, 2021) with approximately 400 keywords that can be changed depending on users purposes.

TALYS code have been extensively employed to obtain theoretical excitation function and IR in various types of nuclear reactions. Danagulyan [60] using TALYS 1.4 studied IRs in proton and alpha-induced reactions for nuclei in the mass number range of A = 44 – 124. The TALYS-calculated data reveal the dependence of IR on the projectile species, while for several nuclei in high-spin states the experimental data were not reproduced well by the calculated ones. In another study of Junhua [61, 62], the experimentally measured data for cross-sections and IRs in $(n, 2n)$ reactions induced by fast neutrons on Eu, Nb, and Ba targets were compared with the calculations using TALYS 1.8 code with different level density models. The general trend of the experimental data and theoretical ones were observed in this case.

For one-step photonuclear reactions (γ, n) in the GDR region, there are several recent studies on TALYS code to validate the cross-sections and IRs, such as in refs [63,

64] of Palvanov (for Se and Pd isotopes), Mazur [65] (for Te isotopes) and Danagulyan [66] (for Sn, Te, Hf, and In isotopes). Notably, Makwana et al. [67] have established new empirical formula for (γ, n) reaction cross-section near GDR peak for elements with $Z > 60$ and reproduced well by the calculations using Talys 1.6 and EMPIRE – 3.2.2 codes. Danagulyan [66] measured the yields of photonuclear reactions on Sn, Te and Hf targets as well as the IRs of ^{117m,g}In, $^{119m,g;121m,g;129m,g}$Te and ^{123m,g}Sn isomeric pairs. The obtained results were considered by using TALYS 1.4 and it was indicated that the disagreements between TALYS-calculated and experimental data may be due to inaccurate model description of the level density. Rahman [68], Naik [69] and Vodin [70] investigated the experimental and TALYS-calculated IRs in a few photonuclear reactions on various targets with multiple particle emissions beyond the GDR region. They concluded that the TALYS code was only able to describe definite reactions with definite models.

According to a growing body of recent studies using TALYS code, it is clear that the use of this code to interpret the cross-section and IR data has attracted interests. Nonetheless, since the measured IRs in photonuclear reactions are mainly induced by bremsstrahlung, the TALYS code is often used in combination with the bremsstrahlung spectra obtained from transportation/Monte-Carlo simulation codes such as GEANT4 [71], MCNP [72] or FLUKA [73]. Recently, P.V.Cuong et al. [74] have incorporated the TALYS-calculated differential cross-section data into the GEANT4 toolkit to proceed with a complete simulation of both bremsstrahlung production and photonuclear reaction process as well as to obtain the IRs. In this work, we employed another method, where only bremsstrahlung spectra obtained from GEANT4 code were used to couple with TALYS-computed cross-sections to calculate analytically the IRs. Although this method seems more schematic than that in ref. [74], it should be free from additional bias from the particle transportation involved in the GEANT4 simulation of photonuclear reaction process.

GEANT4 toolkit

GEANT4 [71] simulation toolkit abbreviation stands for GEometry ANd Tracking, which is a toolkit for Monte Carlo simulations of the passage of particles through matter. This toolkit provides all functionality needed to simulate the detector system, including the interactions of particles, the geometry of the detector system, and the detector response. GEANT4 is a freely available object-oriented software package based on C++, where users build their simulation applications based upon existing virtual

classes. With GEANT4, users can add more capabilities as needed, for example adding new physical processes or changing the response of some detector. GEANT4 has been developed for high-energy physics applications, starting from CERN, an international collaboration with participants from more than 10 laboratories in Europe, the USA, Japan, Russia and Canada. So far, GEANT4 has been employed in various fields such as nuclear and accelerator physics as well as medical and space science.

To utilize GEANT4 for simulation, users have to provide some necessary definitions and the so-called user actions. The geometry setup including detectors and other passive materials needs to be defined by the users. This can be done by overriding the methods in the virtual class G4VUserDetectorConstruction. The geometry should be defined together with the materials used in the simulation. The next mandatory user class overrides the virtual class G4VUserPhysicsList, which defines the particles and physical processes. The last necessary user class to be implemented is the G4VUserPrimaryGenerator Action, in which the methods for creating particles to be tracked are defined. To extract useful information from the simulation output, a set of user action classes can be used, namely G4UserRunAction, G4UserEventAction, G4UserStackingAction, G4UserTrackingAction and G4UserSteppingAction. These virtual classes, which can be overridden by users, allow them to interact with the track of particles in any medium at different levels.

In this work, GEANT4 was used to simulate as close as possible the experimental condition including the geometry and materials of the setup, the primary electron beam and all possible interactions and radiations to obtain the flux distribution as a function of bremsstrahlung energies. This distribution was then combined with the theoretical cross-section data calculated by TALYS code, yielding the theoretical IRs. One of the reasons for choosing GEANT4 as a simulation tool is that it is widely known within the nuclear physics community, with strong support from the community, especially in maintaining up-to-date experimental cross-section database. On top of that, unlike MCNP [72], which is also a well-known simulation package, GEANT4 is a free and open-source software package. And the TALYS code is employed to calculate the cross-section since it has the completeness of reliable nuclear models, flexibility and user-friendliness.

The main goal of this work is to study the IRs of several isomeric pairs produced in two types of reactions, namely photonuclear reaction (γ, n) and neutron capture reaction (n, γ). Therefore, the outlines of these reactions are represented in the following

section.

1.3 Photonuclear reaction

Studying nuclear reactions induced by photons or so-called photonuclear reactions plays a crucial role in understanding the interaction mechanism between photons and nucleus as well as the structure of the nucleus. Furthermore, these reactions are widely used for a variety of applications, such as radiation shielding design, radiation transport, absorbed dose calculations for nuclear medicine, the technology of fusion-fission reactors, nuclear transmutation, and waste management [75]. In recent decades, the advanced photon sources with strong intensity and high quality combined with state-of-the-art detector technology paved the way for new scientific discoveries and technological applications [76].

This section focuses on a description of the formation and features of photonuclear reactions below and above the particle-separation threshold, especially in the GDR region.

1.3.1 Formation of photonuclear reaction and photon sources

In 1934, Chadwick and Goldhaber published the first experimental paper on a photonuclear reaction [77]. They observed the emission of a proton and a neutron from the photonuclear reaction on deuterium target induced by 2.6 MeV photons originating from ThC". Three years later, by the use of 440 keV proton beam impinging on ^{7}Li target, Bothe and Gentner [78] observed the nuclear transmutation and the emission of 17 MeV γ-rays. These high-energy γ-rays were then employed to carry out a number of photonuclear reactions on various isotopes. In 1947, Baldwin and Klaiber [79] used a continuous γ-ray spectrum (bremsstrahlung) for the first time to study photonuclear reactions. The bremsstrahlung with end-point energy range of 10 to 100 MeV had been generated from a betatron accelerator at the General Electric Laboratory to investigate the excitation function. In August 1959, the first Gordon Research Conference on photonuclear reactions [80] was organized at the Kimball Union Academy. Since then, this topic has developed quickly in scientific findings and applications parallel with the development of high-intensity and fine-quality photon sources and advanced detection techniques.

According to the timelines, there are several photon sources exploited and employed to induce the photonuclear reactions [76]:

- 1937: (p, γ) reaction and subsequent photodissociation (Bothe, Gentner)
- 1947: Bremsstrahlung from betatron (Baldwin, Klaiber)
- 1953: Positron annihilation in flight (Colgate, Gilbert)
- 1963: Laser Compton Backscattering (Milburn, Arutyunian, Tumanian)
- 1969: Bremsstrahlung from Van de Graaff accelerator (Metzger)
- 1983: Tagged photons (Knowles et al.)
- 1980s: High-performance bremsstrahlung (Kneissl, Richter)
- 1990s: High-performance laser Compton backscattering (Litvinenko, Ohgaki, Pietralla)

Currently, popular photon sources used to study photonuclear reactions consist of bremsstrahlung and quasi-monoenergetic photon sources. There are three methods to produce the latter including positron annihilation, tagged photons being thin-target bremsstrahlung photons with simultaneous detection of the corresponding decelerated electrons, and Laser Compton Backscattering resulting from the collision of relativistic electrons and laser beam. However, the disadvantage of the first two methods is low intensity and low energy resolution. For the third one, high-intensity quasi-monoenergetic and fully-polarized photon beam can be produced in various energy ranges such as keV photons in AIST, MeV photons in ELI-NP, NewSUBARU, HIGS and LLNL, and GeV photons in Spring-8 [81]. This method requires the use of modern, expensive equipments and high techniques. Therefore, bremsstrahlung beam is employed as an effective photon source in many studies of photonuclear reaction. Bremsstrahlung is electromagnetic radiation resulting from the deceleration of a charged particle by another charged particle, e.g., an electron by an atomic nucleus. Using particle accelerators such as the Betatron and Microtron accelerate the energy of electrons, which then impinge on a heavy target to induce the bremsstrahlung. Bremsstrahlung has a continuous spectrum with end-point energy equal to the energy of accelerated electrons. The energy spectrum of the bremsstrahlung photons is often calculated using Monte Carlo simulation codes such as GEANT4, FLUKA and MCNP.

1.3.2 Cross-section of photonuclear reaction

This subsection describes the cross-section of photonuclear reactions on medium and heavy nuclei with various incident photon energies. The first energy region of interest is from particle emission threshold up to 30 MeV. The second is incident energy less than the particle emission threshold. The last one is the photon energy range of 30 to 140 MeV. Fig. 1.3 illustrates the general total photon absorption cross-section below 30 MeV.

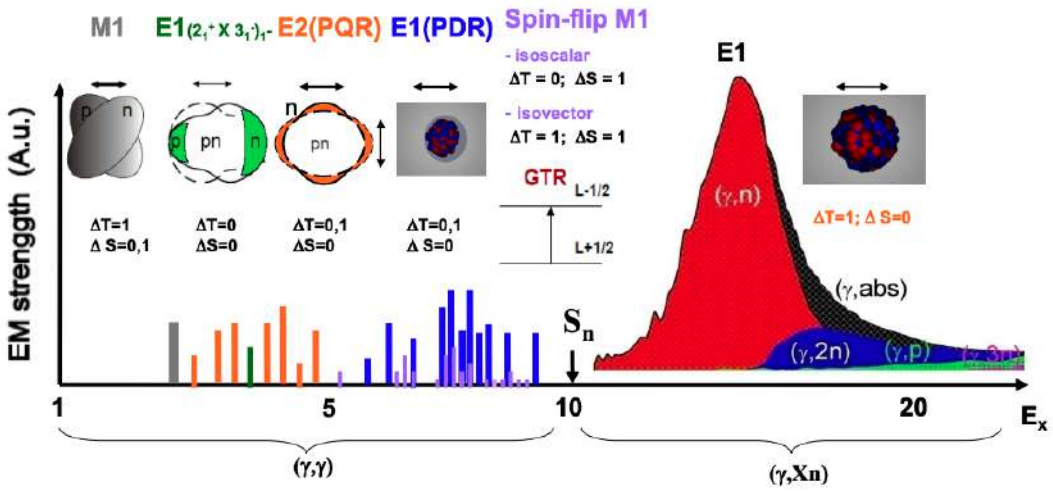

FIGURE 1.3: The general total photon absorption cross-section below 30 MeV (taken from the presented slice of N.Tsoneva at ERICE2014).

1. *Above particle emission threshold up to 30 MeV*

   If the photon energy is higher than the particle evaporation threshold S_n and up to 30 MeV for most medium and heavy nuclei, the photon wavelength is comparable to the nucleus diameter. The giant resonance, a remarkable feature, may occur due to the collective excitation rapidly broadening the level width and coalescing the levels. In other words, the cross-sections depending on the incident energy, arise a giant peak as in Fig. 1.3.

   The various observed giant resonances can be classified according to their multipolarity and character (isoscalar or isovector) [82, 83]. In general, three kinds of giant resonances are observed (i) Giant Monopole Resonance (GMR) corresponding to the collective motion of the nucleus around a single pole, (ii) Giant Dipole Resonance (GDR), corresponding to two poles oscillating against each other (iii) Giant Quadrupole Resonance (GQR), corresponding to the oscillation of four poles in a quadrupole deformed nucleus. Following macroscopic descriptions, the isoscalar character ($\Delta T = 0$) of the giant resonance can be described as the oscillation in

a phase of protons and neutrons, while the isovector character ($\Delta T = 1$) corresponds to neutrons oscillating against the protons. Giant magnetic resonances occur with a spin-flip ($\Delta S = 1$), while electric ones do not. Schematics for the possible giant resonances are shown in Fig. 1.4.

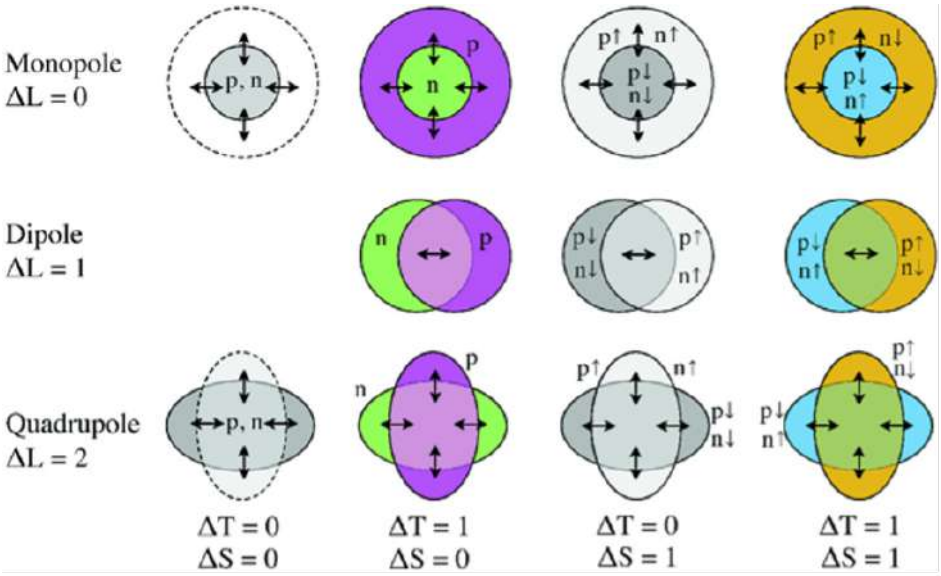

FIGURE 1.4: An schematic illustration of various giant resonance modes of monopole ($L = 0$), dipole ($L = 1$) and quadrupoles ($L = 2$), their magnetic ($\Delta S = 1$) or electric ($\Delta S = 0$), isovector ($\Delta T = 1$) or isoscalar ($\Delta T = 0$) characters [83].

The strongest resonance is the isovector giant electric dipole resonance, first discovered by Bothe and Gentner [78] in a photonuclear reaction and later described by Migdal as an out-of-phase oscillation of the proton fluid against the neutron fluid [84]. Therefore, the region above S_n up to 30 MeV is often called Giant Dipole Resonance (GDR). The energy dependence of the GDR cross-section for the medium and heavy nuclei has often been approximated by a Lorentzian function [76]:

$$\sigma_{GDR}(E_\gamma) = \sum_i \sigma_i \frac{(E_\gamma \Gamma_i)^2}{(E_\gamma^2 - E_i^2)^2 + (E_\gamma \Gamma_i)^2}, \tag{1.18}$$

where σ_i, E_i and Γ_i are the GDR peak cross-section, energy and decay width, respectively. The index $i = 1$ for spherical nuclei and $i = 1, 2$ for deformed nuclei. For instance, the GDR peak energy is 13.5 MeV, and the 4 MeV width for the heavy spherical target nucleus ^{208}Pb. With a non-spherical nucleus ^{160}Gd regarding the prolate deformation, the photonuclear cross-section curve has two peaks: one corresponding to a dipole vibration along the axis of deformation and the other

perpendicular to that axis. Two Lorentz functions have been fitted giving $E_1 = 12.23$ MeV, $\Gamma_1 = 2.27$ MeV and $E_2 = 15.96$ MeV, $\Gamma_2 = 5.28$ MeV. The GDR in light nuclei is often fragmented. The experimental GDR in ^{28}Si has four well-separated peaks. This splitting is probably due to shell effects.

The sum of the photoabsorption cross-section is express as:

$$\int_0^\infty \sigma_{GDR}(E_\gamma) dE_\gamma = 60 \frac{NZ}{A} \quad (MeV \cdot mb). \tag{1.19}$$

Which depends on the target nucleus mass, neutron and proton numbers (A, N and Z), following the dipole sum rule [85]. The peak width spans between 3 and 10 MeV, where the smallest values are for closed-shell nuclei and the greatest values are for nonspherical nuclei [86]. The peak energy is within the range of 13 and 25 MeV and slowly varies as a function of mass number.

To explain the GDR, Goldhaber, and Teller [87] proposed that the giant peak was due to protons and neutrons oscillating against each other in the electromagnetic field of incident photons. Two years later, Steinwedel and Jensen [88] proposed a two-fluid model of the GDR based on a similar idea. They assumed that the nucleus behaved as a nuclear fluid with constant density. In the giant dipole mode, the variation of the neutron and proton density was governed by hydrodynamical equations. The Goldhaber-Teller mechanism or the Steinwedel-Jensen one can obtain the resonance energy function depending on the mass number, $A^{-1/6}$ or $A^{-1/3}$ respectively. However, comparing with the experimental results, this dependence can be better described in the combination two mechanisms. For medium and heavy nuclei, the centroid energy of GDR can be estimated by [76]:

$$E_{GDR} = 31.2 \cdot A^{-1/3} + 20.6 \cdot A^{-1/6}. \tag{1.20}$$

2. *Below particle emission threshold*

In the low-energy region below the S_n, the photon wavelength is significantly longer than the nuclear diameter resulting in dominant elastic and inelastic scattering processes, which exhibit a few isolated absorption lines in this region. At the lowest energy, Thomson elastic scattering on the nucleus can occur. The differential cross-section at angle θ is given by [89]:

$$\frac{d\sigma}{d\Omega} = \frac{(Ze)^4}{2(Mc^2)^2}(1 + cos^2\theta). \tag{1.21}$$

This cross-section is independent of the photon's energy and amounts only to a few nanobarns (nb). Therefore, elastic scattering of photons off nuclei is often considered sub-dominant or even negligible.

The photons with slightly higher energy and below the S_n are absorbed by the target nucleus resulting in the "small" resonances. In this case, a resonant absorption process of photons by the nucleus leading to the subsequent re-emission of γ radiation has happened, so-called resonance photon-scattering reaction or nuclear resonance fluorescence. One conducted the nuclear resonance fluorescence experiments to detect and study "small" resonances such as scissor resonance M1, two-phonon state E1, pygmy quadrupole resonance E2, pygmy dipole resonance E1 and spin-flip M1 (Fig 1.4).

Pygmy resonance

The pygmy dipole resonance (PDR) is found to be a common feature in neutron (proton) rich nuclei as a core nucleus and the excess neutrons (protons) vibrating against the core described by Suzuki [90]. The PDR often appears at the top of the low-energy tail of the GDR. The energy centroid of the resonance and its magnitude are smaller than that of the GDR since the restoring force depends on the number of excess neutrons (protons). A review about the pygmy dipole resonance can be found in Ref. [91]. Another pygmy resonance predicted theoretically and studied experimentally is pygmy quadrupole resonance (PQR) in skin nuclei [92].

Scissors resonance

The scissors resonance is a magnetic dipole resonance M1, which is located at fairly low energies $\approx$ 3 MeV believed to be present only in deformed nuclei [93]. It has been observed in rare-earth nuclei [94], and in actinides [95, 96] . This resonance is generally viewed as the neutrons oscillating against the protons in a scissors-like motion.

Magnetic dipole spin-flip resonance

The magnetic dipole spin-flip resonance results from spin-flip collective excitations [97], where nucleons with spin $\uparrow$ oscillate against those with spin$\downarrow$, acting as

isoscalar mode of excitation. In addition, isovector excitation mode is possible, where protons with spin ↑ oscillate against neutrons with spin ↓ and vice versa.

3. *In the energy range of 30 to 140 MeV*

   In this region, the photon wavelength is comparable to the size of intranuclear distance. The neutron-proton pair in the nucleus is likely to absorb the photon and then released from the nucleus as the quasi-deuteron emission. Besides, two or more nucleons can also be released from the target nucleus by the direct reaction leading to the formation of various reaction products. The QD cross-section, $\sigma_{QD}(E_\gamma)$, is expressed in the model of Chadwick et al. [98] based on a Levinger-type theory [99] as follows:

$$\sigma_{QD}(E_\gamma) = L\frac{NZ}{A}\sigma_d(E_\gamma)f(E_\gamma), \tag{1.22}$$

   where L, $\sigma_d(E_\gamma)$ and $f(E_\gamma)$ are the Levinger parameter, experimental deuteron photo-disintegration cross-section and Pauli-blocking function, respectively.

1.3.3 Photonuclear reaction (γ, n)

In the GDR region, the emission probability of a single neutron is highest compared with that of multi-neutrons, a proton, or a charged particle. Since the reaction threshold of (γ, n) reaction is less than that of $(\gamma, 2n)$ and $(\gamma, 3n)$ reactions, and (γ, n) reaction is not been affected by the hindrance of the coulomb barrier as in the proton-, charged particle-induced reactions. Therefore, the (γ, n) cross-section dominates in the GDR region. The (γ, n) reaction is a three-step process. In the first step, the target nucleus absorbs the incident photons to form compound nucleus at a high excited state and emit the prompt γ radiation. In the second step, after reaching statistical equilibrium, the compound nucleus decays through a specific exit channel (mostly single neutron emission) as an evaporation process to form a residual nucleus. In the final step, this residual nucleus deexcites to the isomeric state or the ground state by the direct γ-decay or the γ-cascade transitions.

The scope of this work is to study IR in the (γ, n) reaction on heavy spherical or deformed nuclei induced by the bremsstrahlung with the end-point energy in the GDR region. This is based on three main reasons. Firstly, in this region, the electromagnetic interaction is well-known, and the absorption of the electric dipole photon E1 is dominant. After absorbing a photon E1, the nucleus with a spin of J_0 is excited to

spin $J_0 \pm 1$, whereby the theoretical consideration is simple. Secondly, although the photonuclear reaction cross-section is very low, the high bremsstrahlung flux and the GDR cross-section result in the high reaction yield enough for the experimental analysis with high accuracy. Finally, the study on the IR in photonuclear reactions reveals considerable interest due to the significant difference from nuclear reactions induced by other projectiles.

1.4 Neutron capture reaction

1.4.1 Neutron and neutron sources

In 1932, Chadwick discovered the existence of neutron by using beryllium to absorb the alpha particles originated from a polonium source [100]. Three years later, he won the Nobel Prize in Physics for this discovery. The neutron is a neutral particle with a mass slightly larger than the mass of the proton. A free neutron is unstable and decays with a mean half-life time of about 636 seconds into a proton by β^- emission. Neutrons are arbitrarily classified according to their kinetic energies into various categories as follows [101]:

- Cold Neutrons (0 eV; 0.025 eV).
- Thermal Neutrons. Neutrons in thermal equilibrium with a surrounding medium. The most probable energy at 20^{o}C (68^{o}F) for Maxwellian distribution is 0.025 eV.
- Epithermal Neutrons (0.025 eV; 0.4 eV).
- Cadmium Neutrons (0.4 eV; 0.5 eV). The kinetic energy of this type of neutrons is below the cadmium cut-off energy (0.5 eV). The natural cadmium foil absorbs neutrons being below 0.5 eV strongly as shown in Figure 1.6, mainly due to ^{113}Cd isotope (12.23 %).
- Epicadmium Neutrons (0.5 eV; 1 eV). Neutrons of kinetic energy above the cadmium cut-off energy. These neutrons are not absorbed by cadmium.
- Slow Neutrons (1 eV; 10 eV).
- Resonance Neutrons (10 eV; 300 eV).
- Intermediate Neutrons (300 eV; 1 MeV).
- Fast Neutrons (1 MeV; 20 MeV).

– Relativistic Neutrons (>20 MeV)

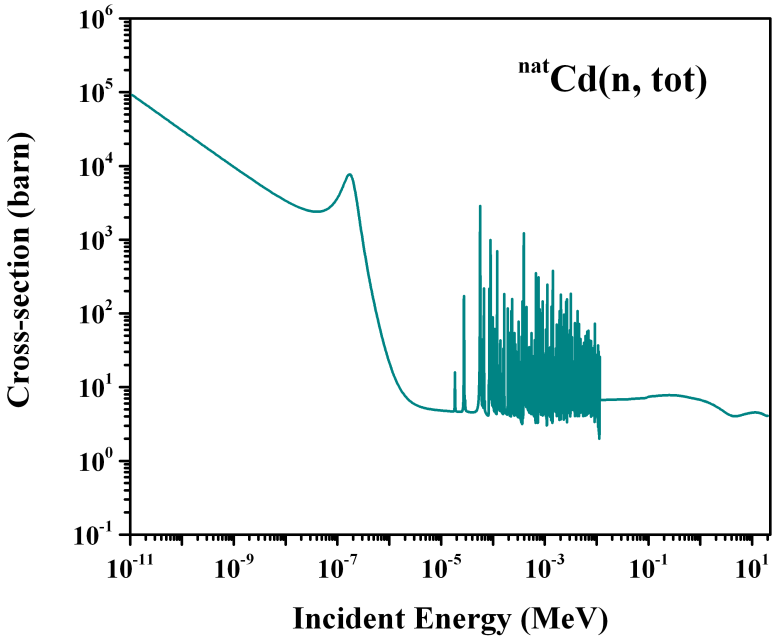

FIGURE 1.5: Total neutron cross-section of ^{nat}Cd, taken from the JEFF-3.3 library.

Neutron sources being available in standard laboratories are of three main categories (a) Accelerators-based neutron source, (b) Radioisotope neutron source and (c) Nuclear reactor-based neutron source. The possibilities of using these neutron sources depend on the type of their applications. All available neutron sources emit fast neutrons of various energies and intensities. We can reduce the speed of fast neutrons through their collision with atoms of the materials (so-called moderators) such as water, graphite, beryllium and hydrocarbons. This process of slowing is called moderating the neutrons. The choice of the appropriate neutron source depends on its energy, intensity, cost, size, portability and shielding requirement.

Depending on the energy, neutrons can induce three main types of interaction with a nucleus such as compound nucleus reaction, scattering, or direct reaction. For fast neutrons, (n,p), (n,α) and (n,2n) reactions are possible. For thermal, epithermal and resonance neutrons, the primary reaction is the capture reaction, in the form of the (n,γ) reaction [102] or other words, the only compound mechanism occur in this case.

1.4.2 Neutron capture reaction (n, γ)

For the non-fissionable nuclei, the only possible reaction with low-energy neutrons is the absorption reaction or neutron capture reaction. Neutron capture reaction (n,γ) irradiated by thermal and epithermal neutrons governed by the compound mechanism. The incident neutrons assumed mostly s-wave neutrons with zero angular momentum are completely absorbed to form a compound nucleus in an excited state. After capturing a neutron, the nucleus with a spin of J_0 is excited to spin J_0, $J_0 \pm 1/2$. The excitation energy of the compound nucleus is close to the neutron binding energy due to the negligible kinetic energy of the incident neutrons. Immediately after, the compound nucleus emits the prompt γ radiation with energies up to several MeV. The compound nucleus continues to decay to the isomeric or ground state of the product nucleus by the direct emission or the cascade transition of γ-rays. In many cases, the product nucleus is a radioactive nucleus, which emits a beta particle to form the nucleus with an increase in atomic number by one.

Studies of neutron capture reaction (n,γ) have contributed to our knowledge of neutron separation energies, γ-ray transition probabilities, decay schemes, and properties of nuclear energy levels. In addition, (n,γ) reaction plays an essential role in nucleosynthesis of elements heavier than iron created by successive neutron capture reactions and β-decay. Owing to high Coulomb barrier, theses elements can not be produced by charged particle reaction. The nucleosynthesis processes involving neutron capture include the slow neutron capture (s-process) and the rapid neutron capture (r-process), depending on the neutron flux and neutron density. The probability of neutron capture is characterized by the neutron capture cross-section.

1.4.3 Neutron capture cross-section

The neutron-induced cross-sections play a crucial role in not only fundamental nuclear research but also applications as nuclear medicine, fuel, dosimeter, shielding calculation, and waste management [103]. The cross-section of neutron capture depends on neutron energy and target nucleus. Figure 1.6 shows neutron capture cross-sections of ^{114,116}Cd (n,γ) and ^{108,110}Pd (n,γ) corresponding in green, blue, orange and violet lines as a function of the incident neutron energy, taken from the JEFF-3.3 library.

Two regions are distinguished in Figure 1.6. For low-energy region, the cross-sections obey a $1/\nu$ dependence with ν being the neutron velocity. Neutrons interacted in this region are mainly thermal neutrons. For higher incident energies, the cross-sections

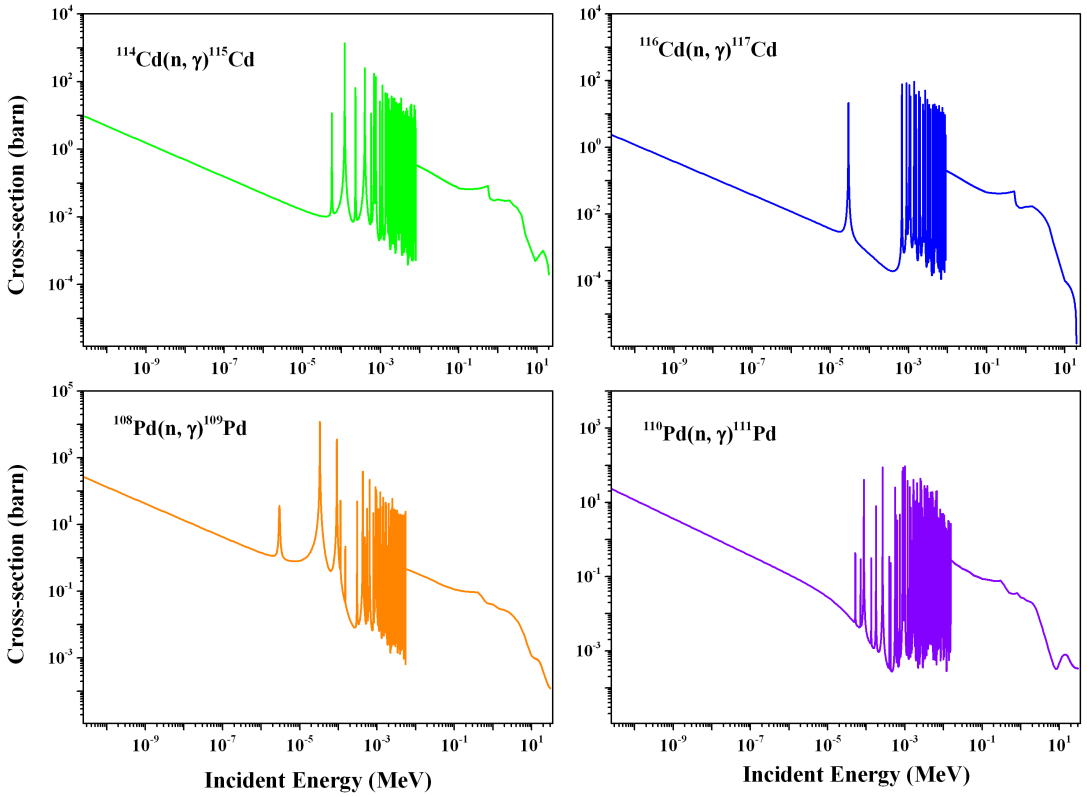

FIGURE 1.6: Neutron capture cross-section of ^{114}Cd, ^{116}Cd, ^{108}Pd and ^{110}Pd.

occur high peaks superimposed on the $1/\nu$ trend. These peaks are so-called resonance peaks. Most of the neutrons interacting in this region are epithermal and resonance neutrons. For heavy nuclei, high and narrow resonances appear in the eV energy range. The Breit-Wigner formula is employed for the single and isolated resonance cross-section as follow [102]:

$$\sigma(E) = g\frac{\pi}{k^2}\frac{\Gamma_0\Gamma_f}{(E-E_r)^2+\Gamma^2/4}, \tag{1.23}$$

where $g = (2J+1)/(2J_0+1)$ is statistical factor or spin factor depending on the total angular momentum of resonance state and initial state (J and J_0); k is the wavenumber; E_r is the centroid energy; $\Gamma_{0(f)}$ is the partial decay width of the entrance (exit) channel and $\Gamma = \hbar/\tau = \sum\Gamma_i$ is the total decay width.

For incident neutron energies of keV, the number of resonances per energy interval increases, resulting in overlapping resonances and an enhanced continuum. The resonances in this region are complex and difficult to detect individually. Therefore, they can be measured by summing the resonances, i.e., calculating the resonance integral. The thermal-neutron cross-section and resonance integral were investigated and determined in refs. [104, 105]. In the fast neutron region, the decrease in neutron capture probability of the nucleus leads to the rapid reduction of the cross-sections.

The Hauser–Feshbach (HF) statistical theory [52] is applied to calculate the cross-section of compound nuclear reaction, which relates to the transmission coefficient. It is difficult to evaluate this coefficient. The level density is employed to estimate the transmission coefficient for forming compound nuclide and γ strength function is powerful for describing the γ-ray emission channel. These quantities are represented in the following section.

1.5 Level density and γ-ray strength function

The investigation of the nuclear level density (LD) and γ-ray strength function (γSF) are crucial for interpreting the underlying nuclear structure. The LD and γSF are the key ingredients in nuclear reaction models, used to predict nuclear reaction rate, cross-section, modeling process in nuclear reactor and astrophysics. In the following subsections, the theory behind the LD and γSF will be presented, along with the models available in TALYS 1.95.

1.5.1 Nuclear level density

The mean spacing D between individual states can be determined by analyzing the discrete spectrum at low excitation energies. However, it becomes more difficult with increasing energy and nuclear mass. At excitation energies above several MeV for medium and heavy nuclei, the spacing D becomes small and at some points, it is impossible to distinguish experimentally between individual states. In this region, the level scheme is often referred to as quasi-continuum. At even higher energies beyond the neutron binding energy, D becomes much narrower than the natural line width Γ of the excited states terminating in overlapping many nuclear resonances. In this case, a continuum of nuclear levels is formed. Therefore, nuclear excitations are frequently classified into three regions, based on a comparison between the mean level spacing D and γ-decay width Γ. Fig. 1.7 [106] illustrates the discrete region, quasi-continuum region, and continuum region. As a result, while counting each level separately is impossible, an average description, namely, the nuclear LD is employed. The LD is inversely proportional to spacing D, and the level density $\rho(E_x, J, \pi)$ is described as the number of nuclear levels per MeV around an excitation energy E_x for a given spin J and parity π.

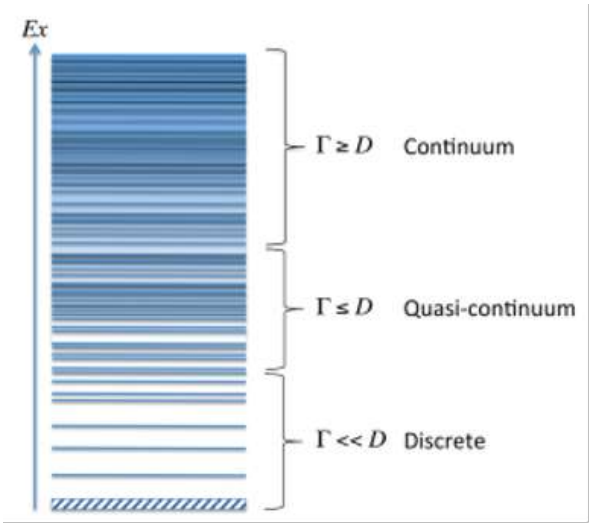

FIGURE 1.7: The energy regimes of nuclear excitation [106].

Several models are available to describe the LD, mainly categorized into semi-empirical and microscopic models. The former, so-called phenomenological LD models, have been built similarly to thermodynamics, while the latter solve the Schrodinger equation for many-body.

The most popular LD models are represented in this subsection ranging from phenomenological analytical expressions to tabulated LD of microscopic models [59].

Phenomenological level density model

The Fermi Gas level density

In 1936, H.Bethe introduced the first theoretical calculation of the LD originated from the comparison of the excited nuclear states and the Fermi gas [107], in which it is presumed the non-interactive movement of particles, and the identical space between single-particle states. The initial formula indicates the dependence of LD on excitation energy E_x as follows:

$$\rho(E_x) = \frac{\sqrt{\pi}}{12}\frac{exp(2\sqrt{aE_x})}{a^{1/4}E_x^{5/4}}. \tag{1.24}$$

Leaned on Bethe's original expression, and the literature data, Ericson [108] suggested a LD formula depending on spin, parity and excitation energy, today so-called Fermi-gas LD:

$$\rho(E_x, J, \pi) = \frac{1}{2}\frac{2J+1}{2\sqrt{2\pi}\sigma^3}exp\left[-\frac{\left(J+\frac{1}{2}\right)^2}{2\sigma^2}\right]\frac{\sqrt{\pi}}{12}\frac{exp(2\sqrt{aU})}{a^{1/4}U^{5/4}}, \tag{1.25}$$

where J, U, a and σ are the spin of the nucleus, effective excitation energy, LD parameter and spin cut-off parameter, respectively.

The effective excitation energy is given by:

$$U = E_x - \Delta, \tag{1.26}$$

where E_x, Δ are true excitation energy and energy shift (an empirical parameter related to pairing energy).

Summing over all spins yields the total LD given by

$$\rho_F^{tot}(E_x) = \frac{\sqrt{\pi}}{12}\frac{exp(2\sqrt{aU})}{a^{1/4}U^{5/4}}\frac{1}{\sqrt{2\pi}\sigma}. \tag{1.27}$$

The total LD can be calculated from the three parameters: a, σ, and Δ. Currently, various values of a, σ, and Δ are available. Furthermore, these parameters can be extracted as either independent or dependent on the excitation energy. Egidy and Bucurescu [109, 110] assembled the parameter values of a, σ, and Δ for more than 300 nuclides.

The back-shifted Fermi gas model

The back-shifted fermi gas (BSFG) model of Dilg [111], proposed by Gilbert and Cameron in 1965 [112] for the LD is based on the Fermi-gas approximation. The expression of LD of the BSFG model is similar in Eq. 1.25 and 1.27. However, the value of effective excitation energy U is changed by $U = E_x - \Delta^{BFM}$, where the energy shift Δ^{BFM} is given by

$$\Delta^{BFM} = \chi \frac{12}{\sqrt{A}} + \delta, \tag{1.28}$$

with χ = -1, 0 and 1 for odd-odd, odd-even and even-even nucleus, respectively and δ- an adjustable parameter to fit experimental data per nucleus.

The constant temperature model

The Constant Temperature Model (CTM) were introduced by Gilbert and Cameron [112]. Within the model, the excitation energy range is divided into a low energy part from 0 MeV up to a matching energy E_M, and a high energy part above E_M, where the respective "constant temperature" law and the Fermi gas model applies. There, the total LD is given as:

$$\rho^{tot}(E_x) = \begin{cases} \rho_T^{tot}(E_x) & if E_x \leq E_M \\ \rho_F^{tot}(E_x) & if E_x \geq E_M. \end{cases} \tag{1.29}$$

When $E_x \geq E_M$, the total LD is determined by Eq. 1.27.

The effective excitation energy $U = E_x - \Delta^{CTM}$, where the energy shift Δ^{CTM} is given by

$$\Delta^{CTM} = \chi \frac{12}{\sqrt{A}}, \tag{1.30}$$

with χ = 0, 1 and 2 for odd-odd, odd-even and even-even nucleus, respectively.

For low excitation energy $E_x \leq E_M$, the constant temperature part of the total LD reads

$$\rho_T^{tot}(E_x) = \frac{1}{T} exp\left(\frac{E_x - E_0}{T}\right), \tag{1.31}$$

here T is nuclear temperature and E_0 is given by

$$E_0 = E_M - T ln[T \rho_F^{tot}(E_M)], \tag{1.32}$$

$$\frac{1}{T} = \frac{dln\rho_F^{tot}}{dE_x}(E_M). \tag{1.33}$$

Additionally, there is the dependence of T on E_0 resulting from discrete level region as follows

$$N_U = N_L + \left(exp\left[\frac{E_U}{T}\right] - exp\left[\frac{E_L}{T}\right]\right) exp\left[\frac{-E_0}{T}\right]. \tag{1.34}$$

The level $N_{L(U)}$ is selected for describing best $\rho_T(E_x)$ of the observed discrete states, reserved in the database. The combination of Eqs. 1.32, 1.33 and 1.34 determines T, E_0 and E_M.

The generalized superfluid model

The Generalized Superfluid Model (GSM) takes superconductive pairing correlations into account according to the Bardeen-Cooper-Schrieffer theory. Similarly, to the CTM, the GSM distinguishes two energy regions corresponding to a phase transition from the superfluid phase to the Fermi gas phase. The separation of these energy regions is at the critical energy U_c.

At the effective excitation energy $U^{'} \leq U_c$, a superfluid behavior is expressed through pairing correlations strongly influencing the LD. In this case, the total LD is given by

$$\rho_{GSM}^{tot}(E_x) = \frac{1}{\sqrt{2\pi}\sigma}\frac{e^S}{\sqrt{D}}, \tag{1.35}$$

where S - the entropy, D - the determinant and σ - spin cut-off parameter related to the temperature and excitation energy.

$$U^{'} = E_x + \chi\Delta_0 + \delta, \tag{1.36}$$

where χ= 2, 1 and 0 for odd-odd, odd-even, and even-even nuclei, respectively; $\Delta_0 = \frac{12}{\sqrt{A}}$ and σ is an adjustable shift parameter to obtain the best description of experimental data per nucleus.

At the effective excitation energy $U \geq U_c$, the LD is described by the Fermi-gas model as in Eqs. 1.25 and 1.27. In this case, the effective excitation energy U is given by $U = E_x - \Delta^{GSM}$.

The parameters are expressed at the critical energy U_c in detail as in [59].

Microscopic level densities

Besides the aforementioned phenomenological models, there are different options employing microscopic approaches described and implemented in TALYS 1.95 [59]. Goriely has calculated LD on the basis of Hartree-Fock calculations for excitation energies up to 150 MeV and for spin values up to $I = 30$, stored as tables. In another approach, Hilaire and Goriely have calculated LD based on the microscopic combinatorial model. This model incorporates detailed microscopic calculations of the intrinsic state density and collective enhancement. Nuclear structure properties determined within the deformed Skyrme-Hartree-Fock-Bogolyubov framework are used in the calculations. The calculations also used tabulated level densities of more than 8500 nuclei for excitation energies up to 200 MeV and for spin values up to $J = 49$. An additional option available in the TALYS 1.95 is based on temperature-dependent Hartree-Fock-Bogolyubov calculations using the Gogny force.

1.5.2 Gamma-ray strength function

The γ-ray strength function (γSF) was first introduced by Bartholomew [113] to describe neutron capture data. The γSF representing the distribution of the average gamma transition probability plays an important role in the description of the gamma transition in a nuclear reaction. The (n, γ) and (γ, n) reaction channels are the best cases to investigate the γSF.

The γ-ray strength function $f_{XL}(E_\gamma)$ describes the average transition strength of a gamma ray at an energy Eγ, electromagnetic character X and multipolarity L.

Two types of radiative strength functions can be distinguished [114] as follows

- The "downward" strength function $\overleftarrow{f_{XL}}$ relates to the average radiative width of gamma decay such as in (n, γ) reaction and is determined for $E_\gamma < S_n$ (neutron separation energy).
- The "upward" strength function $\overrightarrow{f_{XL}}$ relates to the cross-section for gamma absorption such as in (γ, n) reaction and is determined for $E_\gamma > S_n$.

The $\overleftarrow{f_{XL}}$ in the de-excitation process depends on the average width of the states $\langle\Gamma_{XL}\rangle$ and the resonance spacing parameter D_{XL}:

$$\overleftarrow{f_{XL}} = \frac{\langle\Gamma_{XL}\rangle}{E_\gamma^{2L+1} D_{XL}}. \tag{1.37}$$

In deexcitation process, to calculate the competition between the emission of γ-ray and other particles, γ-ray transmission coefficients are used as input to Hauser-Feshbach

calculations. Therefore, the γSF is closely connected to the γ-transmission coefficient $T_{XL}(E\gamma)$ given by:

$$\overleftarrow{f_{XL}} = \frac{T_{XL}(E_\gamma)}{2\pi E_\gamma^{2L+1}}. \tag{1.38}$$

The $\overrightarrow{f_{XL}}$ in the excitation process depends on the γ-absorption cross-section $\sigma_{XL}(E_\gamma)$ as follows:

$$\overrightarrow{f_{XL}} = \frac{1}{(2L+1)(\pi\hbar c)^2}\frac{\langle\sigma_{XL}\rangle}{E_\gamma^{2L+1}}. \tag{1.39}$$

Eq. 1.39 means that the shape and parameters of the upward γSF is determined by the photoabsorption cross-section σ_{XL} summed over all spins and parities.

In the Brink-Axel hypothesis, the upward and downward strengths are approximatly equal given that the same states are populated equally whether it is populated from above or below: $\overleftarrow{f_{XL}}(E_\gamma) = \overrightarrow{f_{XL}}(E_\gamma) = f_{XL}$.

There are different theoretical models that are widely used to interpret the γSF for different modes of excitations and multipole types. Eight γSF models including phenomenological and microscopic models are employed in TALYS 1.95 [59].

The Standard Lorentzian model (SLO)

This is the model implementing the Brink-Axel hypothesis and is widely used to describe the giant electric dipole resonance (GEDR) strength. The strength is given by

$$f_{XL}^{SLO} = \frac{1}{(2L+1)(\pi\hbar c)^2}\frac{\sigma_{XL}E_\gamma\Gamma_{XL}^2}{(E_\gamma^2 - E_{XL}^2)^2 + E_\gamma^2\Gamma_{XL}^2}, \tag{1.40}$$

where σ_{XL}, E_{XL} and Γ_{XL} represent the peak cross-section, centroid energy, and width of the GEDR, respectively.

Although the SLO model describes well the GEDR close to the resonance centroid for medium and heavy nuclei, it often predicts the γSF lower than experimentally observed strength at and below the neutron separation energy S_n.

The generalized Lorentzian model (GLO)

The generalized Lorentzian model (GLO) of Kopecky and Uhl [115] is applied for $E1$ radiation. The GLO has energy- and temperature-dependent width given by

$$f_{XL}^{GLO}(E_\gamma, T) = \frac{1}{3(\pi\hbar c)^2}\left[\frac{E_\gamma \widetilde{\Gamma}_{E1}(E_\gamma)}{(E_\gamma^2 - E_{E1}^2)^2 + E_\gamma^2 \widetilde{\Gamma}_{E1}(E_\gamma^2)} + \frac{0.7\Gamma_{E1}4\pi^2T^2}{E_{E1}^3}\right]\sigma_{E1}\Gamma_{E1}, \tag{1.41}$$

where the energy-dependent damping width $\widetilde{\Gamma}(E_\gamma)$ is given by

$$\widetilde{\Gamma}(E_\gamma) = \Gamma_{E1}\frac{E_\gamma^2 + 4\pi^2T^2}{E_{E1}^2}. \tag{1.42}$$

And T is the nuclear temperature of the final state related to a LD model. For the Fermi gas model, T is given by

$$T = \sqrt{\frac{E_n + S_n - \Delta - E_\gamma}{a(S_n)}}, \tag{1.43}$$

where E_n, S_n, Δ and $a(S_n)$ are the incident neutron energy, neutron binding energy, pairing correction and LD parameter, respectively.

The GLO describes well both the low energy region and the peak region of the GEDR for spherical nuclei but underestimates highly deformed nuclei in the mass range $A \sim 150 - 175$ [116].

In addition, there are various microscopic γSF for $E1$ radiation have been stored in tables such as [59]:

- **Hartree-Fock BCS model**: This is a microscopic model for $E1$ radiation. Goriely and Khan calculated gamma-ray strength functions according to the Hartree-Fock Bardeen-Cooper-Schrieffer (HF-BCS) model with Quasiparticle Random Phase Approximation (QRPA) and stored them as tables.

- **Hartree-Fock-Bogolyubov model**: This is also a microscopic option calculated by Goriely using Hartree-Fock-Bogolyubov (HFB) model with QRPA.

- **Goriely's hybrid model**: This is a Lorentzian model with energy and temperature-dependent width which results in a different type of functional form at low energy than that of Kopecky-Uhl.

- **Goriely T-dependent HFB**: In this model, Goriely extended the temperature dependence of HFB model with QRPA.

- **T-dependent RMF**: This is the temperature-dependent relativistic mean field model calculated by Daoutidis and Goriely.

– **Gogny DIM HFB+QRPA**: This is HFB model with QRPA calculated by Goriely based on the D1M version of the Gogny force.

1.6 Objectives

Considering all the above-mentioned points, the main goals of this work are as follows:

1. To determine the experimental IR of spherical and deformed nuclei in (γ, n) and (n, γ) reactions irradiated by bremsstrahlung and thermal-epithermal neutrons, respectively. The natural Eu, Hg, Cd, Ce, Se and Pd targets were employed to investigate the IR owing to the scarce data with wide discrepancies, various nuclear structure and shape, and their crucial roles in many applications such as medicine, therapy, biology, electronics, material science and nuclear reactor.

2. To consider several effects affecting the IR value as excitation energy, spin difference, angular momentum transfer, nucleon configuration, and reaction channel effects.

3. To compute the theoretical IR in (γ, n) reaction using TALYS 1.95 code in combination with the GEANT4 toolkit to consider and validate our experimental data and the others in the existing literature.

4. To contribute experimental results with high accuracy as new data and/or additional ones into the Nuclear Data Bank for the purposes of fundamental research and applications, and the validity of theoretical nuclear models.

Chapter 2

Experimental and theoretical methods

In practice, measurements were carried out by means of the activation technique in combination with off-line γ-ray spectrometer. The activation technique was applied to generate radioisotopes of interest. The principle of this technique is to convert stable isotopes to radioisotopes by using nuclear reactions. It is possible to identify the radioisotopes and determine their activity relying on the information of typical γ-rays. Those are the energy and peak area measured by γ-spectroscopy, and the intensity and the half-life originated from the nuclear data. Several advantages of this experimental method are the uncomplicated experimental setup, reasonably priced experimental apparatus in comparison with the online measurement system, and the simultaneous determination of various radioisotopes [117] This work selected the activation technique due to its sensitivity, accuracy, economy, and convenience.

The irradiation sources, samples, experimental scheme and γ-spectroscopy as well as the experimental IR expression and necessary corrections are outlined in this chapter. In addition, the theoretical IR calculation using TALYS 1.95 code and GEANT4 toolkit is also demonstrated.

2.1 Experimental method

2.1.1 Irradiation sources

The irradiation sources, namely the thermal, epithermal, mixed energies neutrons and the bremsstrahlung, were generated from the Microtron MT-25 electron accelerator at the FLNR, JINR institute, Dubna. The MT-25 accelerator and its characterization will be presented in the following subsection.

Microtron MT-25

The Microtron MT-25 was designed by C. Simane and M. Vognar from Czechoslovakia in the 1970s [118]. It is a small cyclic electron accelerator. The electrons are increased the velocity by one radio frequency field (RF) with constant electric field and uniform magnetic field. The electrons move in circular orbits with the same point contact in the vacuum chamber. The accelerating cavity excited by the RF field is placed at the point contact. In other words, the electrons are accelerated when they travel across the electric field of the accelerating cavity. After reaching a predefined energy value, the accelerated electrons are expelled from the beam extractor [119]. The schematic layout and image of Microtron MT-25 are shown in Fig. 2.1. In the left layout, the numbers from 1 - 9 represent the magnetron, phase shifter, circulator, water load, accelerating cavity, main magnet (vacuum chamber), electron trajectories, adjustable beam extractor, and first deflector, respectively.

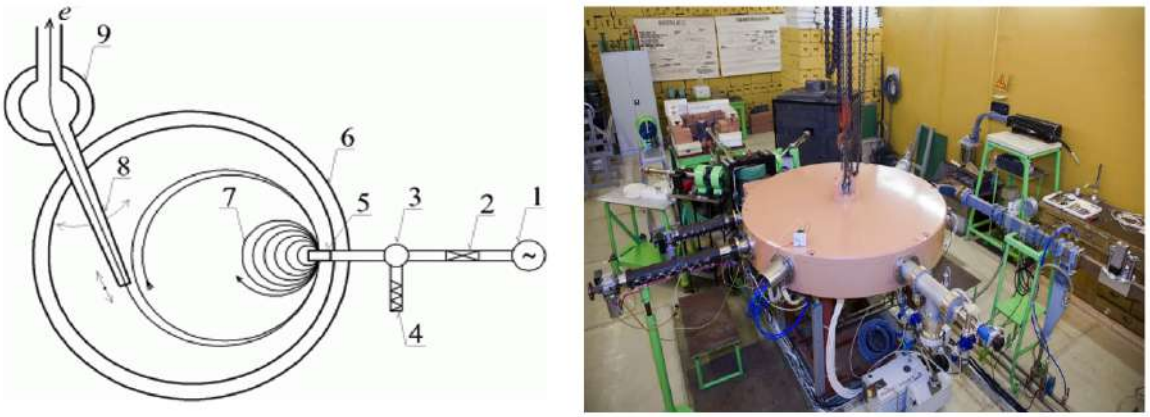

FIGURE 2.1: Schematic drawing and image of MT-25 Microtron.

The MT-25 is the accessible source for the investigation of nuclear reactions induced by electrons, bremsstrahlung and neutrons. It is also the equipment to produce artificial radioactive isotopes for various purposes. Additionally, the MT-25 serves as a rather intensive source of both photons and neutrons, which can be used for a number of different methods and techniques, such as photon activation and thermal-epithermal neutron activation. Table. 2.1 presents the dominant parameters of the MT-25.

Bremsstrahlung source

The bremsstrahlung radiations have many applications in material science and technology, activation analysis, and the medical field. In this work, they are employed as

TABLE 2.1: Main parameters of MT-25 microtron [118, 120].

Maximum electron energy	25 MeV
Energy range	10 – 25 MeV
Mean beam current	20 μA
Pulsed current duration	2.2×10^{-6}
Beam spot diameter	5 mm
Monochromatization	50 keV
Power consumption	20 kW
Bremsstrahlung beam	
Bremsstrahlung intensity	10^{14} s^{-1}
Neutron beam	
Thermal neutron flux	10^{9} s^{-1} cm^{-2}
Epithermal neutron flux	5. 10^{7} s^{-1} cm^{-2}
Fast neutron intensity	10^{12} s^{-1}

projectiles to investigate the photonuclear reactions. Fig 2.2 shows the production of bremsstrahlung using the accelerated electrons and proper converter.

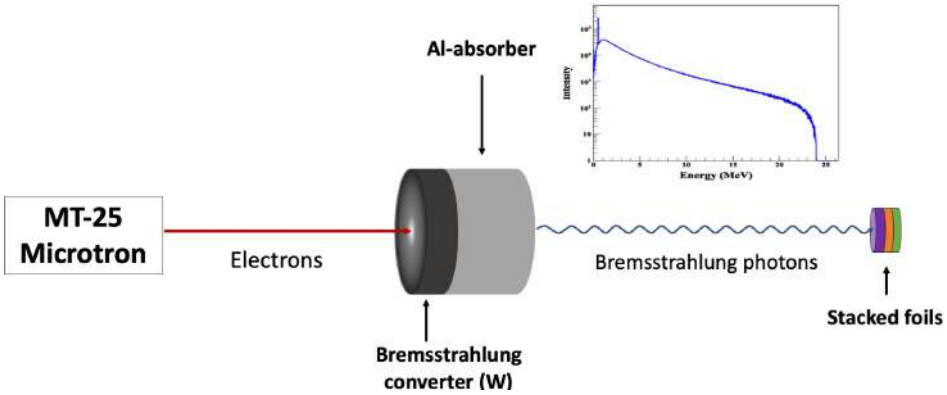

FIGURE 2.2: The scheme for production of bremsstrahlung source.

The accelerated electrons impinged on an electron-photon converter made of a 3 mm thickness W disk and cooled by water to generate the bremsstrahlung photons. To absorb low-energy electrons passing the converter, the Al absorber of 20 mm thickness was placed behind the converter. The MT-25 accelerator can generate a electron beam with energy ranging from 10 to 25 MeV, with energy sptep of 1 MeV. The electron beam has typically small energy spead of about 30–40 keV (up to 600 W of average beam power). These allows for measurement of IRs at a certain bremsstrahlung end-point energy which can be strictly defined.

Thermal and epithermal neutron source

To generate the thermal and epithermal neutrons using an electron beam from the accelerator, one can employ two layouts as in Fig. 2.3 and Fig. 2.4.

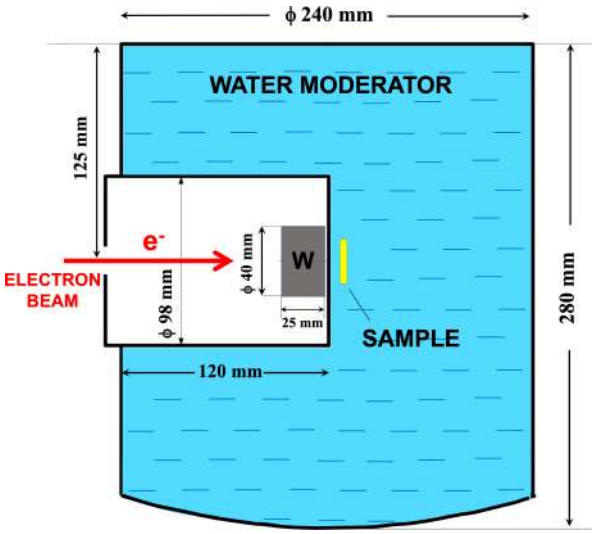

FIGURE 2.3: A schematic illustration of the production method for the source of mixed thermal-epithermal neutron and gamma.

In the first scheme, a mixture of photons and thermal-epithermal neutrons can be created. The W-disk of 25 mm thick and 40 mm in diameter enclosed by water was employed as a simultaneous electron-γ and γ-neutron converter. This mixed source can be employed for the activate measurement following by a simultaneous photon-neutron irradiation. Using this scheme, bremsstrahlung source can be produced by the electron beam impinging on the W-disk target, while neutrons can be produced from the (γ, n) reaction by bremsstrahlung flux on the this target as well. In this setup, neutrons can be moderated in water to obtain a mixed thermal-epithermal neutron source.

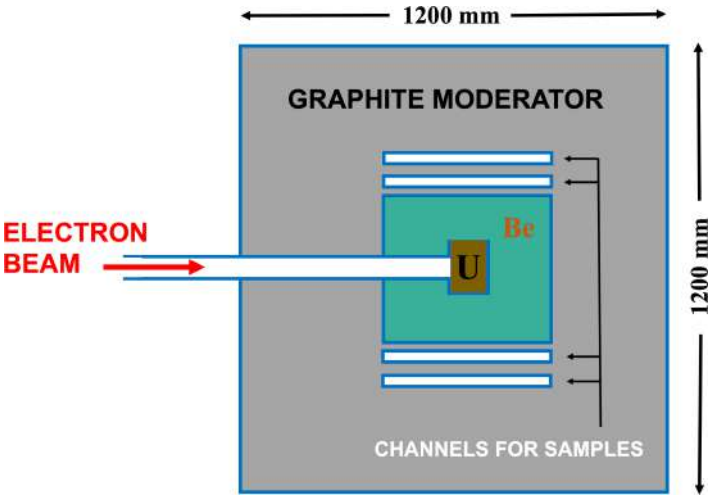

FIGURE 2.4: A schematic illustration of the production method for the thermal and epithermal neutrons.

In the second scheme, the thermal and epithermal neutrons can be produced. The bremsstrahlung flux was attained during the electron beam impinged on the U electron-γ converter with cylinder shape of 10 mm diameter and length surrounded by Be. The

neutron beam was created by (γ, n) photonuclear and (γ, f) fission reactions on U target with high energy part and by (γ, n) photonuclear reaction of Be with low energy part of the bremsstrahlung photon flux. In addition, Be can generate more neutrons from its interaction with the scattered photons from U. Therefore, the use of U together with Be as a photon-neutron converter could generate neutron flux with higher intensity than a single U converter. This U-Be converter was surrounded by a 120 x 120 x 120 cm^3 graphite cube served as the principal neutron moderator. The thermal neutron flux at the central position of the graphite cube was 4.10^8 neutron/s.cm^2 at an electron energy of 25 MeV and a current of 20 μA. The detailed construction of this neutron source can be found in Ref. [121].

This work used the second layout to investigate the IRs in thermal and epithermal neutron capture reactions.

2.1.2 Sample irradiation

Before irradiating samples, it is necessary to prepare and determine the mass of sample, the mean electron current of the electron accelerator, and the irradiation duration to assure the counting statistics of the characteristic γ-rays. These issues can be solved by preliminary estimation in the reaction yield using the activation method. Additionally, the proper irradiation duration is selected on the basis of the reaction cross-section and half-life of the product nuclei. The maximum exposed duration is five times of the half-life. After the irradiation, the waiting time is also determined based on the half-life of the product isotopes of interest. To study IRs in the photonuclear and neutron capture reactions, this work used natural samples with the high purity of Se, Pd, Cd, Ce, Eu and Hg elements. The reasons for choosing these samples are the scarce IR data with large discrepancies of isomeric pairs of interest, various nuclear structure and shape, and their prominent roles in numerous applications.

Europium (Eu) is a rare-earth element and the softest lanthanide with atomic number Z = 63. Owing to its phosphorescence, Eu is applied in the manufacture of fluorescent glass, and color TV/computer screens. In astrophysics, the abundance of Eu in stellar spectra can be used to classify stars and give the information about the origin of stars. Moreover, Eu is employed in nuclear reactor control rods due to it is a good neutron absorber [122]. Natural europium consists of two isotopes, ^{151}Eu and ^{153}Eu, with abundances of 47.81 and 52.19%, respectively. The ground states of odd-even

spherical ^{151}Eu and deformed ^{153}Eu nuclei are the $d_{5/2^+}$ proton single-particle state and the $[413]\frac{5}{2}^+$ proton single-particle state, respectively [123].

Mercury (Hg), Z = 80, is a heavy, silvery-white element and is the only metallic element to be liquid at standard conditions for temperature and pressure. In the past, using Hg was widespread in thermometers, sphygmomanometers, fluorescent lamps, cosmetics and medicine. However, the use of Hg in applications has significantly reduced today due to its toxicity [122]. The natural mercury includes ^{196}Hg, ^{198}Hg, ^{199}Hg, ^{200}Hg, ^{201}Hg, ^{202}Hg and ^{204}Hg isotopes with abundances of 0.15, 9.97, 16.87, 23.1, 13.18, 29.86 and 6.87%, respectively. The nuclei ^{196}Hg and ^{198}Hg belong to the nuclear range with Z=73–81 and A=182–206. They lie between strongly deformed nuclei of rare-earth elements and the region of spherical nuclei in the vicinity of A = 208. The nuclei ^{198}Hg and ^{196}Hg are spherical even-even nuclei with ground-state spin of 0^+. Their nucleon configuration is well described by single-particle model. They have two proton holes with respect to the 6^{th} closed shell of protons (Z = 82) or in other words, the last ten protons arrange in the subshell $(1h_{11/2})^{10}$. Six neutrons of ^{198}Hg and four neutrons of ^{196}Hg nuclei occupy the orbit $1i_{13/2}$. Hence, the high-spin Hg isomers are expected in the nuclear reaction.

Palladium (Pd), Z = 46, is a rare and lustrous silvery-white metal. It is used for a broad range of applications comprising the jewelry, dentistry, blood sugar test strips, aircraft spark plugs, surgical instruments, electrical contacts, and catalytic converters in the automobile industry [122]. Naturally occurring palladium consist of six isotopes ^{102}Pd, ^{104}Pd, ^{105}Pd, ^{106}Pd, ^{108}Pd, and ^{110}Pd with abundances of 1.02, 11.14, 22.33, 27.33, 26.46 and 11.72%, respectively. The nuclei ^{108}Pd and ^{110}Pd are known as vibrational even-even nuclei with ground-state spin of 0^+.

Cadmium (Cd) element, Z = 48, is soft, silvery-white metal. Cadmium is a common component of electric batteries, pigments, coatings, and electroplating and has a significant role in nuclear reactor engineering, being the main compound in the control rod [122]. Natural cadmium is composed of 8 isotopes ^{106}Cd, ^{108}Cd, ^{110}Cd, ^{111}Cd, ^{112}Cd, ^{113}Cd, ^{114}Cd and ^{116}Cd with abundances of 1.25, 0.89, 12.47, 12.8, 24.11, 12.23, 28.75 and 7.51%, respectively. The Cd isotopes have two proton holes with respect to the 5^{th} closed shell (Z = 50). The nuclei ^{114}Cd and ^{116}Cd are vibrational even-even nuclei with ground-state spin of 0^+.

Cerium (Ce) is a rare-earth element with Z = 58. It is a soft, ductile, and silvery-white metal that tarnishes when exposed to air. Ce and its compounds are used widely

in the glass polish, catalytic converters, white LED light sources, pigments, nanomaterials, nuclear fuel and scintillation detectors ($CeBr_3$, $LaBr_3(Ce)$) [122]. Naturally occuring cerium comprises four stable isotopes ^{136}Ce, ^{138}Ce, ^{140}Ce and ^{142}Ce with abundances of 0.186, 0.251, 88.449 and 11.114%, respectively. The nuclei ^{138}Ce and ^{140}Ce are spherical even-even nuclei with ground-state spin of 0^+. Following the single-particle model, the Ce isotopes have eight protons filling the subshell $(1g_{7/2})^8$. It is worth noting that ^{138}Ce nucleus has two neutron holes while ^{140}Ce nucleus is a magic one since its neutrons filled up the 6^{th} closed shell (N = 82). This is also the reason why the abundance of ^{140}Ce is much greater than others.

Selenium (Se), Z = 34, is nonmetal and appears in red, black or grey depending on the temperature change. The use of Se is known in the glass production, pigments, electronics, material science, biology, supplements and the production of therapeutic and medical radioisotopes [122]. Selenium has six natural isotopes including ^{74}Se, ^{76}Se, ^{77}Se, ^{78}Se, ^{80}Se and ^{82}Se with abundances of 0.86, 9.23, 7.6, 23.69, 49.8 and 8.82%, respectively. The nuclei ^{74}Se and ^{82}Se are known as vibrational even-even nuclei with ground-state spin of 0^+.

The characteristics of irradiated samples, the electron current (I_e), the electron energy (E_e) and the irradiation time (t_{irr}) in the photonuclear and neutron capture reaction experiments are given in Table 2.2.

TABLE 2.2: Characteristics of irradiated samples, electron current and energy, and irradiation time.

Symbol	Sample	Purity [%]	Weight [g]	Diameter [cm]	I_e [μA]	E_e [MeV]	$t_{irr}(\gamma, n)$ [min.]	$t_{irr}(n, \gamma)$ [min.]
Eu	Eu_2O_3	99.99	0.1	1	15	14 - 23	60 - 90	
Hg	$HgCl_2$	99.99	0.3	1	15	14 - 24	60	
Pd1	PdO	99.99	0.323	1	15	24 - 25	30	
Pd2	PdO	99.99	0.323	1	15	25		90
Cd1	Cd	99.99	0.719	1	15	24 - 25	60	
Cd2	Cd	99.99	0.719	1	15	25		120
Ce1	Ce_2O_3	99.99	0.8	1	12 - 14	25	60	
Ce2	Ce_2O_3	99.99	0.8	1	12 - 14	25		90
Se1	SeO_2	99.99	0.248	1	12	25	20	
Se2	SeO_2	99.99	0.248	1	12	25		90

For the (γ, n) reaction, the samples were exposed to the bremsstrahlung (Fig. 2.2) at 5cm distance from the W converter.

For the (n, γ) reaction, the samples were irradiated without and with the 2 mm-thick Cd cover and placed at 40 cm distance from the center of the graphite cube (Fig. 2.4),

where the Cd ratio is 2.5. The Cd ratio is defined as the ratio of the activity of a bare sample to that of a Cd-covered sample. Au foils were used to monitor the neutron flux in this case.

2.1.3 Gamma spectroscopy

After a definite cooling time, the γ-ray activities of the studied samples were determined by a spectrometer including a HPGe detector with 60.5 mm diameter and 31 mm length attached with the preamlifier, amplifier, and ADC and PC-based 8192 channel analyzer (CANBERRA) for the data processing as in Fig. 2.6. The HPGe is one type of semiconductor detector used most commonly for γ-rays spectroscopy studies. In a semiconductor detector, electron-hole pairs are created as a result of electrons being excited from the valence band to the conduction band due to thermal excitation and γ-ray interactions. The germanium semiconductors must be maintained at $\sim$ 77 K with liquid nitrogen in order to reduce thermal noise because of the low energy gap of 1.12 eV between the conduction and valence band. In that way, only γ-ray interactions will contribute to the energy signal by creating electron-hole pairs. Compared to the inorganic scintillation detector NaI(Tl), the performance in terms of the energy resolution of the HPGe is about an order of magnitude better than the scintillation detector, whereas, its efficiency is worse than that of the scintillation detector. Therefore, germanium detectors are the preferred choice for high energy-resolution studies in nuclear physics. The energy resolution of the used spectrometer is 1.8 keV at the 1332.5 keV γ-peak of ^{60}Co isotope.

The samples were placed at various distances from the end cap of the HPGe detector. The γ-ray counting duration was decided by taking care of activities of the product nuclei, the photo-peak areas of the characteristic γ-rays, and the Compton background. The measurements were performed with random errors less than 0.5–2% for the γ-rays of interest. The product nuclei have been identified relied on their half-lives and γ-ray energies. The used γ-spectrometer illustrated in Fig. 2.5 consists of the HPGe detector, electronics to collect, amplify and process the signals produced by the detector, and a computer coupled with processing software to display, and analyze the spectrum. The γ-ray spectra were measured and analysed by employing the Gamma Vision software. This software can determine the count numbers under the photo-peaks and corresponding energy, and its user-interface is displayed in Fig. 2.7.

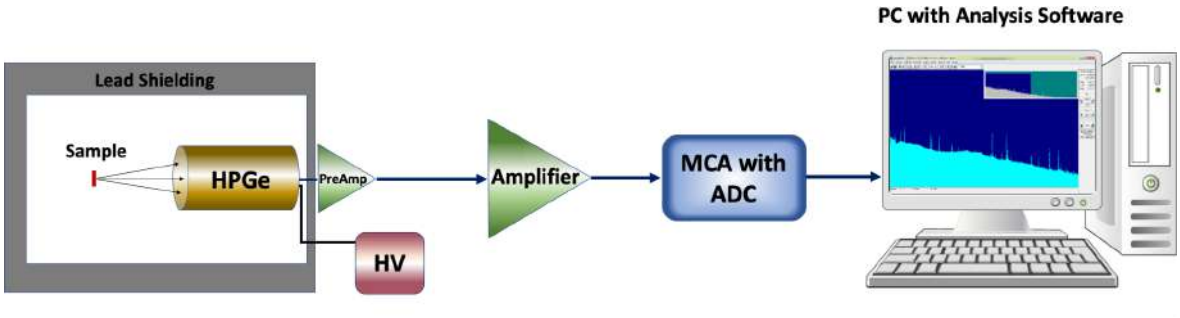

FIGURE 2.5: The gamma spectrometer diagram.

FIGURE 2.6: HPGe detector of Chemistry of transactinides Department, FLNR, JINR, Dubna.

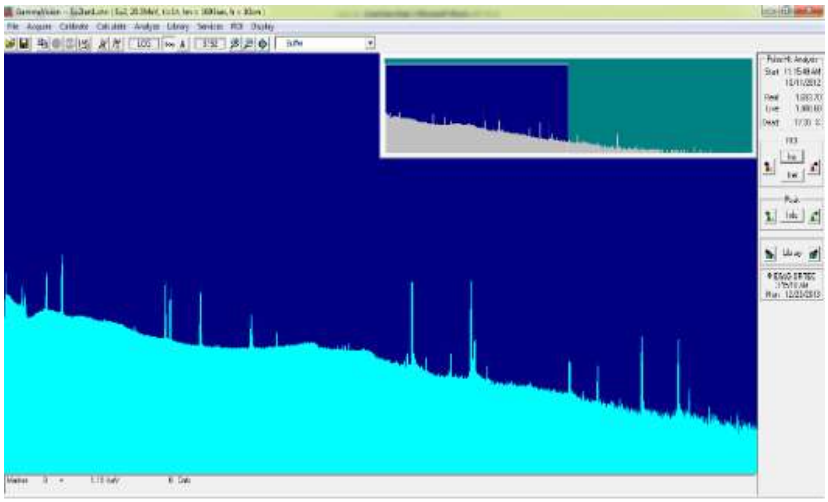

FIGURE 2.7: Gamma Vision software.

Before each measurement, the energy and efficiency calibration was performed using the QCY and QCYK mixed nuclide sources with known γ-rays energies and radioactivity. These sources contain ^{241}Am, ^{133}Ba, ^{57}Co, ^{60}Co, ^{113}Sn, ^{22}Na, ^{54}Mn, ^{137}Cs, ^{139}Ce, and ^{134}Cs, covering wide range of γ-rays energies from 59.54 keV (^{241}Am) to 1365.19 keV (^{134}Cs). The energy calibration employed a linear function of energy versus ADC channel number of the corresponding full-energy peaks to obtain a set of energy calibration parameters, namely gain and offset. These parameters were then applied to the offline measurements of the γ-rays of interest.

For γ-ray spectrometer, the detection efficiency is the important parameter in the measurement and data analysis. It contains the full-energy peak efficiency and the total efficiency. The full-energy peak (photo-peak) efficiency is the ratio between the number of the detected photon at the energy of interest and the number of photons that are emitted from the source. The total efficiency is the ratio of the number of pulses recorded to the total photon emitted from the source. This efficiency is used to correct the coincidence-summing effect. The photo-peak efficiency can be calculated using the following formula:

$$\varepsilon(E) = \frac{N}{A \times e^{-\lambda t} \times I_\gamma \times t_m}, \tag{2.1}$$

where N, t_m, A, λ, t and I_γ are the number of counts, measurement time, known activity, decay constant, period from the date of manufacture of the source and γ-ray intensity, respectively.

The photo-peak efficiency ε was calibrated, and was fitted by using the fittinf function as follow:

$$\varepsilon(E) = exp(\sum_{i=0}^{5} a_i ln(E)^i), \tag{2.2}$$

where E is the γ-ray energy, and a_i is the fitting parameters.

The measured efficiency and fitted curves at distances of 5, 10 and 20 cm are shown in Fig. 2.8. The detailed calculation and fitting parameters of the HPGe efficiency curve were represented in [124].

2.1.4 Experimental IR determination

In the activation time t_1, there are two processes taking place simultaneously, namely the formation of an isomeric pair and their decay. The isomeric pair production during

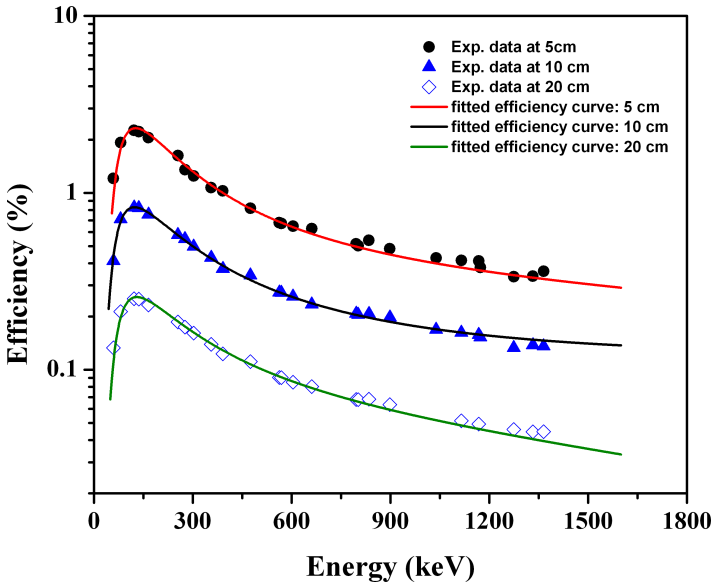

FIGURE 2.8: The efficiency curve for the HPGe detector used in the present work.

time t_1 can be demonstrated by the below differential equations:

$$\frac{dN_m}{dt} = Y_m - \lambda_m N_m, \tag{2.3}$$

$$\frac{dN_g}{dt} = Y_g - \lambda_g N_g + P_{mg}\lambda_m N_m, \tag{2.4}$$

here m,g - isomeric and ground state; N – number of nuclei; Y – yield; λ - decay constant; P – isomeric transition probability.

The decay equations of the isomeric pair during cooling and measuring time (t_2 and t_3) mimic Eqs. 2.3 and 2.4 but the terms Y_i are absent. The solution of the above equations in three timing intervals and the subsequent integral of the reduced activity over t_3 results in

$$\frac{S_m}{\varepsilon_m I_m} = Y_m \Lambda_3^m \Lambda_6^m \Lambda_9^m, \tag{2.5}$$

$$\frac{S_g}{\varepsilon_g I_g} = Y_g \Lambda_2^g \Lambda_5^g \Lambda_8^g + Y_m(\Lambda_1^g \Lambda_5^g \Lambda_8^g + \Lambda_3^g \Lambda_4^g \Lambda_8^g + \Lambda_3^g \Lambda_6^g \Lambda_7^g), \tag{2.6}$$

where S, ε, I – the photo-peak area, absolute photo-peak efficiency, branching ratio (γ-ray intensity of the number of photons within 100 disintegrations), respectively, and Λ_i - time-dependent term presented as follows:

$$\Lambda_1^g = \frac{P_{m,g}}{\lambda_g}\left[1 - \frac{\lambda_m\lambda_g}{\lambda_m - \lambda_g}\left(\frac{e^{-\lambda_g t_1^g}}{\lambda_g} - \frac{e^{-\lambda_m t_1^g}}{\lambda_m}\right)\right], \tag{2.7}$$

$$\Lambda_2^g = \frac{1}{\lambda_g}(1 - e^{-\lambda_g t_1^g}), \tag{2.8}$$

$$\Lambda_3^g = \frac{1}{\lambda_g}(1 - e^{-\lambda_m t_1^g}), \tag{2.9}$$

$$\Lambda_3^m = \frac{1}{\lambda_m}(1 - e^{-\lambda_m t_1^m}), \tag{2.10}$$

$$\Lambda_4^g = P_{mg}\frac{\lambda_m}{\lambda_m - \lambda_g}(e^{-\lambda_g t_2^g} - e^{-\lambda_m t_2^g}), \tag{2.11}$$

$$\Lambda_5^g = e^{-\lambda_g t_2^g}, \tag{2.12}$$

$$\Lambda_6^g = e^{-\lambda_m t_2^g}, \tag{2.13}$$

$$\Lambda_6^m = e^{-\lambda_m t_2^m}, \tag{2.14}$$

$$\Lambda_7^g = P_{mg}\left[1 - \frac{\lambda_m\lambda_g}{\lambda_m - \lambda_g}\left(\frac{e^{-\lambda_g t_3^g}}{\lambda_g} - \frac{e^{-\lambda_g t_3^g}}{\lambda_m}\right)\right], \tag{2.15}$$

$$\Lambda_8^g = 1 - e^{-\lambda_g t_3^g}, \tag{2.16}$$

$$\Lambda_9^m = 1 - e^{-\lambda_m t_3^m}. \tag{2.17}$$

In the same irradiation, cooling, and measurement conditions, an equality of corresponding time of those processes for the isomeric and ground states is assumed, namely, $t_1^m = t_1^g = t_1$, $t_2^m = t_2^g = t_2$ and $t_3^m = t_3^g = t_3$.

The IR is obtained from the Eqs. 2.5 and 2.6 as following:

$$\frac{1}{IR} = \frac{\frac{S_g I_m \varepsilon_m}{S_m I_g \varepsilon_g}\Lambda_3^m\Lambda_6^m\Lambda_9^m - \Lambda_1^g\Lambda_5^g\Lambda_8^g - \Lambda_3^g\Lambda_4^g\Lambda_8^g - \Lambda_3^g\Lambda_6^g\Lambda_7^g}{\Lambda_2^g\Lambda_5^g\Lambda_8^g}. \tag{2.18}$$

Based on the photo-peak area, absolute photo-peak efficiency, branching ratio and time dependent parameters one can be calculated the IR as in the above Eq. 2.18.

Since several γ-rays spectra under different experimental conditions (such as time intervals of cooling and measurement) were used to calculate the IRs in this work, the final result was computed by the average value $\overline{IR}$ determined from γ-rays spectra obtained for all experimental conditions. The relative uncertainty was calculated by the following formula:

$$\varepsilon(\overline{IR}) = \frac{\sigma(\overline{IR})}{\overline{IR}} = \frac{\sqrt{\sum_{n}^{i=1} \sigma_i^2(IR)/n}}{\overline{IR}}, \tag{2.19}$$

where $\sigma_i(IR)$ - the IR uncertainty determined in i^{th} experimental condition and n - the number of experimental conditions.

To enhance the precision of the measured photo-peak areas, the necessary corrections for the accompanying effects must be considered.

2.1.5 Spectrum analysis-necessary correction

The IR determination following Eq. 2.18 depends on many factors, in which S_m and S_g play a significant role. In this work, the criteria for choosing the γ-rays in the data analysis were the followings: (a) Their intensities are higher than that of other γ-rays, (b) they are well resolved in the gamma spectra and (c) they are free of the contamination from the products of other nuclear reactions. However, in some cases, the overlapped peaks resulting from the γ-rays interference of other reaction products were used in data analysis. The counts of these peaks must be corrected by using the decay curve method or the peak ratio method. Moreover, the counts can be lost due to the self-absorption and coincidence summing effects.

Self-absorption effect

The error may occur by the self-absorption effect, especially with low energy γ-peaks and with a thick sample, when the measurement is performed. For samples with thickness t that is known very well about the composition and concentration of elements, the self-absorption coefficient is given by [125]

$$F_g = \frac{\mu t}{1 - e^{-\mu t}}, \tag{2.20}$$

here μ, t are the linear attenuation factor and the target thickness, respectively. The μ data are taken from [126].

Coincidence summing corrections

Coincidence or cascade summing is an intrinsic behavior of a γ-ray detector system where two or more γ-rays from single disintegration come very close in time and result in only one summed pulse. This effect also means losing the count of the actual γ-peak. To correct the count loss of the actual γ-peak due to the coincident summing effect, this work used the formula [127] to calculate the correction factor C_c as follows:

$$C_c = \frac{1}{1 - \sum_{i=1}^{i=j} f_i \times \varepsilon_t(i)}, \tag{2.21}$$

where f_i is the fraction of photon with energy i, which is in coincidence with the γ-ray of interest. The $\varepsilon_t(i)$ is the total efficiency of the coincidence photon with energy i.

Consequently, the true number of counts can be determined by multiplying the measured value with F_g and C_c.

2.2 Theoretical IR calculation in (γ, n) reaction

As aforementioned, the bremsstrahlung has been used to induce photonuclear reaction. Therefore, a combination of the differential cross-section dataset calculated by TALYS 1.95 code and bremsstrahlung spectra simulated by transportation code GEANT4 is implemented to calculate the IR following the Eq. 1.9.

2.2.1 Bremsstrahlung spectra simulation in GEANT4

The Geant4 toolkit has been used to simulate the energy flux of γ-rays in the secondary target. A user application has been written based on an example named "examples/basic/B1" provided in the Geant4 package. Fig. 2.9 shows the diagram of the Geant4 user application in this work.

In this application, the generation of the primary particles as a form of an electron beam in the current setup by Monte-Carlo sampling has been implemented using the built-in primary generator class G4GeneralParticleSource. This class allows one to run macro-type commands directly before simulation to change the particle species, their energy spectral, spatial and angular distribution without changing the user codes. In

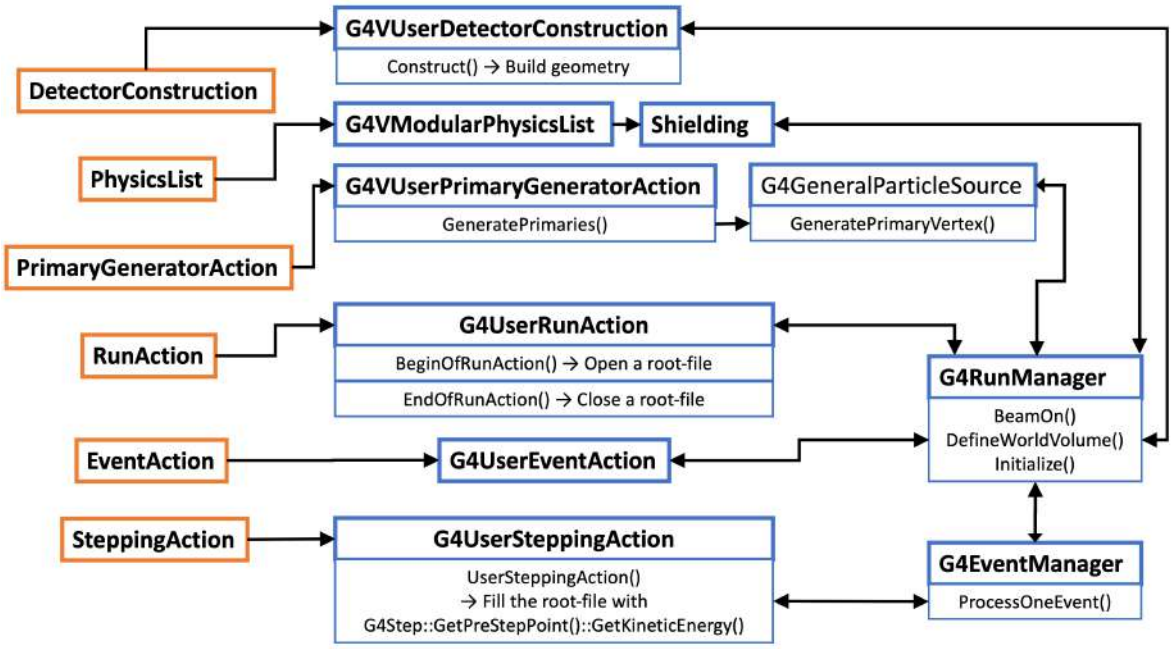

FIGURE 2.9: Diagram of the Geant4 user application.

this work, a beam of electrons was simulated with a circular beam profile and a gaussian profile of beam energy given by the actual experimental conditions.

To simplify the user codes, the packaged physics list named "Shielding" were used to describe the physical interactions of particles in matters. It is a convenient and ready-to-use physics list of Geant4, which was constructed by expert developers at the SLAC facility in the USA. The "Shielding" physics list has been primarily designed for simulating a shielding, high energy or underground detector, where all possible emergent radiations and their interactions need to be considered. This physics list contains the best-guess selection of electromagnetic and hadronic physics, including the G4EmStandardPhysics for electromagnetic physics, the G4EmExtraPhysics for additional physics related to synchrotron radiation and gamma nuclear physics. Therefore, this list was considered suitable to simulate the γ-rays energy flux at the secondary target for the current experimental setup.

The geometry of the experimental setup has been modeled as detailed as possible using a user implementation code derived from virtual G4DetectorConstruction class, as shown in Fig. 2.10 for the photonuclear (left) and neutron capture reactions (right).

The production of bremsstrahlung has been simulated by using Monte Carlo calculation implemented in the GEANT4 toolkit. GEANT4 tracks the history of individual particles, while the average behavior is a combination of effects from individual particles. The processes to track photons can be enabled after target modeling and particle

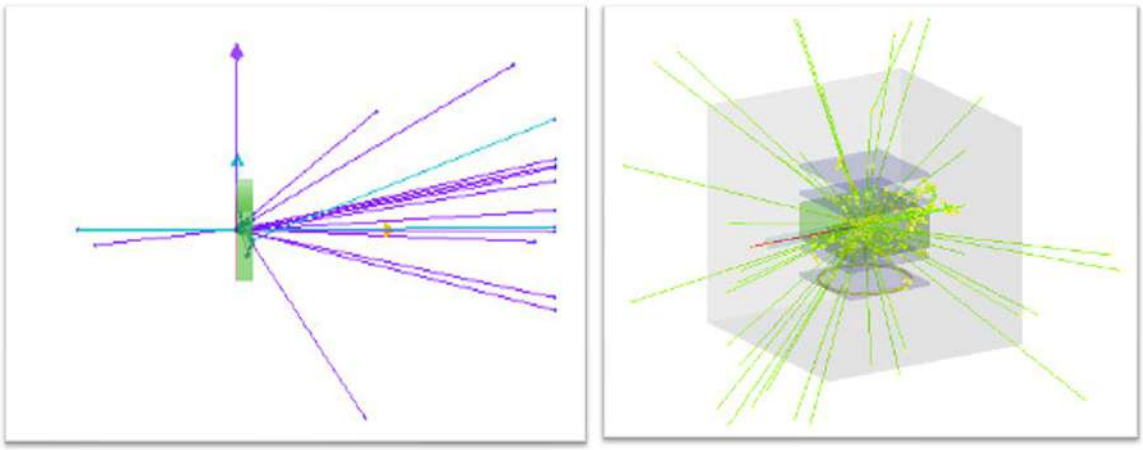

FIGURE 2.10: GEANT4 simulation of experimental setups for photonuclear reaction (left) and neutron capture (right).

source configuration. The so-called "delta" δ information of the tracked photons are extracted and the energy of the photon before interacting with the target was stored as a form of a CERN ROOT [128] NTuples file. Details are implemented in the user-defined "G4UserSteppingAction" class in GEANT4. By analyzing the NTuples file, the bremsstrahlung was found as an energy function of the outgoing photons which is illustrated in Fig. 2.11. Bremsstrahlung radiation was produced when the electron beam with high energy impinges on the primary target (converter). A 3 mm W has been used as the converter. The bremsstrahlung spectrum depends on the type of target material and the energy of the incident electron beam. In this work, the bremsstrahlung spectrum for the end-point energies of 10 to 25 MeV with the step of 1 MeV has been simulated separately. The bremsstrahlung spectra have energies in the range from 0 to incident electron beam energy. In analogy, the neutron spectrum shown in Fig. 2.12 is the GEANT4 simulation result following the experimental scheme in Fig. 2.4. This spectrum may be served in the further investigation.

2.2.2 Cross-section calculation in TALYS

In TALYS 1.95 code, the default keywords are the projectile, target element, target mass, and projectile energy. There are nearly 340 keywords in TALYS 1.95 that can implemented depending on the user's purpose. In this work, in addition to default keywords, the keywords relating to level density models and γSFs were employed to calculate the cross-sections of the interested photodisintegration reactions in the GDR region. The output contains the cross-section files corresponding to the reaction channels. Moreover, when the keyword *outbasic* is set *y* in the input file, all the information

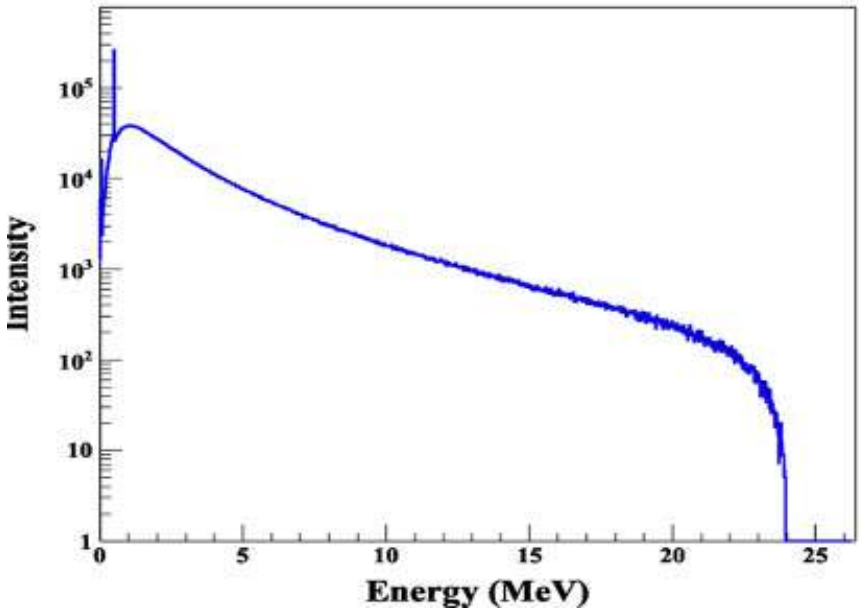

FIGURE 2.11: The bremsstrahlung with end-point energy of 24 MeV calculated by Geant4.10.06 version.

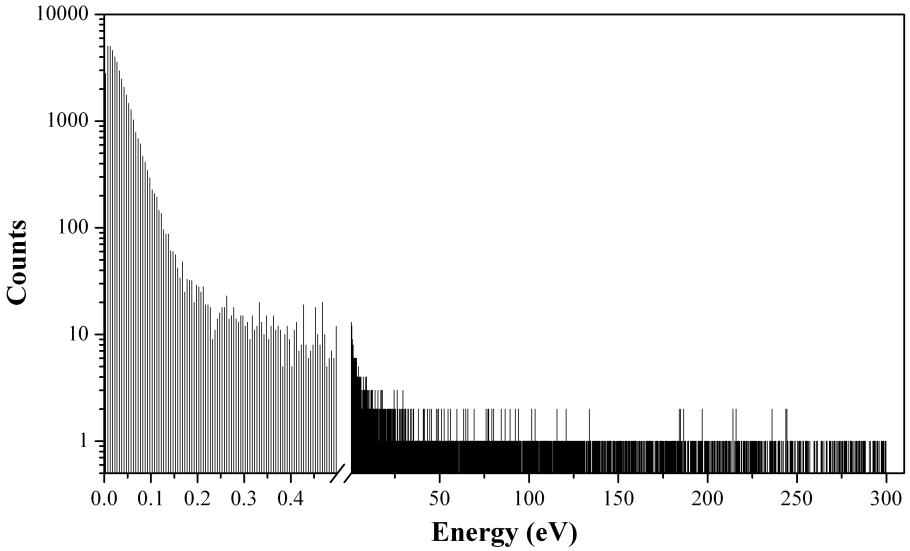

FIGURE 2.12: Geant4 simulated neutron energy at a distance of 30 cm from the primary target.

of nuclear structure can be extracted in the output file, comprising all fundamental information required for the reaction calculation as the population of levels, optical-model parameters, transmission coefficients, γ strength functions, discrete levels, level densities and reaction cross-sections.

In detail, this work used the TALYS 1.95 code to compute the (γ, n) reaction cross-section in the photon energy range of 10 to 25 MeV on natural Cd, Ce, Se, Pd, Eu and Hg targets using six level density models. Which include three phenomenological LD models (Ld1-3) and three microscopic LD models (Ld4-6):

- Ld-1: Constant Temperature Model + Fermi gas model.
- Ld-2: Back-shifted Fermi gas model.
- Ld-3: Generalised superfluid model.
- Ld-4: Microscopic level densities (Skyrme force) from Goriely's tables.
- Ld-5: Microscopic level densities (Skyrme force) from Hilaire's combinatorial tables.
- Ld-6: Microscopic level densities (temperature dependent HFB, Gogny force) from Hilaire's combinatorial tables.

In nuclear reactions, in addition to the level density, the γSF representing the distribution of the average γ transition probability is also a crucial ingredient for predicting the reaction cross-sections. Thus, for each Ld model, this work employed eight γSFs available in TALYS 1.95 one by one to obtain the differential cross-sections of products, comprising

- S1: Kopecky-Uhl generalized Lorentzian.
- S2: Brink-Axel Lorentzian or standard Lorentzian strength (SLO).
- S3: Hartree-Fock BCS tables.
- S4: Hartree-Fock-Bogolyubov tables.
- S5: Goriely's hybrid model.
- S6: Goriely T-dependent HFB.
- S7: T-dependent RMF.
- S8: Gogny D1M HFB+QRPA.

The used keywords are represented in Appendix B.

Chapter 3

Results and Discussion

In this chapter, the experimental IR results obtained from (γ, n) and (n, γ) reactions are represented in four first sections. In the last section, the theoretical values calculated by TALYS code for (γ, n) reaction are illustrated.

- Section 3.1: IRs of $^{195m,g;197m,g}$Hg and ^{152m1,m2}Eu in the (γ, n) reactions induced by bremsstrahlung with end-point energy within GDR region.
- Section 3.2: IRs in (n, γ) neutron capture reactions induced by thermal and resonance neutrons on ^{108,110}Pd and ^{114,116}Cd.
- Section 3.3: The nuclear channel effect in the IRs of ^{109m,g}Pd and $^{115m,g}Cd$ produced from (γ, n) and (n, γ) reactions are investigated.
- Section 3.4: IRs in inverse (γ, n) and (n, γ) reactions producing isomeric pairs ^{137m,g}Ce, ^{115m,g}Cd, ^{109m,g}Pd, and ^{81m,g}Se are present and discussed.
- Finally, section 3.5 summarizes theoretical IR calculations of isomeric pairs produced by (γ, n) reactions on Se, Pd, Ce, Eu and Hg targets in the GDR region using TALYS code.

The results in Section 3.1 have been published by us in Refs. [23, 129]. And our results in Section 3.2 have been revealed in Refs. [130, 131]. The results in Section 3.3 have been reported in Refs. [132, 133]. The results in Section 3.4 have been presented in conferences and proceedings by us [134, 135]. A part of the results in Section 3.5 has been accepted for publication in Ref. [136].

3.1 Isomeric Ratios in (γ, n) reactions

3.1.1 ^{152m1,m2}Eu

One of the goals of this work is to measure experimental IR of ^{152m1}Eu$(8^-)/^{152m2}$Eu(0^-) formed in $^{153}Eu(\gamma, n)^{152}Eu$ reaction within the whole GDR region to explore several internal effects on the IR such as excitation energy, spin difference of the isomeric and ground states and the channel effect. This is demanded by very limited numbers of investigation on the IR of ^{153}Eu isotope, as well as the discrepancy and incompleteness of the IR data in the GDR region.

Until now, there were only a handful numbers of measurements for isomeric ratio of ^{152m1}Eu$(8^-)/^{152m2}$Eu(0^-) in different energy regimes. One has been performed by Vishnevsky et al. [137] at 12 MeV bremsstrahlung end-point energy using the $^{153}Eu(\gamma, n)^{152}Eu$ reaction i.e. at excitation energy of the residual nucleus ^{152}Eu near the (γ, n) reaction threshold. The authors have performed the calculation of IR using TALYS code in the framework of the statistical mechanism of nuclear reaction and compare the results with the measured IR. In another experimental findings, Kolev [40] reported the IR of ^{152m1}Eu$(8^-)^{152m2}$Eu(0^-) at 43.0 MeV end-point bremsstrahlung energy and interpreted the IR result with the calculation based on the model of compound nucleus-particle evaporation and final gamma de-excitation. It was pointed out in this study that the statistical model, combined with HVM gives successful description of the reaction mechanism at least in 50% of the investigated reactions. Tonchev et al. [123] measured the IRs of ^{152m1}Eu$(8^-)/^{152m2}$Eu(0^-) in both (γ, n) reaction and (n, γ) neutron capture reaction in order to explore the effect of the nuclei quadrupole deformation on the IR. It is well known that photonuclear reaction is distinct with other nuclear reaction types by the low transfer momentum and resonant characteristics of absorption cross-section, which provides valuable information on nuclear reaction mechanism and structure. Interestingly enough, ^{153}Eu nucleus is deformed and in the GDR region of $^{153}Eu(\gamma, n)^{152}Eu$ reaction with energy range of 8.6 - 22 MeV, there are two maxima of the corresponding to the oscillation between an oblate and a prolate spheroidal shape [138, 139]. Therefore, the current study is expected to contribute additional data the the current nuclear database, thereby providing more robust and complete theoretical interpretation of nuclear reaction.

The spherical and deformed shapes of ^{151}Eu and ^{153}Eu are characterized by one peak and two peaks, respectively, of the total photoneutron cross-section in the GDR

illustrated in Fig. 3.26. The (γ, n) reactions on the Eu target results in the existence of the residual nuclei ^{150}Eu and ^{152}Eu in ground states ^{150g}Eu (5^-) and ^{152g}Eu (3^-) and in isomeric states ^{150m}Eu (0^-) and ^{152m1}Eu (8^-) or ^{152m2}Eu (0^-), respectively.

In the scope of this work, experimental IR of the pair of ^{152m1}Eu $(8^-)/^{152m2}$Eu (0^-) has been investigated by means of (γ, n) reaction in the GDR. The irradiation of Eu sample is described in subsection 2.1.2 using bremsstrahlung end-point energy of 14 to 23 MeV with the step of 1 MeV. The decay characteristics and the most intense γ-rays of ^{152m1}Eu and ^{152m2}Eu taken from [140] is shown in Table 3.1. Figure 3.1 exhibits the simplified decay schemes of ^{152m1}Eu and ^{152m2}Eu produced in the $^{153}Eu(\gamma, n)^{152m1,m2}Eu$ reaction. The ^{152m1}Eu with 8^- states decays to 3^- ground state by emission of a cascade of γ-rays transitions with energies of 39.7, 18.2 and 89.9 keV and intensities of 0, 1.26 and 89.8%, respectively. Thus, the isomeric transition coefficient P between ^{152m1}Eu(8^-) and ^{152m2}Eu(0^-) can be considered to be zero. For the IR calculation, the most intense γ-ray 89.9 keV was selected. As shown in the bottom part of Fig. 3.1, the ^{152m2}Eu(0^-) state decays by two ways: (1) by β^- 72% to ^{152}Gd following by the emission of 1314.7, 940.4 and 344.3 keV γ-rays, which have a relatively low intensities of 0.956, 0.604 and 2.44%, respectively, and (2) by electron capture and β^+ decay with intensity of 28%, then follow by emission of γ-rays with energies of 547.4, 963.4, 841.6, 562.9 and 121.8 keV and intensities of 0.009, 11.67, 14.20, 0.22 and 7.0%, respectively. For the IR calculation, the most strongly emitted characteristic γ-rays with energies of 121.8, 841.6 and 963.4 keV for ^{152m2}Eu(0^-) have been selected.

TABLE 3.1: γ-rays decay properties of reaction products of ^{152m1,m2}Eu used in the IR calculation [140].

Nuclear reaction	Reaction product	Spin, Parity $[J^\pi]$	Half-life [h]	Reaction threshold [MeV]	γ-ray energy [keV], (Intensity,%)	Isomeric transition coefficient P[%]
$^{153}Eu(\gamma, n)^{152m1}Eu$	^{152m1}Eu	8^-	1.6	8.7	89.8 (70.0)	0
$^{153}Eu(\gamma, n)^{152m2}Eu$	^{152m2}Eu	0^-	9.274	8.6	121.8 (7.00)	
					841.6 (14.20)	
					963.4 (11.67)	

Figure 3.2 shows a typical offline γ-rays spectrum obtained from the $^{153}Eu(\gamma, n)^{152}Eu$ reaction with bremsstrahlung end-point energy of 17 MeV. The irradiation time, the cooling time and the measurement time are 90 min, 20 min and 140 min, respectively, while the sample is placed at a distance of 5 cm from the detector.

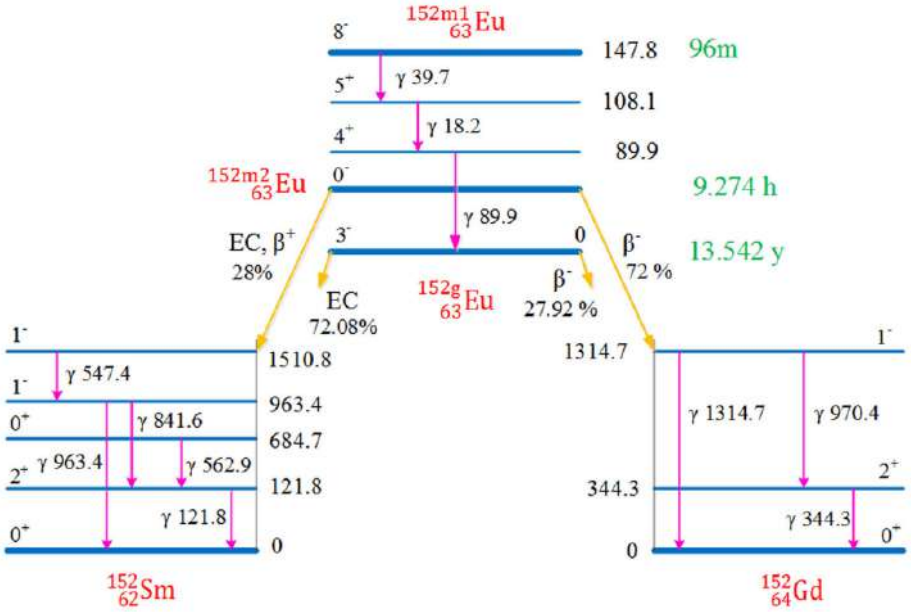

FIGURE 3.1: Simplified decay diagram of ^{152m1,m2}Eu [23].

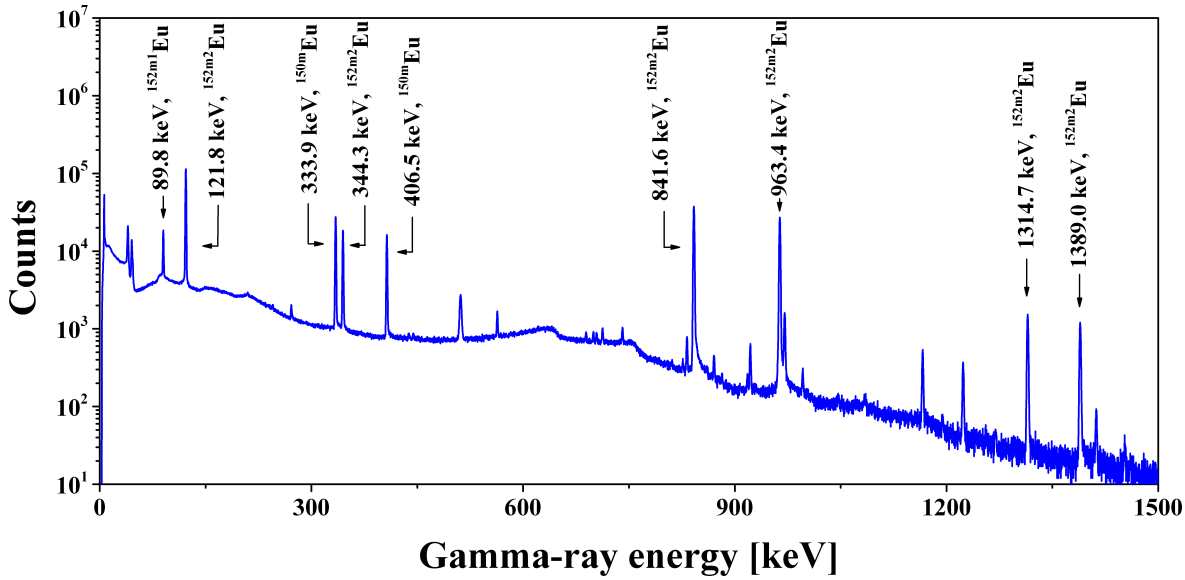

FIGURE 3.2: A typical energy spectrum of Eu sample irradiate with 17 MeV bremsstrahlung [23].

Due to the long half-lives and low formation probability, the decays of ground states ^{150g}Eu and ^{152g}Eu were not observed for the given irradiation time, as their characteristic γ-rays did not appear on the spectra. Nevertheless, those of the isomeric states ^{150m}Eu(0^-), ^{152m1}Eu(8^-) and ^{152m2}Eu(0^-) can be clearly seen. In order to improve the accuracy of the IR determination, the effects relating to coincidence summing and self-absorption have been taken into account. The self-absorption factor for the gamma rays of 89.8, 121.8, 841.6 and 963.4 keV has been estimated by the formula 2.20. The coincidence summing for the cascade of 121.8 and 841.6 keV has been corrected by the factor as in Eq. 2.21. The factors used to correct those two effects are illustrated in Tab. 3.2.

TABLE 3.2: A summary of corrections for self-absorption and summing coincidence for given γ-ray energies.

γ-ray energy, keV (Intensity, %)	Self-absorption correction, F_g t = 0.3 g/cm2	Summing coincidence correction, C_c at h = 5 cm
89.8(70.0)	1.19	1
121.8(7.0)	1.09	1.0026
841.6(14.2)	1	1.0006
963.4(11.67)	1	1

As a result, the IR of ^{152m1}Eu(8^-)/^{152m2}Eu(0^-) has been determined basing on Eq. 2.18. Likewise, the IR calculation is applied to other energy spectra of the irradiated Eu targets. The IRs of ^{152m1}Eu(8^-)/^{152m2}Eu(0^-) in the $^{153}Eu(\gamma, n)$ reaction induced by bremsstrahlung end-point energies of 14 - 23 MeV are demonstrated in Table 3.3 and shown in Figure 3.3. And Table 3.4 details the uncertainty sources in the determined isomeric ratio of ^{152m1}Eu(8^-) and ^{152m2}Eu(0^-). The total uncertainty of the determined isomeric ratio was estimated to be 7.0%.

In the Table 3.3, the measured data of this work listed together with that of the others in the literature. So far, only four measurements on the IR of ^{152m1}Eu(8^-)/^{152m2}Eu(0^-) exists in the literature [137, 40, 141, 41]. These complied IRs are shown in Figure 3.3 as a function of bremsstrahlung end-point energies within and above the GDR region. From Table 3.3 and Figure 3.3, one can see that the IRs from [141] data are much lower than the present data, while the data from [40] give a low value of IR at high energy, in contrast with the trend of the IR toward high energy region. The higher IR values of present work compared to other works [141, 40] may be due to the fact that the proper correction of the internal conversion phenomena and self-absorption for 89.8 keV γ-ray of ^{152m1}Eu has been carefully taken into an account in

TABLE 3.3: The IR of ^{152m1,m2}Eu in the (γ, n) reaction.

Nuclear reaction	This work		Other works	
	End-point Energy (MeV)	Isomeric ratio $IR = Y_{hs}/Y_{ls}[10^{-2}]$	End-point Energy (MeV)	Isomeric ratio $IR = Y_{hs}/Y_{ls}[10^{-2}]$
$^{153}Eu(\gamma, n)^{152m1,m2}Eu$	14	0.47 ± 0.03	12	0.12 ± 0.01 [137]
	15	0.63 ± 0.04	12.5	0.14 ± 0.02 [141]
	16	0.72 ± 0.05	13	0.22 ± 0.02 [141]
	17	0.85 ± 0.06	13.5	0.27 ± 0.02 [141]
	19	1.37 ± 0.09	14	0.35 ± 0.03 [141]
	20	1.72 ± 0.12	14.5	0.38 ± 0.03 [141]
	21	1.85 ± 0.13	15	0.47 ± 0.03 [141]
	22	1.95 ± 0.13	15.5	0.54 ± 0.04 [141]
	23	1.90 ± 0.13	16	0.61 ± 0.04 [141]
			16.5	0.60 ± 0.04 [141]
			17	0.62 ± 0.05 [141]
			17.5	0.75 ± 0.04 [141]
			18	0.76 ± 0.05 [141]
			18	1.02 ± 0.10 [41]
			24	1.99 ± 0.20 [41]
			43	1.12 ± 0.20 [40]

TABLE 3.4: A summary of error sources considered in the IR calculation of ^{152m1,m2}Eu.

Random Errors	[%]	Systematic Errors	[%]
Counting statistical	1	Sample-detector distance	1
Detector efficiency	2	γ-ray selection	1
Half-life	1	e-beam variation	1
γ-ray intensity	3	Irradiation time	1.5
		Cooling time	1
Statistical errors	6.5	Systematic errors	2.5
Total error of the measured IR			7

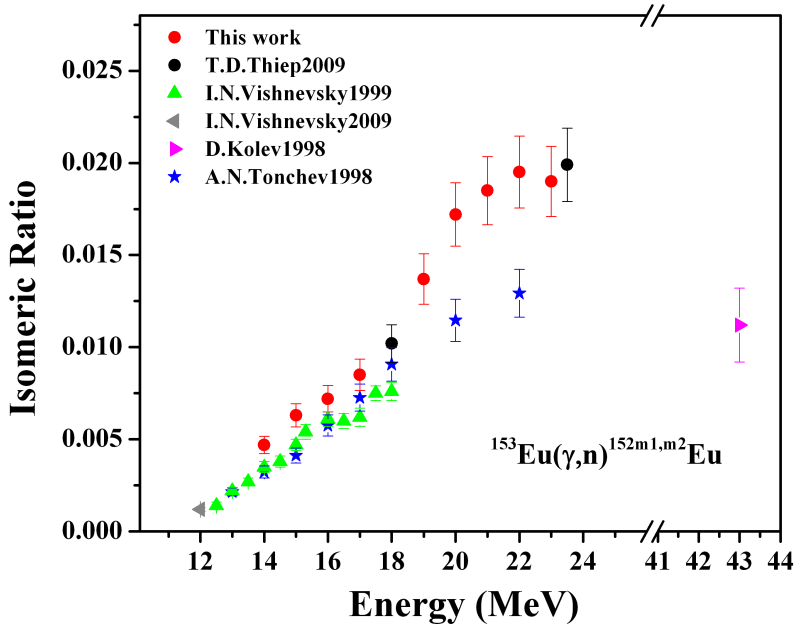

FIGURE 3.3: IRs of ^{152m1}Eu$(8^-)/^{152m2}$Eu(0^-) versus the bremsstrahlung end-point energies [23].

the present work. The lower IR at 12 MeV bremsstrahlung end-point energy from [137] can be explained by the fact that the excitation energy is low and the contributions of direct and pre-equilibrium processes are low and not exceeding 5–10%, as pointed out by author in [137], while these process can be significant at higher energies. Therefore, the data for IR in the GDR region are needed to be measured, and the present data offer a more complete picture of the systematic of IR throughout the GDR region. This fact also infers that the IR results in this work could serve as new benchmarks for theoretical calculations focusing on the aforementioned mechanism througout the GDR energy region. In addition, the IR results for ^{152m1}Eu$(8^-)/^{152m2}$Eu(0^-) isomers produced in the $^{153}Eu(\gamma, n)$ reaction are well related to the quadrupole deformation characteristics of these isomeric states. Indeed, it was also discussed in [123] that the state of nuclear deformation could be altered when the nucleus was produced in an isomeric state, while it may not be the case for the ground state. Our results on the IRs of ^{152m1}Eu(8^-) and ^{152m2}Eu(0^-) in the GDR region, therefore, can be considered as a continuation of the work in Ref. [123], and also contribute more information to discuss the effect on nuclear deformation changes for these isomeric states, particulary when a deformed nucleus is excited with different energies.

It is expected that the IR in (γ, n) reaction may exibit a gradual changes (increase or decrease) in the energy region of the reaction threshold energy toward the end of GDR

region, then becomes stable or insignificantly increases for beyond this energy region. This comes from the definition of the IR in the case of excitation with bremsstrahlung, as presented in [37]. This trend is also observed from the systematic of the IRs measured in this work, which shows an increase of the IR when the the excitation energy increase. Beyond the GDR region, the increase is insignificantly higher. This effect can be called excitation energy effect in IR.

Apart from the dependence of the excitation energy, it is well-known that the IR also depends strongly on target spin, the spin of isomeric and ground states, as well as the spin difference between states. Examples of such effects can be found in [137, 142, 41, 143, 144, 48, 145], where the IRs in mass number regions with Z = 74–82 and A = 183–207 were measured for (γ, p) reaction of even–odd nuclei and for (γ, n) reaction of odd–even nuclei. In these nuclear region, the last proton $(h_{11/2})$ of even-odd nuclei and the last neutron $(h_{13/2})$ of odd-even nuclei have large values of angular momentum. This results in the population of high spin isomers odd-odd nuclei through (γ, n) and (γ, p) reactions, thus the difference in spins of the isomeric and ground states are very high. The experimental IRs were compared with the ones calculated by the HVM, and it was shown that for the aforementioned nuclei, the IRs are usually low. In particular, for ^{196m,g}Au the spin difference $\Delta s = 10$, the $IR = 2.94 \times 10^{-4}$ [48] and 3.1×10^{-4} [144] at 18 and 24 MeV; for ^{194m,g}Ir, $\Delta s = 10$, the $IR = 2.9 \times 10^{-4}$ [142] and 10^{-3} [144] at 24 MeV; for ^{182m,g}Ta, $\Delta s = 7$, the $IR = 2.2 \times 10^{-4}$ [144] and $IR = 7.7 \times 10^{-4}$ [145] at 24 and 15 MeV; for ^{190m,g}Ir, $\Delta s = 7$, the $IR = 8.0 \times 10^{-4}$ [143] and $IR = 6.1 \times 10^{-4}$ [137] at 22 and 16 MeV; for ^{206m,g}Tl, $\Delta s = 12$, the $IR = 2.4 \times 10^{-5}$ [144] at 24 MeV. In this case of residual nucleus ^{152}Eu, during the decay process of primary and intermediate levels, the isomeric states ^{152m1}Eu (8^-) and ^{152m2}Eu (0^-) are formed with a large spin difference between them $(\Delta s = 8)$. Therefore the low IR value of ^{152m1m2}Eu (e.g. IR = 8.5 x 10^{-3} at 17 MeV) seems to be justified. This is called as effect of spin difference in IR, which is the higher spin difference, the lower isomeric ratio.

The average excitation energy used in this study with an electron energy of 23.0 MeV is determined to be 14.5 MeV. This value is calculated by using the formula (4) from Ref. [146]. At the same excitation energy 14.5 MeV, the IR of ^{152m1}Eu$(8^-)/^{152m2}$Eu(0^-) produced in the $^{153}Eu(n, 2n)^{152}Eu$ reaction is 0.270 ± 0.030 [147]. Around this excitation energy regime, similar results are also reported for $^{153}Eu(n, 2n)^{152}Eu$ in Ref. [148]. For the excitation energies of 13.5, 14.1 and 14.8 MeV, the IRs of 0.239 ± 0.038, 0.277 ± 0.042 and 0.315 ± 0.047 were reported. The main

difference of those experiments compared with the present work is that the isomeric states are formed in $(n, 2n)$ reactions, where the neutron brings significantly higher input angular momentum in the entrance channel compared to that of the photon in (γ, n) reaction. This so-called nuclear channel effect can be also seen in [149, 45, 42, 150].

3.1.2 ^{195m,g}Hg and ^{197m,g}Hg

So far, there is a dearth of data for IRs of isomeric pairs formed by nuclear reactions with Hg isotopes, especially, the IR in $^{196}Hg(\gamma, n)^{195m,g}Hg$ and $^{198}Hg(\gamma, n)^{197m,g}Hg$ photonuclear reactions. In an experimental study performed by Zheltonozhsky et al. [151], the IRs in the $^{198}Hg(\gamma, n)$ and $^{197}Au(d, 2n)^{197}Hg$ reactions in the energy range of 8-17 MeV and 8-50 MeV, respectively, were measured and the role of low-lying structure on the IR was discussed. In another study employing (n, 2n) reactions, Kasugai et al. [152] measured the independent cross-sections for the isomeric and ground states of ^{195m,g}Hg and ^{197m,g}Hg isomeric pairs, where the IRs for each isomeric pair can be inferred from the cross-sections data. Tilbury and Yaffe [153] studied the IRs of ^{195m,g}Hg , ^{197m,g}Hg and ^{196m,g}Au produced in ^{197}Au(p, 3n) , ^{197}Au(p, n) and ^{197}Au(p, pn) reactions with proton energies of 8–60 MeV. The obtained data shows a dominant role of the compound nucleus mechanism of the nuclear reactions at low excitation energies, as well as a non-negligible contribution of the direct and pre-equilibrium processes in higher energy regimes. Similar arguments were also drawn in a measurement of IR with the incident-particle energies ranging from the threshold value of the $^{197}Au(p, n)^{197m,g}Hg$ reaction up to 20 MeV (Gritsyna et al. [154]). Hansen et al. [155] investigated the excitation functions of isomeric and ground states of ^{197}Hg using (p, n) reaction with an incident proton energy of 4 to 13 MeV. The results in the energy range above 7 MeV were can be reasonably explained by the optical model calculation of Bjorklund and Fernbach. Detail exploration for the excitation functions of isomeric pairs of ^{195m,g}Hg and ^{197m,g}Hg was performed by Al-Abyad et al. [156] through the $^{196}Hg(n, 2n)$ and $^{198}Hg(n, 2n)$ reactions using quasimonoenergetic neutrons from the Julich variable energy compact cyclotron CV-28 with an energy range of 7.6–12.5 MeV. They performed theoretical calculations employing the STAPRE and EMPIRE-2.19 codes. These codes were developed under the framework of the statistical and pre-compound model formalisms to describe the formation of both the isomeric and ground states. The results of such calcualtions were compared with the experimental data. It was found that

the agreement between the experiment and theory is only in approximate terms. Vandenbosch and Huizenga [55] measured the IR and the excitation functions of ^{197m,g}Hg and ^{195m,g}Hg isomeric pairs produced in the $^{197}Au(p,n)$, $^{197}Au(d,2n)$, $^{196}Hg(n,\gamma)$, $^{196}Hg(d,p)$, $^{198}Hg(n,2n)$, $^{198}Hg(\alpha,\alpha n)$, and $Pt(\alpha,xn)$ reactions. The statistical reaction model revealed the dominant role of the compound nucleus formation in these reactions. In addition, relatively small amounts of angular momentum were transferred in reactions, which proceed predominantly by a direct interaction mechanism.

Photonuclear reactions were also used to study the isomeric pairs of ^{195}Hg and ^{197}Hg. Ishkhanov et al. [157, 158] measured the yields of the isomeric and ground states in the $^{196}Hg(\gamma,n)^{195}Hg$ and $^{198}Hg(\gamma,n)^{197}Hg$ reactions at 19.5 and 29.1 MeV bremsstrahlung end-point energies, where IRs of corresponding isomeric pairs can be determined. In photonuclear reaction, the mechanism of electric dipole absorption of gamma quantum is well known to dominate in the GDR region. In this mechanism, the γ quantum transfers to the nucleus a $1\hbar$ angular momentum that independent with the γ quantum energy. Due to such effect, the spin range of the excited levels can be restricted and the interpretation of the reaction mechanism becomes simple. In this sense, the study on photonuclear reactions has continued to be an attractive subject [159, 149, 157, 160, 161]. Following the above considerations, a part of this thesis is dedicated for the study the IRs of ^{195m,g}Hg and ^{197m,g}Hg. These isomeric pairs were produced in an experiment employing $^{196}Hg(\gamma,n)$ and $^{198}Hg(\gamma,n)$ reactions with the excitation energies in the GDR energy region. The obtained IRs are used to discuss the effect of excitation energy, nucleon configuration and the reaction channel effects on the IRs. Furthermore, new data on IRs in the present work are expected to contribute the Nuclear Database and provide benchmarks for theoretical nuclear reaction models. The natural mercury sample irradiated by the bremsstrahlung with end-point energies of 14 to 24 MeV with the step of 1 MeV. Detailed nucleon configuration of those nuclei can be found in [162]. Two isomeric pairs of ^{195m,g}Hg and ^{197m,g}Hg were produced in the $^{196}Hg(\gamma,n)$ and $^{198}Hg(\gamma,n)$ reactions. Figs. 3.4 and 3.5 show the simplified decay schemes of these isomeric pairs into Au isotopes. Details decay characteristics and γ-rays radiation emitted from those decays are presented in Table 3.5 taken from [140]. In this Table, γ-rays with high intensities and independent of the contribution of other nuclear reactions were chosen for the IR calculations. Both isomeric states ^{195m}Hg and ^{197m}Hg have the same spin of $13/2^+$, while both ground states ^{195g}Hg and ^{197g}Hg have the same spin of $1/2^-$.

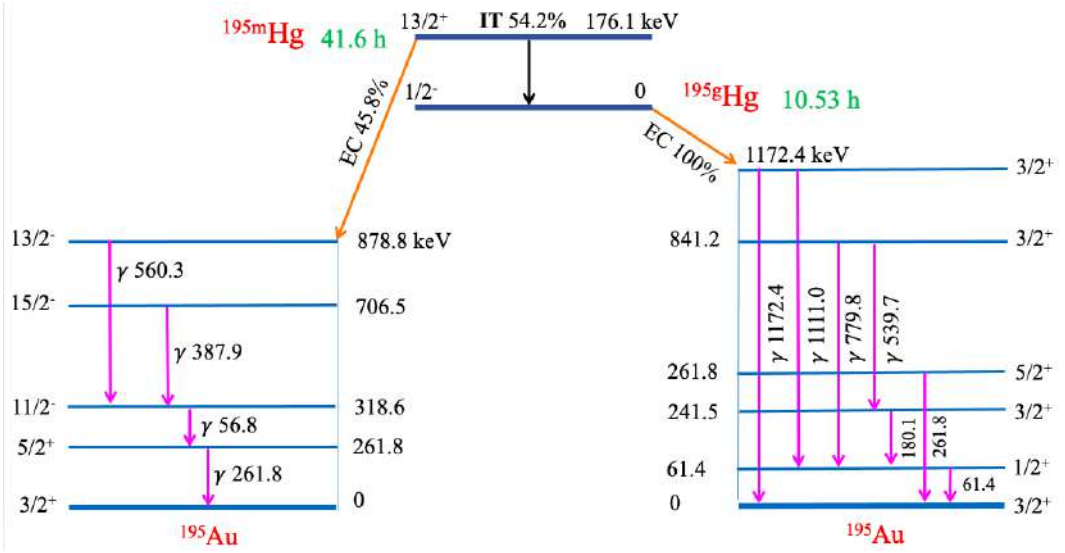

FIGURE 3.4: Simplified decay schemes of ^{195m}Hg and ^{195g}Hg [129].

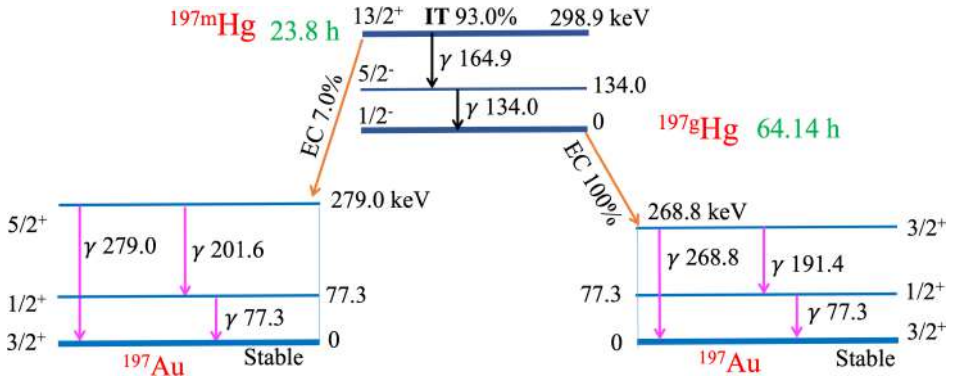

FIGURE 3.5: Simplified decay schemes of ^{197m}Hg and ^{197g}Hg [129].

TABLE 3.5: γ-rays decay properties of reaction products of ^{195m,g}Hg and ^{197m,g}Hg used in the IR calculation [140].

Nuclear Reaction	Reaction Threshold [MeV]	Nuclear state	Spin Parity [J^π]	Decay Mode [%]	Half-life [h]	γ-ray Energy [keV]	Intensity [%]
$^{196}Hg(\gamma,n)^{195m}Hg$	9.06	^{195m}Hg	13/2+	IT: 54.2	41.6	261.7	30.9
				EC: 45.8		560.3	7.0
$^{196}Hg(\gamma,n)^{195g}Hg$	8.88	^{195g}Hg	1/2-	EC: 100	10.53	779.8	7.0
						1172.4	1.24
$^{198}Hg(\gamma,n)^{197m}Hg$	8.78	^{197m}Hg	13/2+	IT: 91.4	23.8	134.0	33.0
				EC: 8.6			
$^{198}Hg(\gamma,n)^{197g}Hg$	8.49	^{197g}Hg	1/2-	EC: 100	64.14	77.3	18.7
						191.4	0.632

Fig. 3.6 shows a typical γ-rays spectrum obtained when the natural Hg sample is irradiated by 20 MeV bremsstrahlung end-point energy for 1 hour and cooled for 2 hours. The measurement time was 1 hour obtaining sufficient statistics to resolve clearly the characteristic γ-rays of isomeric pairs ^{195m,g}Hg and ^{197m,g}Hg.

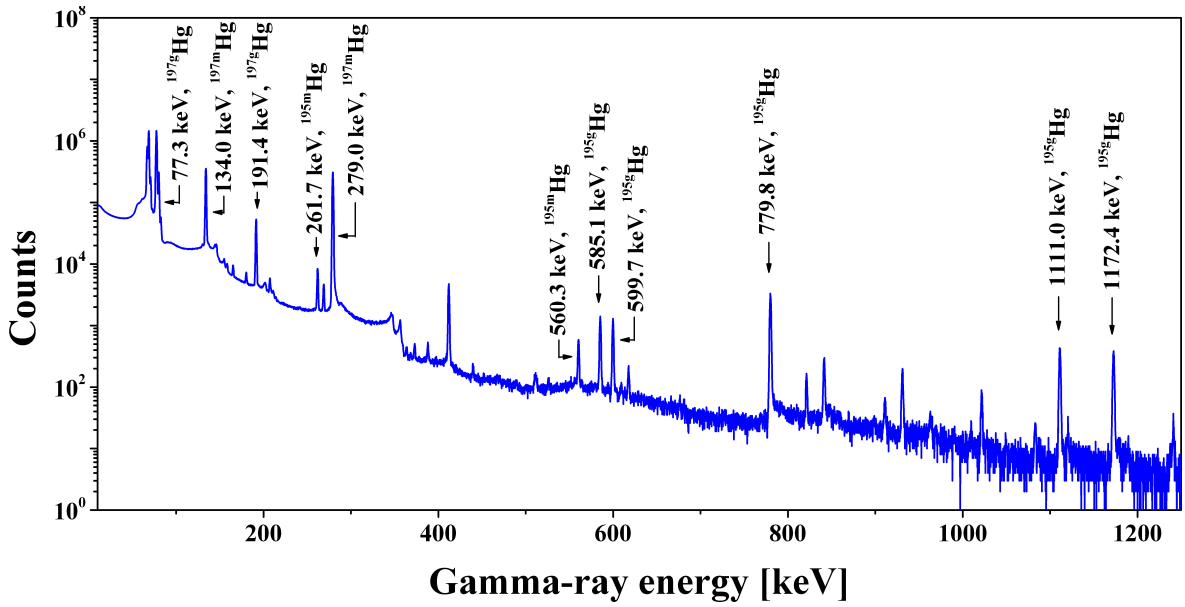

FIGURE 3.6: A typical energy spectrum of the natural Hg sample measured for 2 hour at a distance of 5 cm from the HPGe detector. The sample were irradiated 20 MeV bremsstrahlung for 1 hours and cooled for 23 hours before the measurement. [129].

The self-absorption and the summing coincidence effect were estimated and corrected as in subsection 2.1.5 and 2.1.5. Table 3.6 shows the calculated values of the self-absorption and summing correction factors F_g and C_c at different distances h between the sample and detector.

TABLE 3.6: A summary of corrections for self-absorption and summing coincidence for given γ-ray energies.

γ-ray energy, keV (Intensity, %)	Self-absorption correction, F_g t = 0.3 g/cm2	Summing coincidence correction, C_c	
		at h = 0 cm	at h = 5 cm
261.7(30.9)	1.09	1.013	1.002
560.3(7.0)	1.02	1.08	1.01
779.8(7.0)	1.01	1.019	1.002
1172.4(1.24)	1	1	1
134.0(33.0)	1.37	1	1
77.3(18.7)	1.33	1.001	1
191.4(0.632)	1.13	1.061	1.008

The IRs obtained in the present work are shown in Table 3.7, together with the literature data published in only six Refs. [153, 157, 158, 57, 163, 164] concerning the IRs of ^{195m,g}Hg and ^{197m,g}Hg.

TABLE 3.7: A summary of IRs determined for $^{195m,g;197m,g}$Hg isomeric pairs produced in (γ, n) reaction [129].

End-point Energy (MeV)	IR of $^{197m,g}Hg$		IR of $^{195m,g}Hg$	
	This work	Other works	This work	Other work
10		0.003 ± 0.0010 [151]		
11		0.016 ± 0.0014 [151]		
12		0.032 ± 0.0018 [151]		
13		0.052 ± 0.003 [151]		
14	0.082 ± 0.008	0.079 ± 0.006 [151]	0.089 ± 0.009	
15	0.096 ± 0.009	0.093 ± 0.005 [151]	0.102 ± 0.010	
16	0.100 ± 0.010	0.104 ± 0.005 [151]	0.114 ± 0.011	
17	0.108 ± 0.011	0.112 ± 0.006 [151]	0.120 ± 0.012	
18	0.114 ± 0.011		0.124 ± 0.012	
19	0.116 ± 0.012		0.128 ± 0.013	
19.5		0.11 ± 0.02 [57]		0.111 ± 0.039 [157]
20	0.119 ± 0.012		0.131 ± 0.013	
21	0.120 ± 0.012		0.129 ± 0.013	
22	0.117 ± 0.012		0.132 ± 0.013	
23	0.118 ± 0.012		0.129 ± 0.013	
24	0.120 ± 0.012		0.133 ± 0.013	
25		0.079 ± 0.022 [157]		
29.1		0.11 ± 0.02 [57]		0.136 ± 0.038 [157, 158]
30		0.118 ± 0.035 [157, 158]		
		0.098 [163]		
		0.053 ± 0.010 [164]		

The systematic errors introduced by the sample to detector distance, electron beam variation, irradiation time and cooling time were estimated to be 2.5%. The error of the IR calculation were propagated and estimated to be 9.5%. These error sources contribute to the total uncertainty of the IR, which is estimated to be about 10%.

Fig. 3.7 graphically shows the data from Table 3.7, i.e. the IRs values as a function of bremsstrahlung end-point energies. Those values were taken from this work and Refs. [153, 157, 158, 57, 163, 164] for the isomeric pairs ^{197m,g}Hg and ^{195m,g}Hg within and above the GDR region.

From the Table 3.7 and Fig. 3.7, good agreements between our results and the data of Zheltonozhsky et al. [151] can be clearly seen in the energy range from 14 to 17 MeV. Meanwhile, the IRs from the Ishkhanov et al. [157] is much lower than our result at 19.5 MeV. This discrepancy can be explained by the fact that the IR results in Ref. [157] was calculated from the yields of isomeric and ground states separately, while IR results of this work were obtained consistently using formula 2.18. Consequently, these IR results are more accurate because the isomeric and ground states were simultaneously measured under the same experimental conditions.

According to the expression (1) in Ref. [37], the IR remains unchanged or insignificantly increases for the photonuclear reaction at the end or beyond the GDR region. This implies that the measured results for ^{197m,g}Hg are compatible with the

data of Gangrsky [57] and Ishkhanov [157, 158], while the data of Toyoaki [163] and Carver [164] are lower. For ^{195m,g}Hg, the data for IR are scarce with only two experimental results found in literature [157, 158], both are in good agreement with our results.

It is worth noting that the obtained IRs of $^{195m,g;197m,g}$Hg increase with the increase of end-point bremsstrahlung energy up to the end of the GDR region. Beyond this region, that becomes unchanged or slowly increases since the pre-equilibrium and direct processes prevail over the compound reaction one.

When comparing the IRs of two isomeric pairs ^{195m,g}Hg and ^{197m,g}Hg in (γ, n) reaction, one finds that the IR of ^{195m,g}Hg is higher while the mass number of the corresponding reactant ^{196}Hg is smaller than the reactant ^{198}Hg. The similar fact was observed in photonuclear reaction of the isotopes of Sb [34], Se [35] and Ba[36]. It is understood that due to the effect of nucleon configuration, the IR in (γ, n) reaction with isotopes of an element generally decreases with the increase of the isotope mass number.

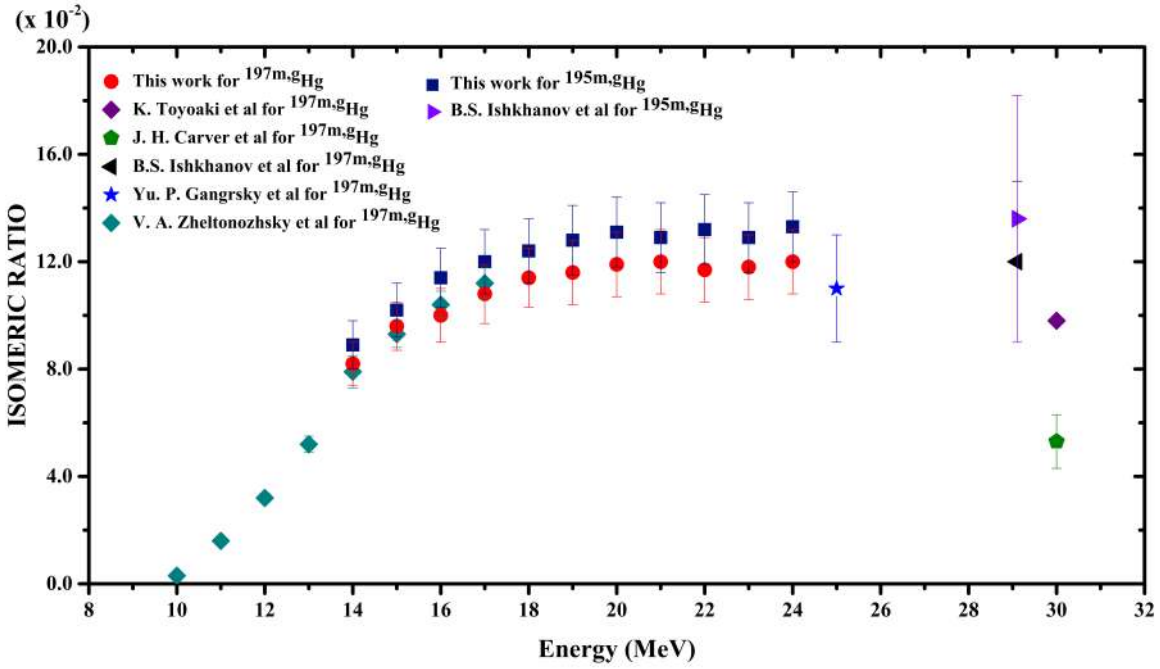

FIGURE 3.7: Measured IRs of $^{195m,g;197m,g}$Hg versus the bremsstrahlung end-point energy.

It is interesting to compare IRs of isomeric pairs produced by different reaction types at similar projectile energy. Table 3.8 shows the IRs of the isomeric pairs ^{197m,g}Hg and ^{195m,g}Hg produced from different nuclear reactions at the projectile energy of 12.5 MeV. Note that the average projectile energy was calculated by formula (4) in Ref. [146].

Using this formula, an average projectile energy of 12.5 MeV, equivalent to the endpoint bremsstrahlung energies of 19 and 18 MeV were calcualted for $^{198}Hg(\gamma,n)^{197m,g}Hg$ and $^{196}Hg(\gamma,n)^{195m,g}Hg$ photonuclear reactions. One can see that IRs of ^{197m,g}Hg and ^{195m,g}Hg varied from reaction to reaction. This feature is due to the entrance channel parameters effect on IR, in which due to the lowest momentum transferred in this type of reaction, the IR in (γ,n) reaction can be explained to be lowest value as well. For ^{69m,g}Zn and ^{71m,g}Zn [42]; ^{58m,g}Co [42]; ^{87m,g}Y [150]; ^{137m,g}Ce [146], ^{52m,g}Mn [45], ^{135m,g}Xe [38], ^{75m,g}Ge [165] and ^{80m,g}Br [166], we also observed similar entrance channel effect. For detail interpretation of the aforementioned effects, different nuclear reactions model incorporating all reaction mechanisms as statistical, direct and pre-equilibrium processes need to be employed. Therefore, the results of this work is significant in the sense that they not only provide additional data to the Nuclear Database, but also can be used for test of these models.

TABLE 3.8: A summary of IRs determined for ^{197m,g}Hg and ^{195m,g}Hg isomeric pairs produced in various nuclear reactions.

Projectile Energy (MeV)	$^{198}Hg(\gamma,n)^{197m,g}Hg$	$^{197}Au(p,n)^{197m,g}Hg$	$^{198}Hg(n,2n)^{197m,g}Hg$	$^{197}Au(d,2n)^{197m,g}Hg$
12.5	0.116 ± 0.012 (This work)	0.63 ± 0.11 [153] 1.1 [154]	0.7 ± 0.18 [156]	0.6 ± 0.06 [151] 0.6 ± 0.06 [55]
Projectile Energy (MeV)	$^{196}Hg(\gamma,n)^{195m,g}Hg$		$^{196}Hg(n,2n)^{195m,g}Hg$	
12.5	0.124 ± 0.012 (This work)		1.07 ± 0.28 [156]	

3.2 Isomeric Ratios in (n,γ) reactions

3.2.1 ^{109m,g}Pd and ^{111m,g}Pd

Among the highlight results of the current thesis, IRs in (n, γ) reactions bombarded by thermal, resonance and mixed thermal-resonant neutrons on ^{108,110}Pd nuclei have been measured. The aim of this research is to accumulate more experimental data for IRs in different neutron energies since there is very limited data for these nuclei existing in literature and for the theoretical interpretation many new measurements are needed. There are only two works [167, 168] for (n,γ) reaction on ^{108}Pd nucleus and three ones [168, 169, 170] for that on ^{110}Pd nucleus. The obtained results is expected to enrich the Nuclear Data Bank and provide additional data for interpretation of the IRs by different theoretical models.

To study IRs of isomeric pairs of Pd isotopes in the (n,γ) reaction, Pd sample is prepared and irradiated by the thermal-resonant neutron source created at the MT-25

Microtron as described in the subsection 2.1.2. The experimental setup is detailed in Fig. 2.4.

Natural palladium consists of ^{102}Pd, ^{104}Pd, ^{105}Pd, ^{106}Pd, ^{108}Pd and ^{110}Pd with the abundances of 1.020, 11.14, 22.33, 27.33, 26.46 and 11.72%, respectively. Through the (n, γ) reaction, the products ^{103}Pd, ^{107}Pd, ^{109}Pd and ^{111}Pd were formed. Among the reaction products, the γ-rays associated with the β^--decays of ^{103}Pd ($T_{1/2}$ = 16.991 days) are with low intensities. Another product ^{107}Pd also decays in β^- process, accompanied by 214.9 keV γ-rays. In the current experimental conditions, those γ-rays of ^{103}Pd and ^{107}Pd were not observed in the spectrum. The reaction products of interest ^{109}Pd and ^{111}Pd exists in the isomeric and ground states where the decays of those states would be visible in the γ-rays spectrum.

Figure 3.8 depicts the simplified decay schemes of the produced isomeric pairs ^{109m,g}Pd and ^{111m,g}Pd as well as their decay modes, life-time, gamma rays with intensities and γ-ray cascades.

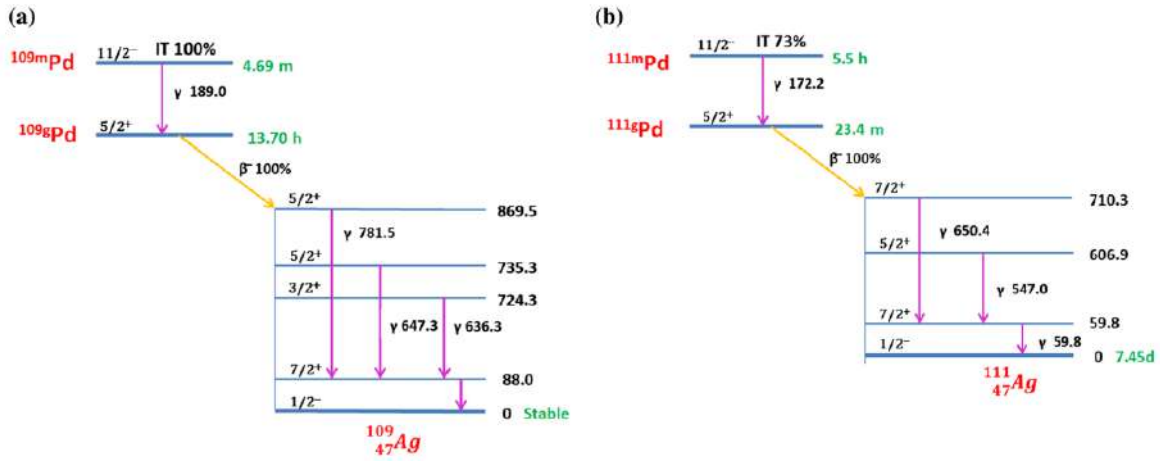

FIGURE 3.8: Simplified decay diagrams of $^{109m,g;111m,g}$Pd [130].

Figure 3.9 presents a typical offline γ-rays spectrum of natural Pd covered with Cd foil. The sample was irradiated for 1.5 h under an electron current of 15 μA, then allows for a cooling time of 11 minutes and measured for 30 minutes at 0 cm distance from the HPGe detector. From the obtained γ-rays spectrum, the characteristic γ-rays of the isomeric pairs ^{109m,g}Pd and ^{111m,g}Pd, listed in Table 3.9, are clearly seen.

Among corrections entered into the calculation of actual γ-rays counts from the decay of isomeric pairs detailed in Chapter 2, the calculated values of the self-absorption and summing correction factors F_g and C_c for the γ-rays used for isomeric pairs ^{109m,g}Pd and ^{111m,g}Pd are listed in Table. 3.10.

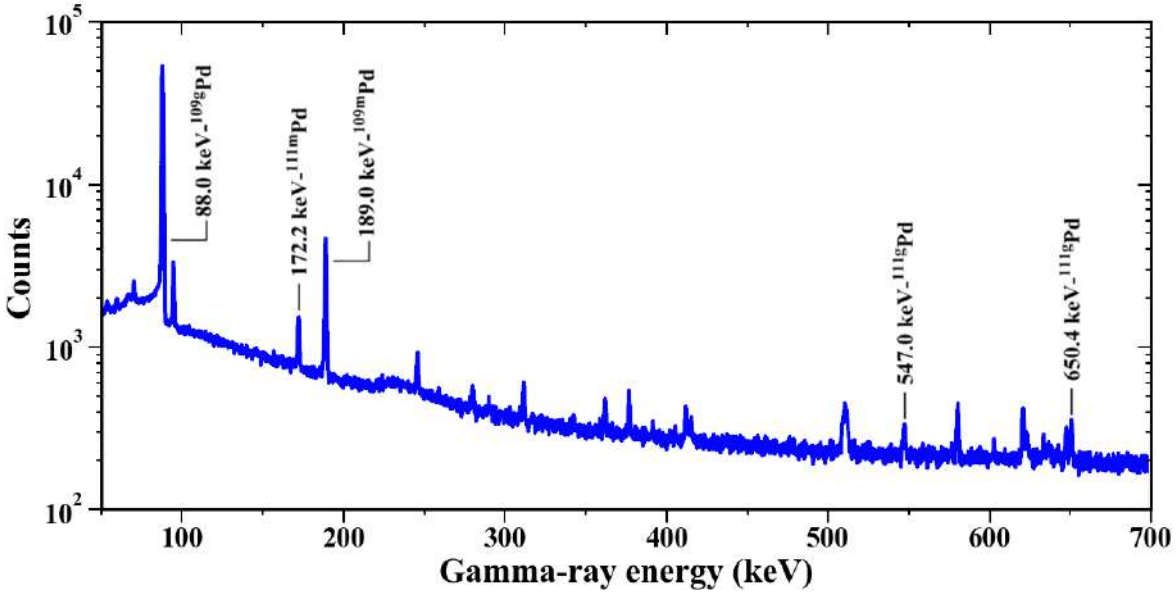

FIGURE 3.9: A typical energy spectrum of Cd-foil-covered natural Pd sample irradiated with energetic neutrons [130].

TABLE 3.9: γ-rays decay properties of reaction products of ^{109m,g}Pd and ^{111m,g}Pd used in the IR calculation [140].

Nuclear Reaction	Target Spin,Parity [J^π]	Nuclear state	Spin, Parity [J^π]	Decay Mode [%]	Half Life	γ-ray Energy [keV]	Intensity [%]
$^{108}Pd(n,\gamma)^{109m}Pd$	0^+	^{109m}Pd	$11/2^-$	IT: 100	4.69 m	189	55.9
$^{108}Pd(n,\gamma)^{109g}Pd$	0^+	^{109g}Pd	$5/2^+$	β^- : 100	13.7 h	88.04	3.6
$^{110}Pd(n,\gamma)^{111m}Pd$	0^+	^{111m}Pd	$11/2^-$	IT: 73 β^- : 27	5.5 h	172.2	34
$^{110}Pd(n,\gamma)^{111g}Pd$	0^+	^{111g}Pd	$5/2^+$	β^- : 100	23.4 m	547 650.4	0.38 0.57

TABLE 3.10: A summary of corrections for self-absorption and summing coincidence for given γ-ray energies of ^{109m,g}Pd and ^{111m,g}Pd.

γ-ray energy, keV (Intensity, %)	Self-absorption correction, F_g t = 0.323 g/cm2	Summing coincidence correction, C_c	
		at h = 0 cm	at h = 5 cm
88.04 (3.6)	1.24	1	1
172.2(34.0)	1.06	1	1
189.0 (55.9)	1.05	1	1
547.0 (0.38)	1.01	1.01	1
650.4 (0.57)	1	1.01	1

Then, the IR was calculated using formula 2.18. Table 3.11 presents the IRs in $^{108}Pd(n,\gamma)^{109m,g}Pd$ and $^{110}Pd(n,\gamma)^{111}Pd$ capture reactions induced by thermal, resonant and mixed thermal-resonant neutrons obtained in the present work, together with IRs available in literature [167, 168, 169, 170]. Table 3.11 also listed the IR values in $^{110}Pd(n,2n)^{109}Pd$, $^{110}Pd(\gamma,n)^{109}Pd$ and $^{114}Cd(n,\alpha)^{111}Pd$ reactions, taken from Refs. [64, 171, 172], which produce the same isomeric pairs.

TABLE 3.11: A summary of IR results for $^{109m,g;111m,g}$Pd in thermal, resonance and mixed thermal-resonant neutron-induced reactions and also in a (γ,n) reaction.

Nuclear reaction	Type of projectile	Product Exc. Energy [MeV]	Isomeric ratio (IR)
$^{108}Pd(n,\gamma)^{109m,g}Pd$	Thermal neutron	6.15	0.023 ± 0.002 [This work]
			0.028 ± 0.005 [167]
			0.018 ± 0.004 [168]
$^{108}Pd(n,\gamma)^{109m,g}Pd$	Resonant neutron	6.15	0.023 ± 0.002 [This work]
			0.028 ± 0.005 [167]
$^{108}Pd(n,\gamma)^{109m,g}Pd$	Mixed Thermal-Resonant neutron	6.15	0.023 ± 0.002 [This work]
$^{110}Pd(\gamma,n)^{109m,g}Pd$	25 MeV Bremstrahlung	6.93	0.065 ± 0.003 [64]
$^{110}Pd(n,2n)^{109m,g}Pd$	14.1 MeV neutron	5.28	0.410 ± 0.039 [64]
			0.41 ± 0.03 [171]
$^{110}Pd(n,\gamma)^{111m,g}Pd$	Thermal neutron	5.75	0.037 ± 0.004 [This work]
			0.263 ± 0.059 [168]
			0.123 ± 0.010 [169]
			0.047 ± 0.001 [170]
$^{110}Pd(n,\gamma)^{111m,g}Pd$	Resonant neutron	5.75	0.037 ± 0.004 [This work]
$^{110}Pd(n,\gamma)^{111m,g}Pd$	Mixed Thermal-Resonant neutron	5.75	0.037 ± 0.004 [This work]
$^{114}Cd(n,\alpha)^{111m,g}Pd$	14.1 MeV neutron	0.96	0.75 ± 0.29 [172]

The associated total uncertainty was estimated to be about 10%, shown in Table 3.12, which consists of the statistical errors of the γ-rays counts, detector efficiency, half-life and γ-ray intensity, and systematic errors from the distance from the detector to sample, the gamma ray selection, the electron beam variation, the irradiation and cooling time. All these error sources are propagated to yield the final uncertainty.

TABLE 3.12: A summary of error sources considered in the IR calculation of ^{109m,g}Pd.

Random Errors	[%]	Systematic Errors	[%]
Counting statistical	1.0 - 2.0	Sample-detector distance	1
Detector efficiency	2	γ-ray selection	1
Half-life	1.5	e-beam variation	1
γ-ray intensity	3	Irradiation time	1.5
		Cooling time	1
Statistical errors	9.6	Systematic errors	2.5
Total error of the measured IR			10.0

In Table 3.11, the product excitation energies of the interested reactions are also

given. For the IR obtained in the current experiment, the product excitation energy is the binding energy of neutron in the compound nuclei ^{109}Pd and ^{111}Pd, corresponding to the neutron capture reactions on ^{108}Pd and ^{110}Pd with thermal, resonant and mixed thermal-resonant neutrons. The binding energies were taken from Ref. [144]. For the IRs obtained in $(n, 2n)$ reaction, the corresponding product excitation energy $E_{pod.ex}$ is calculated by

$$E_{pod.ex} = E_{ex} - S_{2n}, \tag{3.1}$$

where E_{ex} and S_{2n} are the target excitation energy and the two neutrons separation energy of the compound nucleus, which were taken from Ref. [173].

In Table 3.11, the product excitation energy in the $^{110}Pd(\gamma, n)^{109m,g}Pd$ photonuclear reaction with 25 MeV end-point bremsstrahlung energy was calculated as follows:

$$E_{pod.ex} = \overline{E_{ex}} - S_n - \varepsilon_n, \tag{3.2}$$

where S_n - the neutron separation energy, taken from Ref. [173], ε_n - the mean kinetic energy of photo-neutrons, taken from Ref. [174], $\overline{E_{ex}}$ - the target excitation energy is equivalent to a mean value of the bremsstrahlung, calculated as follows:

$$\overline{E_{ex}} = \frac{\int_{E_0}^{E_{th}} E\sigma(E)\phi(E, E_0)dE}{\int_{E_0}^{E_{th}} \sigma(E)\phi(E, E_0)dE}, \tag{3.3}$$

where $\sigma(E)$ the excitation function, taken from Ref. [64] and $\phi(E, E_0)$ the Schiff formula for the bremsstrahlung photon flux, described in Ref. [175], E_0 the end-point bremsstrahlung energy and E_{th} the reaction threshold energy, taken from Ref. [173].

For the $^{114}Cd(n, \alpha)^{111m,g}Pd$ reaction, the product excitation energy was calculated as:

$$E_{pod.ex} = E_{ex} - S_\alpha - E_C, \tag{3.4}$$

where E_{ex} the target excitation energy, S_α the separation of α particle and E_C the Coulomb barrier for a in ^{115}Cd nucleus. S_α and E_C values were calculated to be 4.48 and 14.8 MeV, respectively.

From Table 3.11, one finds some discrepancies between our IR results compared with the data from Refs. [168, 169, 170] in neutron capture reactions. In our experiment, the variation of electron beam intensity was 1%, thus the neutron flux from the accelerator

can be considered as constant. In fact, the discrepancies may come from the following sources: (a) In Refs. [168, 169, 170], the neutron source was a reactor, while in our experiment the neutron flux was obtained from the accelerator. As a results, the neutron spectra were different, leading to the difference in IR; (b) In this work, the high-resolution HPGe semiconductor detector and more advanced spectra processing program were used for offline γ spectroscopy. Therefore, the gamma spectra and their processing are much better than that in the previous works, where the authors used the scintillation detectors, the end-window beta counter and radiochemical techniques [168, 169, 170]; (c) the IR in Refs. [168, 169, 170] was calculated as the ratio of the separately determined values of the cross-sections of the isomeric and ground states while in our case the IR was obtained directly by using formula 2.18 in Chapter 2. Since in our case, isomeric and ground states were simultaneously measured under the same experimental conditions, the IR results are expected to be more accurate.

It is important to note that for the IR of ^{111m,g}Pd from Ref. [168], the comparison in Table 3.11 between our IR result and that in Ref. [168] is only preliminary. This is because the authors in that article reported only the upper estimate for the cross-section, which led to the large difference between the two IR values.

The IRs for ^{109m,g}Pd as well as ^{111m,g}Pd isomeric pairs reported in Table 3.11 are the same for thermal, resonant and mixed thermal-resonant neutron capture reactions, although they have been measured separately. This can be explained by the fact that in both cases, the momentum transfer from the neutrons to the nuclei is the same and equal to $1/2\hbar$ and the excitation energies of the compound nuclei are almost the same because the kinetic energies of the neutrons are insignificant compared to the neutron binding energies.

The IR of the isomeric pair ^{109m,g}Pd obtained in our work for thermal neutron capture reaction is equal to the average value of the data in Refs. [167] and [168]. For the resonant neutron, the IR value in our experiment is compatible with that in Ref. [167]. The obtained IR in the present work for the mixed thermal-resonant neutrons is the first measurement as no data existed in literature.

For the isomeric pair ^{111m,g}Pd produced in the reaction with thermal neutrons, our IR value is the lowest when compared with the data in Refs. [168, 169, 170], in which the data in Ref. [168, 169] are unexpectedly high. In the case of the resonant and mixed thermal-resonant neutron-induced reaction, there are no data for isomeric pair ^{111m,g}Pd existed in literature, therefore the IR obtained in the present work can be

considered as the first measurement.

Among all reactions that produce isomeric pairs ^{109m,g}Pd, IRs in the $^{108}Pd(n,\gamma)^{109m,g}Pd$ reactions are very small in comparison with that in $^{110}Pd(\gamma,n)^{109m,g}Pd$ and $^{110}Pd(n,2n)^{109m,g}Pd$ reactions, although the product excitation energies in these reactions are insignificantly different. On the other hand, IR obtained in the $^{110}Pd(n,\gamma)^{111m,g}Pd$ is much smaller than that in the $^{114}Cd(n,\alpha)^{111m,g}Pd$ reactions, even though the product excitation energy in the $^{110}Pd(n,\gamma)^{111m,g}Pd$ reactions is much higher than that in $^{114}Cd(n,\alpha)^{111m,g}Pd$ reactions. The so-called impulse effect in IR can be an explanation for such phenomena, that is, for nuclear reactions induced by different projectiles leading to the same isomeric pair, the higher impulse of the projectile, the higher the IR in the isomeric pair. This effect were also discussed in Refs. [55, 156, 146, 23, 176, 165]

3.2.2 ^{115m,g}Cd and ^{117m,g}Cd

Cadmium element and its isotopes are subjects of intensive studies because of their important role for nuclear reactor engineering. Cd strongly absorbs the thermal and resonant neutrons, thus it has been selected among other materials as the main compound in the control rod. Their neutron capture cross-sections are among the most important properties for nuclear reactor engineering. Despite this importance, the current nuclear data of the neutron capture reaction on Cd isotope is yet to be completed. The available data of thermal neutron capture cross-sections and resonance integrals of Cd isotopes were complied in Ref. [177]. In the present work, the IRs in (n,γ) reactions induced by thermal, resonant and mixed thermal-resonant neutrons on ^{114}Cd and ^{116}Cd has been studied. This research is aimed at accumulating more experimental data since there are scarce data in general, especially for these nuclei in the existing literature. Furthermore, many new measurements are needed for the theoretical interpretation. Therefore, the results in this work may lead to richer information on Cadmium element.

The isomeric pairs $^{115m,g;197m,g}$Cd were produced by the neutron capture reaction on the a high-purity (99.99%) natural Cd sample. The optimum secondary target mass, the average electron current and the irradiation were determined to be 0,7193 g, 15 μA and 120 minutes, respectively, based on the estimated count rates in offline measurement for the γ-rays of interested emitted for the residual isomeric pairs. The thermal, resonant, and mixed thermal-resonant neutron sources were produced by an

intense electron beam impinged on an Uranium primary target, after being selected by the Cd foil covered or uncovered the sample. This setup is detailed in Chapter 2. For neutron flux monitoring Au foils were used.

Two isomeric pairs ^{115m,g}Cd and ^{117}Cd were produced by low-energy neutron capture reactions onto the natural Cd target. The resonance integral and thermal neutron cross-section of ^{114}Cd are 0.34 ± 0.02 and 14.1 ± 0.7 barn, while those of ^{117}Cd are 0.075 ± 0.020 and 1.6 ± 0.3 barn [177]. The simplified schemes of the isomeric pairs ^{115m,g}Cd and ^{117m,g}Cd are shown in Figs. 3.10 and 3.11, which also show the respective the γ-rays together γ cascades de-excited in the daughter nuclei ^{115}In and ^{117}In.

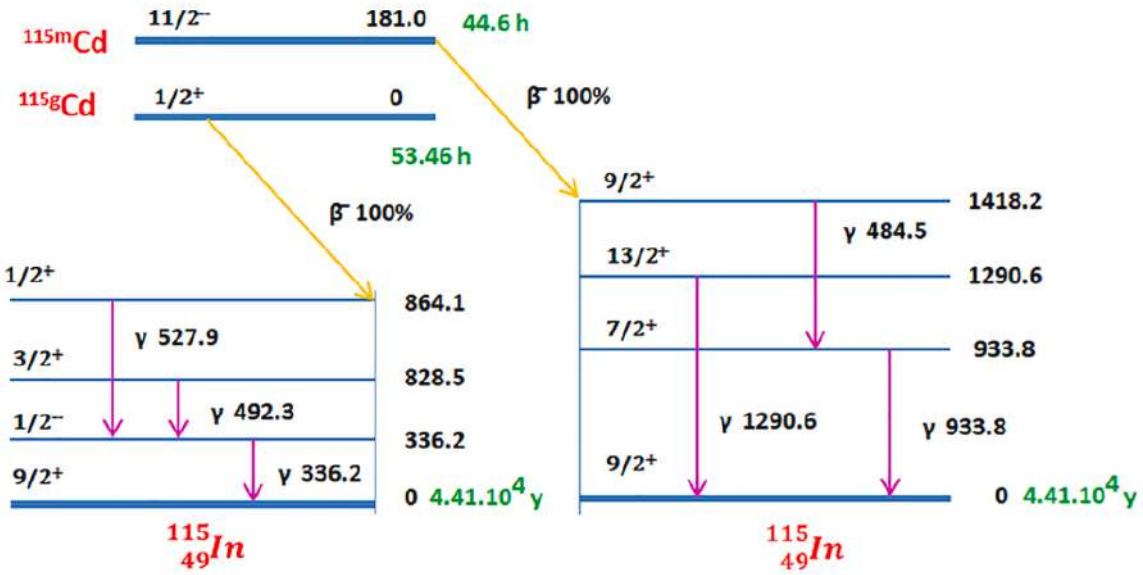

FIGURE 3.10: ^{115m,g}Cd isomeric pair: a simplified decay scheme [131].

The selection of proper γ-rays of the isomeric and ground states is crucial in the determination of IR. Similar to the other IR determination in this work, the interested γ-rays in cadmium isomeric pairs were chosen so that their intensities are higher than that of other γ-rays, they are well seperated in the γ-spectra and also free from the contributions from other nuclear reactions with natural Cd, thus ensures good photopeak area processing and counting statistics. Table 3.13 listed the spectroscopic characteristics and selected γ-rays used for the isomeric ratio calculations of isomeric pairs ^{115m,g}Cd and ^{117m,g}Cd.

Since the life-times of isomeric pair ^{117m,g}Cd are shorter than that of isomeric pair ^{115m,g}Cd, the cooling and measurement time intervals were different. To determine IR of ^{117m,g}Cd, the first batches of γ-rays spectra ontained under shorter measurement and also cooling time were used. For IR of ^{115m,g}Cd, the spectra obtained with longer

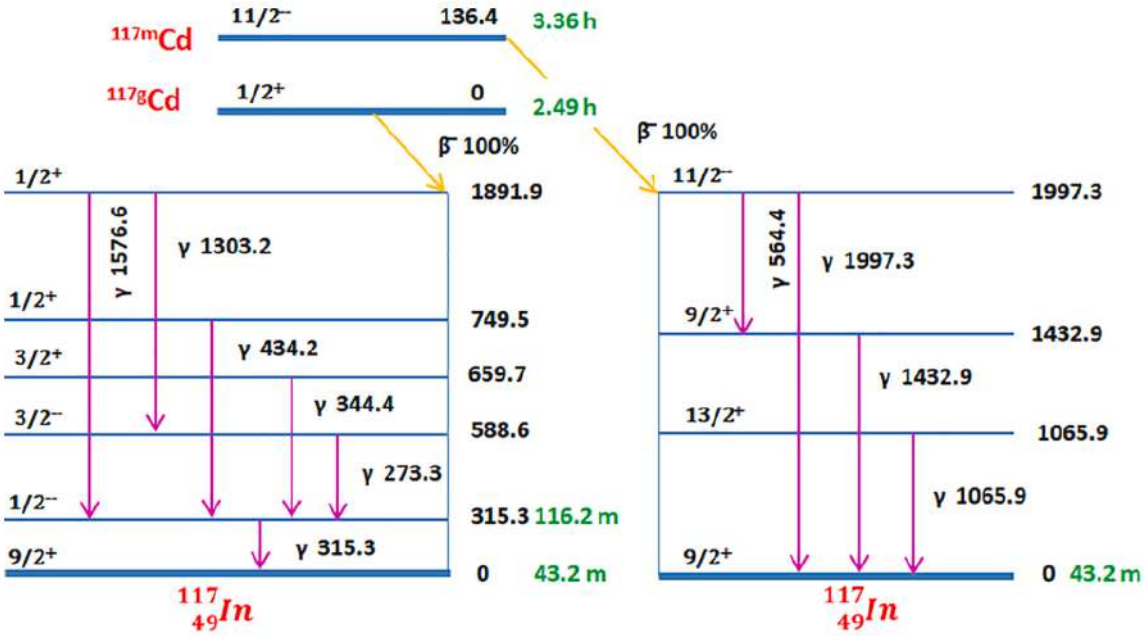

FIGURE 3.11: ^{117m,g}Cd isomeric pair: a simplified decay scheme [131].

TABLE 3.13: The decay properties of selected γ-rays for IR calculations for the ^{115m,g}Cd and ^{117m,g}Cd isomeric pairs [140].

Nuclear reaction	Target Spin [J^π]	Nuclear state	Spin,Parity [J^π]	Decay Mode [%]	Half-life	γ-ray Energy [keV]	Intensity [%]
$^{114}Cd(n,\gamma)^{115m}Cd$	0^+	^{115m}Cd	$11/2^-$	β^- : 100	44.6 d	933.8	2
$^{114}Cd(n,\gamma)^{115g}Cd$	0^+	^{115g}Cd	$1/2^+$	β^- : 100	2.23 d	336.2	45.9
						492.3	8.03
						527.9	27.45
$^{116}Cd(n,\gamma)^{117m}Cd$	0^+	^{117m}Cd	$11/2^-$	β^- : 100	3.36 h	564.4	14.7
						1065.9	23.1
						1432.9	13.4
$^{116}Cd(n,\gamma)^{117g}Cd$	0^+	^{117g}Cd	$1/2^+$	β^- : 100	2.49 h	273.3	28
						344.4	17.8
						1303.3	

cooling-measurement time were used.

Figure 3.12 presents a γ-rays spectrum of the natural Cd sample covered by Cd foil irradiated in the neutron source for 120 minutes and measured for 30 minutes with the cooling time of 67 minutes at a distance of 0 cm from the detector. The interested γ-rays of ^{117m,g}Cd stand out well in this γ-rays spectrum, but for ^{115m,g}Cd isomeric pair only the γ-rays 336.2, 492.3, 527.9 keV of interest of the ground state are seen and γ-ray 933.8 keV of the isomeric state did not emerge. Fig 3.13 shows the γ-rays spectrum obtained when the neutron source irradiated the sample uncovered by Cd foil for 2 hours, following by a cooling time of 13.94 days and measured for 12 hours at the distance of 0 cm (surface) from the detector. One observes a absent of the characteristic γ-rays of ^{117m,g}Cd, while the interested γ-rays of ^{115m,g}Cd are clearly seen. Therefore, the spectra processing is straightforward with reduced error.

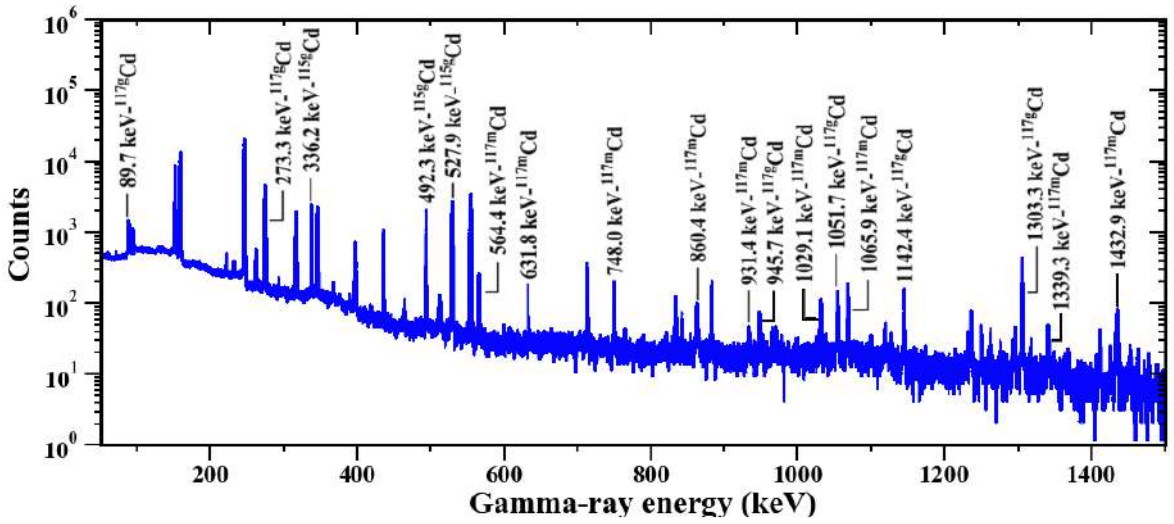

FIGURE 3.12: A typical energy spectrum of Cd-foil-covered natural Cd sample irradiated with energetic neutrons [131].

In the IR calculation, proper correction of the self-absorption and summing effect is important, as detailed in Chapter 2. These values calculated for the γ-rays of isomeric pairs ^{115m,g}Cd and ^{117m,g}Cd are presented in Table 3.14, where the linear attenuation coefficients were taken from Ref. [178].

The IR was calculated using the formula 2.18 in Chapter 2. The obtained results for IRs of ^{115m,g}Cd and ^{117m,g}Cd are presented in Table 3.15 together with the data available in literature [179, 180, 181, 182]. In this table, the IR values of isomeric pair ^{115m,g}Cd produced in $^{116}Cd(\gamma,n)^{115}Cd$, $^{116}Cd(n,2n)^{115}Cd$, $^{115}In(n,p)^{115m,g}Cd$ and $^{118}Sn(n,\alpha)^{115}Cd$ reactions [41, 183, 184, 185, 172] as well as the isomeric pair ^{117m,g}Cd produced in $^{120}Sn(n,\alpha)^{117}Cd$ reaction [186, 187] are also shown hereby for

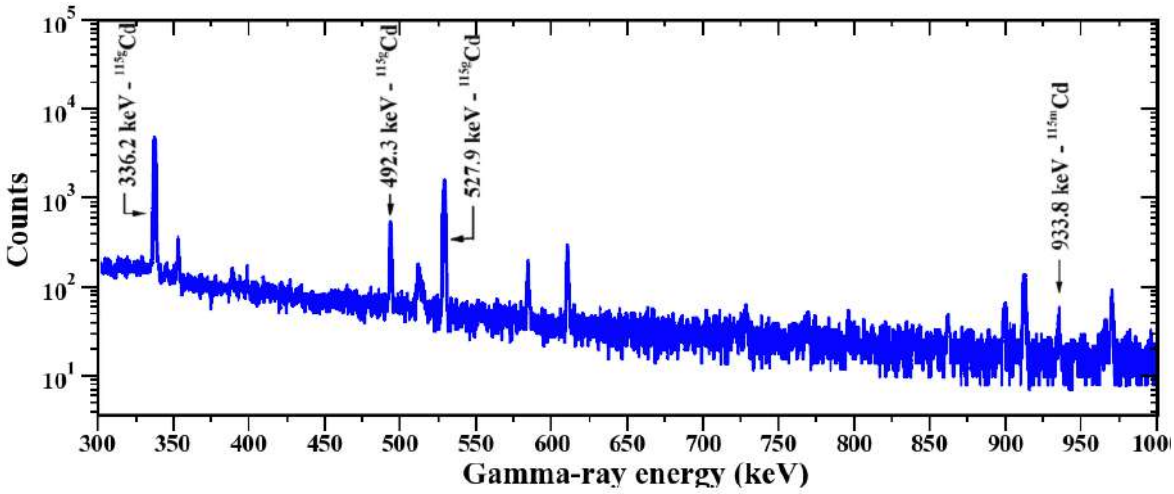

FIGURE 3.13: A typical energy spectrum of Cd-foil-uncovered natural Cd sample irradiated with energetic neutrons [131].

TABLE 3.14: A summary of self-absorption and summing coincidence correction factors for the γ-rays of interest of $^{115m,g;117m,g}$Cd [131].

Nuclear state	γ-ray energy, keV (Intensity, %)	Self-absorption factor F_g	Summing coincidence factor C_c
^{115g}Cd	336.2(45.9)	1.065	1.075
^{115g}Cd	492.3(8.03)	1.05	1.108
^{115g}Cd	527.9(27.45)	1.041	1.11
^{115m}Cd	933.7(2.0)	1.011	1
^{117m}Cd	564.4(14.7)	1.035	1.022
^{117m}Cd	1065.9(23.1)	1	1
^{117m}Cd	1432.9(13.4)	1	1.028
^{117g}Cd	273.3(28.0)	1.083	1.018
^{117g}Cd	344.4(17.8)	1.055	1
^{117g}Cd	1303.3(18.4)	1	1.062

interpretation.

TABLE 3.15: A summary of IRs results for ^{115m,g}Cd and ^{117m,g}Cd isomeric pairs produced in different type of nuclear reactions.

Nuclear Reaction and Product	Target Spin [$\hbar$]	Type of Projectile	Product Ex. Energy, MeV	Isomeric Ratio IR
$^{116}Cd(\gamma,n)^{115m,g}Cd$	0^+	24 MeV Bremsstrahlung	6	0.158 ± 0.016 [41]
$^{114}Cd(n,\gamma)^{115m,g}Cd$	0^+	Thermal neutron	6.1	0.116 ± 0.012 [This work] 0.120 ± 0.083 [182] (cal.) 0.094 ± 0.036 [179] (cal. TC) 0.085 ± 0.038 [179] (cal. GR) 0.088 ± 0.034 [179] (cal. IC) 0.080 ± 0.031 [179] (cal. R)
$^{114}Cd(n,\gamma)^{115m,g}Cd$	0^+	Resonant neutron	6.1	0.137 ± 0.014 [This work] 0.085 ± 0.035 [179] (cal. CL) 0.1 ± 0.051 [179] (cal. R/Cd)
$^{114}Cd(n,\gamma)^{115m,g}Cd$	0^+	Mixed Ther. and Res.	6.1	0.112 ± 0.011 [This work]
$^{116}Cd(n,2n)^{115m,g}Cd$	0^+	14.1 MeV neutron	5.4	0.921 ± 0.130 [183]
		14.4 MeV neutron	5.7	0.694 ± 0.074 [184]
		14.8 MeV neutron	6.1	0.710 ± 0.131 [185]
$^{115}In(n,p)^{115m,g}Cd$	$9/2^+$	14.9 MeV neutron	3.5	0.616 ± 0.118 [172]
$^{118}Sn(n,\alpha)^{115m,g}Cd$	0^+	14.9 MeV neutron	1.4	0.261 ± 0.090 [172]
$^{116}Cd(n,\gamma)^{117m,g}Cd$	0^+	Thermal neutron	5.8	0.209 ± 0.021 [This work] 0.54 ± 0.10 [180] 0.24 ± 0.03 [181] 0.192 ± 0.017 [179] (cal. TC) 0.173 ± 0.026 [179] (cal. GR) 0.223 ± 0.075 [179] (cal. IC) 0.192 ± 0.0177 [179] (cal. R)
$^{116}Cd(n,\gamma)^{117m,g}Cd$	0^+	Resonant neutron	5.8	0.324 ± 0.032 [This work] 0.282 ± 0.044 [179] (cal. CL) 0.288 ± 0.027 [179] (cal. R/Cd)
$^{116}Cd(n,\gamma)^{117m,g}Cd$	0^+	Mixed Ther. and Res.	5.8	0.237 ± 0.024 [This work]
$^{120}Sn(n,\alpha)^{117m,g}Cd$	0^+	14.0 MeV neutron	0.8	0.931 ± 0.137 [186] 1.015 ± 0.141 [187]

Table 3.16 details the sources of uncertainty contributing to the total uncertainty in IR determination, which was estimated to be about 10.0%.

TABLE 3.16: A summary of the error sources considered in the IR calculations of $^{115m,g;117m,g}$Cd.

Random Errors	[%]	Systematic Errors	[%]
Counting statistical	0.5 - 2.0	Sample-detector distance	1
Detector efficiency	2	γ-ray selection	1
Half-life	0.4 - 1.5	e-beam variation	1
γ-ray intensity	0.2 - 2.0	Irradiation time	1.5
		Cooling time	1
Statistical errors	9.6	Systematic errors	2.5
Total error of the measured IR			10

Similarly to the previous Section 3.2.1, the excitation energy $E_{prod.ex}$ of reaction product nuclei can be found as follows:

- For the $^{116}Cd(\gamma,n)^{115m,g}Cd$ reaction, of which IR data were taken from another experiment performed using Microtron MT-25 accelerator [41], the $E_{prod.ex}$ is calculated using the Eqs. 3.2 and 3.3, where the bremsstrahlung photon flux was calculated using Geant4 [71] simulation performed in this work. Fig. 3.22 depicts the bremsstrahlung spectra calculated by Geant4 simulation for various end-point energies.

- For isomeric pairs ^{115m,g}Cd and ^{117m,g}Cd formed in the neutron capture reactions, the $E_{prod.ex}$ is the binding energies of neutron in the compound nuclei ^{115}Cd and ^{117}Cd respectively.

- The product excitation energies of reactions $^{116}Cd(n,2n)^{115m,g}Cd$, $^{115}In(n,p)^{115m,g}Cd$ and $^{118}Sn(n,\alpha)^{115m,g}Cd$ and $^{120}Sn(n,\alpha)^{117m,g}Cd$ were calculated by a conventional method, in which the Coulomb potentials of proton and alpha were taken into account.

The available data in literature related to IRs in Cd isotopes in neutron capture reactions are very limited, with only two publications for $^{114}Cd(n,\gamma)^{115m,g}Cd$ reaction [179, 182] and three works for $^{116}Cd(n,\gamma)^{117m,g}Cd$ reaction [180, 181, 182]. Among these available data in literature and this work, there are essentially two methods of determining IR: (1) direct method using formula 2.18, (2) as the ratio of separately measured cross-sections of the isomeric and ground states. Using the latter method, neutron capture cross-sections of stable Cd isotopes have been measured by A. M. Gicking, K. Takahashi and K. S. Krane [179] using TRIGA reactor at the Oregon State University. In that work, the samples were irradiated in five different facilities under various neutron flux characteristics: in the thermal column (TC), in the central core, in the outer core or G-ring (GR), a cadmium-lined in-core irradiation site (IC) and a fast pneumatic transfer system, and the rabbit (R). The thermal neutron cross-sections of the isomeric and ground states of both isomeric pairs ^{115m,g}Cd and ^{117m,g}Cd have been determined these facilities and also their resonant integrals at the cadmium lined in-core irradiation tube and the rabbit. Using their cross-section data, IRs were calculated in the present work to be of 0.094 ± 0. 036 and 0.192 ± 0.017 for isomeric pairs ^{115m,g}Cd and ^{117m,g}Cd produced in the thermal neutron capture reactions, respectively for the irradiation in (TC); 0.085 ± 0.038 and 0.173 ± 0.026, respectively for irradiation in

(GR), 0.088 ± 0.034 and 0.223 ± 0.075, respectively for irradiation in (IC); and 0.080 ± 0.031 and 0.192 ± 0.0177, respectively for irradiation in (R). Similarly, the IRs for isomeric pairs ^{115m,g}Cd and ^{117m,g}Cd in the resonant neutron capture reactions have been calculated to be 0.085 ± 0.035 and 0.282 ± 0.044 for the irradiation in (CL); 0.1 ± 0.051 and 0.288 ± 0.027, respectively for the irradiation in (R/Cd) facilities. It is to note that in Table 3.15, the mark (cal. X) means the calculated value of IR obtained from corresponding irradiation facility X (For example, fourth row 0.094 ± 0.036 [179] (cal. TC) means the calculated IR is 0.094 ± 0.036 measured in TC irradiation facility).

The thermal neutron capture cross-section of ^{114}Cd leading to the ^{115}Cd was obtained from the work of S. Pearlstein, R. F. Milligan [182] using gold as a standard in a cavity located in the thermal column of the Brookhaven National Laboratory Medical Reactor. The authors have determined the cross-sections of the isomeric and ground states of this isomeric pair to be 0.036 ± 0.007 and 0.300 ± 0.150 barn, respectively. Then, we calculated IR to be of 0.120 ± 0.083. In the D. Decat and P. Del Marmol work [180], the authors have measured the IR and independently the capture cross-section for the ground state of ^{117}Cd produced in thermal neutron capture reaction on ^{116}Cd nucleus using the BR 1 reactor at Mol. In that work, IR was determined by the direct method and the obtained value is 0.54 ± 0.10 for isomeric pair ^{117m,g}Cd. C. W. Tang, R. L. Eng, and C. D. Coreyell [181] also determined the IR of isomeric pair ^{117m,g}Cd by the direct method, using $^{116}Cd(n,\gamma)^{117}Cd$ reaction induced by thermal neutron at M. I. T reactor. The obtained IR was 0.24 ± 0.03.

Following comments can be made from the results obtained in Table 3.15:

- Compared with the data from A. Gicking et al. [179] and S. Pearlstein, R. F. Milligan [182] for $^{114}Cd(n,\gamma)^{115m,g}Cd$ reaction, the IR results obtained in this experiment is different. This may come from the fact that the IRs of the authors are determined as the ratio of the separately determined values of the cross-sections of the isomeric and ground states, while in our case the IR was obtained consistently by using formula 2.18. This makes the results more accurate because the isomeric and ground states were simultaneously measured under the same experimental conditions. On other hand, the author used the Oregon State University TRIGA and the Brookhaven National Laboratory medical reactors as neutron sources, while in this work, accelerator-driven neutron source was used, where the neutron energy spectra are different. The significant difference between our result and the calculated value in Ref [179] for the case of the resonant neutron can be explained

with the same reason.

- For $^{116}Cd(n,\gamma)^{117m,g}Cd$ reaction, in general, a large discrepancy is also seen when comparing our results with the data from Refs. [180, 181], except when our results for the thermal and resonant neutrons is compared with the data in Ref. [179]. In Ref. [179],the Oregon State University TRIGA reactor as a neutron source and a p-type GEM HP(Ge) crystal detector were used for gamma spectra measurement. In Ref. [180], the sample irradiation was performed at the BR1 reactor at Mol and measured with a 3×3 inches NaI(TI) crystal. The results in Ref. [181] was obtained at the M. I. T. reactor and the gamma spectra were measured with the NaI(Tl) and small Ge(Li) detectors. Therefore, the discrepancy in the calculated IRs in this work and in Refs. [180, 181] may be explained by the difference in neutron spectra in various sources and also the lower energy resolution of γ-rays detector used in those works.

- Our results on IRs in both $^{114}Cd(n,\gamma)^{115}Cd$ and $^{116}Cd(n,\gamma)^{117}Cd$ reactions, induced by mixed thermal and resonant neutrons can be considered as first measurements, since no existing data found in the existing literature.

- One can see from Table 3.15 that the IRs in the capture reactions with thermal, resonant and mixed thermal-resonant neutrons are lower than that in $^{116}Cd(\gamma,n)^{115m,g}Cd$, $^{116}Cd(n,2n)^{115m,g}Cd$, $^{115}In(n,p)^{115m,g}Cd$ and $^{118}Sn(n,\alpha)^{115m,g}Cd$ reactions, which produce the same isomeric pair of ^{115}Cd nucleus. This can be explained by the fact that the intake momentum of the target in the neutron capture reactions is lower than that in the (γ,n) reaction and the (n,p) and (n,α) reactions using 14 MeV neutrons. In detail, the intake momentum is $1/2\hbar$, $1\hbar$ and much higher than $1\hbar$ for the thermal-resonant neutron capture reaction, the photonuclear reaction within the GDR region, and the 14 MeV neutron reaction, respectively. This results in the lower IR in the thermal and resonant neutron capture reactions compared with the IR of two former reactions. It happens even when the product excitation energies in the neutron capture reactions are equal to or higher than that in the other reactions (see 3.15). Similarly, the lower value of IR in $^{116}Cd(n,\gamma)^{117m,g}Cd$ reaction compared to that in $^{120}Sn(n,\alpha)^{117m,g}Cd$ can be also explained.

- The IR obtained in the present work for neutron capture reaction with thermal and resonant neutron could serve as a good testing ground to study further using

Talys code. It is worth noting that this reaction kind is a simple one-step reaction and typical for the compound mechanism of nuclear reaction. It is well known that the more simple processes involved in a reaction the more definite information can be obtained. However, in order to check a nuclear model, more measurements are needed to be performed.

3.3 Influence of nuclear channel effect on IRs in (γ, n) and (n, γ) reactions

3.3.1 For ^{109m,g}Pd

Complementing the results in previous Section 3.2.1 for the IR of isomeric pair ^{109m,g}Pd produced in neutron capture reaction, this section present experimental result on IR of the same isomeric pair produced in photonuclear reaction. The purpose of this is to shed light on the nuclear channel effect on this isomeric pair and further enrich the Nuclear database of IR for this nucleus.

In this experiment, the same high-purity PdO target target as presented in Section 3.2.1 were used. This target is irradiated by the the bremsstrahlung flux of 24 MeV end-point energy for 30 minutes. To avoid the interference from (n, γ) capture reactions, caused by the neutron background from reactions on the accelerating structure or the breaking target itself, the sample was covered by cadmium foil of 2 mm thickness. The sample was irradiated for 90 minutes by an electron beam with average current of 15 μA. The irradiation time was optimized for γ-rays of interest emitted from ^{109m,g}Pd to ensure good statistics.

The simplified decay scheme of the isomeric pairs ^{109m,g}Pd is depicted in Fig. 3.8, which shows the γ-rays emitted from the deexcitation of isomeric state as well as the β-decay process of the ground state. the decay characteristics and γ-rays used for the IR calculation of isomeric pairs ^{109m,g}Pd are detailed in Table 3.9. We chose the γ-rays with highest intensity, being well separated in the γ-rays spectrum and free from contamination of the other reaction products.

The offline γ-rays spectrum obtained following the irradiation of PdO target with 24 MeV bremsstrahlung is shown in Fig. 3.14. The irradiation time was 20 minutes, the cooling time was 40 minutes and the measurement time was 10 minutes at a distance of 5 cm from the detector. The characteristic γ-rays from the isomeric and ground state of ^{109}Pd are clearly observed in the spectra.

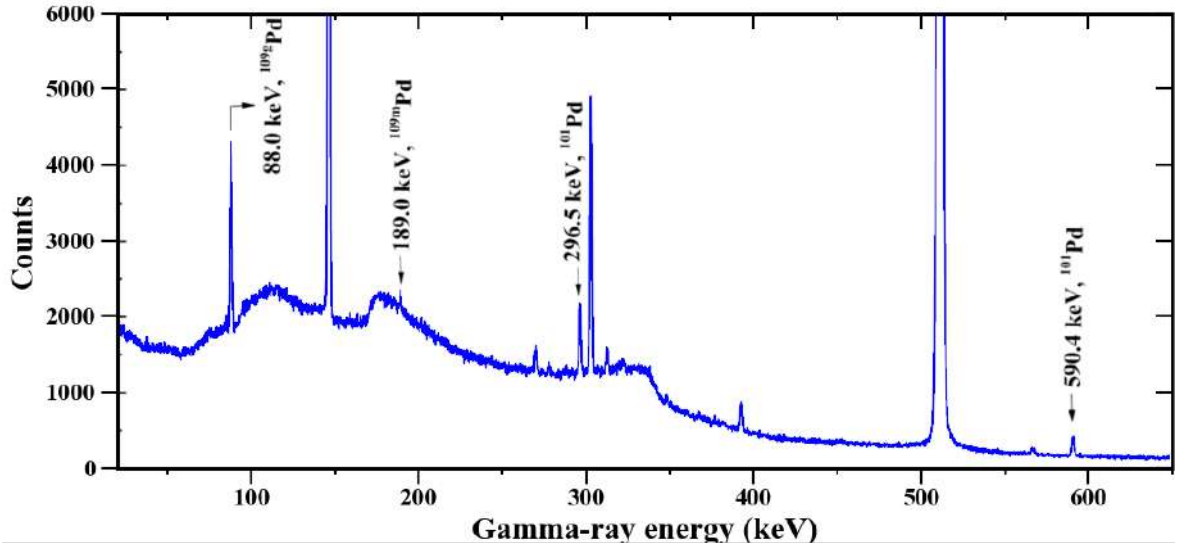

FIGURE 3.14: A γ-rays energy spectrum of Pd sample irradiated with 24 MeV bremsstrahlung [132].

In the experiment using photonuclear reaction, the correction factor for self-absorption C_c was found to be 1.0 and 1.0; and the correction factor for coincidence summing F_g were 1.26 and 1.05 for 88.0 and 189.0 keV γ-rays, respectively at the distance of 0 and 5 cm from the detector.

The IRs were determined using the formula 2.18. In Table 3.17, the IRs from photonuclear reaction $^{110}Pd(\gamma,n)^{109m,g}Pd$ are presented together with those from neutron capture reaction $^{108}Pd(n,\gamma)^{109m,g}Pd$ taken from the previous Section 3.2.1. The corresponding reaction product excitation energies $E_{prod.ex}$ were also listed, in which $E_{prod.ex}$ for (γ,n) reaction is calculated using the formulas 3.2 and 3.3 described in the Section 3.2.1. The IRs of ^{109m,g}Pd available in literature for the (γ,n), (n,γ) and $(n,2n)$ reactions are also represented in Table 3.17.

TABLE 3.17: The IRs of ^{109m,g}Pd in thermal, resonance and mixed thermal-resonant neutron capture reactions and in (γ,n) reaction.

Nuclear Reaction and Product	Type of Projectile	Product Ex. Energy, MeV	Isomeric Ratio IR
$^{108}Pd(n,\gamma)^{109m,g}Pd$	Thermal neutron	6.15	0.023 ± 0.002 [This work]
			0.028 ± 0.005 [167]
			0.018 ± 0.005 [168]
$^{108}Pd(n,\gamma)^{109m,g}Pd$	Resonant neutron	6.15	0.023 ± 0.002 [This work]
			0.028 ± 0.005 [167]
$^{108}Pd(n,\gamma)^{109m,g}Pd$	Mixed Ther. and Res.	6.15	0.023 ± 0.002 [This work]
$^{110}Pd(\gamma,n)^{109m,g}Pd$	24 MeV Bremstrahlung	6.5	0.069 ± 0.007 [This work]
	25 MeV Bremsstrahlung	6.93	0.065 ± 0.003 [64]
$^{110}Pd(n,2n)^{109m,g}Pd$	14.1 MeV	5.28	0.410 ± 0.039 [64]
	neutron		0.41 ± 0.03 [171]

The total uncertainty, comprising of statistical errors, the systematic errors from the

distance from the detector to sample, the γ-ray selection, the electron beam variation, the irradiation and cooling times was estimated to be about 10%.

From the results summarized in Table 3.17, the IR obtained in the present work for $^{110}Pd(\gamma, n)$ is in very good agreement (within 1 σ) with previous work [64]. On the other hand, the present IR result for (γ, n) reaction is higher than that for the (n, γ) reaction, though the product excitation energies in (γ, n) and (n, γ) are not significantly different. These IR results are also much lower compared to the IR of the same isomeric pair produced by $(n, 2n)$ reaction with comparable product excitation energy [64, 171]. This can be explained by the fact that the intake impulse in (γ, n) reaction is higher than that in (n, γ) reaction, while that in $(n, 2n)$ reaction is highest among all reactions, causing the IR in $(n, 2n)$ exceed that in the (γ, n) and (n, γ) reactions. In addition, in the cases of (γ, n) and (n, γ) reactions, the angular momentum transfer to the target nuclei is lower, namely $L = 1$ and $1/2\hbar$, which results in the compound nuclei with spins $J_c = J_0, J_0 \pm 1$ and $J_0, J_0 \pm 1/2$, respectively. This restricts the spin range of excited levels and makes the IR in those nuclei much lower than that the other reaction. The intake impulses and angular momentum transfer dependent on IR is part of the so-called channel effect in a nuclear reaction, where the IRs in different nuclear reactions are different and depend on the projectile type, intake impulse, excitation energy, spins of the isomeric and ground states as well as the nuclear reaction mechanisms.

3.3.2 For ^{115m,g}Cd

Complementing of the previous Section 3.2.2, this section presents the results of the $^{116}Cd(\gamma, n)^{115m,g}Cd$ photonuclear reaction obtained in the present work. This reaction also produced the isomeric pair ^{115m,g}Cd and until now the data for this reaction in existing literature are very rare. On the other hand, to benchmark the model calculation of nuclear reactions, not only one more a large number of nuclear data are needed. The results of this investigation will be used to examine the role of the nuclear channel effect and they also can provide the nuclear data for theoretical interpretation of nuclear reactions as well as for nuclear applications.

The isomeric pair ^{115m,g}Cd is formed through $^{116}Cd(\gamma, n)^{115m,g}Cd$ photonuclear reaction and $^{116}Cd(n, \gamma)^{115m,g}Cd$ neutron capture reaction, as mentioned in Section 3.2.2. The decay characteristics and γ-rays emitted from the decay of ^{115m,g}Cd are listed in Table 3.13, in which γ-rays used in the isomeric ratio calculation of the isomeric pair ^{115m,g}Cd are also presented in this table.

In this experiment with photonuclear reaction, a target sample made from natural cadmium were also used. The isotopic abundances of cadmium isotopes in this target is mentioned in the Section 3.2.2. When irradiated by 24 MeV bremsstrahlung, γ-rays of the isomeric pair ^{115m,g}Cd as product $^{116}Cd(\gamma,n)^{115m,g}Cd$ photonuclear reaction are seen very clearly (see Fig. 3.15). Other γ-rays appeared in this spectrum come from different products of the interaction between the bremsstrahlung and the other cadmium isotopes.

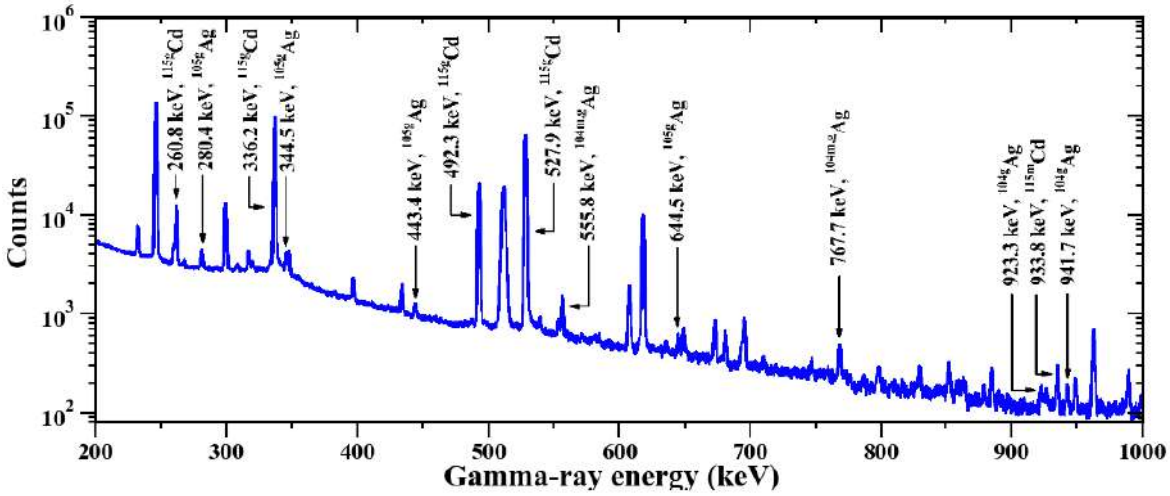

FIGURE 3.15: A γ-rays energy spectrum of Cd sample irradiated with 24 MeV bremsstrahlung in 60 minutes, then 275.5 minutes cooling and 20 minutes of measurements at 5 cm position from the surface of HPGe detector [133].

Figure 3.16 presents the simplified schemes of $^{114}Cd(n,\gamma)^{115m,g}Cd$, $^{116}Cd(\gamma,n)^{115m,g}Cd$, $^{116}Cd(n,2n)^{115m,g}Cd$, $^{115}In(n,p)^{115m,g}Cd$ and $^{118}Sn(n,\alpha)^{115m,g}Cd$ reactions, which lead to the same isomeric pair ^{115m,g}Cd. These reactions were studied and their corresponding characteristics are summarized in Table 3.18. In the case of (n,γ) reaction on ^{114}Cd, the product excitation energy listed in Table 3.18 was calculated by using the formulas 3.2 and 3.3 mentioned in the Section 3.2.1.

The IR value was calculated based on using activation method by using the formula 2.18 for the γ-rays of interest from the decay of ^{115m,g}Cd, where the associated uncertainty sources were properly propagated to yield the final uncertainty of IR. In this analysis, the correction on the self-absorption and coincidence summing effected were estimated as in Chapter 2.

The IR value measured in the present work for $^{116}Cd(\gamma,n)^{115m,g}Cd$ reaction is in 1σ agreement with the previous work in [41], where the same bremsstrahlung end-point energy was used.

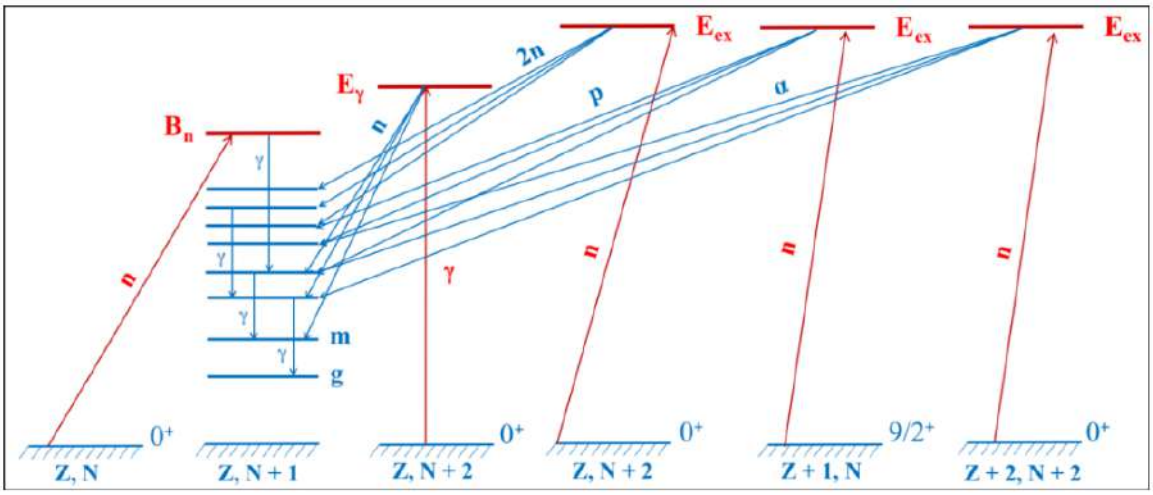

FIGURE 3.16: Simplified scheme of the production of ^{115m,g}Cd from (n,γ), (γ,n), $(n,2n)$, (n,p) and (n,α) reactions [133].

TABLE 3.18: The IRs of ^{115m,g}Cd produced in different nuclear reactions.

Nuclear Reaction and Product	Target Spin [$\hbar$]	Type of Projectile	Product Ex. Energy, MeV	Isomeric Ratio IR
$^{116}Cd(\gamma,n)^{115m,g}Cd$	0^+	24 MeV Bremsstrahlung	6	0.165 ± 0.016 [This work]
				0.158 ± 0.016 [41]
$^{114}Cd(n,\gamma)^{115m,g}Cd$	0^+	Thermal neutron	6.1	0.116 ± 0.012 [This work]
				0.120 ± 0.083 [182]
$^{114}Cd(n,\gamma)^{115m,g}Cd$	0^+	Epither. neutron	6.1	0.137 ± 0.014 [This work]
				0.085 ± 0.035 [179]
				0.1 ± 0.051 [179]
$^{114}Cd(n,\gamma)^{115m,g}Cd$	0^+	Mixed Ther. and Epither.	6.1	0.112 ± 0.011 [This work]
				0.080 ± 0.028 [179]
$^{116}Cd(n,2n)^{115m,g}Cd$	0^+	14.1 MeV neutron	5.4	0.921 ± 0.130 [183]
		14.4 MeV neutron	5.7	0.694 ± 0.074 [184]
		14.8 MeV neutron	6.1	0.710 ± 0.131 [185]
$^{115}In(n,p)^{115m,g}Cd$	$9/2^+$	14.9 MeV neutron	3.5	0.616 ± 0.118 [172]
$^{118}Sn(n,\alpha)^{115m,g}Cd$	0^+	14.9 MeV neutron	1.4	0.261 ± 0.090 [172]

In the previous works listed Table 3.18, the $^{116}Cd(n,2n)^{115m,g}Cd$, $^{115}In(n,p)^{115m,g}Cd$ and $^{118}Sn(n,\alpha)^{115m,g}Cd$ reactions were studied by fast neutrons of nearly the same energy. Therefore, the momentum transferred to the target nuclei is nearly the same. However, IRs of isomeric pairs obtained in three reactions are different, with the highest value in $^{116}Cd(n,2n)^{115m,g}Cd$ and the lowest in $^{118}Sn(n,\alpha)^{115m,g}Cd$. The difference in the product excitation energies could be an explanation for this interesting feature. According to Table 3.18, the reaction product excitation energy is highest in $^{116}Cd(n,2n)^{115m,g}Cd$ reaction and lower in $^{115}In(n,p)^{115m,g}Cd$ and $^{118}Sn(n,\alpha)^{115m,g}Cd$ reactions due to the Coulomb barrier of proton and α particles. As a result, the probability to excite high-spin states becomes lower, therefore IR is lower. On other hand, it is worth noting that in (γ,n), $(n,2n)$, (n,p) and (n,α) reactions, especially for nuclear reactions with emission of charge-particles, the direct and pre-equilibrium processes play important role in suppressing the formation of high-spin states.

In addition to the difference in product excitation energy, the IRs of isomeric pair ^{115m,g}Cd created in different nuclear reactions are, in principle, different. This effect is called the nuclear channel effect on the IR, which may result in the various IR values of the identical isomeric pair produced from the different reactions. The channel effect on IR can be also found in the cases of isomeric pair $^{135m,g}Xe$ populated in $^{134}Xe(n,\gamma)$, $^{136}Xe(\gamma,n)$, $^{136}Xe(n,2n)$ reactions and in the photo-fission of ^{232}Th, ^{233}U and ^{237}Np [149]; isomeric pair $^{58m,g}Co$ in $^{58}Fe(p,n)$, $^{nat}Fe(d,xn)$, $^{55}Mn(\alpha,n)$ and $^{59}Co(n,2n)$ reactions with projectile energies of the threshold to 14.12 MeV, 12.97 MeV, 25.52 MeV and 13 MeV, repectively [27]; isomeric pair ^{75m,g}Ge through $(n,2n)$, (n,p) and (n,α) reactions measured over 13.73 MeV to 14.77 MeV [165]; isomeric pair ^{87m,g}Y produced from the $^{93}Nb(\gamma,\alpha 2n)$ and $^{nat}Zr(\gamma,pxn)$ reactions with the bremsstrahlung end-point energy of 45 - 70 MeV [150], and ^{137m,g}Ce produced in photoneutron reaction $^{138}Ce(\gamma,n)$, neutron capture reaction $^{136}Ce(n,\gamma)$ and two simultaneous reactions in the mixed photon–neutron field [146].

3.4 IRs of ^{137m,g}Ce, ^{115m,g}Cd, ^{109m,g}Pd, and ^{81m,g}Se in inverse reactions

The inverse nuclear reactions, when a projectile of one reaction is the ejectile of another reaction, have been subjects for many experimental as well as theoretical studies since

1960s [188, 189]. Inverse reactions including photonuclear and thermal neutron capture reactions play an important role in astrophysics and the study of nuclear structure and nuclear reaction mechanisms [189, 190, 191].

In this work, IR of ^{137m,g}Ce, ^{115m,g}Cd, ^{109m,g}Pd, and ^{81m,g}Se produced in inverse (γ, n) and (n, γ) reactions by activation method, namely $^{138}Ce(\gamma,n)^{137m,g}Ce$, $^{136}Ce(n,\gamma)^{137m,g}Ce$, $^{116}Cd(\gamma,n)^{115m,g}Cd$, $^{114}Cd(n,\gamma)^{115m,g}Cd$, $^{110}Pd(\gamma,n)^{109m,g}Pd$, $^{108}Pd(n,\gamma)^{109m,g}Pd$, $^{82}Se(\gamma,n)^{81m,g}Se$ and $^{80}Se(n,\gamma)^{81m,g}Se$ were investigated.

The offline γ-rays spectra obtained following the irradiation of Ce, Cd, Pd and Se targets with 25 MeV bremsstrahlung and thermal neutrons are shown in Figs. 3.17 - 3.21. The characteristic γ-rays from ^{137m,g}Ce, ^{115m,g}Cd, ^{109m,g}Pd, and ^{81m,g}Se are clearly observed in the spectra.

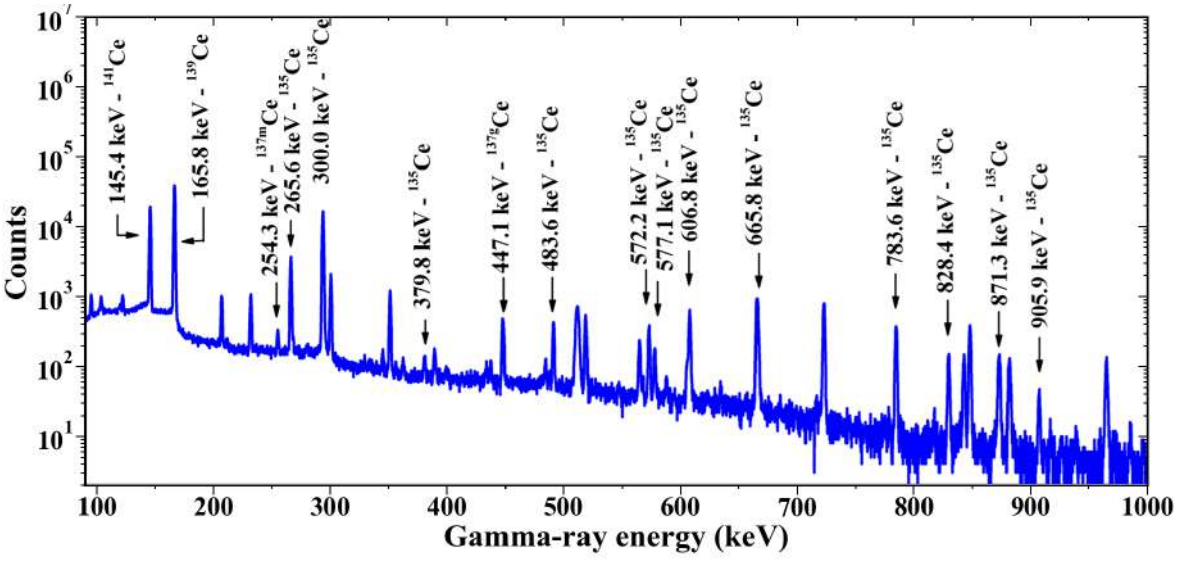

FIGURE 3.17: A typical γ-rays energy spectrum of a Ce sample irradiated with 25 MeV bremsstrahlung within 60 minutes, waited for 60 minutes and then measured for 20 minutes at 5 cm from the surface of HPGe detector [135].

The selected γ-rays and spectroscopic characteristic data [140] used for the IR calculation were determined and shown in Table 3.19. The losses of the interested γ-rays count due to the self-absorption and summing coincidence effects, which contributed to the IR determination error were corrected as the formulas 2.20 and 2.21.

Table 3.20 presents the experimental results of this work together with the existing data, which were taken from Refs. [167, 146, 64, 57, 194, 195, 196, 179, 168, 192, 193]. The product excitation energies for (γ, n) reaction were calculated by using Eqs. 3.2 and 3.3, while those for (n, γ) capture reaction induced by thermal neutron is equal to the binding energy of neutron in compound nuclei formed in these reaction. The error of IRs came from two sources. The first included uncertainties related to the IR

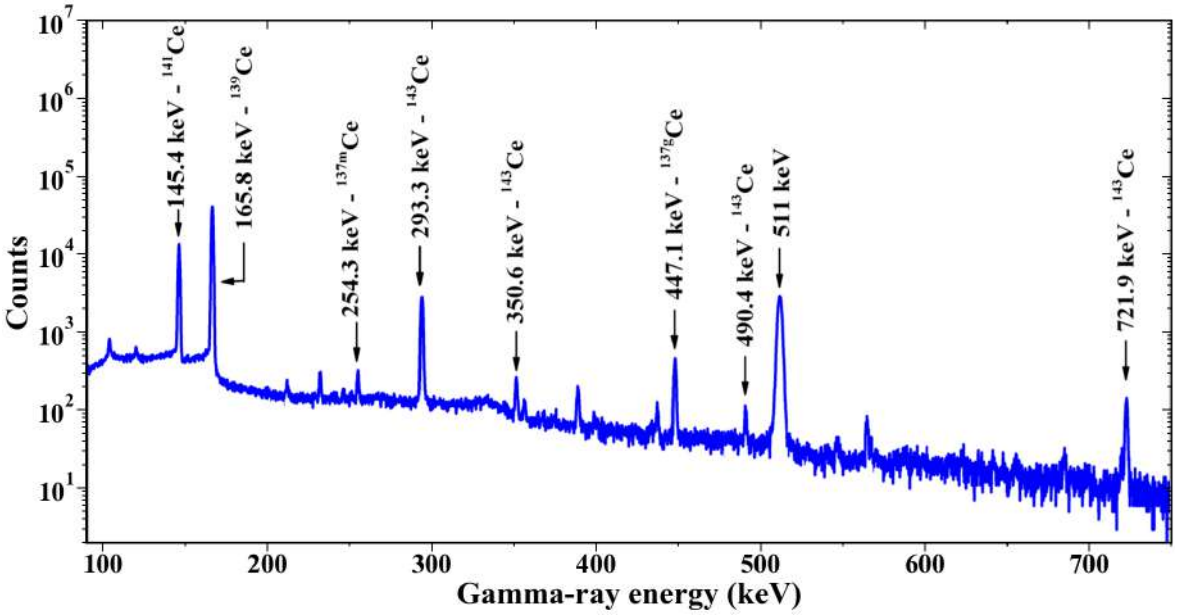

FIGURE 3.18: A γ-rays energy spectrum from the Ce sample. The sample was irradiated by energetic neutrons for 90 minutes, following by a cooling time of 35 minutes and then measured for 60 minutes at a position of 0 cm from the HPGe detector [135].

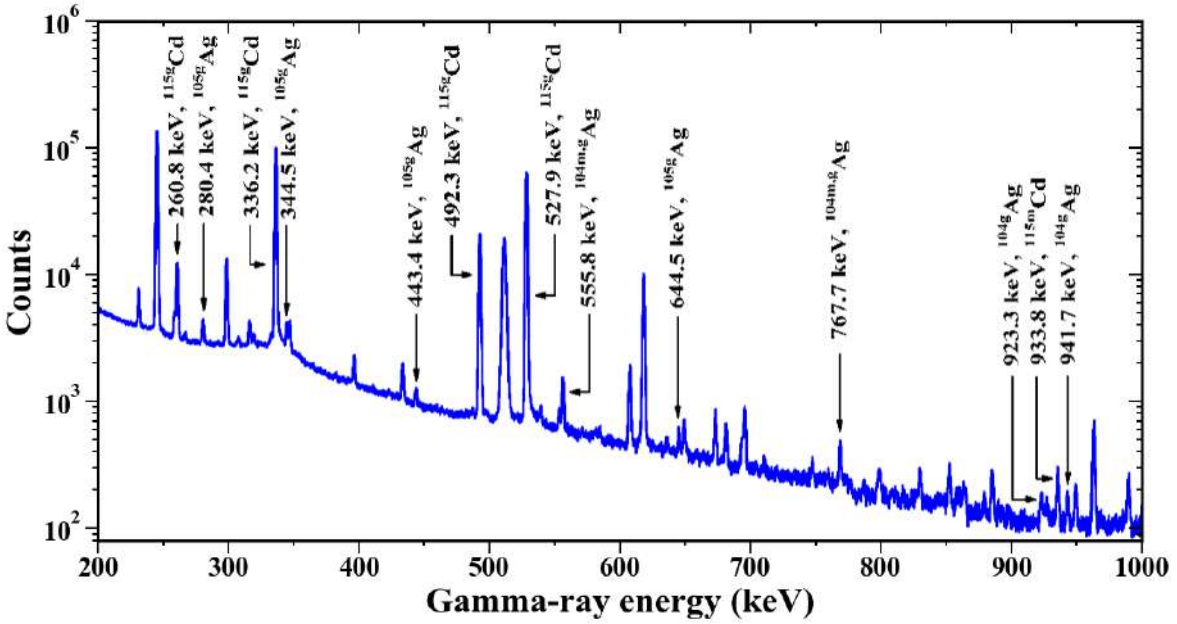

FIGURE 3.19: A γ-rays energy spectrum of the Cd sample measured for 275.5 minutes at a distance of 5 cm from the HPGe detector. The sample was irradiated by 25 MeV bremsstrahlung for 60 minutes, following by a cooling time of 20 minutes [135].

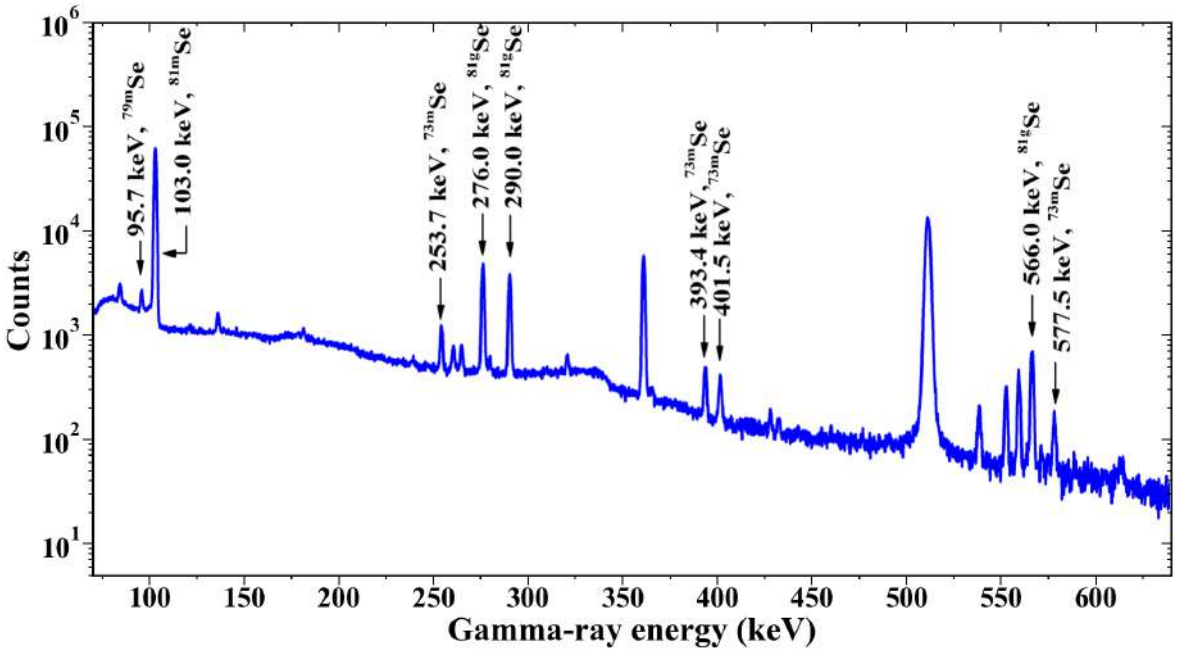

FIGURE 3.20: A γ-rays energy spectrum of the Se sample measured for 10 minutes on the surface of the HPGe detector. The sample was irradiated by 25 MeV bremsstrahlung for 20 minutes, following by a cooling time of 60 minutes [135].

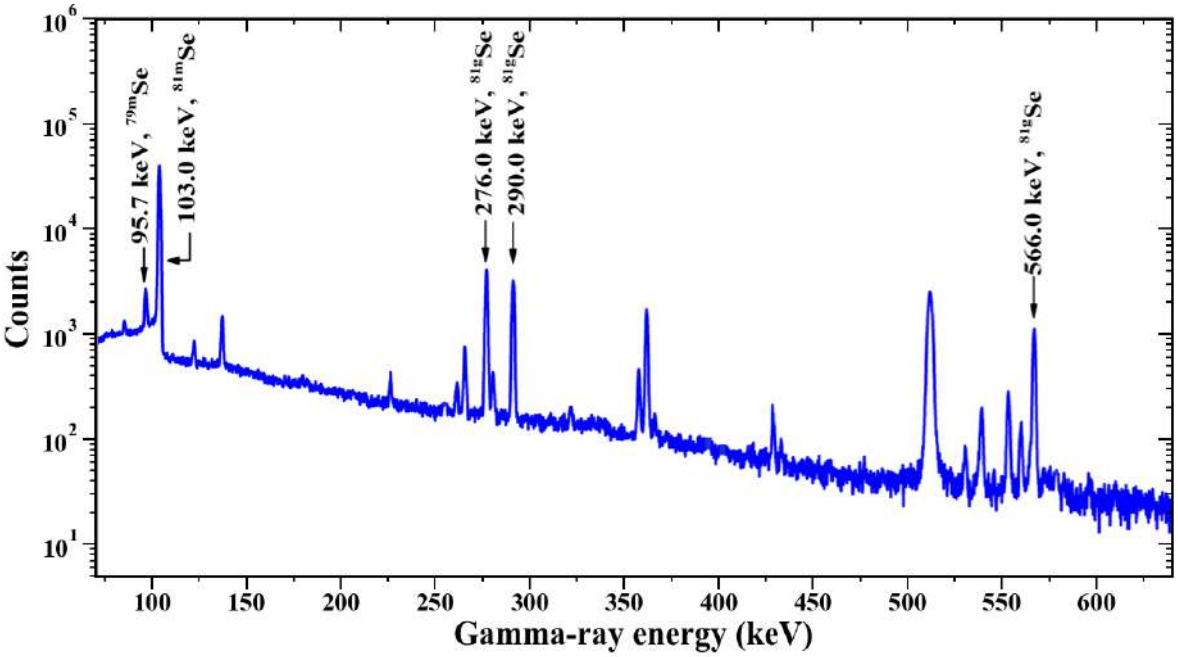

FIGURE 3.21: A γ-rays energy spectrum of the Se sample measured for 10 minutes on the surface of the HPGe detector. The sample was irradiated by neutrons for 90 minutes, following by a cooling time of 25 minutes [135].

TABLE 3.19: Selected gamma rays and spectroscopic characteristic data [140].

Nuclear Reaction	Target Spin, Parity, [J^π]	Nuclear state	Spin Parity [J^π]	Decay Mode [%]	Half Life	γ-ray Energy [keV]	Intensity [%]
$^{138}Ce(\gamma,n)^{137}Ce$	0^+	^{137m}Ce	11/2-	IT: 99.2	34.4 h	254.3	99.2
$^{136}Ce(n,\gamma)^{137}Ce$				EC: 0.78			
$^{138}Ce(\gamma,n)^{137}Ce$	0^+	^{137g}Ce	3/2+	EC: 100	9.0 h	447.1	1.8
$^{136}Ce(n,\gamma)^{137}Ce$							
$^{116}Cd(\gamma,n)^{115}Cd$	0^+	^{115m}Cd	11/2-	β^- : 100	44.6 d	933.8	2
$^{114}Cd(n,\gamma)^{115}Cd$							
$^{116}Cd(\gamma,n)^{115}Cd$	0^+	^{115g}Cd	1/2+	β^- : 100	2.23 d	336.2	45.9
$^{114}Cd(n,\gamma)^{115}Cd$						527.9	27.45
$^{110}Pd(\gamma,n)^{109}Pd$	0^+	^{109m}Pd	11/2-	IT: 100	4.69 m	189	55.9
$^{108}Pd(n,\gamma)^{109}Pd$							
$^{110}Pd(\gamma,n)^{109}Pd$	0^+	^{109g}Pd	5/2+	β^- : 100	13.7 h	88.04	3.6
$^{108}Pd(n,\gamma)^{109}Pd$							
$^{82}Se(\gamma,n)^{81}Se$	0^+	^{81m}Se	7/2+	IT: 99.95	57.28 m	103	13
$^{82}Se(n,\gamma)^{81}Se$				β^- : 0.05			
$^{82}Se(\gamma,n)^{81}Se$	0^+	^{81g}Se	1/2-	β^- : 100	18.45 m	276	0.7
$^{80}Se(n,\gamma)^{81}Se$						290	0.55

calculations using formula 2.18 and the second was from systematic uncertainties. The total error of the IR determination was estimated to be about 10.0%.

TABLE 3.20: The IRs of the studied inverse reactions.

Nuclear Reaction and Product	Type of Projectile	Product Ex. Energy [MeV]	Isomeric Ratio IR
$^{138}Ce(\gamma,n)^{137m,g}Ce$	25 MeV Bremsstrahlung	5.5	0.221 ± 0.022 [This work] 0.19 ± 0.02 [57]
$^{136}Ce(n,\gamma)^{137m,g}Ce$	Thermal neutron	7.4	0.112 ± 0.011 [This work] 0.109 ± 0.01 [146] 0.15 ± 0.01 [194] 0.088 ± 0.006 [195]
$^{116}Cd(\gamma,n)^{115m,g}Cd$	25 MeV Bremsstrahlung	5.8	0.165 ± 0.016 [This work] 0.168 ± 0.02 [196]
$^{114}Cd(n,\gamma)^{115m,g}Cd$	Thermal neutron	6.1	0.116 ± 0.012 [This work] 0.099 ± 0.0033 [179]
$^{110}Pd(\gamma,n)^{109m,g}Pd$	25 MeV Bremsstrahlung	6.3	0.069 ± 0.007 [This work] 0.065 ± 0.003 [64]
$^{108}Pd(n,\gamma)^{109m,g}Pd$	Thermal neutron	6.1	0.023 ± 0.002 [This work] 0.018 ± 0.005 [168], 0.028 ± 0.005 [167]
$^{82}Se(\gamma,n)^{81m,g}Se$	25 MeV Bremsstrahlung	6.9	0.556 ± 0.055 [This work] 0.56 ± 0.02 [192]
$^{80}Se(n,\gamma)^{81m,g}Se$	Thermal neutron	6.7	0.114 ± 0.014 [This work] 0.204 ± 0.024 [194] 0.136 ± 0.011 [167] 0.096 ± 0.009 [193]

From the experimental results obtained in the present work (summarized in Table 3.20), it can be seen that the IRs in inverse (γ,n) and (n,γ) reactions, which lead to the same isomeric pairs ^{137m,g}Ce, ^{115m,g}Cd, ^{109m,g}Pd, and ^{81m,g}Se are different due to the reaction channel effect. The IRs in (γ,n) reactions are significantly higher than

that in (n, γ) reactions. This trend can be explained by the intake angular momentum and impulse, transferred to the target nuclei from the projectiles, namely the higher intake angular momentum and impulse the higher isomeric ratio. For the (γ, n) reactions, the IRs of this work and that of Refs. [57, 64, 196, 192] within the error limit are in good agreement. Likewise, for the (n, γ) reactions, our result and the data from the references are in an agreement except for ^{81m,g}Se, which is in agreement with Refs.[167, 193] and be considerably less than that from Ref. [195].

3.5 Theoretically calculated IRs in (γ, n) reactions

In this work, the IRs of isomeric pairs produced in (γ, n) reactions on Se, Pd, Ce, Eu and Hg targets induced by bremsstrahlung with end-point energy range of 10 to 25 MeV were theoretically calculated by the formula 1.9. In which, the flux distribution as a function of bremsstrahlung end-point energy $\phi(E)$ was obtained by the GEANT4 simulation toolkit [71]. This distribution was then combined with the theoretical cross-section data $\sigma_m(E)$ and $\sigma_g(E)$ calculated by TALYS 1.95 code to yield the theoretical IRs.

3.5.1 Bremsstrahlung spectra simulation

To simulate as close as possible the experimental condition including geometry and materials of the setup, the primary electron beam and all possible interactions and radiations were described by using GEANT4 toolkit leading to a realistic description of the flux distribution. The bremsstrahlung spectra were calculated for the end-point energies from 10 to 25 MeV with the step of 1 MeV using the Geant4.10.06 version as in Fig. 3.22.

3.5.2 Cross-section calculation

The cross-sections of (γ, n) reaction on Pd, Se, Ce, Eu and Hg targets irradiated by photons with energies from the reaction threshold to 25 MeV are predicted by Talys 1.95 code. To investigate the IRs in various the level density models, we changed six level density models. For each level density model, we employed eight γSFs one by one to obtain the differential cross-sections of isomers. The six level density models and eight γSF are described in subsection 2.2.2. A total of 48 computations for each target were made. All possible reaction channels leading to the same reaction product are included

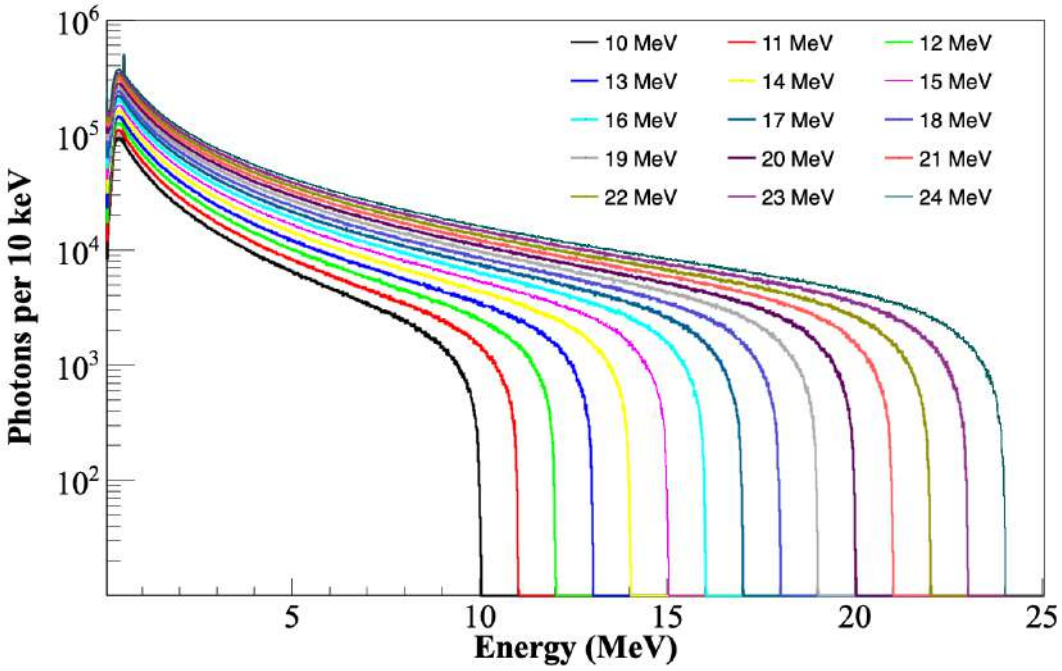

FIGURE 3.22: Bremsstrahlung energy spectra calculated by the GEANT4 toolkit with 500 millions primary particles.

throughout the calculation. Figs. 3.23 to 3.27 show the total cross-sections of the population of ^{109}Pd, $^{73,81}Se$, $^{137,139}Ce$, $^{150,152}Eu$ and $^{195,197}Hg$ from (γ, n) reactions using **ldmodel 1** (Ld1) and **Strength 2** (s2). In those figures, the contribution of the direct, preequilibrium and compound reaction processes is also illustrated. For all calculated reactions, the dominant contribution was owing to compound process, while the contribution of preequilibrium was insignificant and the direct process did not occur. The compound reactions happened in whole energy range from the reaction threshold to 25 MeV, while the preequilibrium reactions started taking place from 15, 20.3, 16, 17.3, 16.7, 14.4, 14.9, 15.8 and 15.3 for ^{110}Pd, ^{74}Se, ^{82}Se, ^{138}Ce, ^{140}Ce ^{151}Eu, ^{153}Eu, ^{196}Hg and ^{198}Hg nuclei, respectively. For ^{110}Pd, the contributions of the preequilibrium and compound mechanisms are 10.1% and 89.9%, respectively. In the case of $^{74,82}Se$, those ones are 3.59%, 96.4% and 9.89%, 90.1%, respectively. For $^{138,140}Ce$, those are 2.41%, 97.6% and 2.88%, 97.1%, respectively. For $^{151,153}Eu$, those are 8.81%, 91.2% and 6.5%, 93.5%, respectively. For $^{196,198}Hg$, those are 2.0%, 98.0% and 2.45%, 97.5%, respectively.

Figs. 3.23 to 3.27 also exhibit the literature cross-sections listed in the Experimental Nuclear Reaction Data Library (EXFOR) database [197] for ^{74}Se, ^{140}Ce, ^{151}Eu, and ^{153}Eu, wherein good agreements between the evaluated experimental data and the TALYS-based calculated results are observed.

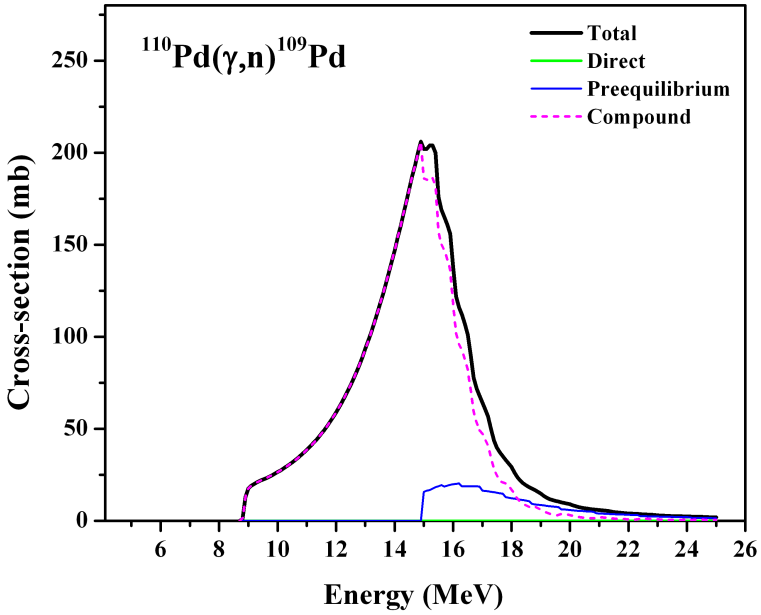

FIGURE 3.23: (γ, n) reaction cross-section for ^{110}Pd calculated by TALYS 1.95.

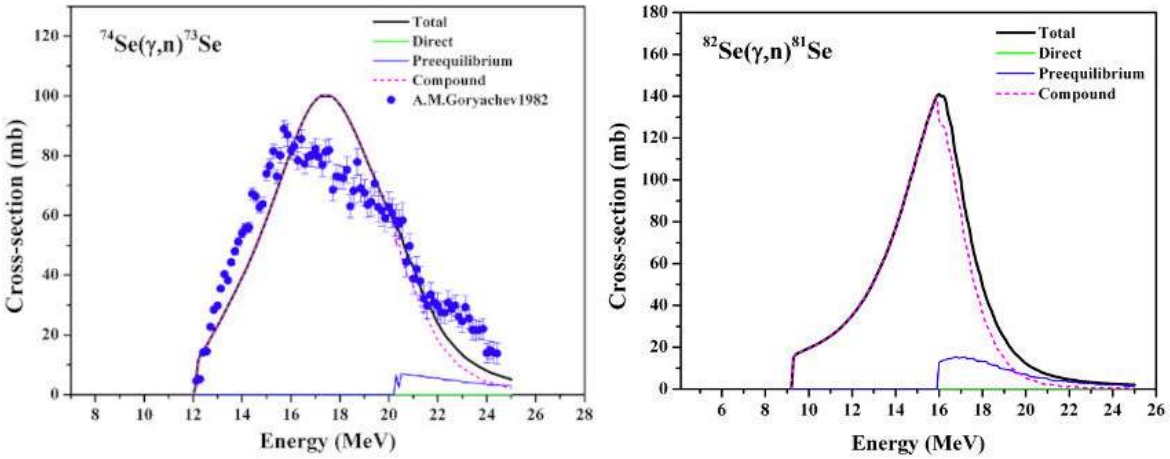

FIGURE 3.24: (γ, n) cross-section of $^{74,82}Se$ calculated by TALYS 1.95 and compared with experimental values [198].

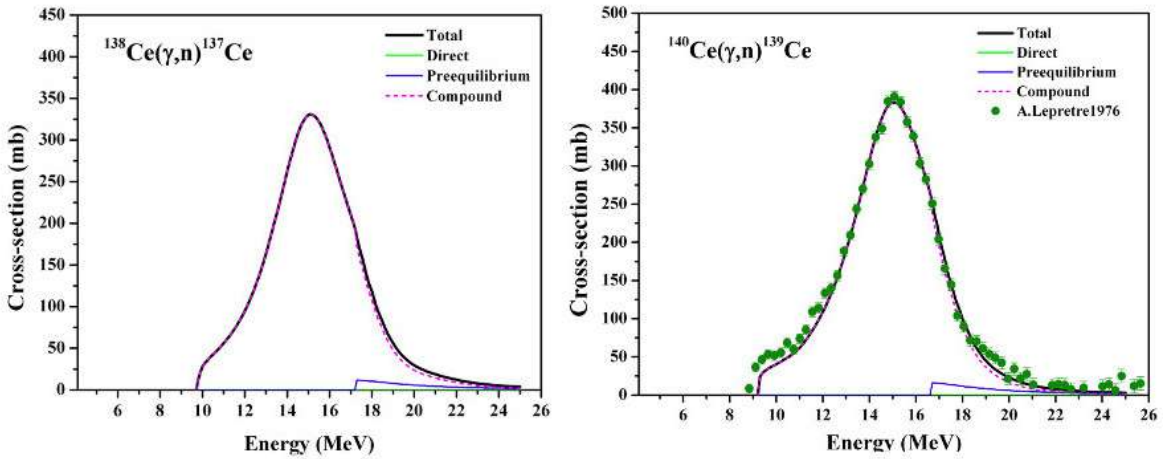

FIGURE 3.25: (γ, n) cross-section for $^{138,140}Ce$ calculated by TALYS 1.95 and compared with experimental values [199].

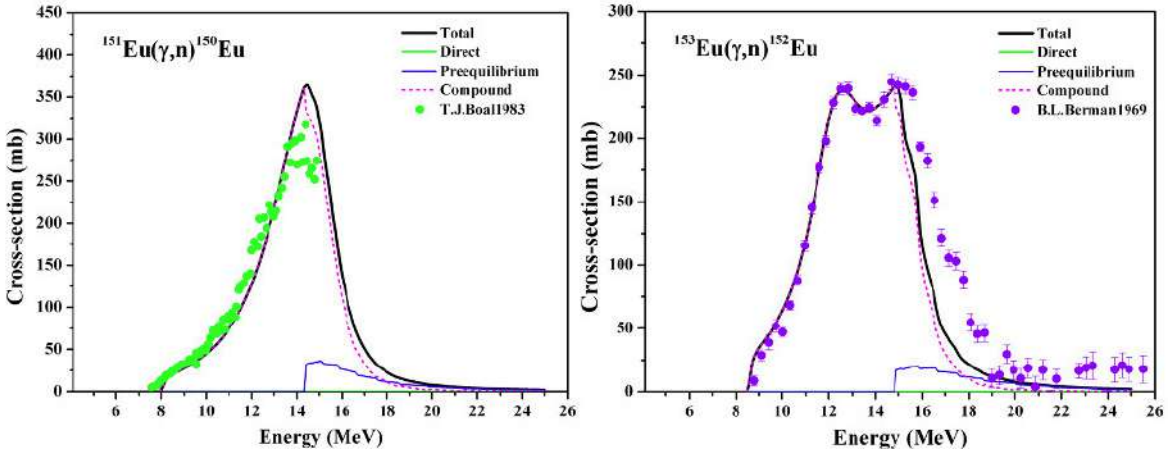

FIGURE 3.26: (γ, n) reaction cross-section for $^{151,153}Eu$ calculated by TALYS 1.95 compared with experimental values [200, 201].

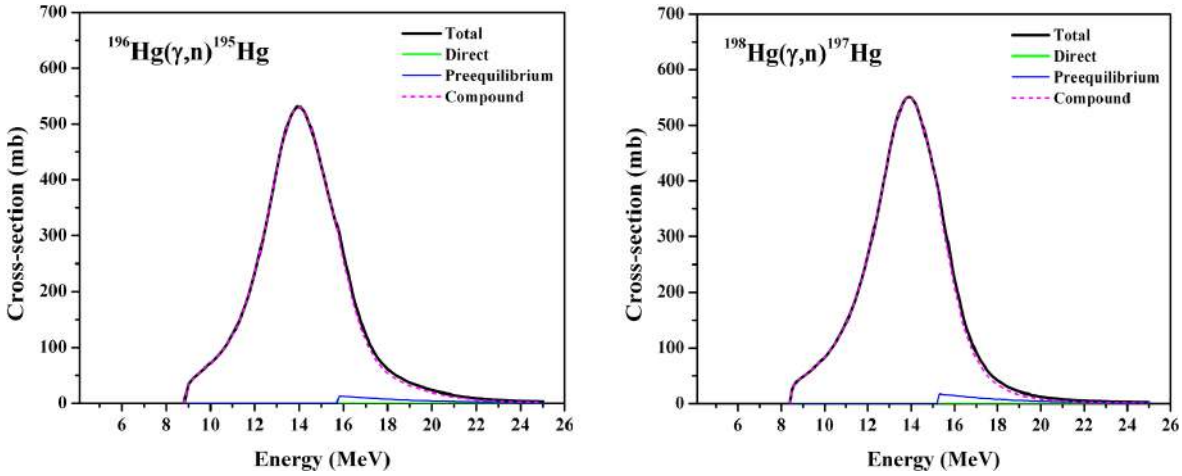

FIGURE 3.27: (γ, n) reaction cross-section for $^{195,197}Hg$ calculated by TALYS 1.95.

Further, the differential cross-sections for the formation of the isomeric pairs $^{73m,g;81m,g}Se$, $^{109m,g}Pd$, $^{137m,g;139m,g}Ce$, $^{150m,g;152m1,g;152m2,g;152m1,m2}Eu$, and $^{195m,g;197m,g}Hg$ were also computed. Fig. 3.28 shows the calculated cross-sections for the formation of the isomeric and ground states of ^{152}Eu nucleus. One can see that the probability for forming $^{152m1}Eu$ with the high spin (8^-) is much smaller than $^{152m2}Eu$ and ^{152g}Eu with the lower spin (0^-) and (3^-), respectively.

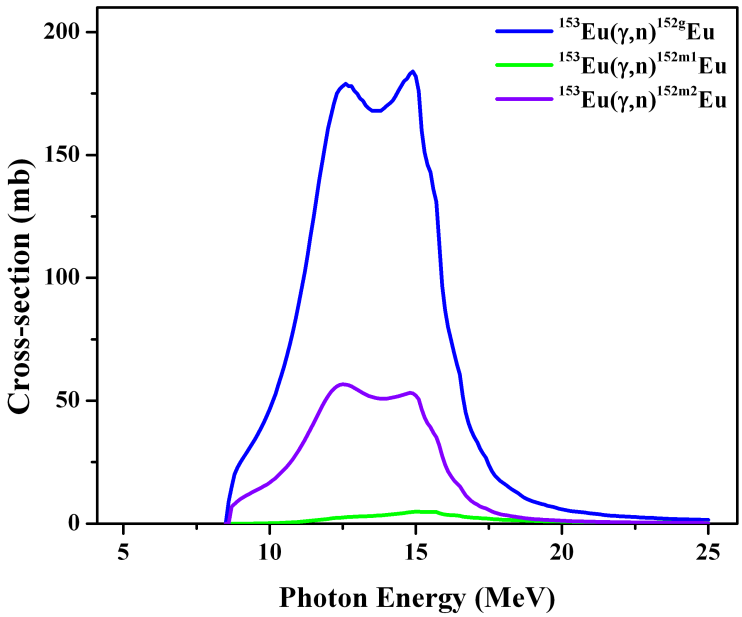

FIGURE 3.28: The calculated cross-sections of isomeric and ground state formation in $^{153}Eu(\gamma,n)^{152}Eu$ reaction.

In addition to the cross-sections, the properties of the target nuclei such as the mass, energy levels, spin, parity, and deformation were revealed in the nuclear structure database of TALYS code originated from the Reference Input Parameter Library (RIPL). The database indicated that $^{138,140}Ce$ and $^{196,198}Hg$ are the spherical even-even nuclei, and $^{74,82}Se$ and ^{110}Pd are vibrational even-even nuclei owing to the residual interaction among the valence nucleons resulting in the vibrational motion in nuclei, and $^{151,153}Eu$ is rotational deformed odd-even nucleus characterized by the rotational bands. However, based on the computed results in Fig. 3.26, the excitation function of $^{151}Eu(\gamma,n)^{150}Eu$ exhibits one resonance peak, while that of $^{153}Eu(\gamma,n)^{152}Eu$ shows two resonance peaks, which is characteristic of deformed nuclei. Hence, ^{151}Eu can be a quasi-spherical deformed nucleus.

3.5.3 IRs in (γ, n) reactions

The IRs following by formula 1.9 resulted from the combination of the differential cross-sections and bremsstrahlung spectra demonstrated in Fig.3.22. The calculated results executed with six various level density models in combination with eight different gamma strength functions differed considerably. Through the comparison between the experimental outcomes and theoretically calculated data, it can ascertain which model best fits the experimental results. The basic information related to the nuclear structure, level populations, optical model parameters, transmission coefficients, reaction cross sections, gamma strength functions, discrete levels and level densities can extract.

The calculated IRs for $^{73m,g;81m,g}Se$, $^{109m,g}Pd$, $^{137m,g;139m,g}Ce$, $^{150m,g;152m1,g;152m2,g;152m1,m2}Eu$, and $^{195m,g;197m,g}Hg$ are illustrated in Figs. 3.29 to 3.39. From these results, it is worth making the following remarks:

General trend of the IR dependence on the energy

It is seen that all figures in this subsection have a general trend of the IR dependence on bremsstrahlung end-point energies of 10 to 25 MeV in both theoretical and experimental data. The IRs for $^{73m,g;81m,g}Se$, $^{109m,g}Pd$, $^{137m,g;139m,g}Ce$, $^{152m1,g;152m1,m2}Eu$, and $^{195m,g;197m,g}Hg$ grow with the enhancement of energy and the IRs for $^{150m,g}Eu$ and $^{152m2,g}Eu$ decreases with increasing energy. It is worth noting that, if the IR of all cases is calculated by the yield ratio of the high-spin state and low-spin one, the IR will rise along with the energy. In details, the IRs go up rapidly from the reaction threshold to the GDR peak energy then increase slightly or reach to a plateau. This fact is reasonable since in low energy region the increase of the angular momentum transferred to the compound nucleus caused the growth of IR along with excitation energy. This ratio enhances moderately in the higher energy region possibly due to the contribution of the direct and pre-equilibrium reaction mechanism.

IRs in (γ, n) reactions on isotopes

a. For Se isotopes

The IR of ^{73m,g}Se calculated by TALYS 1.95 code describes well the experimental datum taken from M. G. Davidov [202] without that of T. D. Thiep [35] and V. M. Mazur [203]. Meanwhile, for ^{81m,g}Se in Fig. 3.30, the calculated IRs describe well the experimental data taken from refs. [35, 203] and B. M. Hue [134]. It is worth noting that the best agreement between the experimental and theoretically calculated data

for ^{81m,g}Se is Ld1-model with s5-γSF (Ld1+s5), Ld2+s6, Ld4+s7, Ld5+s2, and Ld6 with s6-γSFs.

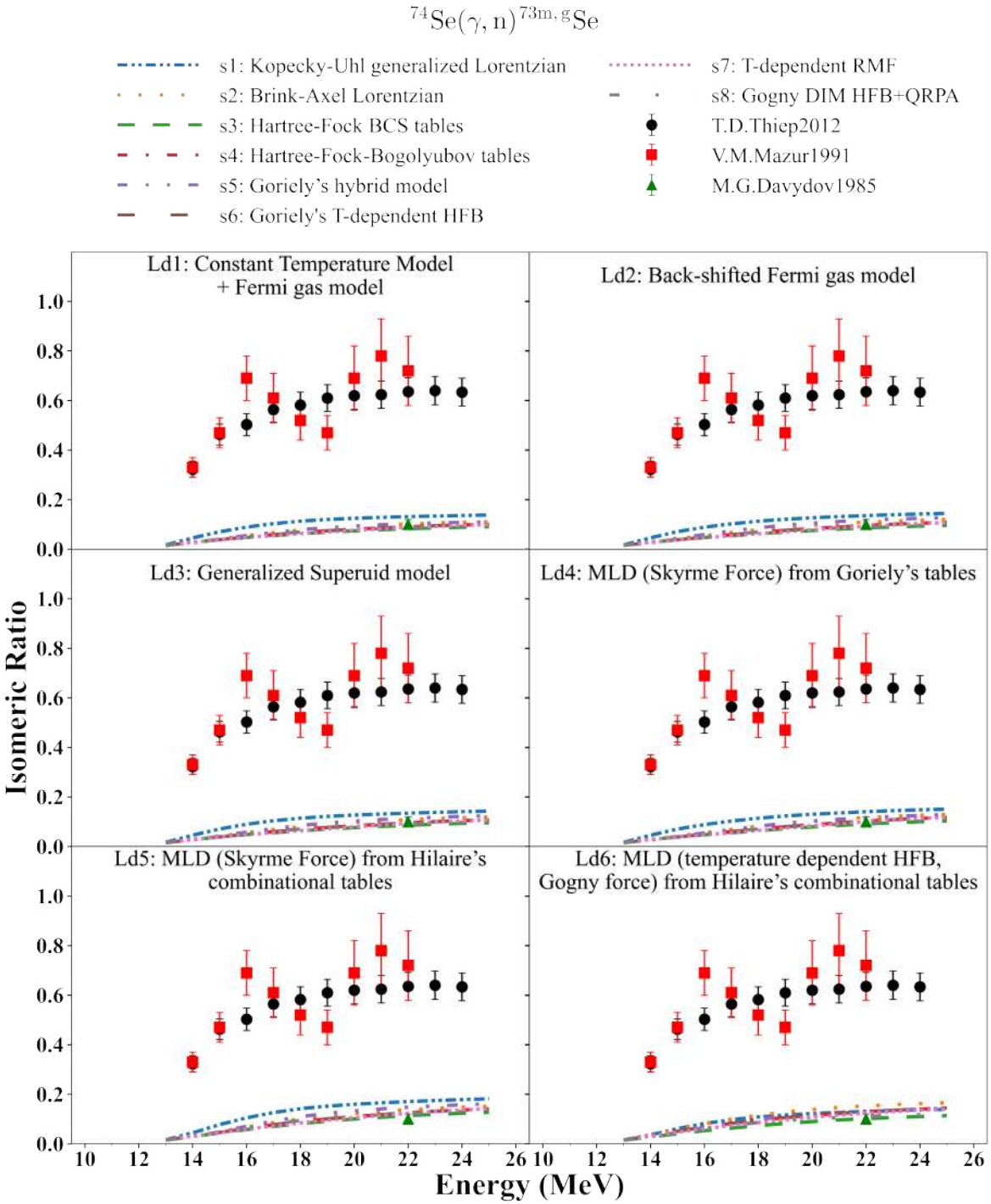

FIGURE 3.29: Theoretically calculated IRs between ^{73g}Se(I=9/2$^+$) and ^{73m}Se(I=3/2$^-$) in comparison with the literature.

From the good agreement for Ld1+s5 (Constant Temperature and Fermi gas level density model in combination with Goriely's hybrid γSF model) and experimental results, the information regarding to the nuclear excited state structure and the level density parameters of ^{81}Se nucleus can be totally extracted in the output file such as:

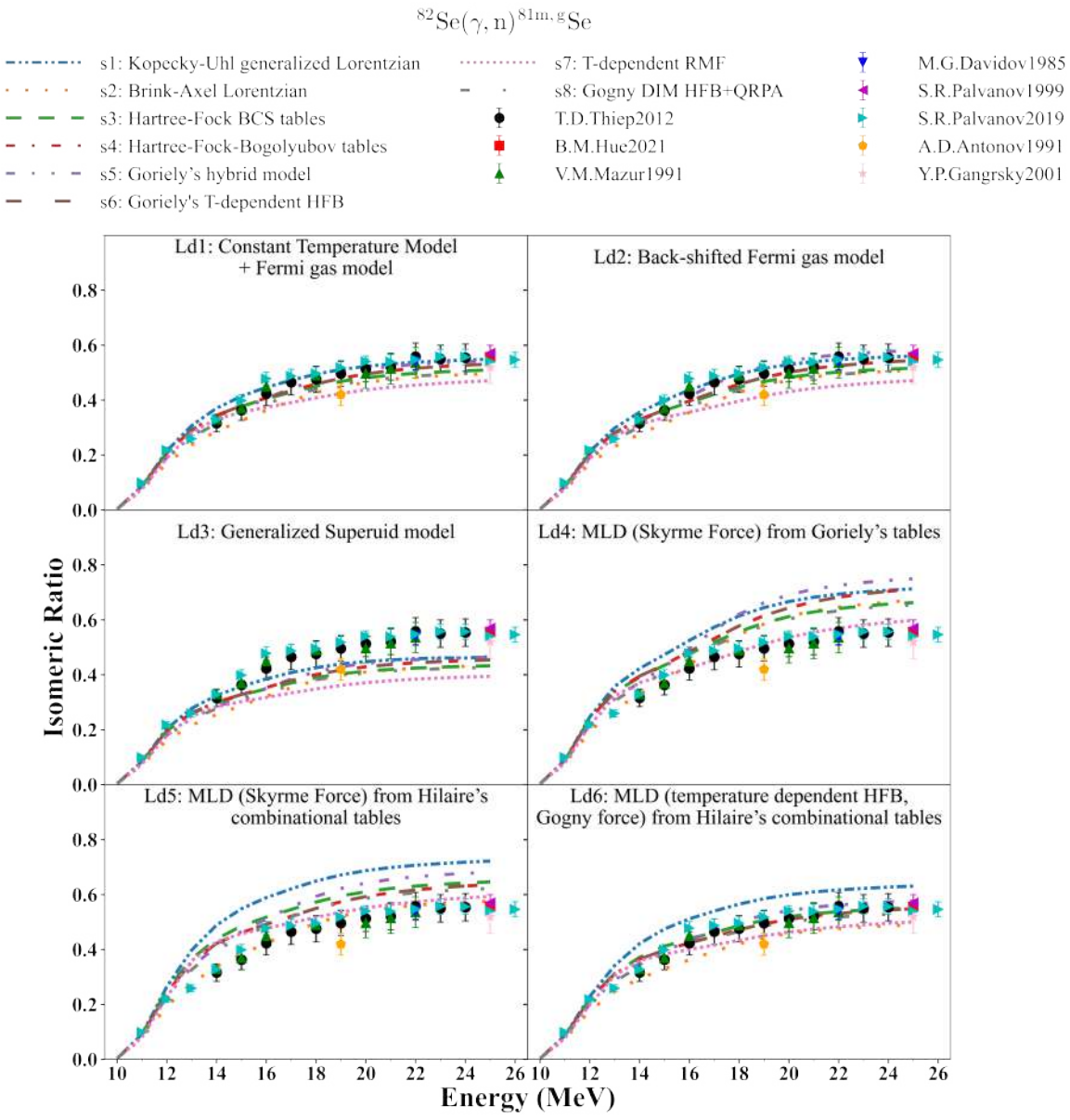

FIGURE 3.30: Theoretically calculated IRs between ^{81m}Se(I=7/2$^+$) and ^{81g}Se(I=1/2$^-$) in comparison with the literature.

$a(S_n)$ = 12.76063 MeV^{-1} (LD parameter at the neutron separation energy),

D_0 = 2 ± 0.8 keV (experimental and theoretical average resonance spacing),

$\tilde{a}$ = 11.04827 MeV^{-1} (asymptotic level density parameter),

γ = 0.1001 MeV (shell damping parameter),

Δ = 1.33333 MeV (pairing energy),

δW = 2.00143 MeV (shell correction energy),

E_x = 5.43118 MeV (matching energy),

N_{low} = 7, N_{top} = 19 (levels for the matching problem),

T = 0.73461 MeV (nuclear temperature),

E_0 = -0.19965 MeV (back-shift energy),

σ = 1.64366 (discrete state spin cut-off parameter),

$\sigma(S_n)$ = 3.97335 (spin cut-off parameter at the neutron separation energy).

Besides, the output file printed a table with the level density parameter a, the spin cut-off parameter and the level density itself, all as a function of the excitation energy. Wherein gamma strength function, transmission coefficient, giant resonance parameters and many other parameters were also represented.

For ^{82}Se nucleus, GDR parameters, gamma strength function f(XL) and transmission coefficient T(XL) are

σ_0(M1) = 1.534, σ_0(E1) = 148;

E(M1) = 9.437 MeV, E(E1) = 16.65 MeV;

Γ(M1) = 4 MeV, Γ(E1) = 5.91 MeV;

f(M1) = 1.7901E^{-10} MeV^{-3}, f(E1) = 8.18775E^{-8} MeV^{-3};

T(M1) = 1.75743E^{-5}, T(E1) = 8.03830E^{-3}.

In Refs. [35, 34, 36], it showed the so-called nucleon configuration effect, which means that the IR in (γ, n) reaction in the GDR region for isotopes of an element decreases with the increase of the isotope mass number. In the case of Se, the experimental IRs of ^{73m,g}Se are higher than that in ^{81m,g}Se while the theoretical IRs are inverse. Taking into this fact and the difference in the experimental and calculated results, one can say that the TALYS code may have to make corrections in the level density as well as the γSF models.

b. For $^{109m,g}Pd$

The IR results of ^{109m,g}Pd presented in Fig. 3.31 show that six Ld-models with most of γSFs predict with certainty the experimental data taken from B. M. Hue [134], S. R. Palvanov [64], H. D. Luc, [204] V. M. Mazur [205], A. G. Belov [206] but not in whole

energy range. There is a good agreement between the theoretical IRs with Ld5+s1 and experimental ones for the energies from 10 to 17 MeV while the theoretical IRs with Ld3+s1/s5 describe exactly experimental ones for the energies from 18 to 25 MeV.

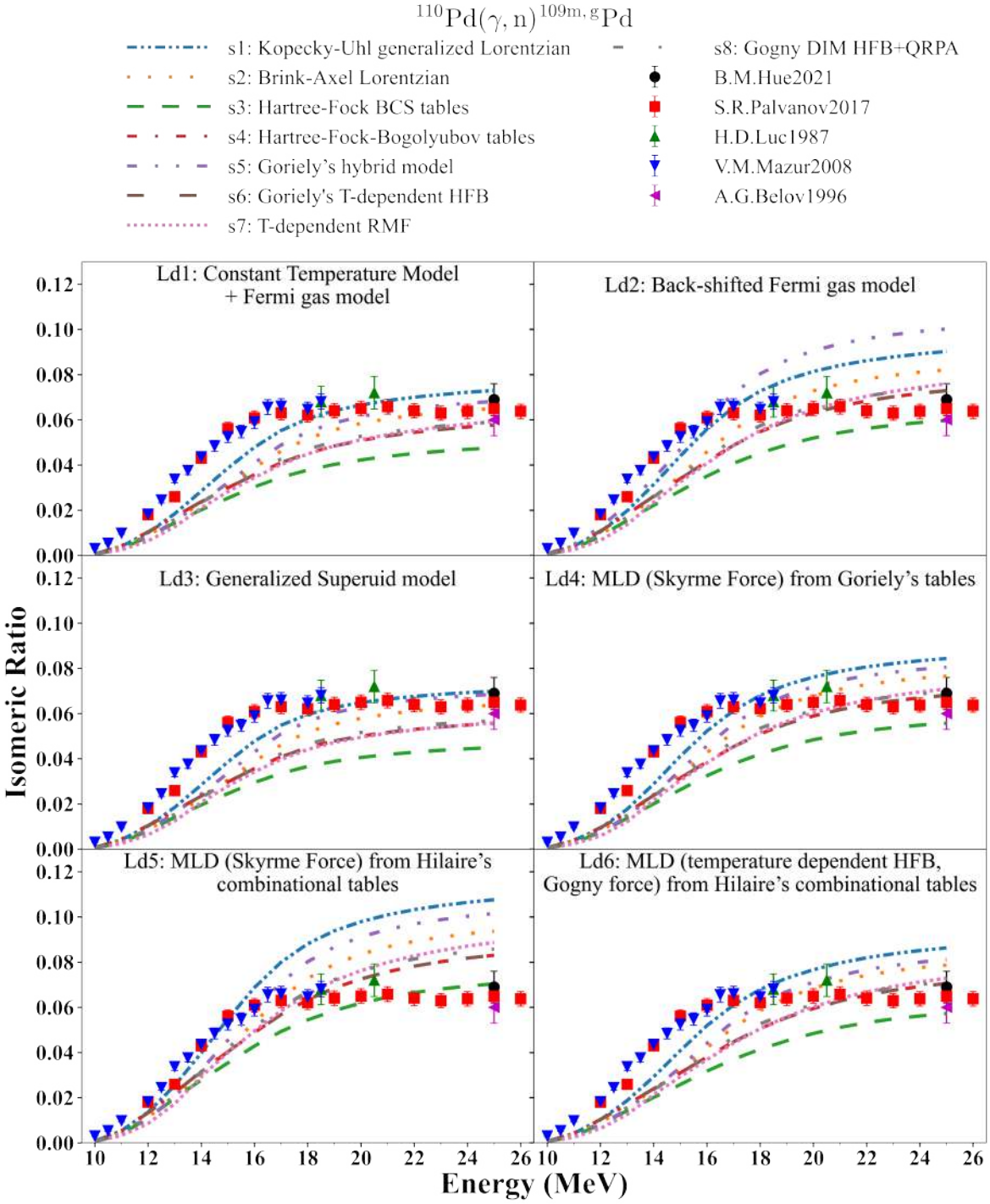

FIGURE 3.31: Theoretically calculated IRs between ^{109m}Pd(I=11/2$^-$) and ^{109g}Pd(I=5/2$^+$) in comparison with the literature.

For Ld3+s5 (Generalised superfluid level density model in combination with Goriely's hybrid γSF model), the model parameters regarding to the nuclear excited state structure and the level density parameters of ^{109}Pd nucleus consists of

$a(S_n) = 15.67741\ MeV^{-1}$,

$D_0 = 182 \pm 33$ eV,

$\tilde{a} = 15.67741\ MeV^{-1}$,

$\gamma = 0.13581$ MeV,

$\Delta = 1.14939$ MeV,

$\delta W = 3.82721$ MeV,

$E_x = 4.10818$ MeV,

$N_{low} = 8$, $N_{top} = 16$,

T = 0.65170 MeV,

$\sigma = 2.81066$,

$\sigma(S_n) = 4.69007$.

For ^{110}Pd nucleus, GDR parameters, gamma strength function f(XL) and transmission coefficient T(XL) are

σ_0(M1) = 1.08, σ_0(E1) = 238.746;

E(M1) = 8.557 MeV, E(E1) = 15.923 MeV;

Γ(M1) = 4 MeV, Γ(E1) = 5.138 MeV;

f(M1) = $1.19106E^{-10}$ MeV^{-3}, f(E1) = $9.62216E^{-8}$ MeV^{-3};

T(M1) = $1.16932E^{-5}$, T(E1) = $9.44653E^{-3}$.

c. For Ce isotopes

Fig. 3.32 presents theoretically calculated IRs for ^{137m,g}Ce and the experimental data taken from B. M. Hue [134], T. D. Thiep [41, 207], S. R. Palvanov [208] Yu. P. Gangrsky [57]. One can see that there are large deviations between theoretical values and the experimental ones taken from [134, 41, 207, 57]. However, the calculated results of Ld4+s5 and Ld5+s1/s5 are close to that of [208].

Fig. 3.33 shows theoretically calculated IRs of ^{139m,g}Ce and the experimental data taken from S.R. Palvanov [209], V. M. Mazur [210], N. Tsoneva [211], A. G. Belov [212]. The theoretical calculations are in good agreement with the experimental ones, especially the Ld4+s2/s5, Ld5+s2 and Ld6+s5 models. It is worth noting that ^{140}Ce is a magic nucleus.

The nucleon configuration effect is observed in the experimental results without the TALYS-based ones for Ce isotopes.

For Ld4+s2 (microscopic level densities (Skyrme force) from Goriely's tables in combination with Brink-Axel Lorentzian γSF model), the model parameters regarding

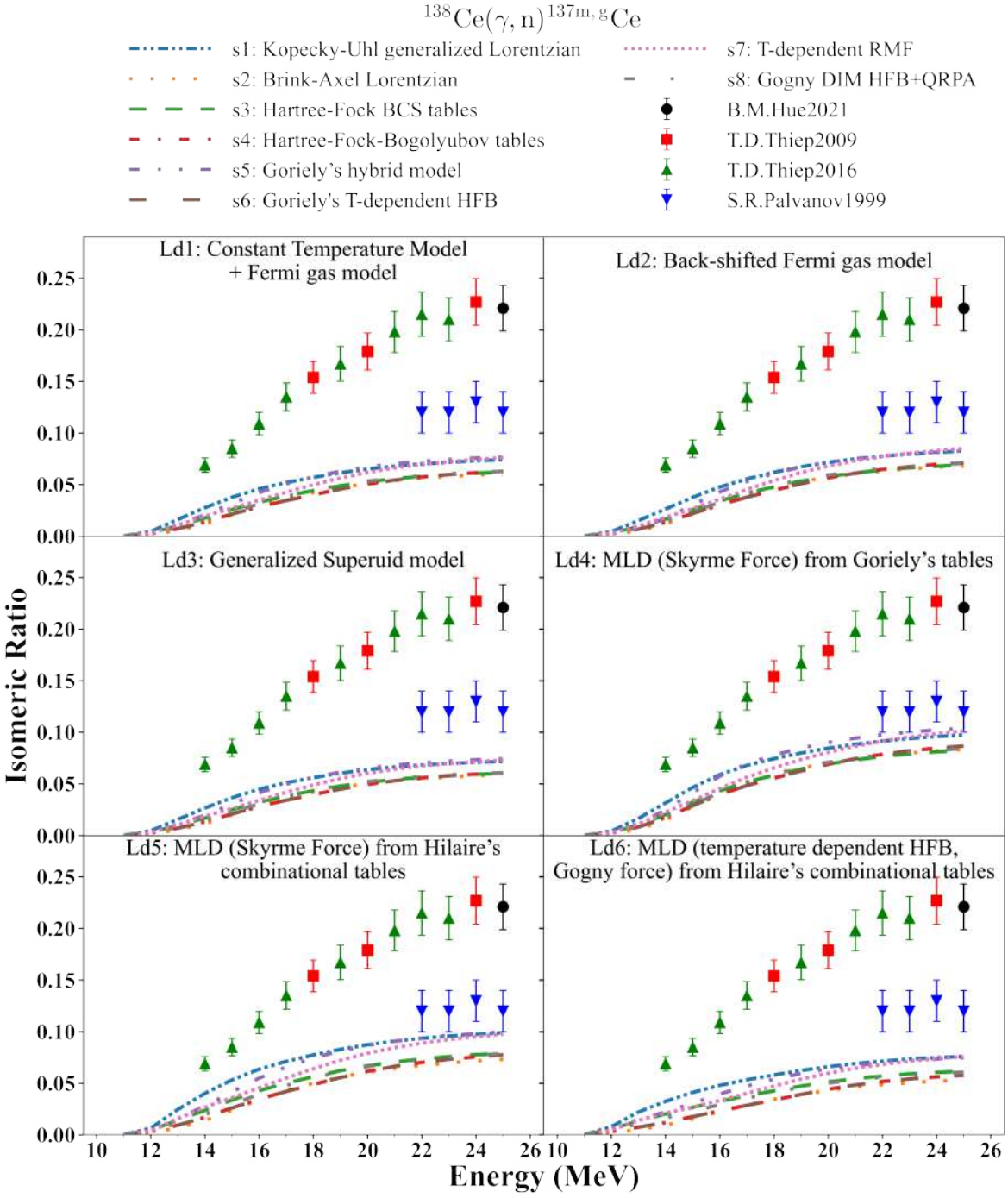

FIGURE 3.32: Theoretically calculated IRs between ^{137m}Ce(I=11/2$^-$) and ^{137g}Ce(I=3/2$^+$) in comparison with the literature.

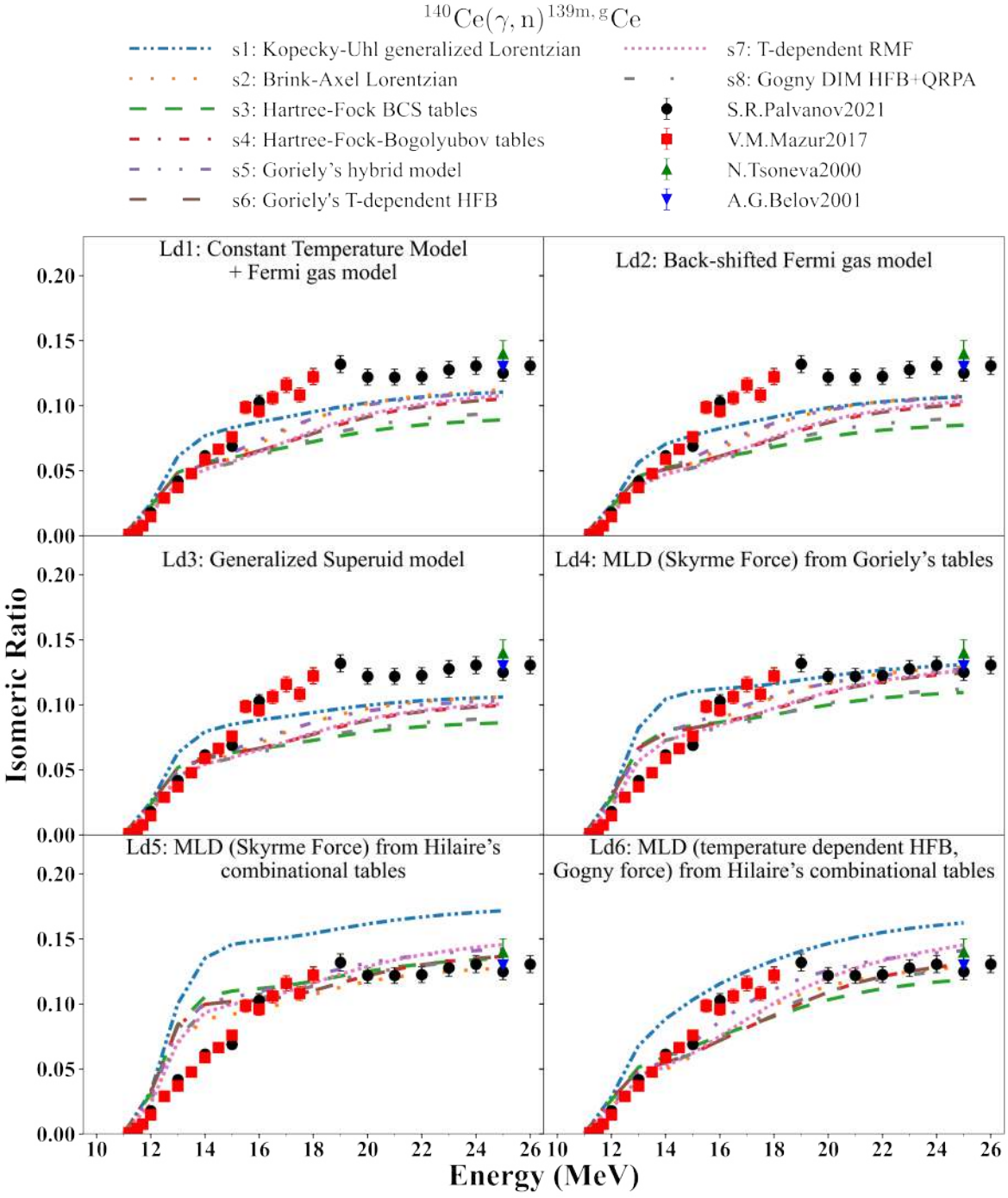

FIGURE 3.33: Theoretically calculated IRs between ^{139m}Ce(I=11/2$^-$) and ^{139g}Ce(I=3/2$^+$) in comparison with the literature.

to the nuclear excited state structure and the level density parameters of ^{139}Ce nucleus include

$a(S_n) = 15.96688\ MeV^{-1}$,

$D_0 = 428.26\ eV$,

$\tilde{a} = 17.21424\ MeV^{-1}$,

$\gamma = 0.08361\ MeV$,

$\Delta = 1.01783\ MeV$,

$\delta W = -1.12045\ MeV$,

$N_{low} = 4$, $N_{top} = 16$,

$\sigma = 2.14087$,

$\sigma(S_n) = 5.52402$.

For ^{140}Ce nucleus, GDR parameters, gamma strength function f(XL) and transmission coefficient T(XL) are

$\sigma_0(M1) = 3.073$, $\sigma_0(E1) = 383$;

$E(M1) = 7.896\ MeV$, $E(E1) = 15.04\ MeV$;

$\Gamma(M1) = 4\ MeV$, $\Gamma(E1) = 4.410\ MeV$;

$f(M1) = 3.26495E^{-10}\ MeV^{-3}$, $f(E1) = 9.43474E^{-8}\ MeV^{-3}$;

$T(M1) = 3.20536E^{-5}$, $T(E1) = 9.26254E^{-3}$.

d. For Eu isotopes

Fig. 3.34 presents theoretically calculated IRs between ^{150m}Eu(I=0^-) and ^{150g}Eu(I=5^-) in ^{151}Eu(γ, n)^{150m,g}Eu reaction and the experimental data taken from I. N. Vishnevsky [137], A. P. Tonchev [123]. The theoretically calculated values are in a good agreement with the experimental data obtained by the authors in Ref. [123] but that deviate significantly from the data at 12 MeV taken from Ref. [137]. It is worth noting that ^{150}Eu is a spherical nucleus [162] as proved in Fig. 3.26.

The product of (γ, n) photonuclear reaction on ^{153}Eu existed in the ground state with the spin of 3^- and two isomeric states with spins of 0^- and 8^- respectively. Fig. 3.35 demonstrates theoretically calculated IRs between ^{152m1}Eu(I=8^-) and ^{152g}Eu(I=3^-), and the experimental data taken from A. P. Tonchev [123]. Fig. 3.36 represents theoretically calculated IRs between ^{152m1}Eu(I=8^-) and ^{152m2}Eu(I=0^-), and the experimental data taken from T. D. Thiep [41, 23], A. P. Tonchev [123], I. N. Vishnevsky [137, 141]. Fig. 3.37 shows theoretically calculated IRs between ^{152m2}Eu(I=0^-) and ^{152g}Eu(I=3^-), and the experimental data taken from A. P. Tonchev [123]. One can see from these figures that there are significant differences between the experimental

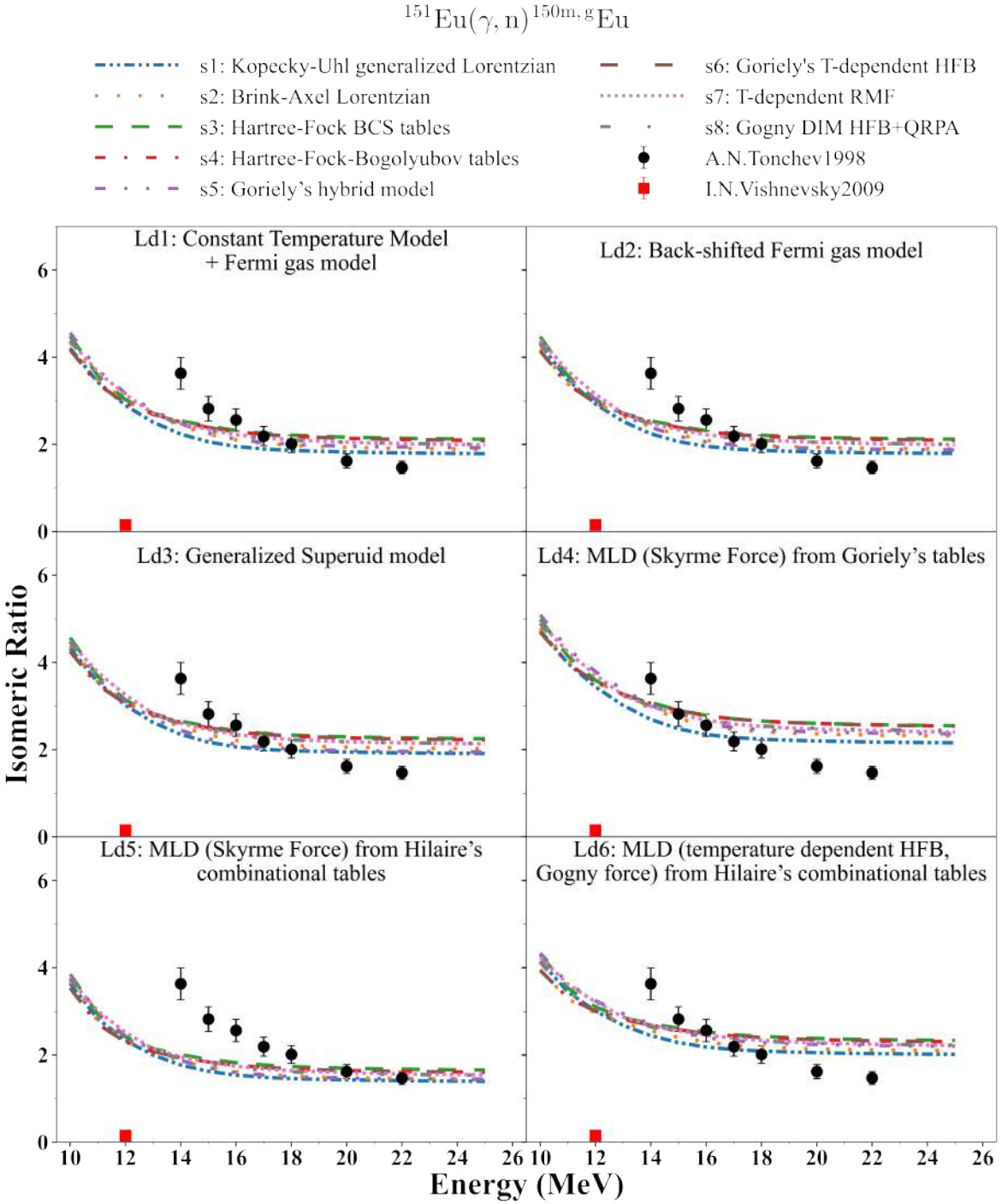

FIGURE 3.34: Theoretically calculated IRs between ^{150m}Eu(I=0$^-$) and ^{150g}Eu(I=5$^-$) in comparison with the literature.

data and theoretical values from TALYS-based calculations. The calculated IRs overestimate the experimental data for $^{152m1,g;152m1,m2}Eu$, whereas, those underestimate the measured values for $^{152m2,g}Eu$. It is worth noting that ^{152}Eu is a strongly deformed nucleus [23] as verified in Fig. 3.26.

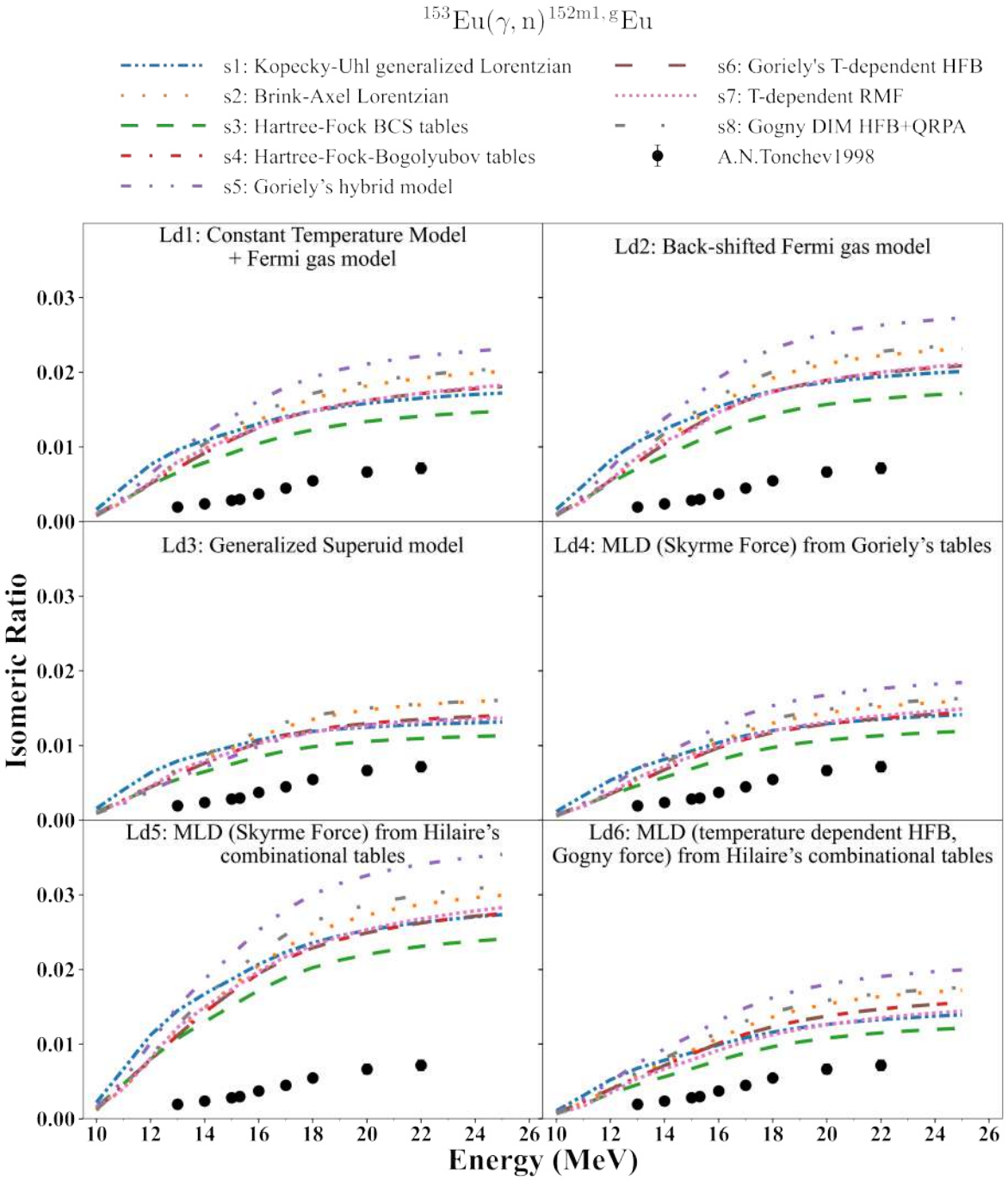

FIGURE 3.35: Theoretically calculated IRs between ^{152m1}Eu(I=8$^-$) and ^{152g}Eu(I=3$^-$) in comparison with the literature.

For Ld1+s2 (Constant Temperature and Fermi gas level density model in combination with Brink-Axel Lorentzian γSF model), the model parameters regarding to the nuclear excited state structure and the level density parameters of ^{152}Eu nucleus

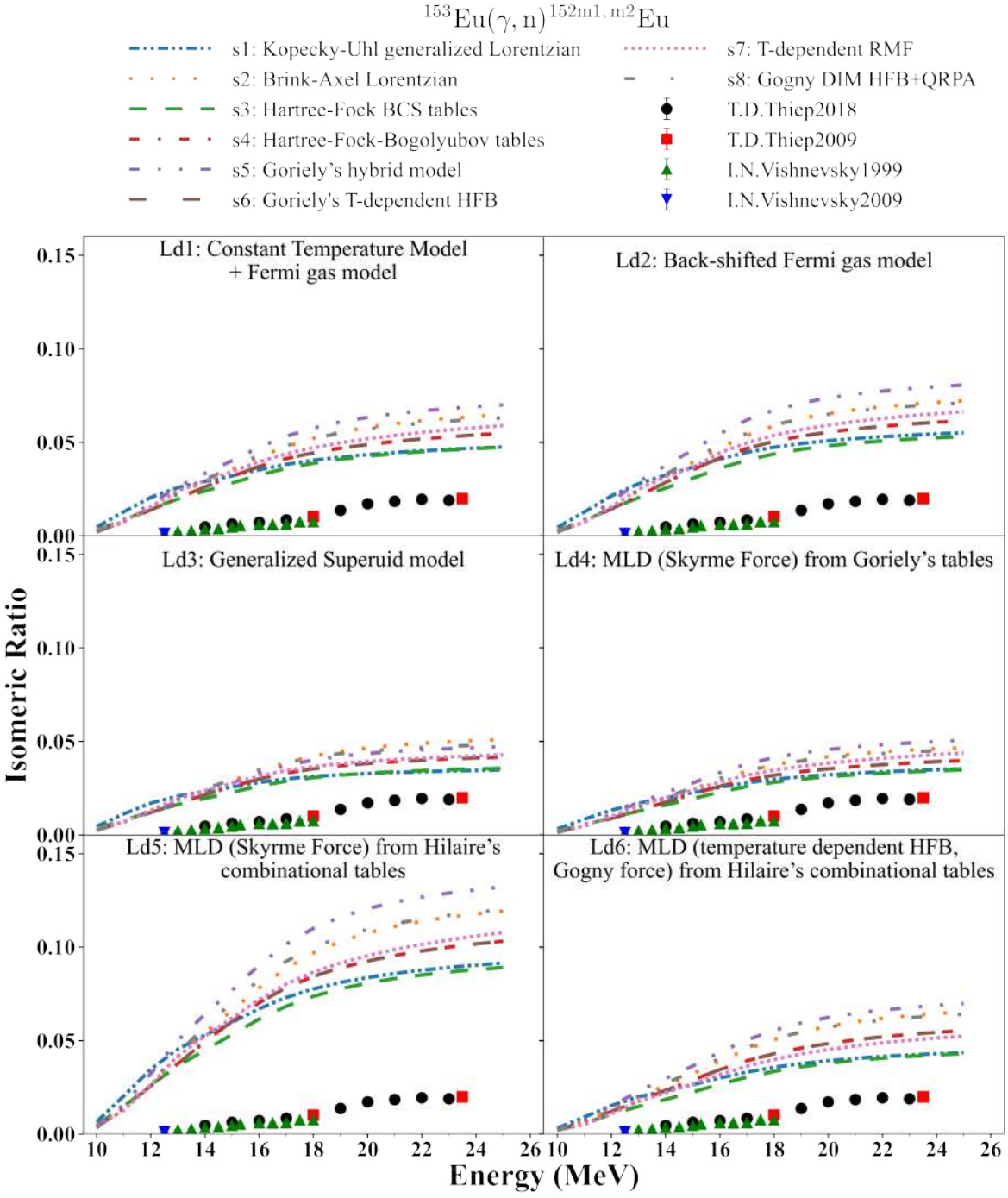

FIGURE 3.36: Theoretically calculated IRs between ^{152m1}Eu(I=8$^-$) and ^{152m2}Eu(I=0$^-$) in comparison with the literature.

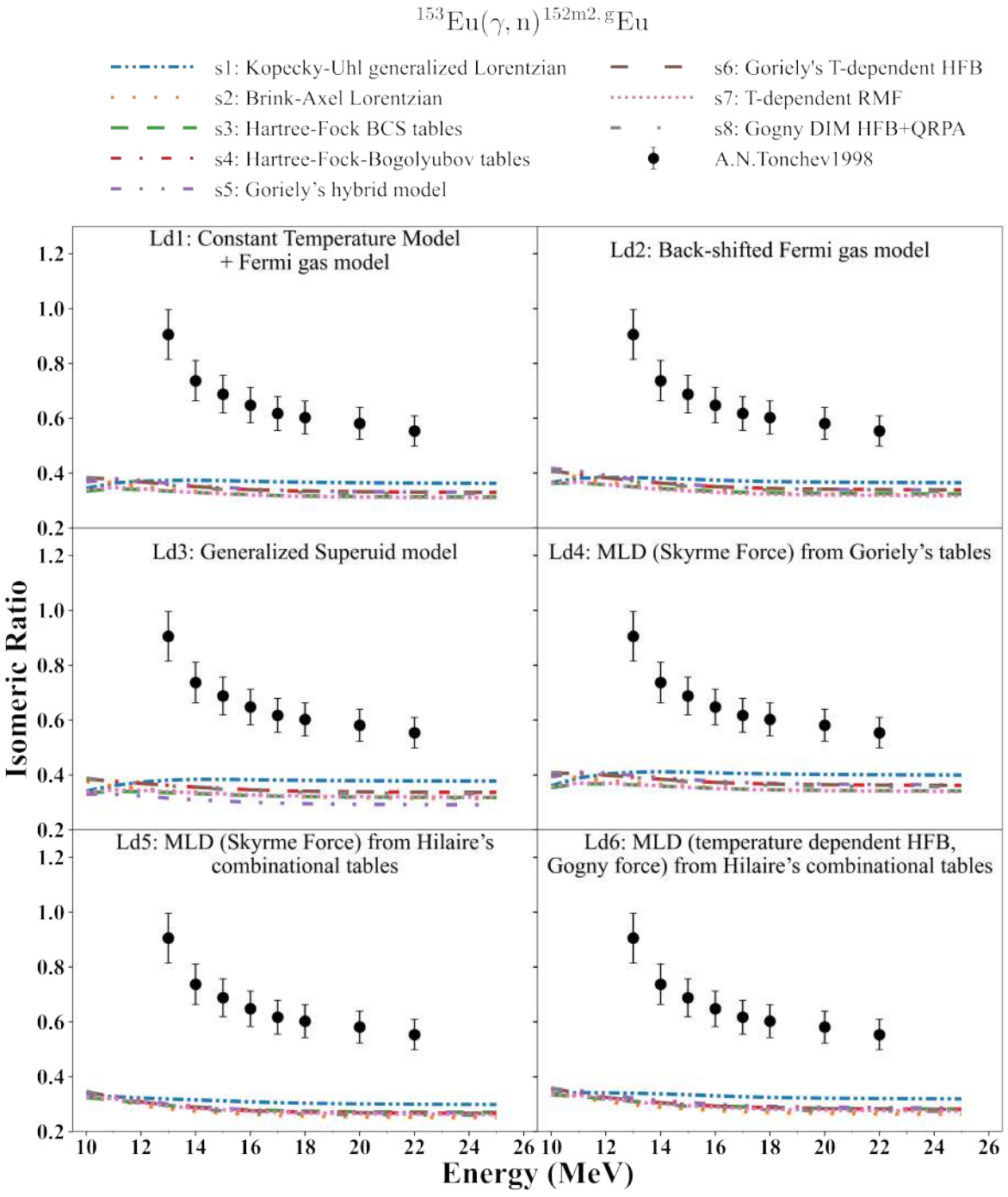

FIGURE 3.37: Theoretically calculated IRs between ^{152m2}Eu(I=0$^-$) and ^{152g}Eu(I=3$^-$) in comparison with the literature.

comprise

$a(S_n) = 23.96007\ MeV^{-1}$,

$D_0 = 0.73 \pm 0.07$ eV,

$\tilde{a} = 18.89487\ MeV^{-1}$,

$\gamma = 0.08115$ MeV,

$\Delta = 0$ MeV,

$\delta W = 4.22048$ MeV,

$E_x = 4.38808$ MeV,

$N_{low} = 2$, $N_{top} = 17$,

T = 0.51830 MeV,

E_0 = -2.23933 MeV,

$\sigma = 3.20887$,

$\sigma(S_n) = 6.25665$.

For ^{153}Eu nucleus, GDR parameters, gamma strength function f(XL) and transmission coefficient T(XL) are

σ_0(M1) = 3.241, σ_0(E1) = 155 and 222;

E(M1) = 7.666 MeV, E(E1) = 12.330 MeV and 15.79 MeV;

Γ(M1) = 4 MeV, Γ(E1) = 2.750 MeV and 5.830 MeV;

f(M1) = $3.40147E^{-10}$ MeV^{-3}, f(E1) = $1.11894E^{-7}$ MeV^{-3};

T(M1) = $3.33939E^{-5}$, T(E1) = $1.09851E^{-2}$.

Instead of being computed by the method in ref. [74], obtained results with another method in this work are in good agreement with that of [74] calculated by Talys 1.8 code in the complete simulation process of the GEANT4 toolkit for bremsstrahlung production and photonuclear reaction process.

e. For Hg isotopes

Fig. 3.38 presents the experimental data taken from T. D. Thiep [129], B. S. Ishkhanov [157] along with the theoretically calculated IRs of ^{195m}Hg(I=13/2$^+$) and ^{195g}Hg(I=1/2$^-$). Fig. 3.39 show the experimental data taken from Yu. P. Gangrsky [57], T. D. Thiep [129], B. S. Ishkhanov [157], V. A. Zheltonozhsky [151] and the theoretically calculated IRs between ^{197m}Hg(I=13/2$^+$) and ^{197g}Hg(I=1/2$^-$).

For ^{195m,g}Hg, six Ld models exactly relatively describe the experimental data. The best description is LD5+s2 model, whereas, for ^{197m,g}Hg, there are large discrepancies between the calculated results and experimental data originating from [129, 151, 57]. Those experimental data are overestimated the calculated values. However, the

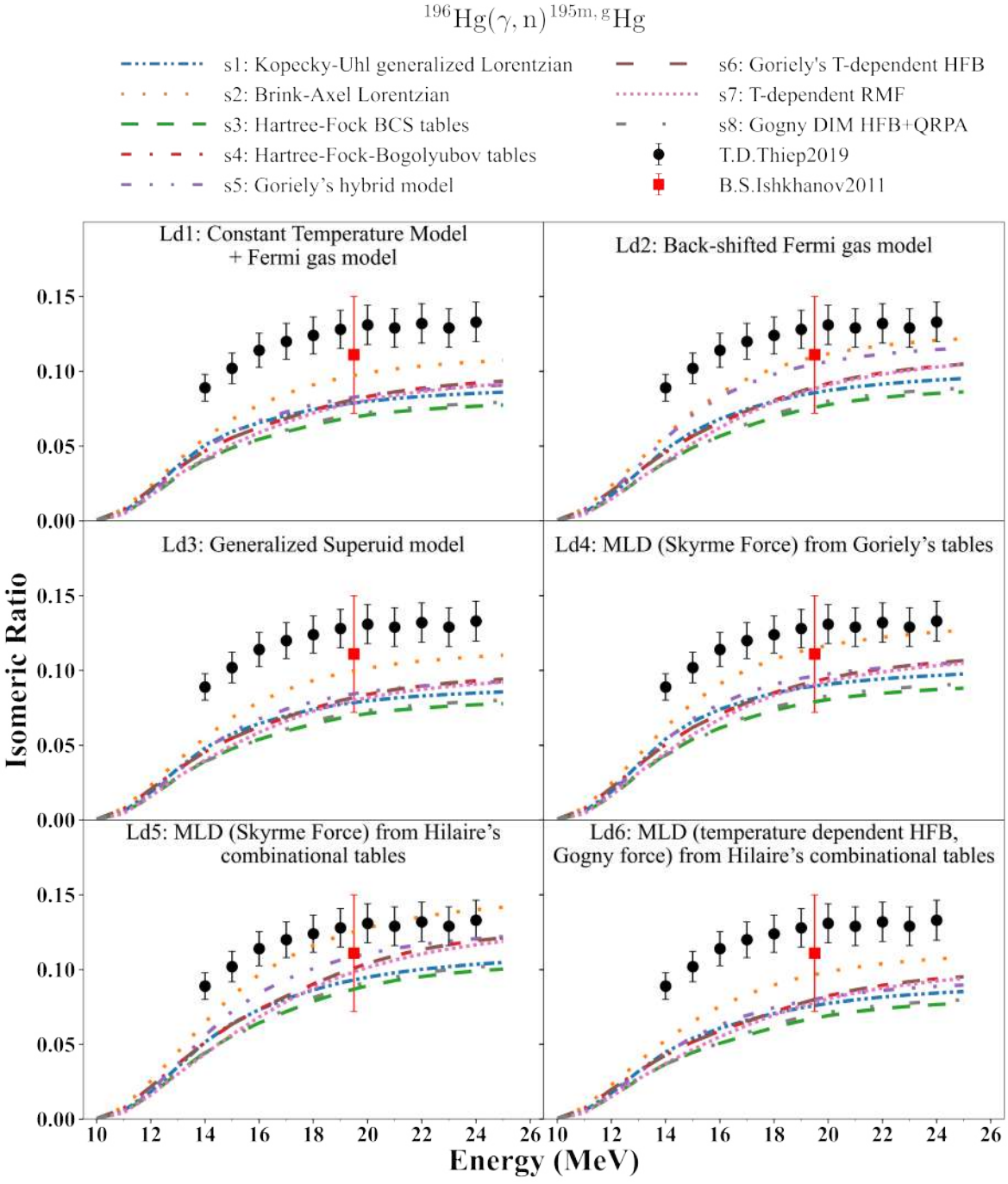

FIGURE 3.38: Theoretically calculated IRs between ^{195m}Hg(I=13/2$^+$) and ^{195g}Hg(I=1/2$^-$) in comparison with the literature.

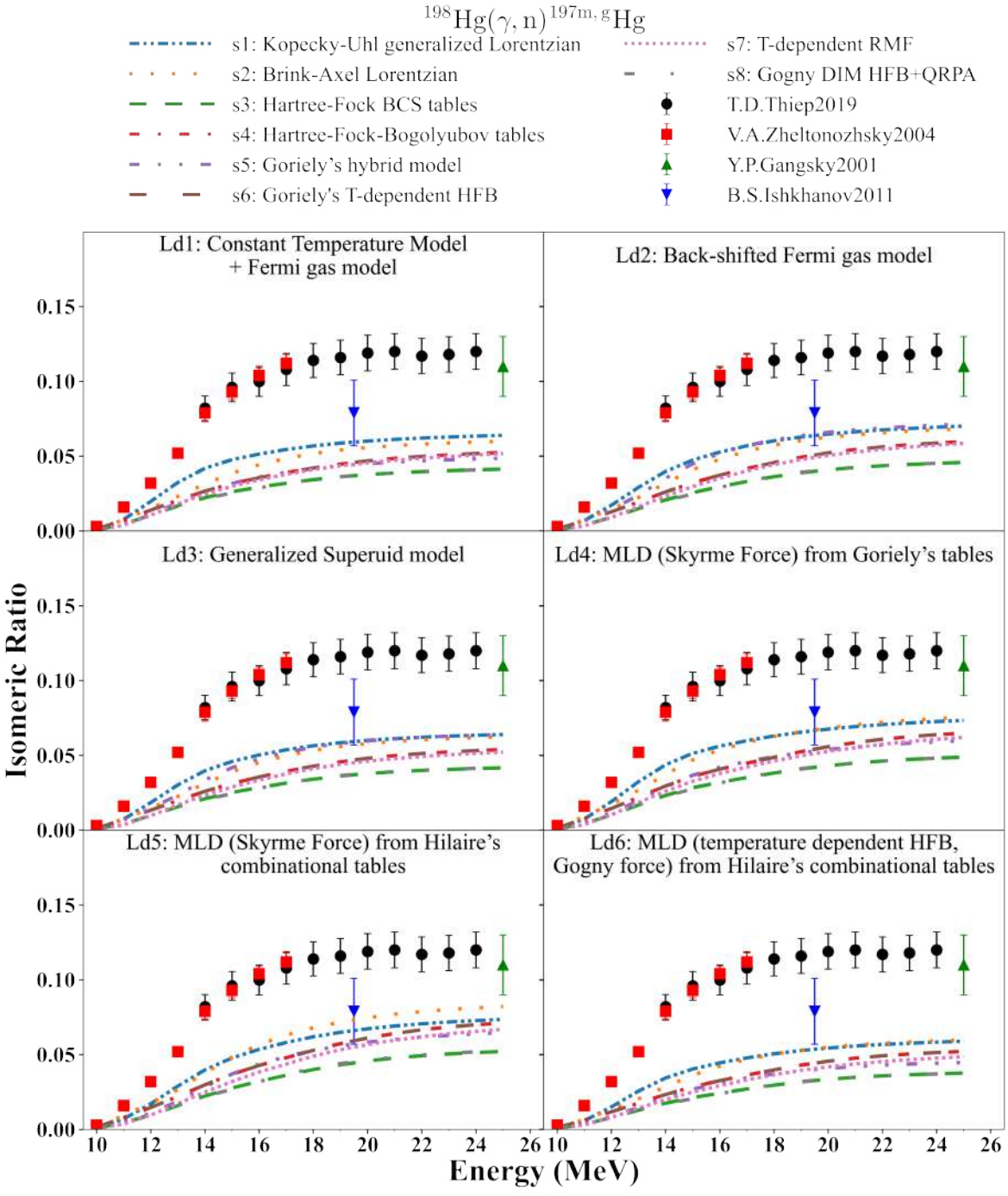

FIGURE 3.39: Theoretically calculated IRs between ^{197m}Hg(I=13/2$^+$) and ^{197g}Hg(I=1/2$^-$) in comparison with the literature.

IR value of Ishkhanov et al. [157] is consistent with that of Ld4+s1/s2 and Ld5+s2 theoretical predictions.

For Ld5+s2 (microscopic level density (Skyrme force) from Hilaire's combinatorial tables in combination with Brink-Axel Lorentzian γSF model), the model parameters regarding to the nuclear excited state structure and the level density parameters of ^{195}Hg nucleus consist of

$a(S_n) = 21.19256\ MeV^{-1}$,

$D_0 = 19.87$,

$\tilde{a} = 23.01361\ MeV^{-1}$,

$\gamma = 0.07468$ MeV,

$\Delta = 0.85934$ MeV,

δW = -1.31645 MeV,

$N_{low} = 8$, $N_{top} = 18$,

$\sigma = 3.57524$,

$\sigma(S_n) = 6.69405$.

For ^{196}Hg nucleus, GDR parameters, gamma strength function f(XL) and transmission coefficient T(XL) are

$\sigma_0(M1) = 3.217$, $\sigma_0(E1) = 546.105$;

$E(M1) = 7.058$ MeV, $E(E1) = 13.918$ MeV;

$\Gamma(M1) = 4$ MeV, $\Gamma(E1) = 3.974$ MeV;

$f(M1) = 3.27509E^{-10}\ MeV^{-3}$, $f(E1) = 9.54788E^{-8}\ MeV^{-3}$;

$T(M1) = 3.21531E^{-5}$, $T(E1) = 9.37361E^{-3}$.

The nucleon configuration effect is demonstrated in both experimental and theoretical results for Hg isotopes. It means that the IR of ^{195m,g}Hg is higher than that of ^{197m,g}Hg.

Conclusions and Outlook

In this work, we have studied the IRs of isomeric pairs of Eu, Hg, Cd, Ce, Se and Pd isotopes in the (γ, n) reactions irradiated by bremsstrahlung with end-point energy in the GDR region as well as the IRs of isomeric pairs of Pd, Cd, Ce and Se isotopes in (n, γ) reactions induced by thermal and epithermal neutrons. The activation method combined with the off-line γ-ray spectroscopy was employed in the experiments. The bremsstrahlung and neutron sources were produced using the MT-25 Microtron, FLNR, JINR, Dubna, Russia. The Eu, Hg, Cd, Ce, Se and Pd targets were chosen to investigate the isomers and IR due to their various nuclear structure, the insufficient IR data or the data with large discrepancies. Moreover, they also play a crucial role in many applications such as medicine, therapy, biology, electronics, material science and nuclear reactor. The study of IR with diverse reaction conditions, particular various projectiles with their energies on the different targets might furnish an indication about the nuclear structure and reaction mechanisms. Accordingly, the obtained experimental results with high accuracy in this thesis have expected to contribute to the Nuclear Data Bank for both fundamental science and applications.

Concerning (γ,n) reactions on Hg, Eu, Cd, Ce, Se and Pd isotopes in the GDR region, we have identified seven isomeric pairs $^{195m,g;197m,g}Hg$, $^{152m1,m2}Eu$, $^{115m,g}Cd$, $^{137m,g}Ce$, $^{81m,g}Se$ and $^{109m,g}Pd$ and measured their IRs. In which, the data of $^{197m,g}Hg$ from 18 to 24 Mev, $^{195m,g}Hg$ from 14 to 24 MeV and $^{152m1,m2}Eu$ for 19, 21 and 23 Mev have been reported for the first time. For (n,γ) reactions on Pd, Cd, Ce and Se isotopes induced by thermal and resonant neutrons, we have recognized six isomer pairs including $^{109m,g;111m,g}Pd$, $^{115m,g;117m,g}Cd$, $^{137m,g}Ce$ and $^{81m,g}Se$ and then determined their IRs. It is worth noting that the results of $^{115m,g;117m,g}Cd$ and $^{109m,g;111m,g}Pd$ irradiated by mixed thermal-resonant neutrons as well as $^{111m,g}Pd$ induced by resonant neutrons are the first measurements. As the most remarkable results of this work, we have devoted the new experimental data of $^{nat}Eu(\gamma, n)^{152m1,m2}Eu$, $^{nat}Hg(\gamma, n)^{195m,g;197m,g}Hg$, $^{nat}Pd(n, \gamma)^{109m,g}Pd$, and $^{nat}Cd(n, \gamma)^{115m,g;117m,g}Cd$. Until now, the IR data of $^{195m,g;197m,g}Hg$, $^{109m,g;111m,g}Pd$, and $^{115m,g;117m,g}Cd$ have

been accepted to Experimental Nuclear Reaction Data Library (EXFOR) of the International Atomic Energy Agency (IAEA). One can access the link (https://www-nds.iaea.org/exfor/) to search for the data.

Our group has been surveying several effects influencing experimental IRs in the photonuclear and neutron-induced reactions for many years. As a continuation of our previous research, this work has selected the different incident energies on the nuclei in a wide range of atomic numbers with the typical nuclear structure, including spherical even-even nuclei $^{138,140}Ce$ (Z = 58) and $^{196,198}Hg$ (Z = 80), spherical-vibrational even-even nuclei $^{74,82}Se$ (Z = 34) and ^{110}Pd (Z = 46), quasi-spherical odd-even nucleus ^{151}Eu (Z = 63) and deformed odd-even nucleus ^{153}Eu. The results of this work provided more information to verify and give unambiguous answers about some effects involved. The first effect was the excitation energy one in (γ, n) reactions in the GDR region, meaning the higher the excitation energy the higher IR. This effect was confirmed by the IR enhancement as the excitation energy increased in the cases of $^{195m,g;197m,g}Hg$ and $^{152m1,m2}Eu$, owing to the growth of the angular momentum of the compound nucleus. The second effect was the nucleon configuration effect, which was observed by the higher the mass number of Hg isotopes, the lower the IR in (γ, n) reaction. The third effect was the large spin difference leading to the very low IR, illustrated in the case of the isomeric pair $^{152m1}Eu(8^-)$ and $^{152m2}Eu(0^-)$. The fourth effect was the reaction channel effect, which caused the IRs of the identical isomeric pair produced in various reactions with the same excitation energy to be different. We have gained a deeper insight into this effect by the study of IRs of the $^{137m,g}Ce$, $^{81m,g}Se$, $^{115m,g}Cd$ and $^{109m,g}Pd$ isomeric pairs in the inverse (γ, n) and (n, γ) reactions with the same product excitation energy to elucidate the influence of intake impulses and angular momentum transfer, being the part of the channel effect. It led to the conclusion that the higher the intake impulses and momentum transfer, the higher the IR values.

To compare the measured IRs of isomeric pairs of Se, Pd, Ce, Eu and Hg nuclei in (γ, n) reactions, we have computed the IRs in the energy range of 10 to 25 MeV by using the TALYS 1.95 statistical nuclear model code and GEANT4 toolkit. The GEANT4 simulated the bremsstrahlung spectrum while the TALYS code calculated the reaction cross-section. We tested the energy-dependent cross-section with six level density models in conjunction with eight γ-strength functions and achieved consistency in the theoretical predictions with the experimental results. The TALYS-based calculation also led to the consequence that the compound mechanism was predominant

in the investigated photonuclear reactions. In addition, the deformed shape of ^{153}Eu nucleus was justified by the display of two resonance peaks in the energy-dependent reaction cross-section curve. The IRs calculated using the six level density models demonstrated a similar shape to the experimental results. In many cases, the theoretical predictions were in good agreement with the experimental data. The information relative to model calculation as the discrete level, level density parameter, spin cut-off, optical model parameters, gamma strength function, and transmission coefficient was entirely in the output file. Theoretical results, moreover, showed the nucleon configuration effect on Hg isotopes without on Se and Ce isotopes. Therefore, one need to make detailed corrections referring to the level density models, the gamma strength function models and other parameters.

Overall, this study dedicated the first-ever outcomes exclusively or contributed additional data to the nuclear data reservoir. The consideration of four effects resulted in more systematic and reliable IRs. Additionally, the current experimental IRs can be employed as precious data for examining nuclear reaction models. The theoretical IR calculations for photonuclear reactions illuminated by bremsstrahlung were performed using the TALYS 1.95 code in combination with the GEANT4 toolkit. From comparison of experimental data and calculated results, the best-fitted model could be ascertained and then valuable information on nuclear level structure, level density, reaction mechanisms, involved effects and other properties could be extracted. The shortcomings of the inexactly described nuclear models need to improve and correct. Further research on this subject is necessary.

The scope of this thesis is the study of IR in (γ, n) reaction with bremsstrahlung endpoint energy in the GDR region and (n, γ) reaction induced by thermal and epithermal neutrons. However, it is well-known that the study of isomers and IR is of particular interest in various types of nuclear reactions. At present, a number of individual discrepancies are existing among the experimental data. Thus, more measurements with higher accuracy are indispensable. To proceed this work, we plan to study the IR in photonuclear and neutron-induced reactions on a large number of nuclei ranging from light to heavy ones, especially for deformed nuclei with unusual properties and types of isomers. In addition, the bremsstrahlung and neutron spectra arising from electron accelerators and other sources with different kinds and thicknesses of materials will be computed. Furthermore, since the current TALYS version is only applicable for projectiles with energy from 1 keV to 200 MeV, it has not yet solved the reactions irradiated

by thermal and resonance neutrons (<300 eV). Hence, we will attempt to resolve this issue in future studies.

List of Publications used for the Thesis content

1. **Bui Minh Hue**, Tran Duc Thiep, Truong Thi An, Phan Viet Cuong, S. M. Lukyanov, and S. Mitrofanov . *Isomeric ratios in neutron capture reaction, induced by thermal, resonant and mixed thermal-resonant neutrons on* ^{114}Cd *and* ^{116}Cd *nuclei*. Nuclear Inst. and Methods in Physics Research, B 502, pp. 46-53 (2021).

2. **Bui Minh Hue**, Tran Duc Thiep, Truong Thi An, Phan Viet Cuong, S. M. Lukyanov, A. G. Belov, and S. Mitrofanov. *The isomeric ratios in (n, γ) neutron capture reactions on* ^{108}Pd *and* ^{110}Pd *nuclei*, Journal of Radioanalytical and Nuclear Chemistry 326, no. 1, 503-509 (2020).

3. Tran Duc Thiep, Truong Thi An, Phan Viet Cuong, **Bui Minh Hue**, A. G. Belov, S. Mitrofanov. *Isomeric yield ratios of* $^{195m,g}Hg$ *and* $^{197m,g}Hg$ *in the* $^{196}Hg(\gamma, n)$ *and* $^{198}Hg(\gamma, n)$ *reactions induced by bremsstrahlung energy within giant dipole resonance region*, Nuclear Inst. and Methods in Physics Research, B. 457, 4-9 (2019).

4. Tran Duc Thiep, Truong Thi An, Phan Viet Cuong, Nguyen The vinh, **Bui Minh Hue**, Le Tuan Anh, A. G. Belov. *Isomeric yield ratio of* $^{152m1}Eu(8\text{-})$ *to* $^{152m2}Eu(0\text{-})$ *produced from* ^{153}Eu (γ, n) ^{152}Eu *reaction in the giant dipole resonance region*, J. Radioanal. Nucl. Chem., 317, 1263–1271 (2018).

5. **Bui Minh Hue**, Tran Duc Thiep. *Theoretical consideration of isomeric ratios in some photonuclear reactions induced by bremsstrahlung with endpoint energy in giant dipole resonance region using Talys 1.95 code*, Nuclear Science and Technology, Vol.12, No. 1, pp. 21-31 (2022).

6. Tran Duc Thiep, Truong Thi An, **Bui Minh Hue**, Phan Viet Cuong, Nguyen Hong Ha, A. G. Belov, S. Mitrofanov. *Investigation of the same isomeric pair,*

produced from different nuclear reactions, Nuclear Science and Technology, Vol.10, No. 1, pp. 01-10 (2020).

7. Tran Duc Thiep, Truong Thi An, **Bui Minh Hue**, Phan Viet Cuong, A. G. Belov, S. Mitrofanov. *The nuclear channel effect in the isomeric ratio of the reaction products*, Nuclear Science and Technology, Vol.9, No. 1, pp. 09-20 (2019).

8. **Bui Minh Hue**, Tran Duc Thiep, *Isomeric Ratios in Several Inverse (γ, n) and (n, γ) Reactions*, Proceedings of 28th International Seminar on Interaction of Neutrons with Nuclei, http://isinn.jinr.ru/proceedings/isinn-28/pdf/HueBui.pdf, (2021).

9. **Bui Minh Hue**, Tran Duc Thiep, *Isomeric Ratios in Inverse (γ, n) and (n, γ) Reactions on Ce, Cd, Pd and Se targets*, Proceedings of the 7th Academic Conference on Natural Science for Young Scientist, Master and PhD. Student from ASEAN Countries (CASEAN-7), p388-396 (2021).

Other publication

1. P.V. Cuong, T.D. Thiep, L.T. Anh, T.T. An, **B.M. Hue**, K.T. Thanh, N.H. Tan, N.T. Vinh, T.T. Anh, *Theoretical calculation by Talys code in combination with Geant4 simulation for consideration of (γ, n) reactions of Eu isotopes in the giant dipole resonance region*, Nuclear Inst. and Methods in Physics Research B, 479 (2020) 68-73.

References

[1] Frederick Soddy. "A Chemical Sign of Life. By S. Tashiro. Pp. ix+ 142.(Chicago: University of Chicago Press; Lon-don: Cambridge University Press.) r doJlar, or 4s. net. Manuals of Health. 1., Food. By Dr. A. Hill." (1917).

[2] Otto Hahn. "Über eine neue radioaktive Substanz im Uran". *Berichte der deutschen chemischen Gesellschaft (A and B Series)* 54.6 (1921), pp. 1131–1142.

[3] CF v. Weizsäcker. "Metastabile Zustände der Atomkerne". *Naturwissenschaften* 24.51 (1936), pp. 813–814.

[4] A Bohr and B Mottelson. *Mat. Fys. Medd. Dan. Vid. Selsk.* 1953.

[5] Ashok Kumar Jain, Bhoomika Maheshwari, and Alpana Goel. *Nuclear Isomers: A Primer*. Springer Nature, 2021.

[6] JM Blatt and VF Weisskopf. *Theoretical nuclear physics. New York: John Wiley and Sons*. 1952.

[7] LW Nordheim. "β-decay and the nuclear shell model". *Physical Review* 78.3 (1950), p. 294.

[8] M. H. Brennan and A. M. Bernstein. "jj Coupling Model in Odd-Odd Nuclei". *Phys. Rev.* 120.3 (1960), pp. 927–933.

[9] GD Dracoulis, PM Walker, and FG Kondev. "Review of metastable states in heavy nuclei". *Reports on Progress in Physics* 79.7 (2016), p. 076301.

[10] Philip Walker and George Dracoulis. "Energy traps in atomic nuclei". *Nature* 399.6731 (1999), pp. 35–40.

[11] MR Bhat. "Evaluated nuclear structure data file (ENSDF)". *Nuclear data for science and technology*. Springer. 1992, pp. 817–821.

[12] Georges Audi et al. "The NUBASE evaluation of nuclear and decay properties". *Nuclear physics A* 729.1 (2003), pp. 3–128.

[13] FG Kondev et al. "The NUBASE2020 evaluation of nuclear physics properties". *Chinese Physics C* 45.3 (2021), p. 030001.

[14] Ashok Kumar Jain et al. “Atlas of nuclear isomers”. *Nuclear Data Sheets* 128 (2015), pp. 1–130.

[15] R. Lic ă et al. “Identification of the crossing point at $N = 21$ between normal and intruder configurations”. *Phys. Rev. C* 95.2 (2017), p. 021301.

[16] R. D. Page et al. “Radioactivity of neutron deficient isotopes in the region N>82>Z”. *Phys. Rev. C* 53.2 (Feb. 1996), pp. 660–670.

[17] M Karny et al. “Shell structure beyond the proton drip line studied via proton emission from deformed 141Ho”. *Physics Letters B* 664.1-2 (2008), pp. 52–56.

[18] B. S. Nara Singh et al. “Influence of the *np* interaction on the β decay of ^{94}Pd”. *Phys. Rev. C* 86.4 (Oct. 2012), p. 041301.

[19] I. Mukha et al. “β-delayed proton decay of a high-spin isomer in ^{94}Ag”. *Phys. Rev. C* 70.4 (Oct. 2004), p. 044311.

[20] J. Park et al. “New and comprehensive β- and βp-decay spectroscopy results in the vicinity of ^{100}Sn”. *Phys. Rev. C* 99.3 (Mar. 2019), p. 034313.

[21] A. Lepailleur et al. “Spectroscopy of ^{26}**F** to Probe Proton-Neutron Forces Close to the Drip Line”. *Phys. Rev. Lett.* 110.8 (Feb. 2013), p. 082502.

[22] D Kolev, Duc Thiep Tran, and V Todorov. “Experimental determination of the isomeric yield ratios of 117mg In and 120mg Sb in photonuclear reactions”. *Comptes Rendus de l’Academie Bulgare des Sciences* 47.12 (1994), pp. 49–52.

[23] Tran Duc Thiep et al. “Isomeric yield ratio of 152m1Eu (8-)–152m2Eu (0-) produced in (γ, n) photonuclear reaction in the giant dipole resonance region”. *Journal of Radioanalytical and Nuclear Chemistry* 317.3 (2018), pp. 1263–1271.

[24] SA Karamian et al. “Isomeric to ground state ratio in the 180 Ta m (γ, γ) 180 Ta m, g reaction”. *Physical Review C* 57.4 (1998), p. 1812.

[25] Nguyen Van Do et al. “Measurement of yield ratios for the isomeric pair 137m, gCe in the 141Pr (γ, x) 137m, gCe reactions with bremsstrahlung end-point energies of 50-, 60-, and 70-MeV”. *Radiation Physics and Chemistry* 176 (2020), p. 109016.

[26] Muhammad Nadeem et al. “Measurements of natCd (γ, x) reaction cross sections and isomer ratio of 115m, gCd with the bremsstrahlung end-point energies of 50 and 60 MeV”. *Chinese Physics C* 45.12 (2021), p. 124002.

[27] S Sudar and SM Qaim. "Isomeric cross-section ratio for the formation of Co m, g 58 in neutron, proton, deuteron, and alpha-particle induced reactions in the energy region up to 25 MeV". *Physical Review C* 53.6 (1996), p. 2885.

[28] Alita SERGEY Danagulyan et al. "Investigation of isomeric ratios in high-energy reactions". *Physics of Atomic Nuclei* 76.3 (2013), pp. 349–354.

[29] K Hilgers, S Sudár, and SM Qaim. "Formation of the isomeric pairs Nd 139 m, g and Nd 141 m, g in proton and He 3-particle-induced nuclear reactions". *Physical Review C* 76.6 (2007), p. 064601.

[30] Avinash Agarwal, IA Rizvi, and AK Chaubey. "Excitation function studies of α induced reactions for niobium and preequilibrium effects". *Physical Review C* 65.3 (2002), p. 034605.

[31] Jean-Michel Daugas et al. "Interplay between angular momentum transfer and nuclear structure in the production of isomers at intermediate energies". *Physical Review C* 63.6 (2001), p. 064609.

[32] V. H. Phong et al. "Observation of a μs isomer in $^{134}_{49}\mathrm{In}_{85}$: Proton-neutron coupling "southeast" of $^{132}_{50}\mathrm{Sn}_{82}$". *Phys. Rev. C* 100.1 (July 2019), p. 011302.

[33] Tran Duc Thiep et al. "The isomeric ratio of fragment 135Xe from photofission of 233U induced by 23.5 MeV bremsstrahlung". *Journal of radioanalytical and nuclear chemistry* 285.3 (2010), pp. 511–517.

[34] TD Thiep et al. "Study of isomeric ratios in the photonuclear reactions 121Sb (γ, n) 120m,gSb; 123Sb (γ, n) 122m,gSb and 86Sr (γ, n) 85m,gSr induced by bremsstrahlung in the energy range 15–20 MeV". *Commun. Phys.* 4.3 (1994), pp. 97–102.

[35] Tran Thiep et al. "Study of the isomeric ratios in photonuclear reactions of natural Selenium induced by bremsstrahlungs with end-point energies in the giant dipole resonance region". *Journal of Radioanalytical and Nuclear Chemistry* 292.3 (2012), pp. 1035–1042.

[36] Tran Thiep et al. "The isomeric ratios in photonuclear reactions of natural barium induced by bremsstrahlungs with endpoint energies in the giant dipole resonance region". *Journal of Radioanalytical and Nuclear Chemistry* 292.1 (2012), pp. 89–96.

[37] Tran Duc Thiep et al. “Study of the isomeric ratios in 107 Ag (γ, n) 106m, g Ag reaction of natural silver induced by bremsstrahlungs with endpoint energies in the giant dipole resonance region”. *Journal of Radioanalytical and Nuclear Chemistry* 299.1 (2014), pp. 477–484.

[38] Tran Duc Thiep et al. “On the role of energy separated in fission process, excitation energy and reaction channels effects in the isomeric ratios of fission product 135 Xe in photofission of actinide elements”. *Physics of Particles and Nuclei Letters* 13.4 (2016), pp. 471–479.

[39] N. N. Tsoneva et al. “Population of isomers in the decay of the giant dipole resonance”. *Phys. Rev. C* 61.4 (2000), p. 044303.

[40] Dimitar Kolev. “Studies of some isomeric yield ratios produced with bremsstrahlung”. *Applied radiation and isotopes* 49.8 (1998), pp. 989–995.

[41] TD Thiep et al. “The isomeric ratios in some photonuclear reactions (γ, n),(γ, p),(γ, 2n) and (γ, np) induced by Bremsstrahlung with end-point energies in the giant dipole resonance region”. *Phys Part Nucl Lett* 6.2 (2009), pp. 209–218.

[42] CD Nesaraja, S Sudár, and SM Qaim. “Cross sections for the formation of 69 Zn m, g and 71 Zn m, g in neutron induced reactions near their thresholds: Effect of reaction channel on the isomeric cross-section ratio”. *Physical Review C* 68.2 (2003), p. 024603.

[43] Tran Duc Thiep et al. “Nuclear reactions with 14 MeV neutrons and bremsstrahlungs in giant dipole resonance (GDR) region using small accelerators”. *Nuclear Physics A* 722 (2003), pp. C568–C572.

[44] F Cserpak et al. “Excitation functions and isomeric ratios of the 63Cu (n, α) 60m, gCo, 65Cu (n, α) 60m, gCo and 60Ni (n, p) 60m, gCo processes from 6 to 15 MeV”. *Phys Rev C* 49.3 (1994), pp. 1525–1533.

[45] Syed M Qaim, S Sudar, and A Fessler. “Influence of reaction channel on the isomeric cross-section ratio”. *Radiochimica acta* 93.9-10 (2005), pp. 503–506.

[46] SM Qaim, A Mushtaq, and M Uhl. “Isomeric cross-section ratio for the formation of 73 m, gSe in various nuclear processes”. *Physical Review C* 38.2 (1988), p. 645.

[47] B Strohmaier, M Fassbender, and SM Qaim. “Production cross sections of ground and isomeric states in the reaction systems 93 N b+ 3 He, 92 Mo+ α, and 9 4, 9 5 Mo+ p”. *Physical Review C* 56.5 (1997), p. 2654.

[48] Tran Duc Thiep et al. "Experimental study and theoretical consideration of the isomeric ratio in the photonuclear reaction 197Au (γ, n) 196m,gAu in the giant dipole resonance region". *Physics of Particles and Nuclei Letters* 3.4 (2006), pp. 223–228.

[49] M Huber et al. "Structure of intermediate states in the photoexcitation of the 89Y isomer". *Nuclear Physics A* 559.2 (1993), pp. 253–265.

[50] J. J. Carroll et al. "Intermediate structure in the photoexcitation of ^{77}Se^{m}, ^{79}Br^{m}, and ^{137}Ba^{m}". *Phys. Rev. C* 48.5 (Nov. 1993), pp. 2238–2245.

[51] Tran Duc Thiep et al. "The study of isomeric ratios in photonuclear reactions forming high spin isomers in the giant dipole resonance region". *Communications in Physics* 24.4 (2014), pp. 381–389.

[52] Walter Hauser and Herman Feshbach. "The inelastic scattering of neutrons". *Physical review* 87.2 (1952), p. 366.

[53] Niels Bohr. "Neutron capture and nuclear constitution". *Nature* 137.3461 (1936), pp. 344–348.

[54] Arjan J Koning, Stephane Hilaire, and Marieke C Duijvestijn. "TALYS: Comprehensive nuclear reaction modeling". *AIP Conference Proceedings*. Vol. 769. 1. American Institute of Physics. 2005, pp. 1154–1159.

[55] R Vandenbosch and JR Huizenga. "Isomeric Cross-Section Ratios for Reactions Producing the Isomeric Pair Hg197, 197m". *Physical Review* 120.4 (1960), p. 1313.

[56] JR Huizenga and Rt Vandenbosch. "Interpretation of isomeric cross-section ratios for (n, γ) and (γ, n) reactions". *Physical Review* 120.4 (1960), p. 1305.

[57] Yu P Gangrsky et al. "Isomeric Ratios in Crossing (ngamma) and (gamman) Reactions". *Bulletin of the Russian Academy of Sciences: Physics* 65.1 (2001), pp. 121–127.

[58] D Kolev and D Bratovanov. "Interpretation of isomeric ratios obtained in photonuclear reactions". *Comptes Rendus de l'Academie Bulgare des Sciences* 48.7 (1995), pp. 39–42.

[59] AJ Koning, Stephan Hilaire, and M Duijvestijn. "TALYS-1.95 A nuclear reaction program, User manual". *NRG, Netherlands* (2009).

[60] AS Danagulyan et al. “Special features of isomeric ratios in nuclear reactions induced by various projectile particles”. *Physics of Atomic Nuclei* 79.3 (2016), pp. 326–334.

[61] Junhua Luo, Suyuan Li, and Li Jiang. “Activation cross section and isomeric cross-section ratio for the 151Eu (n, 2n) 150m, gEu process”. *Radiation Physics and Chemistry* 148 (2018), pp. 43–49.

[62] Junhua Luo et al. “Activation cross section and isomeric cross-section ratio for the (n, 2n) reaction on 132,134 Ba”. *Radiochimica Acta* 105.10 (2017), pp. 779–787.

[63] Satimbay Palvanov and Turgunali Akhmadzhanov. “Investigation of isomer ratios in the reactions (γ, n) and (n, 2n) on nuclei 76Ge and 82Se”. *Bulletin of National University of Uzbekistan: Mathematics and Natural Sciences* 2.4 (2019), pp. 246–256.

[64] SR Palvanov et al. “Excitation of isomeric states in reactions (γ, n) and (n, 2n) on 110Pd nucleus”. *World J Res Rev (WJRR)* 5.5 (2017), pp. 28–31.

[65] VM Mazur et al. “Excitation of the 119 Te m, 121 Te m, 123 Te m, 127 Te m, and 129 Te m isomers in (γ, n) reactions from 10 to 22 MeV”. *Physical Review C* 87.4 (2013), p. 044604.

[66] AS Danagulyan et al. “Photonuclear reactions on 112,118,124 Sn, natTe, and natHf targets”. *Physics of Atomic Nuclei* 77.11 (2014), pp. 1313–1320.

[67] Rajnikant Makwana et al. “New empirical formula for (γ, n) reaction cross section near GDR peak for elements with Z$\leq$60.” *Chinese Physics C* 41.4 (2017), p. 044105.

[68] Md Shakilur Rahman et al. “Photonuclear Studies for the Isomeric Yield Ratios in the Production of natFe (γ, xnp) 52m, gMn with 50-, 60-, and 70-MeV Bremsstrahlung”. *EPJ Web of Conferences*. Vol. 106. EDP Sciences. 2016, p. 04008.

[69] Haladhara Naik et al. “Measurement of flux-weighted average cross sections for 197Au (γ, xn) reactions and isomeric yield ratios of 196m, gAu with bremsstrahlung”. *Nuclear Physics A* 948 (2016), pp. 28–45.

[70] O. M. Vodin et al. “Isomer Ratios in Photonuclear Reactions With Multiple Neutron Emission”. *Prob. Atomic Sci. Technol.* 2019.3 (2019), pp. 38–46.

[71] Sea Agostinelli et al. "GEANT4—a simulation toolkit". *Nuclear instruments and methods in physics research section A: Accelerators, Spectrometers, Detectors and Associated Equipment* 506.3 (2003), pp. 250–303.

[72] R.Arthur Forster et al. "MCNP™ Version 5". *Nuclear Instruments and Methods in Physics Research Section B: Beam Interactions with Materials and Atoms* 213 (2004). 5th Topical Meeting on Industrial Radiation and Radioisotope Measurement Applications, pp. 82–86. ISSN: 0168-583X.

[73] Giuseppe Battistoni et al. "Overview of the FLUKA code". *Annals of Nuclear Energy* 82 (2015), pp. 10–18.

[74] Phan Viet Cuong et al. "Theoretical calculation by Talys code in combination with Geant4 simulation for consideration of γ, n reactions of Eu isotopes in the giant dipole resonance region". *Nuclear Instruments and Methods in Physics Research Section B: Beam Interactions with Materials and Atoms* 479 (2020), pp. 68–73.

[75] AR Junghans et al. "Photon data shed new light upon the GDR spreading width in heavy nuclei". *Physics Letters B* 670.3 (2008), pp. 200–204.

[76] A Zilges et al. "Photonuclear reactions—From basic research to applications". *Progress in Particle and Nuclear Physics* 122 (2022), p. 103903.

[77] James Chadwick and Maurice Goldhaber. "A 'Nuclear Photo-effect': Disintegration of the Diplon by γ-Rays". *Nature* 134.3381 (1934), pp. 237–238.

[78] W Bothe and W Gentner. "Atomumwandlungen durchγ-strahlen". *Zeitschrift für Physik* 106.3 (1937), pp. 236–248.

[79] GC Baldwin and GS Klaiber. "Photo-fission in heavy elements". *Physical Review* 71.1 (1947), p. 3.

[80] *Gordon research conference on photonuclear physics*. https://www.grc.org/photonuclear-reactions-conference/1959/. 1959.

[81] Ryoichi Hajima. "Status and perspectives of compton sources". *Physics Procedia* 84 (2016), pp. 35–39.

[82] Josef Speth and Adriaan van der Woude. "Giant resonances in nuclei". *Reports on Progress in Physics* 44.7 (1981), p. 719.

[83] A Van der Woude. "GIANT-RESONANCES". English. *Progress in Particle and Nuclear Physics* 18 (1987), pp. 217–293. ISSN: 0146-6410.

[84] A.B. Migdal. “Quantum collective excitation modes in nuclear physics”. *J.Phys. (USSR)* 8 (1994), p. 331.

[85] JS Levinger and HA Bethe. “Dipole transitions in the nuclear photo-effect”. *Physical Review* 78.2 (1950), p. 115.

[86] BM Spicer. “The giant dipole resonance”. *Advances in nuclear physics*. Springer, 1969, pp. 1–78.

[87] M Goldhaber and E Teller. “On nuclear dipole vibrations”. *Physical Review* 74.9 (1948), p. 1046.

[88] Helmut Steinwedel, J Hans D Jensen, and Peter Jensen. “Nuclear dipole vibrations”. *Physical Review* 79.6 (1950), p. 1019.

[89] PB Moon. “The hard components of scattered gamma-rays”. *Proceedings of the Physical Society. Section A* 63.11 (1950), p. 1189.

[90] Yasuyuki Suzuki, Kiyomi Ikeda, and Hiroshi Sato. “New type of dipole vibration in nuclei”. *Progress of Theoretical Physics* 83.2 (1990), pp. 180–184.

[91] S Krewald and J Speth. “Pygmy dipole resonances”. *International Journal of Modern Physics E* 18.07 (2009), pp. 1425–1451.

[92] Thomas Aumann. “Low-energy dipole response of exotic nuclei”. *The European Physical Journal A* 55.12 (2019), pp. 1–14.

[93] Kris Heyde, Peter von Neumann-Cosel, and Achim Richter. “Magnetic dipole excitations in nuclei: Elementary modes of nucleonic motion”. *Reviews of Modern Physics* 82.3 (2010), p. 2365.

[94] D Frekers et al. “Spin excitations in the deformed nuclei 154Sm, 158Gd and 168Er”. *Physics Letters B* 244.2 (1990), pp. 178–182.

[95] AS Adekola et al. “Discovery of low-lying E 1 and M 1 strengths in Th 232”. *Physical Review C* 83.3 (2011), p. 034615.

[96] M Guttormsen et al. “Scissors resonance in the quasicontinuum of Th, Pa, and U isotopes”. *Physical Review C* 89.1 (2014), p. 014302.

[97] Josef Speth. *Electric and magnetic giant resonances in nuclei*. Vol. 7. World Scientific, 1991.

[98] MB Chadwick et al. “Pauli-blocking in the quasideuteron model of photoabsorption”. *Physical Review C* 44.2 (1991), p. 814.

[99] David O Hunt, Ari Brynjolfsson, and Raymond D Cooper. *Handbook of photonuclear reactions*. Tech. rep. ARMY NATICK LABS MA NATICK United States, 1963.

[100] James Chadwick. "Possible existence of a neutron". *Nature* 129.3252 (1932), pp. 312–312.

[101] *Neutron energy*. https://www.nuclear-power.com/nuclear-power/reactor-physics/atomic-nuclear-physics/fundamental-particles/neutron/neutron-energy/.

[102] Kenneth S Krane. *Introductory nuclear physics*. John Wiley & Sons, 1991.

[103] JJ Schmidt and A Lorenz. "The IAEA nuclear data programme its role in the nuclear community and its services to developing countries" (1980).

[104] Nguyen Van Do et al. "Thermal neutron cross-section and resonance integral of the 186 W (n, γ) 187 W reaction". *Nuclear Instruments and Methods in Physics Research B* 266.6 (2008), pp. 863–871.

[105] Nguyen Thi Hien et al. "Measurements of the thermal neutron cross-section and resonance integral for the 108Pd (n, γ) 109Pd reaction". *Nuclear Instruments and Methods in Physics Research Section B: Beam Interactions with Materials and Atoms* 424 (2018), pp. 37–42.

[106] M. Guttormsen et al. "Experimental level densities of atomic nuclei". *Eur. Phys. J. A* 51.12 (2015), p. 170.

[107] H. A. Bethe. "An Attempt to Calculate the Number of Energy Levels of a Heavy Nucleus". *Phys. Rev.* 50.4 (1936), pp. 332–341.

[108] Torleif Ericson. "The statistical model and nuclear level densities". *Advances in Physics* 9.36 (1960), pp. 425–511.

[109] Till von Egidy and Dorel Bucurescu. "Systematics of nuclear level density parameters". *Phys. Rev. C* 72.4 (2005), p. 044311.

[110] T. von Egidy and D. Bucurescu. "Experimental energy-dependent nuclear spin distributions". *Phys. Rev. C* 80.5 (2009), p. 054310.

[111] W Dilg et al. "Level density parameters for the back-shifted fermi gas model in the mass range 40< A< 250". *Nuclear Physics A* 217.2 (1973), pp. 269–298.

[112] A Gilbert and AGW Cameron. "A composite nuclear-level density formula with shell corrections". *Canadian Journal of Physics* 43.8 (1965), pp. 1446–1496.

[113] G A Bartholomew. "Neutron Capture Gamma Rays". *Annual Review of Nuclear Science* 11.1 (1961), pp. 259–302.

[114] R. Capote et al. "RIPL – Reference Input Parameter Library for Calculation of Nuclear Reactions and Nuclear Data Evaluations". *Nuclear Data Sheets* 110.12 (2009). Special Issue on Nuclear Reaction Data, pp. 3107–3214. ISSN: 0090-3752.

[115] J. Kopecky and M. Uhl. "Test of gamma-ray strength functions in nuclear reaction model calculations". *Phys. Rev. C* 41.5 (1990), pp. 1941–1955.

[116] J. Kopecky, M. Uhl, and R. E. Chrien. "Radiative strength in the compound nucleus ^{157}Gd". *Phys. Rev. C* 47.1 (1993), pp. 312–322.

[117] Nguyen Van Do. "Cac phuong phap phan tich hat nhan". *Nha xuat ban Dai hoc Quoc gia Hanoi* (2004).

[118] OD Maslov and SN Dmitriev. "Use of MT-25 microtron for scientific and applied investigations" (2003).

[119] Tran Duc Thiep. "May gia toc". *NXB Khoa hoc va Ky thuat* (2002).

[120] AG Belov et al. "Microtron MT-25 and its Areas of Use". *Workshop on Application of Microtron in Nuclear Physics* 26.4 (1993), pp. 20–25.

[121] N Sodnom et al. *A project of the laboratory of activation analysis on the basis of microtron of MPR*. Tech. rep. Joint Inst. for Nuclear Research, 1989.

[122] *Wikipedia*. https://www.wikipedia.org.

[123] AP Tonchev et al. "Deformation on isomeric excitation of Eu isotopes in (γ, n) and (n, γ) reactions". *Physical Review C* 58.5 (1998), p. 2851.

[124] Bui Minh Hue. "Master Thesis". *Hanoi University of Science* (2013).

[125] Klaus Debertin and Richard G Helmer. *Gamma-and X-ray spectrometry with semiconductor detectors*. North Holland, 1988. ISBN: 0444871071.

[126] *NIST: X-Ray Mass Attenuation Coefficients - Table 3*. 2019. URL: http://www.nist.gov/pml/x-ray-mass-attenuation-coefficients.

[127] D Montgomery and G Montgomery. "A method for assessing and correcting coincidence summing effects for germanium detector efficiency calibrations". *Journal of Radioanalytical and Nuclear Chemistry* 193.1 (1995), pp. 71–79.

[128] Rene Brun and Fons Rademakers. "ROOT—An object oriented data analysis framework". *Nuclear instruments and methods in physics research section A: accelerators, spectrometers, detectors and associated equipment* 389.1-2 (1997), pp. 81–86.

[129] Tran Duc Thiep et al. "Isomeric yield ratios of 195m, gHg and 197m, gHg in the 196Hg (γ, n) and 198Hg (γ, n) reactions induced by bremsstrahlung energy within giant dipole resonance region". *Nuclear Instruments and Methods in Physics Research Section B: Beam Interactions with Materials and Atoms* 457 (2019), pp. 4–9.

[130] Bui Minh Hue et al. "The isomeric ratios in (n, γ) neutron capture reactions on 108 Pd and 110 Pd nuclei". *Journal of Radioanalytical and Nuclear Chemistry* 326.1 (2020), pp. 503–509.

[131] Bui Minh Hue et al. "Isomeric ratios in neutron capture reaction, induced by thermal, resonant and mixed thermal-resonant neutrons on 114Cd and 116Cd nuclei". *Nuclear Instruments and Methods in Physics Research Section B: Beam Interactions with Materials and Atoms* 502 (2021), pp. 46–53.

[132] Tran Duc Thiep et al. "Investigation of the same isomeric pair, produced from different nuclear reactions". *Nuclear Science and Technology* 10.1 (2020), pp. 1–10.

[133] Tran Duc Thiep et al. "The nuclear channel effect in the isomeric ratio of the reaction products". *Nuclear Science and Technology* 9.1 (2019), pp. 9–20.

[134] Bui Minh Hue and Tran Duc Thiep. "Isomeric ratios in several inverse (γ, n) and (n, γ) reactions". *Proceedings of the International Seminar on Interaction of Neutrons with Nuclei (ISINN-28)* (2021). URL: http://isinn.jinr.ru/proceedings/isinn-28/pdf/Hue_Bui.pdf.

[135] Bui Minh Hue and Tran Duc Thiep. "Isomeric ratios in inverse (γ, n) and (n, γ) reactions on Ce, Cd, Pd and Se targets". *Proceedings of the 7th Academic Conference on Natural Science for Young Scientist, Master and PhD. Student from ASEAN Countries (CASEAN-7)* 7 (2021), pp. 388–396.

[136] Bui Minh Hue and Tran Duc Thiep. "Theoretical consideration of isomeric ratios in some photonuclear reactions induced by bremsstrahlung with endpoint energy in giant dipole resonance region using Talys 1.95 code". *Nuclear Science and Technology* 12.1 (2022), pp. 21–31.

[137] IN Vishnevsky et al. “Isomeric yield ratios in nuclei Ir 190 and Eu 150, 152”. *Physical Review C* 79.1 (2009), p. 014615.

[138] Samuel S Dietrich and Barry L Berman. “Atlas of photoneutron cross sections obtained with monoenergetic photons”. *Atomic Data and Nuclear Data Tables* 38.2 (1988), pp. 199–338.

[139] AV Varlamov et al. “Atlas of giant dipole resonances”. *Parameters and Graphs of Photonuclear Reaction Cross Sections. INDC (NDS)-394, IAEA NDS, Vienna, Austria* (1999), pp. 1–311.

[140] *NuDat3.0 - National Nuclear Data Center, Brookhaven National Laboratory.* URL: https://www.nndc.bnl.gov/nudat3/.

[141] IN Vishnevsky et al. “Excitation of isomeric states in the (γ, n) reactions on the transition nuclei 152 Eu and 184 Re”. *Physics of Atomic Nuclei* 62.5 (1999), pp. 880–885.

[142] Tran Duc Thiep et al. “Study of the isomeric ratios in photonuclear reactions of natural platinum induced by end-point bremsstrahlung energies in the giant dipole resonance region”. *Journal of Radioanalytical and Nuclear Chemistry* 303.3 (2015), pp. 1857–1864.

[143] Yu P Gangrsky et al. “Isomeric ratios in reactions induced by gamma rays and fast neutrons in the isotopes of Re, Ir, and Au”. *Physics of Atomic Nuclei* 67.7 (2004), pp. 1227–1232.

[144] AG Belov et al. *Excitation of high spin isomers in photonuclear reactions.* Tech. rep. Joint Institute for Nuclear Research, 2004.

[145] Tran Duc Thiep et al. “Study on the isomeric ratios in (γ, p)-photonuclear reactions from targets Zr and W in the giant dipole resonance region”. *Communications in Physics* 16.3 (2006), pp. 163–169.

[146] Tran Duc Thiep et al. “Channel effect in isomeric ratio of 137m, g Ce produced in different nuclear reactions”. *Journal of Radioanalytical and Nuclear Chemistry* 314.3 (2017), pp. 1777–1784.

[147] SM Qaim et al. *Handbook of spectroscopy.* CRC, Boca Raton, 1981.

[148] Junhua Luo, Li Jiang, and Suyuan Li. “Activation cross section and isomeric cross section ratios for the (n, 2n) reaction on Eu153”. *Physical Review C* 96.4 (2017), p. 044617.

[149] Tran Thiep et al. “Study of the isomeric ratio of fission product Xe produced in the photo-fission of Th and U induced by end-point bremsstrahlung energy of 13.5 MeV.” *Journal of Radioanalytical and Nuclear Chemistry* 303.1 (2015).

[150] H Naik et al. “Isomeric yield ratios of 87m, g Y from different nuclear reactions”. *The European Physical Journal A* 50.7 (2014), pp. 1–13.

[151] VA Zheltonozhsky, VM Mazur, and ZM Bigan. “Investigation of the excitation of metastable states of 197 Pt and 197 Hg in (γ, n) and (d, 2 n) reactions”. *Physics of Atomic Nuclei* 67.5 (2004), pp. 875–881.

[152] Yoshimi Kasugai et al. “Measurement of activation cross sections for mercury isotopes in the neutron energy range between 13.4 and 14.9 MeV”. *Journal of nuclear science and technology* 38.12 (2001), pp. 1048–1056.

[153] RS Tilbury and L Yaffe. “Nuclear isomers Hg197m, g, Hg195m, g and Au196m, g formed by bombardment of gold with protons of energies from 8 to 60 MeV”. *Canadian Journal of Chemistry* 41.10 (1963), pp. 2634–2641.

[154] VT Gritsyna et al. “Ratio of the cross sections for the production of the isomer and ground states of nuclei in the (p, n) reaction at the energies from the threshold to 20 MeV”. *Sov. Phys. JETP* 17 (1963), pp. 1186–1189.

[155] LF Hansen et al. “Ta181 (p, n) W181 and Au197 (p, n) Hg197 excitation functions between 4 and 13 MeV”. *Nuclear Physics* 30 (1962), pp. 389–398.

[156] M Al-Abyad et al. “Cross sections and isomeric cross-section ratios in the interactions of fast neutrons with isotopes of mercury”. *Physical Review C* 73.6 (2006), p. 064608.

[157] BS Ishkhanov, VN Orlin, and S Yu Troschiev. “Photonuclear reactions on mercury isotopes in the region of the giant-dipole-resonance energy”. *Physics of Atomic Nuclei* 74.5 (2011), pp. 706–713.

[158] BS Ishkhanov and S Yu Troshchiev. “Yields of photonuclear reactions on Hg isotopes under a bremsstrahlung beam with a maximum energy of 29.1 MeV”. *Bulletin of the Russian Academy of Sciences: Physics* 75.4 (2011), pp. 566–568.

[159] D De Frenne et al. “Independent isomeric yield ratios and primary angular momenta in the photofission of U 2 3 5, 2 3 8 with 12-30-MeV bremsstrahlung”. *Physical Review C* 29.5 (1984), p. 1777.

[160] Nguyen Van Do et al. "Isomeric yield ratios for the natSb (γ, xn) 120m, g, 122m, gSb reactions measured at 40-, 45-, 50-, 55-, and 60-MeV bremsstrahlung energies". *Nuclear Instruments and Methods in Physics Research Section B: Beam Interactions with Materials and Atoms* 283 (2012), pp. 40–45.

[161] Md Shakilur Rahman et al. "Measurement of flux-weighted average cross-sections and isomeric yield ratios for 103 Rh (g, xn) reactions in the bremsstrahlung end-point energies of 55 and 60 MeV". *The European Physical Journal A* 52.7 (2016), pp. 1–12.

[162] Pierre Marmier and Eric Sheldon. *Physics of Nuclei and Particles: Volume II*. Vol. 2. Academic Press, 2013.

[163] Toyoaki Kato and Yoshinaga Oka. "Yields of photonuclear reactions for photon-activation analysis with high-energy bremsstrahlung". *Talanta* 19.4 (1972), pp. 515–525.

[164] JH Carver, GE Coote, and TR Sherwood. "Isomeric (γ, n) cross section ratios and the spin dependence of the nuclear level density". *Nuclear Physics* 37 (1962), pp. 449–456.

[165] FMD Attar et al. "Cross-sections for the formation of isomeric pair 75Gem, g through (n, 2n),(n, p) and (n, α) reactions measured over 13.73 MeV to 14.77 MeV and calculated from near threshold to 20 MeV neutron energies". *Nuclear Physics A* 828.3-4 (2009), pp. 253–266.

[166] R Debuyst and A Vander Stricht. "Excitation functions and yield ratios for the isomeric pair 80Br 80mBr formed in (d, 2n),(α, np),(α, p) and (p, n) reactions on selenium". *Journal of Inorganic and Nuclear Chemistry* 30.3 (1968), pp. 691–698.

[167] CT Bishop, HK Vonach, and JR Huizenga. "Isomer ratios for some (n, γ) reactions". *Nuclear Physics* 60.2 (1964), pp. 241–249.

[168] ML Sehgal, HS Hans, and PS Gill. "Thermal neutron cross-sections for producing some isomers". *Nuclear Physics* 12.3 (1959), pp. 261–268.

[169] SK Mangal and PS Gill. "Thermal neutron activation cross-sections for isomer production". *Nuclear Physics* 36 (1962), pp. 542–548.

[170] MN Namboodiri et al. "Isomeric cross-section ratios in the (n, γ) reactions on 130Te and 110Pd". *Journal of Inorganic and Nuclear Chemistry* 28.1 (1966), pp. 1–4.

[171] Dac Luc Hoang et al. "Isomeric yield ratios in the productions of Sm 143m, g, Nd 141m, g, Zr 89m, g and Pd 109m, g by 14 MeV neutrons and 15-20.5 MeV bremsstrahlung". *Bulgarian Journal of Physics* 14.2 (1987), pp. 152–156.

[172] D Brune and JJ Schmidt. *Handbook on Nuclear Activation Cross-sections: Neutron, Photon and Charged-particle Nuclear Reaction Cross-section Data*. Vol. 156. International Atomic Energy Agency, 1974.

[173] Richard B Firestone and VS Shirley. *Table of isotopes, 8th edn, CD ROM edition, Version 1.0*. 1996.

[174] AM Goriachev and GL Zalesnyi. "Determination of parameters of the back-shift Fermi gas model from measurement of the average energy in photo-neutron spectra". *Bull USSR Acad Sci* 54.11 (1990), pp. 2240–2243.

[175] LI Schiff. "Energy-angle distribution of thin target bremsstrahlung". *Physical review* 83.2 (1951), p. 252.

[176] S Sudár and SM Qaim. "Cross sections for the formation of Hg 195 m, g, Hg 197 m, g, and Au 196 m, g in α and He 3-particle induced reactions on Pt: Effect of level density parameters on the calculated isomeric cross-section ratio". *Physical Review C* 73.3 (2006), p. 034613.

[177] SF Mughabghab. "Thermal neutron capture cross sections resonance integrals and g-factors". *INDC(NDS)* (2003), p. 440.

[178] *X-Ray Mass Attenuation Coefficients*. https://physics.nist.gov/PhysRefData/XrayMassCoef/tab3.html. 2021.

[179] AM Gicking, K Takahashi, and KS Krane. "Neutron capture cross sections of stable Cd isotopes". *The European Physical Journal A* 55.4 (2019), pp. 1–10.

[180] D Decat and P Del Marmol. "Thermal Neutron Activation Cross Section of 116Cd for the Production of the 117Cd Isomers". *Radiochimica Acta* 6.1 (1966), pp. 29–31.

[181] CW Tang, RL Eng, and CD Coryell. *Isomeric-yield ratios of sup117 Cd in the (n, gamma) and (d, p) reactions.* Tech. rep. Massachusetts Inst. of Tech., Cambridge, 1973.

[182] S Pearlstein and RF Milligan. "Thermal cross section and resonance integrals of cadmium-114". *Nuclear Science and Engineering* 26.2 (1966), pp. 281–282.

[183] R Jo Prestwood and BP Bayhurst. "(n, 2 n) Excitation Functions of Several Nuclei from 12.0 to 19.8 Mev". *Physical Review* 121.5 (1961), p. 1438.

[184] Wen-deh Lu, N Ranakumar, and RW Fink. "Activation Cross Sections for (n, 2 n) Reactions at 14.4 MeV in the Region Z= 40- 60: Precision Measurements and Systematics". *Physical Review C* 1.1 (1970), p. 350.

[185] CS Khurana and HS Hans. "Cross-sections for (n, 2n) reactions at 14.8 MeV". *Nuclear Physics* 28.4 (1961), pp. 560–569.

[186] Emil Beták et al. "Activation cross sections for reactions induced by 14 MeV neutrons on natural tin and enriched 112Sn targets with reference to 111In production via radioisotope generator 112Sn (n, 2n) 111Sn→ 111In". *Radiochimica Acta* 93.6 (2005), pp. 311–326.

[187] Michael Fleming, Jiri Kopecky, and Jean-Christophe Sublet. *Integro-Differential Verification and Validation, FISPACT-II & TENDL-2014 nuclear data libraries*. Culham Centre for Fusion Energy, 2015.

[188] SG Cohen, PS Fisher, and EK Warburton. "Inverse Photonuclear Reactions N 14 (p, γ) O 15 and N 15 (p, γ) O 16 in the Region of the Giant Resonance". *Physical Review* 121.3 (1961), p. 858.

[189] HG Wahsweiler and Walter Greiner. "Angular Distributions for the Inverse Photonuclear Process in Si 28 IN the Eigenchannel Reaction Theory". *Physical Review Letters* 19.3 (1967), p. 131.

[190] Peter Mohr et al. "Relation between the 16 O (α, γ) 20 Ne reaction and its reverse 20 Ne (γ, α) 16 O reaction in stars and in the laboratory". *The European Physical Journal A-Hadrons and Nuclei* 27.1 (2006), pp. 75–78.

[191] M Beard et al. "Photonuclear and radiative-capture reaction rates for nuclear astrophysics and transmutation: 92–100 Mo, 88 Sr, 90 Zr, and 139 La". *Physical Review C* 85.6 (2012), p. 065808.

[192] SR Palvanov. "Cross Section of Excitation of Isomer States 81m,gSe in the Reaction (γ, n) and (n, 2n)". *Journal of Scientific and Engineering Research* (2018), pp. 41–45.

[193] Shoji Nakamura et al. "Thermal-Neutron Capture Cross Sections and Resonance Integrals of the 80Se (n, γ) 81m, 81gSe Reactions". *Journal of nuclear science and technology* 45.2 (2008), pp. 116–122.

[194] Bernard Keisch. "Yield ratios of isomers produced by neutron activation". *Physical Review* 129.2 (1963), p. 769.

[195] S Torrel and KS Krane. "Neutron capture cross sections of 136, 138, 140, 142 Ce and the decays of 137 Ce". *Physical Review C* 86.3 (2012), p. 034340.

[196] A.V Kyryjenko et al. "Investigation of the cadmium nuclei isomers state excitation in the photonuclear reactions". *Uzhgorod University Scientific Herald, Series Physics* 19 (2006), pp. 85–89.

[197] VV Zerkin and B Pritychenko. "The experimental nuclear reaction data (EXFOR): Extended computer database and Web retrieval system". *Nuclear Instruments and Methods in Physics Research Section A: Accelerators, Spectrometers, Detectors and Associated Equipment* 888 (2018), pp. 31–43.

[198] AM Goryachev. "The studying of the photoneutron reactions cross sections in the region of the giant dipole resonance in zinc, germanium, selenium, and strontium isotopes". *Voprosy Teoreticheskoy i Yadernoy Fiziki* 8 (1982), p. 121.

[199] A Leprêtre et al. "A study of the giant dipole resonance in doubly even tellurium and cerium isotopes". *Nuclear Physics A* 258.2 (1976), pp. 350–364.

[200] TJ Boal, EG Muirhead, and DJS Findlay. "The photoneutron cross section of 151Eu, 153Eu and 156Gd in the giant resonance region". *Nuclear Physics A* 406.2 (1983), pp. 257–268.

[201] BL Berman et al. "Giant resonance in deformed nuclei: Photoneutron cross sections for Eu 153, Gd 160, Ho 165, and W 186". *Physical Review* 185.4 (1969), p. 1576.

[202] MG Davydov et al. "Isomeric ratios of photonuclear reaction yields for gamma activation analysis". *Atomnaya Ehnergiya* 58.1 (1985), pp. 47–50.

[203] VM Mazur, IV Sokolyuk, and ZM Bigan. "Transversal cross sections of (. gamma., n) sup m reaction for sup 78, 80'82 Se in region of giant E1-resonance. Poperechnye secheniya reaktsii (gamma, n) sup m dlya yader sup 78'80'82 Se v oblati gigantskogo E1-rezonansa". *Yadernaya Fizika;(USSR)* 54.4 (1991).

[204] Hoang Dac Luc et al. "Isomeric Yield Ratios In The Productions of Sm143m, g Sm143m, g Sm143m, g Sm143m, g by 14 MeV Neutrons and 15-20.5 MeV Bremstrahlungs, Bulg". *J. Phys* 14.2 (1987), pp. 152–156.

[205] VM Mazur, ZM Bigan, and DM Symochko. "Excitation of 109Pd and 112In nuclear isomers in (γ, n) reactions". *Physics of Particles and Nuclei Letters* 5.4 (2008), pp. 374–378.

[206] AG Belov et al. "Excitation of isomeric 1h11/2 states in the reactions (γ, n)". *Physics of Atomic Nuclei* 59.4 (1996), pp. 553–559.

[207] Tran Duc Thiep et al. "Isomeric ratio of 137mCe to 137gCe produced in 138Ce (γ, n) 137m, gCe photonuclear reaction induced by end-point bremsstrahlung energies from 14 to 17, 21 to 23 and at 19 MeV". *Journal of Radioanalytical and Nuclear Chemistry* 311.1 (2017), pp. 887–892.

[208] SR Palvanov and O Razhabov. "Isomer yield ratios of photonuclear reactions at E γmax 25 and 30 MeV". *Atomic Energy* 87.1 (1999), pp. 533–536.

[209] SR Palvanov, FR Egamova, and MI Mamayusupova. "Study Of Isomer Ratio in (n; 2n) and (γ, n) Reactions on the 140Ce Nucleus". *Acta Physica Polonica B, Proceedings Supplement* 14.4 (2021), pp. 827–833.

[210] VM Mazur, ZM Bigan, and PS Derechkej. "Study of the excitation of 11/2- isomeric state of the nucleus 139 Ce in reaction (gamma, n) m in the giant E1-resonance region". *Yaderna Fyizika ta Energetika* 18.2 (2017), pp. 146–150.

[211] N Tsoneva et al. "Isomeric ratios in odd N= 81 isotones". *AIP Conference Proceedings*. Vol. 529. 1. American Institute of Physics. 2000, pp. 753–756.

[212] AG Belov et al. "Excitation of isomeric 1h 11/2 states in nuclear reactions induced by γ rays and neutrons and in beta decay". *Physics of Atomic Nuclei* 64.11 (2001), pp. 1901–1908.

Appendix A

Geant4 simulation codes

Geant4 simulation code written in C++ programming language to mimic the experimental setup and simulate the bremsstrahlung and neutron energy flux is given in this Appendix

A.1 Main program

```
#include "B1DetectorConstruction.hh"
#include "B1ActionInitialization.hh"
#include "Shielding.hh"
#ifdef G4MULTITHREADED
#include "G4MTRunManager.hh"
#else
#include "G4RunManager.hh"
#endif
#include "G4UImanager.hh"
#include "B3PhysicsList.hh"
#include "G4VisExecutive.hh"
#include "G4UIExecutive.hh"
#include "Randomize.hh"
#include "Shielding.hh"
int main(int argc,char** argv)
{
#ifdef G4MULTITHREADED
  G4MTRunManager* runManager = new G4MTRunManager;
  runManager->SetNumberOfThreads(16);
#else
```

```
  G4RunManager* runManager = new G4RunManager;
#endif
  runManager->SetUserInitialization(new B1DetectorConstruction
     ());
  runManager->SetUserInitialization(new Shielding);
  runManager->SetUserInitialization(new B1ActionInitialization
     ());
  runManager->Initialize();
  G4VisManager* visManager = new G4VisExecutive;
  G4UImanager* UImanager = G4UImanager::GetUIpointer();
  if (argc!=1)
    {
      G4String command = "/control/execute ";
      G4String fileName = argv[1];
      UImanager->ApplyCommand(command+fileName);
    }
  else {
G4UIExecutive* ui = 0;
      if ( argc == 1 ) {
        ui = new G4UIExecutive(argc, argv);
      }
        UImanager->ApplyCommand("/control/execute init_vis.mac
           ");
        ui->SessionStart();
        delete ui;
  }
  delete visManager;
  delete runManager;
}
```

A.2 Geometry declaration

A.2.1 Bremsstrahlung irradiation

```
#include "B1DetectorConstruction.hh"
#include "G4RunManager.hh"
#include "G4NistManager.hh"
#include "G4Box.hh"
#include "G4Tubs.hh"
#include "G4LogicalVolume.hh"
#include "G4PVPlacement.hh"
#include "G4RotationMatrix.hh"
#include "G4Transform3D.hh"
#include "G4SDManager.hh"
#include "G4MultiFunctionalDetector.hh"
#include "G4VPrimitiveScorer.hh"
#include "G4PSEnergyDeposit.hh"
#include "G4PSDoseDeposit.hh"
#include "G4VisAttributes.hh"
#include "G4PhysicalConstants.hh"
#include "G4SystemOfUnits.hh"
#include "G4SubtractionSolid.hh"
#include "G4GeometryManager.hh"
#include "G4PhysicalVolumeStore.hh"
#include "G4LogicalVolumeStore.hh"
#include "G4SolidStore.hh"
#include "G4UnionSolid.hh"
#define N_CHAMBER 4
#define N_SAMPLE 121*3
#define N_SAMPLE_ONE 121

B1DetectorConstruction::B1DetectorConstruction()
: G4VUserDetectorConstruction(),
  fScoringVolume(0) { }
B1DetectorConstruction::~B1DetectorConstruction() { }
G4VPhysicalVolume* B1DetectorConstruction::Construct()
{
```

```
G4NistManager* nist = G4NistManager::Instance();
G4bool checkOverlaps = true;
G4double world_sizeXY = 40.*cm;
G4double world_sizeZ  = 80.*cm;
G4Material* world_mat = nist->FindOrBuildMaterial("
   G4_Galactic");
G4Box* solidWorld =
        new G4Box("World",
                  0.5*world_sizeXY, 0.5*world_sizeXY, 0.5*
                     world_sizeZ);
G4LogicalVolume* logicWorld =
        new G4LogicalVolume(solidWorld,
                            world_mat,
                            "World");
G4VPhysicalVolume* physWorld =
        new G4PVPlacement(0, G4ThreeVector(), logicWorld,
           "World", 0, false, 0, checkOverlaps);
G4double primTar_sizeR = 25.*mm;
G4double primTar_sizeZ  = 2.*mm;
G4Tubs* primTar =
        new G4Tubs("PrimaryTarget",0, primTar_sizeR,
           primTar_sizeZ/2,0,twopi);
G4Material* primTar_mat = nist->FindOrBuildMaterial("G4_W
   ");
G4LogicalVolume* logicPrimTar =
        new G4LogicalVolume(primTar, primTar_mat, "
           PrimaryTarget");
G4double primTarZpos=0*mm;
new G4PVPlacement(0, G4ThreeVector(0,0,primTarZpos),
   logicPrimTar, "PrimaryTarget", logicWorld, false, 0,
   checkOverlaps);
G4double nhom_sizeR = 25.*mm;
G4double nhom_sizeZ  = 20.*mm;
G4Tubs* nhom =
```

```
            new G4Tubs("Nhom", 0, nhom_sizeR,nhom_sizeZ/2,0,
                twopi);
    G4Material* nhom_mat = nist->FindOrBuildMaterial("G4_Al");
    G4LogicalVolume* logicNhom =
            new G4LogicalVolume(nhom, nhom_mat, "Nhom");
    G4double nhomZpos=nhom_sizeZ/2. + primTar_sizeZ/2.;
    new G4PVPlacement(0, G4ThreeVector(0,0,nhomZpos),
        logicNhom, "Nhom", logicWorld, false, 0, checkOverlaps)
        ;
    G4double secTar_sizeR = 5.*mm;
    G4double secTar_sizeZ  = 0.05*mm;
    G4Tubs* secTar =
            new G4Tubs("SecondaryTarget", 0, secTar_sizeR,
                secTar_sizeZ/2, 0, twopi);
    G4Material* secTar_mat = nist->FindOrBuildMaterial("G4_Eu
        ");
    G4LogicalVolume* logicSecTar =
            new G4LogicalVolume(secTar, secTar_mat, "
                SecondaryTarget");
    G4double distanceSecTar=3.*cm;
    G4double secTarZpos = primTar_sizeZ/2+nhom_sizeZ+
        distanceSecTar+secTar_sizeZ/2.;
    new G4PVPlacement(0, G4ThreeVector(0,0,secTarZpos),
        logicSecTar, "SecondaryTarget", logicWorld, false, 0,
        checkOverlaps);
    fScoringVolume = logicSecTar;
    return physWorld;
}
```

A.2.2 Neutron irradiation

```
#include "B1DetectorConstruction.hh"
#include "G4RunManager.hh"
#include "G4NistManager.hh"
```

```
#include "G4Box.hh"
#include "G4Tubs.hh"
#include "G4LogicalVolume.hh"
#include "G4PVPlacement.hh"
#include "G4RotationMatrix.hh"
#include "G4Transform3D.hh"
#include "G4SDManager.hh"
#include "G4MultiFunctionalDetector.hh"
#include "G4VPrimitiveScorer.hh"
#include "G4PSEnergyDeposit.hh"
#include "G4PSDoseDeposit.hh"
#include "G4VisAttributes.hh"
#include "G4PhysicalConstants.hh"
#include "G4SystemOfUnits.hh"
#include "G4SubtractionSolid.hh"
#include "G4GeometryManager.hh"
#include "G4PhysicalVolumeStore.hh"
#include "G4LogicalVolumeStore.hh"
#include "G4SolidStore.hh"
#include "G4UnionSolid.hh"
#define N_CHAMBER 4
#define N_SAMPLE 121*3
#define N_SAMPLE_ONE 121

B1DetectorConstruction::B1DetectorConstruction()
: G4VUserDetectorConstruction(),
  fScoringVolume(0) { }
B1DetectorConstruction::~B1DetectorConstruction() { }
G4VPhysicalVolume* B1DetectorConstruction::Construct()
{
    G4GeometryManager::GetInstance()->OpenGeometry();
    G4PhysicalVolumeStore::GetInstance()->Clean();
    G4LogicalVolumeStore::GetInstance()->Clean();
    G4SolidStore::GetInstance()->Clean();
```

```
G4NistManager* nist = G4NistManager::Instance();
G4bool checkOverlaps = true;
G4double world_sizeXY = 200.*cm;
G4double world_sizeZ  = 200.*cm;
G4Material* world_mat = nist->FindOrBuildMaterial("
    G4_Galactic");
G4Box* solidWorld =
  new G4Box("World",0.5*world_sizeXY, 0.5*world_sizeXY, 0.5*
      world_sizeZ);
G4LogicalVolume* logicWorld =
  new G4LogicalVolume(solidWorld, world_mat, "World");
G4VPhysicalVolume* physWorld =
  new G4PVPlacement(0, G4ThreeVector(), logicWorld, "World",
       0, false, 0, checkOverlaps);
G4double GM_sizeXY = 120.*cm;
G4double GM_sizeZ  = 120.*cm;
G4Material* GM_mat = nist->FindOrBuildMaterial("G4_GRAPHITE
    ");
G4Box* solidGM =
  new G4Box("GraphiteModerator", 0.5*GM_sizeXY, 0.5*
      GM_sizeXY, 0.5*GM_sizeZ);
G4LogicalVolume* logicGM =
  new G4LogicalVolume(solidGM, GM_mat, "GraphiteModerator");
G4VPhysicalVolume* physGM=new G4PVPlacement(0, G4ThreeVector
    (0,0,0),"GraphiteModeratorPV", logicGM, physWorld, false,
     0, checkOverlaps);
G4double BP_sizeR = 3.*cm;
G4double BP_sizeZ  = 60*cm-0.5*cm;
G4Material* BP_mat = nist->FindOrBuildMaterial("G4_Galactic
    ");
G4Tubs* solidBP =
  new G4Tubs("BeamPipe", 0, BP_sizeR,BP_sizeZ/2,0,twopi);
G4LogicalVolume* logicBP =
```

```
            new G4LogicalVolume(solidBP, BP_mat, "
                BeriliumChamber");
G4double BP_posZ = GM_sizeZ/2 - BP_sizeZ/2;
new G4PVPlacement(0, G4ThreeVector(0,0,BP_posZ), "
    BeriliumChamberPV", logicBP, physGM, false, 0,
    checkOverlaps);
G4double BeC_sizeY = 20.*cm;
G4double BeC_sizeXZ  = 50.*cm;
G4Material* BeC_mat = nist->FindOrBuildMaterial("G4_Be");
G4Box* solidBeC =
            new G4Box("BeriliumChamber",              0.5*
                BeC_sizeXZ, 0.5*BeC_sizeY, 0.5*BeC_sizeXZ);
G4Tubs* solidBP_4sub =
  new G4Tubs("BeamPipe_4sub", 0, BP_sizeR,BP_sizeZ/2,0,twopi
      );
G4VSolid* solidBeC_sub  = new G4SubtractionSolid("
    BeriliumChamber-BeamPipe", solidBeC, solidBP_4sub, 0,
    G4ThreeVector(0.,0.,BP_posZ));
G4LogicalVolume* logicBeC =
            new G4LogicalVolume(solidBeC_sub, BeC_mat, "
                BeriliumChamber");
G4PVPlacement* physBeC = new G4PVPlacement(0, G4ThreeVector
    (0,0,0), "BeriliumChamberPV", logicBeC, physGM, false, 0,
     checkOverlaps);
G4double UTar_sizeR = 1*cm;
G4double UTar_sizeZ  = 1.*cm;
//G4Material* UTar_mat = nist->FindOrBuildMaterial("G4_U");
G4Material* UTar_mat = nist->FindOrBuildMaterial("G4_U");
G4double* isoi=UTar_mat->GetElement(0)->
    GetRelativeAbundanceVector();
size_t niso=UTar_mat->GetElement(0)->GetNumberOfIsotopes();
G4cout<<"NIST NATURAL URANIUM"<<G4endl;
for (G4int i=0;i<niso;i++)
```

```
{G4cout<<UTar_mat->GetElement(0)->GetIsotope(i)->GetName()
   <<" - fraction = "<<isoi[i]<<G4endl;}
G4Tubs* solidUTar =
  new G4Tubs("UraniumTarget", 0, UTar_sizeR,UTar_sizeZ/2,0,
     twopi);
G4LogicalVolume* logicUTar =
        new G4LogicalVolume(solidUTar, UTar_mat, "
           UraniumTarget");
new G4PVPlacement(0, G4ThreeVector(0,0,0), "UraniumTargetPV
   ", logicUTar, physBeC, false, 0, checkOverlaps);
G4double SC_sizeY = 2.*cm;
G4double SC_sizeXZ  = 50.*cm;
G4Material* SC_mat = nist->FindOrBuildMaterial("G4_AIR");
G4Box* solidSC[N_CHAMBER];
G4LogicalVolume* logicSC[N_CHAMBER];
G4VPhysicalVolume* physSC[N_CHAMBER];
G4double SC_posY[]={-30*cm,-15*cm,15*cm,30*cm};
G4double Sample_R_out = 1.*cm;
G4double Sample_R_in = 0.*cm;
G4double Sample_Z = 1.5*cm;
G4Tubs* solidSample[N_SAMPLE];
G4LogicalVolume* logicSample[N_SAMPLE];
G4double Sample_posXpos[]={-24*cm,-19*cm,-14*cm, -9*cm, -4*
   cm,0*cm, 4*cm, 9*cm,14*cm,19*cm, 24*cm};
G4double Sample_posZpos[]={-24*cm,-19*cm,-14*cm, -9*cm, -4*
   cm,0*cm, 4*cm, 9*cm,14*cm,19*cm, 24*cm};
G4Material* Sample_mat = nist->FindOrBuildMaterial("G4_Cd");
for (G4int i=0;i<N_CHAMBER;i++){
    char tmp[50];
    sprintf(tmp,"_%d",i);
    G4String tmpid=(G4String) tmp;
    solidSC[i] =
            new G4Box("SampleChamber"+tmpid, 0.5*SC_sizeXZ,
               0.5*SC_sizeY, 0.5*SC_sizeXZ);
```

```
    logicSC[i] =
            new G4LogicalVolume(solidSC[i], SC_mat, "
                SSSSampleChamber"+tmpid);
    physSC[i] = new G4PVPlacement(0, G4ThreeVector(0,SC_posY
        [i],0), "SampleChamberPV"+tmpid, logicSC[i], physGM,
        false, 0, checkOverlaps);
}
G4int nn = N_SAMPLE_ONE;
G4int n = (G4int) sqrt(N_SAMPLE_ONE);
G4int nchamberwsample = 3;
G4int chamberids[] ={0,2,3};
for (G4int i=0;i<nchamberwsample;i++){
    for (G4int k=0;k<nn;k++){
        G4int j = i*N_SAMPLE_ONE+k;
        G4int xx = k/n;
        G4int zz = k%n;
        char tmp[50];
        sprintf(tmp,"_%d",j);
        G4String tmpid=(G4String) tmp;
        solidSample[j] =
                new G4Tubs("SampleSolid"+tmpid, Sample_R_in,
                    Sample_R_out,Sample_Z/2,0,twopi);
        logicSample[j] =
                new G4LogicalVolume(solidSample[j],
                    Sample_mat, "Sample"+tmpid);
        G4RotationMatrix* rotM = new G4RotationMatrix;
        rotM->rotateX(90.*deg);
        new G4PVPlacement(rotM, G4ThreeVector(Sample_posXpos
            [xx],0,-Sample_posZpos[zz]), "SamplePV"+tmpid,
            logicSample[j], physSC[chamberids[i]], false, 0,
            checkOverlaps);
    }
}
fScoringVolume = logicSC[0];
```

```
    for (G4int i=0;i<N_SAMPLE;i++){
         logicSample[i]->SetVisAttributes(Yellow);
    }
  return physWorld;
}
```

A.3 Stepping Actions

```
#include "B1SteppingAction.hh"
#include "B1EventAction.hh"
#include "B1DetectorConstruction.hh"
#include "G4Step.hh"
#include "G4Event.hh"
#include "G4RunManager.hh"
#include "G4LogicalVolume.hh"
#include "G4SystemOfUnits.hh"
#include "g4root.hh"

B1SteppingAction::B1SteppingAction(B1EventAction* eventAction)
: G4UserSteppingAction(),
  fEventAction(eventAction),
  fScoringVolume(0)
{}
B1SteppingAction::~B1SteppingAction()
{}
void B1SteppingAction::UserSteppingAction(const G4Step* step)
{
  if (!fScoringVolume) {
    const B1DetectorConstruction* detectorConstruction
      = static_cast<const B1DetectorConstruction*>
        (G4RunManager::GetRunManager()->
           GetUserDetectorConstruction());
    fScoringVolume = detectorConstruction->GetScoringVolume();
```

```
  }
  G4LogicalVolume* volume
    = step->GetPreStepPoint()->GetTouchableHandle()
      ->GetVolume()->GetLogicalVolume();//prestep on Primary
          target
  if (volume != fScoringVolume) return;
  G4double preE=step->GetPreStepPoint()->GetKineticEnergy();
  if (step->GetPreStepPoint()->GetStepStatus()==fGeomBoundary
     &&step->GetTrack()->GetDefinition()->GetParticleName()=="
     gamma"&&preE>0){
       //G4cout<<"eeee"<<preE<<G4endl;
       G4AnalysisManager* analysisManager = G4AnalysisManager::
          Instance();
       analysisManager->FillNtupleDColumn(0,0);
       analysisManager->FillNtupleDColumn(1,preE);
       analysisManager->AddNtupleRow();
  }
  G4double edepStep = step->GetTotalEnergyDeposit();
  fEventAction->AddEdep(edepStep);
}
```

A.4 Run Actions

A.4.1 Bremsstrahlung irradiation

```
    #include "B1RunAction.hh"
#include "PrimaryGeneratorAction.hh"
#include "B1DetectorConstruction.hh"
// #include "B1Run.hh"
#include "G4RunManager.hh"
#include "G4Run.hh"
#include "G4AccumulableManager.hh"
#include "G4LogicalVolumeStore.hh"
#include "G4LogicalVolume.hh"
```

```
#include "G4UnitsTable.hh"
#include "G4SystemOfUnits.hh"
#include "G4GeneralParticleSource.hh"

class G4GeneralParticleSource;
B1RunAction::B1RunAction()
: G4UserRunAction(),
  fEdep(0.),
  fEdep2(0.)
{
  // Register accumulable to the accumulable manager
  G4AccumulableManager* accumulableManager =
      G4AccumulableManager::Instance();
  accumulableManager->RegisterAccumulable(fEdep);
  accumulableManager->RegisterAccumulable(fEdep2);
  G4AnalysisManager* analysisManager=G4AnalysisManager::
      Instance();
  analysisManager->CreateNtuple("BremSpec","step Inform");
  analysisManager->CreateNtupleDColumn("id");
  analysisManager->CreateNtupleDColumn("E");
  analysisManager->FinishNtuple();
}
B1RunAction::~B1RunAction()
{}
void B1RunAction::BeginOfRunAction(const G4Run*)
{
  G4RunManager::GetRunManager()->SetRandomNumberStore(false);
  G4AccumulableManager* accumulableManager =
      G4AccumulableManager::Instance();
  accumulableManager->Reset();
  G4AnalysisManager* analysisManager = G4AnalysisManager::
      Instance();
  G4String fileName = "result";
  analysisManager->OpenFile(fileName);
```

```
}
void B1RunAction::EndOfRunAction(const G4Run* run)
{
  G4int nofEvents = run->GetNumberOfEvent();
  if (nofEvents == 0) return;
  G4AccumulableManager* accumulableManager =
     G4AccumulableManager::Instance();
  accumulableManager->Merge();
  G4double edep  = fEdep.GetValue();
  G4double edep2 = fEdep2.GetValue();
  G4double rms = edep2 - edep*edep/nofEvents;
  if (rms > 0.) rms = std::sqrt(rms); else rms = 0.;
  const B1DetectorConstruction* detectorConstruction
   = static_cast<const B1DetectorConstruction*>
     (G4RunManager::GetRunManager()->
        GetUserDetectorConstruction());
  G4double mass = detectorConstruction->GetScoringVolume()->
     GetMass();
  G4double dose = edep/mass;
  G4double rmsDose = rms/mass;
  const PrimaryGeneratorAction* generatorAction
   = static_cast<const PrimaryGeneratorAction*>
     (G4RunManager::GetRunManager()->
        GetUserPrimaryGeneratorAction());
  G4String runCondition;
  if (generatorAction)
  {
    const G4GeneralParticleSource* particleGun =
       generatorAction->GetParticleGun();
    runCondition += particleGun->GetParticleDefinition()->
       GetParticleName();
    runCondition += " of ";
    G4double particleEnergy = particleGun->GetParticleEnergy()
       ;
```

```
    runCondition += G4BestUnit(particleEnergy,"Energy");
  }
  G4AnalysisManager* analysisManager = G4AnalysisManager::
      Instance();
  analysisManager->Write();
  analysisManager->CloseFile();
  if (IsMaster()) {
    G4cout
     << G4endl
     << "--------------------End of Global Run
        ------------------------------";
  }
  else {
    G4cout
     << G4endl
     << "--------------------End of Local Run
        ------------------------------";
  }
}
void B1RunAction::AddEdep(G4double edep)
{
  fEdep  += edep;
  fEdep2 += edep*edep;
}
```

A.4.2 Neutron irradiation

```
#include "B1SteppingAction.hh"
#include "B1EventAction.hh"
#include "B1DetectorConstruction.hh"
#include "G4Step.hh"
#include "G4Event.hh"
#include "G4RunManager.hh"
#include "G4LogicalVolume.hh"
```

```
#include "G4SystemOfUnits.hh"
#include "g4root.hh"
B1SteppingAction::B1SteppingAction(B1EventAction* eventAction)
: G4UserSteppingAction(),
  fEventAction(eventAction),
  fScoringVolume(0) {}
B1SteppingAction::~B1SteppingAction() {}
void B1SteppingAction::UserSteppingAction(const G4Step* step)
{
  if (!fScoringVolume) {
    const B1DetectorConstruction* detectorConstruction
      = static_cast<const B1DetectorConstruction*>
        (G4RunManager::GetRunManager()->
           GetUserDetectorConstruction());
    fScoringVolume = detectorConstruction->GetScoringVolume();
  }
  // get volume of the current step
  G4LogicalVolume* volume
    = step->GetPreStepPoint()->GetTouchableHandle()
      ->GetVolume()->GetLogicalVolume();//prestep on Primary
         target
  G4String volumeName= volume->GetName();
  if (volumeName.substr(0,6) != "Sample") return;
  G4int volumenum=atoi((volumeName.substr(7,volumeName.length
     ()-6)).c_str());
  G4double preE=step->GetPreStepPoint()->GetKineticEnergy()/
     keV;
  if (step->GetTrack()->GetDefinition()->GetParticleName()=="
     neutron"
          &&preE>0){
    //G4cout<<"vol. "<<volumenum<<"- E = "<<preE<<G4endl;
    G4AnalysisManager* analysisManager = G4AnalysisManager::
       Instance();
    analysisManager->FillNtupleDColumn(0,volumenum);
```

```
        analysisManager->FillNtupleDColumn(1,preE);
        analysisManager->AddNtupleRow();
    }
    if (volume != fScoringVolume) return;
    G4double preE=step->GetPreStepPoint()->GetKineticEnergy();
    if (step->GetPreStepPoint()->GetStepStatus()==fGeomBoundary
       &&step->GetTrack()->GetDefinition()->GetParticleName()=="
       gamma"&&preE>0){
        G4AnalysisManager* analysisManager = G4AnalysisManager::
            Instance();
        analysisManager->FillNtupleDColumn(0,0,preE);
        analysisManager->AddNtupleRow(0);
    }
    // collect energy deposited in this step
    G4double edepStep = step->GetTotalEnergyDeposit();
    fEventAction->AddEdep(edepStep);
}
```

Appendix B

Input file of TALYS code

This work has used not only default parameters but also adjusted parameters in TALYS 1.95 code. To calculate the differential cross-section of isotopes of interest, the parameters relating to the level density models and gamma strength functions have also been taken into account. One typical input file consists of the following parameters:

Input keywords for TALYS calculations

\# **General**

projectile g

element Eu

mass 0

energy 8.0 25. 0.1

channels y

\# **Compound nucleus**

compound y

widthmode 1

resonance y

\# **Pre-equilibrium**

preeqmode 2

mpreeqmode 2

preeqspin 1

\# **Gamma emission**

gammax 6

strength 1

strengthM1 2

\# **Level densities**

ldmodel 1

shellmodel 1

spincutmodel 1

Output

fileresidual y

components y

Appendix C

CERN ROOT analysis code to calculate IRs using energy flux spectra from GEANT4 and the cross-section outputs from TALYS

```
#include "TF1.h"
#include "TTree.h"
#include "TFile.h"
#include "TH1.h"
#include "TGraph.h"
TGraph* grc_Ce137g;
TGraph* grc_Ce137m;
TGraph* grflux;

Double_t grc_Ce137g_tf1_f(Double_t *x, Double_t *) { return
   grc_Ce137g->Eval(x[0]);}
Double_t grc_Ce137m_tf1_f(Double_t *x, Double_t *) { return
   grc_Ce137m->Eval(x[0]);}
Double_t grflux_tf1_f(Double_t *x, Double_t *) {
    if (x[0]>25000000) return 0;
    else
        return grflux->Eval(x[0]);}
Double_t grProd_Ce137g_tf1_f(Double_t *x, Double_t *) {
    if (x[0]>25000000) {
```

```
        return 0;
    }else{
        return grc_Ce137g->Eval(x[0])*grflux->Eval(x[0]);
    }
}
Double_t grProd_Ce137m_tf1_f(Double_t *x, Double_t *) {
    if (x[0]>25000000) {
        return 0;
    }else{
        return grc_Ce137m->Eval(x[0])*grflux->Eval(x[0]);
    }
}
void cal()
{
    grc_Ce137g=new TGraph("talyscross_Ce137mg.txt","%lg %lg %*
       lg");
    grc_Ce137m=new TGraph("talyscross_Ce137mg.txt","%lg %*lg %
       lg");
//     grc_Ce137g->Draw("APL");
//     grc_Ce137m->SetLineColor(2);
//     grc_Ce137m->Draw("PLSAME");
    TF1* grc_Ce137g_tf1=new TF1("grc_Ce137g_tf1",
       grc_Ce137g_tf1_f,9000000,30000000);
    TF1* grc_Ce137m_tf1=new TF1("grc_Ce137m_tf1",
       grc_Ce137m_tf1_f,9000000,30000000);
    grc_Ce137g_tf1->SetNpx(2000);
    grc_Ce137m_tf1->SetNpx(2000);
    TFile* f=TFile::Open("hflux_12MeV.root");
    TH1F* hflux = (TH1F*)f->Get("hflux");
    //hflux->Draw();
    Int_t nbins = hflux->GetNbinsX();
    Double_t xx[500];
    Double_t yy[500];
    for (Int_t i=0;i<nbins;i++){
```

```
        xx[i] = hflux->GetBinCenter(i+1);
        yy[i] = hflux->GetBinContent(i+1)/hflux->GetBinWidth
            (1);
    }
    grflux = new TGraph(nbins,xx,yy);
    TF1* grflux_tf1=new TF1("grflux_tf1",grflux_tf1_f
        ,9000000,30000000);
    TF1* grProd_Ce137g_tf1=new TF1("grProd_Ce137g_tf1",
        grProd_Ce137g_tf1_f,9000000,30000000);
    TF1* grProd_Ce137m_tf1=new TF1("grProd_Ce137m_tf1",
        grProd_Ce137m_tf1_f,9000000,30000000);
    //grc_Ce137g_tf1->Draw();
    //grc_Ce137m_tf1->Draw("same");
    grflux_tf1->Draw();
    grProd_Ce137g_tf1->Draw("same");
    grProd_Ce137m_tf1->Draw("same");
    cout<<grProd_Ce137g_tf1->Integral
        (10000000,25000000,0.0001)<<endl;
    cout<<grProd_Ce137m_tf1->Integral
        (10000000,25000000,0.0001)<<endl;
    cout<<grProd_Ce137m_tf1->Integral
        (10000000,25000000,0.0001)/grProd_Ce137g_tf1->Integral
        (10000000,25000000,0.0001)<<endl;
    for (Int_t i=0;i<grc_Ce137g->GetN();i++){
        cout<<grc_Ce137g->GetX()[i]<<"\t"<<grflux_tf1->Eval(
            grc_Ce137g->GetX()[i])<<endl;
    }
}
```